# Two dimensional flow of variable viscosity fluids

by

Maashutha Samuel Tshehla,

B.Sc., B.Sc. Hons., M.Sc., (Appl. Maths., UNIN)

Thesis Presented for the Degree of

**DOCTOR OF PHILOSOPHY**

in the Department of Mathematics and Applied Mathematics

FACULTY OF SCIENCE

UNIVERSITY OF CAPE TOWN





August 31, 2009

**Supervisor: Prof. T. G. Myers**

# Abstract

This work concerns the flow of variable viscosity fluids with a free surface and between parallel plates.

In Chapters 3 and 4, the study is extended to shear rate dependent viscosity models; namely the power law, Carreau and Ellis models, for both flows with a free surface and between parallel plates. Analytical and numerical techniques are employed to solve for the velocity, flow rate and temperature profiles. In general, the Carreau model cannot be solved analytically. However, the case where a small variation in the viscosity is considered allows for analytical progress. The results for the shear rate viscosity models reveal that the flow controlling parameters such as the power law index have a profound effect on the velocity, viscosity, flow rate and temperature of the fluid. The viscosity models were further investigated for specific polymeric materials and the results revealed that the power law model fails to predict the flow accurately, particularly in low shear rate regions.

In Chapter 5, a temperature dependent viscosity model is investigated for both flows with a free surface and between parallel plates. Shear heating effects are included and the fluid viscosity decreases exponentially with temperature. For flow with a free surface, the solutions for the velocity, flow rate and temperature profiles are obtained by using an asymptotic analytical technique and subsequently, the Runge−Kutta numerical scheme is applied to gain a full solution. In general, the results illustrate that when the viscosity variation parameter increases the viscosity of the fluid decreases. The velocity and tem-

perature increases when the viscosity variation parameter increases. The flow controlling parameters such as the Brinkman and Biot numbers have a significant effect on both the resulting velocity and the temperature profiles of the fluid. For flow between parallel plates, the temperature dependent model allows for analytical progress when the pressure gradient is neglected. The Runge−Kutta method and the shooting numerical techniques are used to obtain full solutions for the temperature and velocity profiles. Results illustrate that the Brinkman number influences the flow characteristics significantly since the temperature and velocity of the fluid increases when the Brinkman number is large.

In Chapter 6, surface tension driven flow and first order correction terms for the lubrication theory with different film height is investigated. The predicted profiles show that the velocity and temperature of the fluid increases significantly. For the first order correction terms, the results also show that the reduced Reynolds and Péclet numbers have significant influence on the resulting velocity and temperature profiles.

# Declaration

*Thesis title: Two dimensional flow of variable viscosity fluids*

I hereby grant the University of Cape Town permission to reproduce the above thesis in whole or in part, for the purpose of research.

I hereby declare that:

- the above thesis is my own work and design, apart from the normal guidance from my supervisor,
- neither the substances nor any part of the above thesis has been submitted in the past, or is being, or is to be submitted for another degree or qualification at this or any other University or Institution of higher learning.

Signature:.....

Date:.....

*In loving memory of my two late Brothers Lepekane Pax Tshehla, (1954-2007), and Moshe Moses Tshehla, (1957-2009) who never got the privilege to see the conclusion of this project.....*

# Acknowledgement

A special word of appreciation goes to my supervisor, Professor T. G. Myers, for his high-valued assistance, encouragement and patience during the preparation of this manuscript. Special blessings should go to him in teaching me the intricacies of Latex, Maple and Matlab, operations of which I had little idea. Special words of gratitude go to Dr J. P. F. Charpin for his supererogatory help and support during this project. His valiant effort, determination, and skillful assistance with the computational work is highly appreciated.

My indebtedness to my fellow students with whom I studied in the Department of Mathematics and Applied Mathematics, University of Cape Town. A special word of thanks goes to my colleagues at work, Faculty of Military Science and University of Stellenbosch for their encouragement.

The funding of this project by the National Research Foundation (NRF), South Africa, for the period 2002−2006 is highly acknowledged.

I thank my MOTHER for her guidance through my youth days. I 'm indebted to all my brothers and sisters for believing in me and giving me the inspiration to hold on. Above all, my sincere gratitude goes to ALMIGHTY GOD WHO kept me ALIVE against all ODDS!!!

University of Cape Town , South Africa Sam Tshehla

August 31, 2009

# Contents

# List of Figures

# List of Tables

# Nomenclature

## Notation and typical unit

| Symbol | Name | Unit |
|---|---|---|
| $Bi = (HK_c/k)$ | Biot number | |
| $Br{=}(\mu_0 U^2/\kappa \triangle T)$ | Brinkman number | |
| $c_p$ | Heat capacity | J kg$^{-1}$ K$^{-1}$ |
| $Ec = (U^2/c_p T_0)$ | Eckert number | |
| $C = (\sigma\varepsilon^3/\mu U)$ | Inverse capillary number | |
| $g$ | Acceleration due to gravity | m s$^{-2}$ |
| $\mathbf{g}$ | Acceleration due to gravity vector | m s$^{-2}$ |
| $h$ | Fluid height | m |
| $H$ | Channel height | m |
| $K$ | Parameter in Power law model | |
| $K_c$ | Heat transfer coefficient | |
| $l$ | Parameter in Carreau model | s |
| $L$ | Channel length | m |
| $m$ | Power law consistency coefficient | Pa s$^{\mathrm{n}}$ |
| $n$ | Power law index | |
| $p$ | Pressure | Pa |
| $p_x$ | Pressure gradient | |

| | | |
|---|---|---|
| $\Delta p$ | Pressure drop | Pa |
| $P = \mu_0 U/\epsilon H$ | Pressure scale | |
| $Pe{=}\rho_0 c_p LU/k$ | Peclet number | Pa |
| $Pr = (\mu_0 c_p/\kappa_0)$ | Prandtl number | |
| $Q$ | Flux | $m^3\ s^{-1}$ |
| $Re{=}\rho_0 UL/\mu_0$ | Reynolds number | |
| $t$ | Time | s |
| $T$ | Temperature | °C |
| $T_0$ | Reference temperature | °C |
| $T_a$ | Ambient temperature | °C |
| $T_s$ | Surface temperature | °C |
| $T_u$ | Upper plate reference temperature | °C |
| $T_s$ | Lower plate reference temperature | °C |
| $\Delta T_0$ | Temperature difference | °C |
| $T_1$ | First order temperature perturbation term | °C |
| $u_1$ | First order velocity perturbation term | $m\ s^{-1}$ |
| $U = \rho g H^2 \sin\beta/\mu_0$ | Velocity scale | $m\ s^{-1}$ |
| $\mathbf{u}$ | Total velocity vector | $m\ s^{-1}$ |
| $(u, v)$ | Cartesian velocity | $m\ s^{-1}$ |
| $(x, y)$ | Cartesian coordinate | m |

**Greek letters**

| | |
|---|---|
| $\alpha$ | Non−dimensional coefficient of viscosity variation |
| $\alpha_1$ | Parameter in Ellis model |
| $\beta$ | Inclined angle |
| $\chi$ | Rate of heat production |

| | | |
|---|---|---|
| $\delta = \varepsilon^2 Re$ | Reduced Reynolds number | |
| $\varepsilon = H/L$ | Aspect ratio | |
| $\dot{\gamma} \approx \partial u/\partial y$ | Shear rate | |
| $\kappa$ | Thermal conductivity | W $m^{-1}$ $K^{-1}$ |
| $\mu$ | Dynamic viscosity | |
| $\mu_0$ | Reference viscosity | |
| $\mu_\infty$ | Dynamic viscosity in high shear rate | |
| $\nu = \mu/\rho$ | Kinematic viscosity | |
| $\lambda$ | Characteristic time for the Carreau model | |
| $\Phi$ | Viscous dissipation function | |
| $\phi$ | Parameter in an Ellis model | |
| $\rho$ | Density | kg/$m^{-13}$ |
| $\tau = \mu\dot{\gamma}$ | Shear stress | |
| $\tau_1$ | Critical stress | |
| $\theta$ | Coefficient of viscosity variation | |
| $\vartheta$ | Arbitrary perturbation parameter | |
| $\sigma$ | Surface tension | |
| $\zeta = \varepsilon^2 Pe$ | Reduced Peclet number | |

# Chapter 1

# Introduction



Matter consists of two states, that is, fluid and solid. The distinction between the two is that a solid can resist any applied shear force, whereas fluid cannot. Thus a fluid is a substance that deforms continuously under the application of the shear (tangential) stress no matter how small the shear stress may be. Fluids can be further classified into, liquids and gases, see [36, 95, 114]. Fluid mechanics is defined as the study of the behaviour of fluids either at rest or in motion. This study takes into account the various properties of fluids and their effects on the resulting flow patterns, in addition to the forces acting between the fluid and its boundaries, see [36, 83]. It also encompasses the applications of some fundamental laws such as, conservation of mass, momentum, and energy, with the purpose of explaining observed fluid behaviour and to predict unobserved fluid behaviour.

## 1.1 Historical background

The study of viscous fluids began in ancient times, when man partially solved the problem of viscous resistance without an understanding of mathematics or mechanics. Development was based on trial and error, which often led to disasters and sometimes remarkable successes, see [107]. For example, sailing ships with oars and irrigation systems were both developed in ancient times. Due to the empirical knowledge at the time, ancient Greek

civilisation emerged and subsequently the Roman Empire during the period (285−212 B. C.), see [74]. Greek mathematicians such as Archimedes formulated the laws of buoyancy and applied them to floating and submerged bodies. From both the birth of Christ to the Renaissance, there was steady improvement in the design of flows such as rivers, canals and water conduits, see [74, 83, 115].

However, contributions in the $15^{th}$ century formed the basic foundation of fluid mechanics, and then in the $18^{th}$ century scientists like Reynolds demonstrated that there are two types of flow in nature; namely, laminar and turbulent flows. Laminar flow is characterised by the smooth motion of the fluid and turbulent flow is characterised by irregular and random motion of the fluid. The contributions of Newton, Euler and Bernoulli led to the development of hydromechanics, which is divided into three branches: the first one is hydrodynamics, which is based on theoretical studies of fluid dynamics, the second is hydraulics, which studies the laws of motion of liquids in tubes, pipes and channels, and is based on experimentation, and the third is hydrostatics which deals with the equilibrium of liquids at rest, see [107]. The concept of boundary layer theory was first established by Ludwig Prandtl in the $19^{th}$ century, in an attempt to combine the two concepts of hydraulics and hydrodynamics. The $20^{th}$ century was marked by many contributions from great mathematicians and engineers, such as the development of aircraft which required a degree of understanding of fluid flow and an accurate prediction of the effect of airflow, see [74, 90, 116]. This subsequently led to the development of aerodynamics.



Before proceeding with the objectives and motivation of this study, the broader discussions of concept and ideas that will be required in the subsequent chapters will be given as an overview. We begin with the discussion of viscosity and a description of various fluids in § 1.2 and 1.3, respectively. This will be followed by a brief introduction of the general viscosity models in § 1.4. The aspirations for carrying out this research is given in § 1.5, followed by a review of existing research for these viscosity models. When a free surface is present on a fluid, the surface tension effect may become important. Therefore, surface

tension driven flow will be discussed and existing research and findings are given in § 1.5.3. Finally, § 1.6 highlights the goal of the study and gives the thesis outline.

## 1.2 Viscosity

Viscosity is defined as the physical property that characterises the flow resistance of fluids, see [61]. It is a key factor in determining the amount of fluid flowing in a channel and may be affected by various factors. Factors that affect viscosity are now discussed.

### 1.2.1 Factors affecting viscosity

In fluids, viscosity can be affected significantly by variables such as shear rate, temperature and pressure:

- Shear rate: For shear thinning fluids, the viscosity decreases with increasing shear rate, while in shear thickening fluids the viscosity increases with increasing shear rate.

- Temperature: In most fluids an increase in temperature results in a decrease in viscosity. The effect of temperature on viscosity is essential for materials that will be subjected to temperature variations in their use, such as motor oils, grease and hot-melt adhesives, see [9, 12, 96].

- Pressure: Fluids subjected to extremely high pressure tend to experience an increase in viscosity, see [22, 23].

## 1.3 Newtonian and non−Newtonian fluids

Newtonian and non−Newtonian fluids are now discussed briefly.

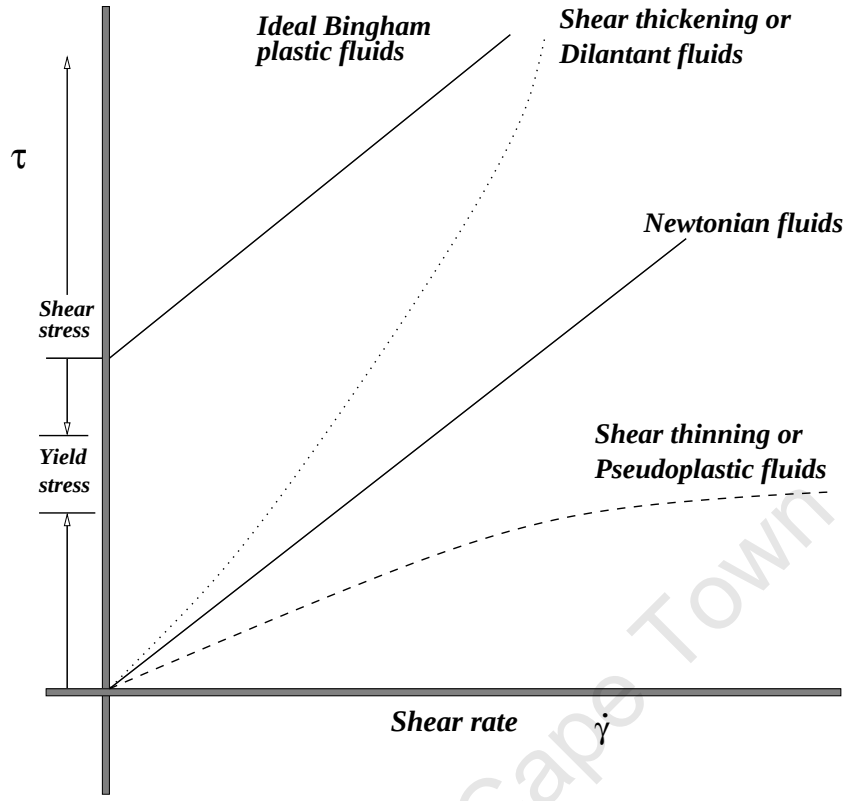


Figure 1.1: Rheological behaviour of various fluids.



### 1.3.1 Newtonian fluids

Fluids which exhibit a linear relationship between the shear stress $\tau$ (the component of stress parallel to the area considered) and the shear rate $\dot{\gamma}$ (the change of shear per unit time), are called Newtonian, as shown in Fig. 1.1. Typical examples of Newtonian fluids include water, alcohol and gasoline, see [12, 22, 23]. Newtonian fluids are described by the relation:

$$\tau = \mu\dot{\gamma} \ , \tag{1.3.1}$$

where $\tau$ is the shear stress of the fluid, $\mu$ is the dynamic viscosity and $\dot{\gamma}$ is the strain rate. This model is widely used in many natural and industrial applications, see [1, 10, 16, 91].

### 1.3.2 Non−Newtonian fluids

Fluids with a non−constant viscosity are called non−Newtonian fluids. These types of fluids exhibit a non−linear relationship between the shear stress and the shear rate as shown in Fig. 1.1. At each specific shear rate, the force required to maintain the motion varies and the viscosity of such fluids will therefore, change as the shear rate varies, see [22, 84]. Typical non−Newtonian fluids include:

- Pseudo−plastics: The dynamic viscosity decreases with increasing shear rate. Examples of pseudo-plastics include, gelatine, clay and blood. This type of flow behaviour is sometimes called shear thinning, see [22, 66, 116].

- Dilatant fluids: These fluids are characterised by an increasing dynamic viscosity with an increase in shear rate, see Fig. 1.1. Dilatancy is frequently observed in fluids such as clay slurries, candy compounds and cornstarch in water. Dilatancy is also referred to as shear thickening flow behaviour, see [90, 96, 116].

There are other types of non−Newtonian fluids like Bingham plastics that behave as a solid under static conditions, see Fig. 1.1. A certain amount of force, called the yield stress, must be applied to the fluid before it starts flowing. Tomato sauce and toothpaste are good examples of this type of fluid. In practice the yield stress will prevent the fluid from pouring from the bottle until the bottle is shaken or struck allowing the fluid to flow freely. Once the yield stress is exceeded and flow begins, plastic fluids may display Newtonian, pseudo−plastic, or dilatant flow characteristics, see [59, 69, 74]. However, although the consequence of these types of fluid is very important in industry, they will not be considered in this study. In the following section the general viscosity models are introduced.

## 1.4 General viscosity models

The study of viscosity models began in the early $18^{th}$ century by Sir Isaac Newton who derived the relation in Equation (1.3.1), see [9]. During the period 1846−1890, Couette and Poiseuille tested Newtonian fluids experimentally and the results revealed that the Newtonian model gives a good fit of data. However, in 1900 several researchers used Equation (1.3.1) to study a wide variety of fluids, see [9]. Their research revealed that many colloidal suspensions and polymer solutions did not obey this linear relation in Equation (1.3.1). This unusual flow behaviour at the time led to further development of Newton's idea to that of non−Newtonian viscosity models, whose viscosity decreases with increasing shear rate, see [9, 61]. Several shear rate dependent viscosity models are available that attempt to describe the non−Newtonian viscosity for shear thinning and shear thickening fluids. These include, the Cross model, Carreau−Yasudau, and the Sisko model [9, 88]. However, their features are similar to the Ellis and Carreau models. Therefore in this study, we will discuss the three shear rate dependent viscosity models namely, the power law, Carreau, and Ellis models and the temperature dependent viscosity model.



### 1.4.1 The power law model

The power law model is one in which the shear stress varies with the power of the strain rate. The viscosity of the fluid $\mu$ can be expressed as:

$$\mu = m\,|\dot{\gamma}|^{n-1}\ , \tag{1.4.2}$$

where $m$ is a constant and $n$ is the power law index. Setting $n = 1$ retrieves the Newtonian case. The case $n < 1$ represents shear thinning fluids, also called pseudo−plastic fluids and as $\dot{\gamma} \to 0$, the viscosity tends to infinity, that is, the power law model predicts that the effective viscosity would decrease with increasing shear rate indefinitely, (see

Fig. 1.1). Examples of shear thinning fluids include fruit juice concentrations, glues, polymer solutions and shampoos. Typically these fluids flow easily under shear stress as some internal structure in the material is broken down, see [9, 68]. Many of these fluids only display shear thinning behaviour at intermediate shear rates. At very low and high shear rate regions, they basically display Newtonian behaviour. To allow such changes in viscosity with respect to shear, the idea of generalised Newtonian fluids was introduced to describe the shear thinning behaviour, see [9]. These generalised Newtonian fluids are primarily used to describe steady state shear flows and also takes into account the variable viscosity effects without normal stress [9, 12]. A fluid whose viscosity increases with shear stress is termed a shear thickening or dilatant fluid, in this case $n > 1$, see [9, 61, 68]. Shear thickening fluids exhibit a fairly concentrated suspension of very small particles, for example, corn-starch and clay slurries. Most shear thickening fluids tend to show shear thinning behaviour at low shear rates, see [43]. Macosko [61] points out that nearly all non−Newtonian fluids show shear thinning behaviour. However, some particular concentrated suspensions show regions of shear thickening. This type of fluid often signals other complications such as instability, phase separation and lack of reversibility. This is one reason why they are less used in industrial practice compared to shear thinning fluids, see [9, 68]. However, in this study we will consider both shear thinning and shear thickening fluids. This is very important for industrial applications since in some polymer solutions or surfactant solutions the power law model can usually be fitted to data with the power law index greater than unity [9].



The power law model is widely applied in industries such as chemical, electro-chemical and pharmaceutical plants, and many heat transfer flow problems have been solved using this model, see [65, 109]. It works relatively well for thick films but it can give divergent results for thin film flow, see [76]. The power law model is useful because of its simplicity, which is another reason for its popularity. When the relationship between $\log(\mu)$ and $\log(u_y)$ is linear, the shear thinning is described by the power law model. However, the power

law model does not describe the behaviour of most shear thinning fluids at very low and high shear rates, and so other models have been suggested to include theses regions, [61]. The models include the Ellis and Carreau models, which exhibit a Newtonian plateau at low shear rates regions. However, unlike the Ellis model, the Carreau model also has a Newtonian plateau at high rates, see [9, 43, 61].

### 1.4.2 The Carreau model

This model gives an expression for the fluid viscosity $\mu$ which varies smoothly from its value at zero shear rate $\mu_0$ to the limiting viscosity at high shear rate $\mu_\infty$. The Carreau model is written:

$$\mu = \mu_\infty + (\mu_0 - \mu_\infty)\left[1 + (\lambda\dot{\gamma})^2\right]^{\frac{n-1}{2}}, \tag{1.4.3}$$

where $\lambda$ and $n$ are the characteristic time and the power law index respectively. Following standard practise, $\mu_\infty$ will henceforth be neglected since its value is always much less than $\mu_0$. Note that when $n = 1$ or $\lambda = 0$, Equation (1.4.3) corresponds to a Newtonian fluid, see [45, 60, 100]. This model poses a challenge since it is more difficult to use than the power law model, as one cannot obtain an analytical solution when describing the fluid film height, and it is therefore less used in practice. However, unlike the power law model, the viscosity of many polymer solutions can be adequately fitted by the Carreau model which gives better predictions for thin film fluids at low shear rate regions, see [61, 76].

### 1.4.3 The Ellis model

The Ellis model is written in the form:

$$\frac{1}{\mu} = \frac{1}{\mu_0}\left[1 + \left|\frac{\mu\ \dot{\gamma}}{\tau_1}\right|^{\alpha_1 - 1}\right], \tag{1.4.4}$$

where $\mu_0$, $\tau_1$ and $\alpha_1$ are, the viscosity at zero shear rate, critical stress and power law index respectively. This model is very important for use in industry, since it overcomes some of

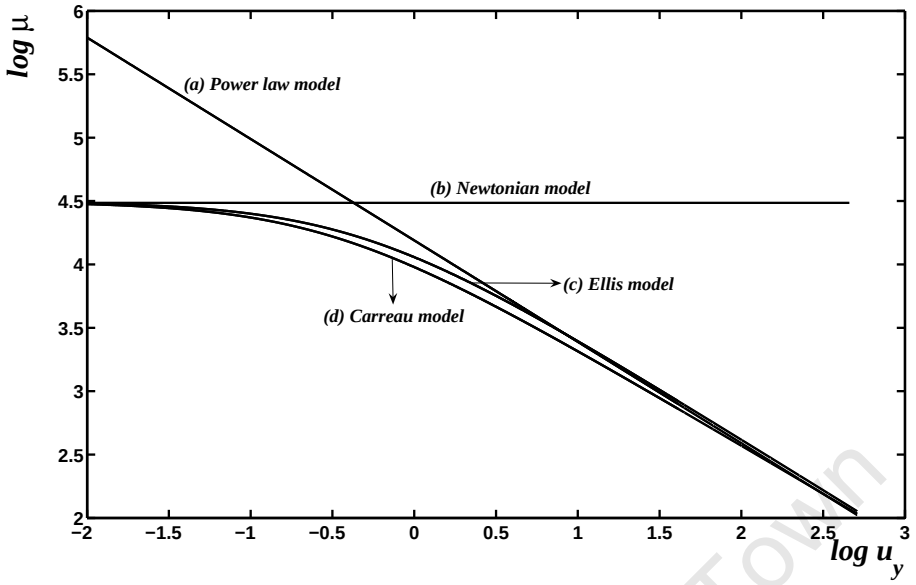


Figure 1.2: Rheological behaviour of viscosity models.

the weaknesses of the power law model. The advantage of this model over the Carreau model is that it is also simple to use and allows for analytical progress when describing the fluid film height. At low shear rates, the Ellis model reduces to the Newtonian model, and at high shear rates the model reduces to the power law model. The Ellis model is often used in the polymer processing industries, see [8, 12, 40].

For illustration purposes, Fig. 1.2 displays the viscosity predicted by the described shear rate dependent viscosity models for aluminum soap. The data can be retrieved from [76]. The figure clearly shows that there is a closer comparison between the Carreau and Ellis models at low shear rates, while the power law model diverges, see § 3.5 for more details. The Newtonian model is constant as displayed in curve (b).

### 1.4.4 The temperature dependent viscosity model

The temperature dependent viscosity model is approximated by the Arrhenius relationship:

$$\mu = \mu_0 e^{-\theta(T-T_0)} \ , \tag{1.4.5}$$

where $\mu_0$ is the reference viscosity at the reference temperature $T_0$ and $\theta$ is the coefficient of viscosity variation with temperature, [24]. This is known as the exponential model for variable viscosity or the Reynolds law, see [67, 77]. In most fluids the greater the viscosity, the stronger the temperature dependence. Equation (1.4.5) has a wide range of practical applications in industry for heat and mass transfer problems, and is also valid for reacting fluids, see [9, 37, 61]. These viscosity models can be retrieved from several references, see [21, 56, 59, 61, 94] for example.

## 1.5 Motivation and literature review

This work is motivated by our interest in studying the hydrodynamics of lubricants in engineering systems with respect to both free surface and parallel plates flow geometry. In engineering systems lubricants are used to reduce friction between the plates or to prevent rusting of the plate's surface. Most of these lubricants are fluids with shear rate dependent viscosity and temperature dependent viscosity. There are many industrial applications for these variable viscosity fluids. For example, the processing of juices, nectars, jellies and melting cheese in the food processing industry as well as polymeric materials in the petrochemical industry. In these situations the determination of certain parameters such as the pressure, velocity and temperature plays an important role in equipment design to improve performance, and productivity, and so there is a need for accurate and tractable solutions, see [62, 84, 89].

In this study, two-dimensional unidirectional fluid flow with variable viscosity will be

considered, either for flow with a free surface or between parallel plates. In § 1.5.1 we will discuss and highlight existing research in literature, involving free surface flow for the shear rate dependent viscosity models and the temperature dependent viscosity model. This will be followed by the discussion of these model for flow between parallel plates in § 1.5.2.

### 1.5.1 Free surface flow

An open channel flow is a flow through a channel whose surface is exposed to the atmospheric pressure and negligible shear stress. The basic balance of the forces is between gravity and viscosity, see [74, 83]. Free surface flow may be complex for a variety of reasons, for example, the geometry of the flow, rough surface and turbulent flow, [95, 115]. Free surface flow appears in a number of practical examples, both artificial (flumes, spillways, canals) and natural (rivers, streams), see [48]. The flow of a thin film fluid with a free surface has been the subject of intense investigation for a number of years and Newtonian fluids are well established in literature, see [22, 47, 84].



#### The power law fluid

One of the most widely used non−Newtonian models in industry is the power law model, see [50, 44]. Heat transfer of a power law fluid on a gravity driven film flow is investigated by Hassanien [44]. The velocity and temperature profiles were presented for a range of power law indices, Prandtl and Nusselt numbers. The results show that the velocity and temperature of the fluid inside the boundary layer is higher for shear thickening fluids and lower for shear thinning fluids. Recently, Chen [20] investigated the effect of a thermo-capillary number and heat transfer on the flow occurring in a thin power law liquid film over a stretching sheet with a free surface. The results show that the velocity and temperature of the fluid are affected significantly by the thermo−capillary

number, Prandtl number and power law indices. For all values of the power law index, the increase in the temperature gradients due to thermo-capillary motion is seen to be more significant, but the velocity and temperature of the fluid increase slightly for higher Prandtl numbers. Shang *et al.* [97] investigated the effect of the power law index and the Prandtl number on the flow behaviour of a power law fluid. The results revealed that for high Prandtl numbers, the velocity and temperature of the fluid increases significantly as the Prandtl number increases. The effect of the power law index showed that the velocity and temperature of the fluid increases slowly as the power law index increases. Wafo Soh *et al.* [101] investigated the fully developed flow of a power law fluid, down an inclined plane. The analytical results were found not to meet the appropriate boundary conditions and they relied on the numerical methods, which are the Runge−Kutta and Newton Raphson methods to obtain the velocity and temperature profiles. The results illustrated an increase in the velocity and temperature profiles for an increasing Brinkman number and the opposite is true for increasing Froude number and the power law index. The power law fluid flow with a free surface is investigated in Chapter 3 with a constant height. For flow with a free surface we consider a purely gravity driven flow such that the modulus sign can be neglected from the power law model. The focus will be on the effect of the power law index on the viscosity, velocity, the flow rate and the temperature profiles. The effect of the Brinkman number on the temperature profiles will be also be investigated.



## The Carreau fluid

The Carreau model has caught the attention of researchers and engineers. Bair [7] and Myers [76] studied the application of non−Newtonian models to thin film flow with a free surface and results showed that the Carreau and Ellis models compare favourably while the power law model can produce inaccurate results for the velocity profiles, see also [93]. Fomin *et al.* [34] investigated the shear rate dependent viscosity models using a

numerical technique, and the results revealed that the Carreau and Ellis models, exhibit Newtonian behaviour near the free surface and power law behaviour near the wall of a rotating cylinder. Further experimental analysis for the Carreau model is detailed in [28, 32, 42] for polymer processing materials. In most of these references, the focus is on the application of shear rate viscosity models in experimental operations. In Chapter 3, the Carreau model will be investigated for flow with a free surface and the velocity and temperature profiles are derived using an asymptotic approach. We extend the pioneering work by Myers [76] to include the energy equation, to the equation governing the flow in order to solve for the temperature of the fluid. The main reason for using an asymptotic analysis is that we can clearly illustrate how the parameters affect the flow by looking into the dominant terms from the governing equations. This approach can be used to validate numerical methods.



## An Ellis fluid

The Ellis model also received considerable attention from researchers for flow with a free surface. Myers [76] investigated the use of shear rate dependent viscosity models on thin film flow. The velocity profiles were plotted for different materials and compared for the Ellis, Carreau and power law models. The results revealed that the Carreau and Ellis models produce similar results. Bair [7] compared the Carreau and Ellis models applied to a shear thinning fluid and the resulting viscosity curves were plotted, illustrating the effect of power law indices. This showed that the two models compared favourably for shear thinning fluids. In recent years, the Ellis model has been used in experimentation to investigate the flow behaviour of shear thinning fluids, see [7, 34, 93]. In Chapter 3, the Ellis model is investigated for flow with a free surface, with special focus on the effect of the flow controlling parameters on the velocity, the flow rate and temperature profiles for the fluid. We follow the analysis in [76] and we consider a purely gravity driven flow. The work is extended to include the temperature profiles for the fluid.

## The temperature dependent viscosity model

The study of the flow of a viscous fluid with temperature dependent properties is of great importance in industries such as food processing, coating and polymer processing [61, 84]. However, most fluids used in industrial systems can be subjected to extreme conditions such as high temperature, pressure and shear rates. External heating such as the ambient temperature and high shear rates can lead to a high temperature being generated within the fluid. This may have a significant effect on the fluid properties. It is a well known fact in fluid dynamics studies, that the property which is most sensitive to temperature rise is viscosity [77]. Fluids used in industrial and natural applications have a viscosity that varies rapidly with temperature and this may give rise to strong feedback effects that can lead to significant changes in the flow structure of the fluid [117]. Due to the strong coupling effect between the Navier−Stokes and energy equations, viscous heating also plays an important role in fluids with strong temperature dependence [24]. In recent years, Costa *et al.* [24] applied the temperature dependent viscosity model to study magma flows. Elbashbeshy *et al.* [29, 30] investigated the influence of a temperature dependent viscosity on heat transfer over a continuous moving surface, using a Runge−Kutta numerical scheme. The results presented show that when the coefficient of viscosity variation parameter increases, the temperature of the fluid (water) increases slightly, whilst the opposite is true for the velocity profiles. Mahmoud [63] discussed the effects of radiation and the coefficient of viscosity variation parameter on hydromagnetic boundary layer flow along a continuously moving vertical plate. The results show that the velocity and temperature of the fluid increases when the viscosity parameter increases, whilst the opposite is true when the magnetic parameter increases. In Chapter 5, the temperature dependent viscosity model will be investigated for flow with a free surface using an asymptotic analysis to solve for the velocity and temperature profiles. The effect of the viscosity variation parameter, Brinkman and Biot numbers on the resulting flow profiles are studied. A full solution will be obtained using the Runge−Kutta numerical

technique. This work is summerised in the paper in progress to appear in the journal: Quaestiones Mathematicae.

### 1.5.2 Flow between parallel plates

Flow between parallel plates is a simple classical representation of the dynamics of fluids in a closed channel. Bounded stationary or moving plates generally characterise the flow, see [66, 74, 114]. The flow of a Newtonian fluid between parallel plates form a classical problem in fluid dynamics (either Couette or Poiseuille flow) and it is well researched in literature, see [22, 95, 116]. However, in the case of non−Newtonian fluids, knowledge of the hydrodynamic and heat transfer behaviour of these fluids is essential to improve the design of equipment which handles such fluids, see [89].

#### The power law fluid

The power law model has been the centre of research for decades. Steady laminar flow of a power law fluid between parallel plates was investigated in [106]. The authors argue that when the power law index is less than unity, the velocity of a power law fluid is small compared to the Newtonian case. However, the power law indices greater than one, showed the velocity profiles which were much higher as compared to the Newtonian case, see also [19, 41, 55] for example. In heated channels, Mahmud [64] argued that the velocity of the power law fluid increases with increasing power law index, which confirms the results in [106]. In this case, the results also revealed that the thermal diffusion ratio increases when the values of the power law index and the velocity ratio increases, see [65, 109]. Ross *et al.* [94] investigated blade coating of a power law fluid. The results illustrated that, depending on the shape and height ratio of the coater, the effect of weakly non−Newtonian behaviour can be either to increase or to decrease both the pressure and the load from the Newtonian values. In recent literature, Maia *et al.* [65]

investigated power law fluids between parallel plates using boundary layer theory. The velocity and temperature profiles were plotted and the results illustrated that when the power law index is greater than unity and the Nusselt number decreases, the velocity and temperature of the fluid increases, see [5] for example. Zheng *et al.* [120] showed that the power law index and Prandtl number influence the velocity and temperature profiles significantly. When both parameters increase, the velocity and temperature of the fluid increase. In Chapter 4, the power law fluid flowing between parallel plates will be investigated further by taking into account the effect of the pressure gradient and the Brinkman number on the flow characteristics. We follow the analysis by Myers [76] and Ross [94] to solve the resulting governing equations. This work is summerised in the paper published in an accredited conference proceeding in [111].

## The Carreau fluid

The Carreau model caught the attention of researchers and engineers over the years for flow between parallel plates. Cox *et al.* [25] investigated the viscous dissipation in die flows using the Carreau model. The results show that when the Nusselt number increases the temperature rises. The Carreau model has been used to investigate the flow of fluids in polymer processing industries, see [4, 15, 60]. For example, Machac *et al.* [60] used experimental data to investigate the falling of a spherical particle through a Carreau model fluid of a shear thinning fluid. The results revealed a good agreement between experimental and calculated terminal velocity data. Pinarbashi *et al.* [87] studied the viscous heating effects on the linear stability of a Poiseuille flow of an inelastic fluid. Their results showed that activation energy parameters, namely the Brinkman number, Carreau parameters and the power law index, have an overall destabilizing effect on the flow, while the Prandtl number played a vital role in stabilizing the flow. Recently, Akyildiz *et al.* [2] investigated the flow of a Carreau fluid using the Runge−Kutta numerical scheme and the results revealed that the fluid velocity increases when the power law index increases.

In Chapter 4, the Carreau model will be investigated with special focus on the effect of the flow controlling parameters, such as the non−dimensional Carreau parameter and the power law index, on the resulting velocity and temperature of the fluid. We first consider a case where the viscosity variation is small and obtain an asymptotic solution for the velocity and temperature profiles. The analytical solution is also obtained when the power law index is zero and the power law index greater than unity. Furthermore, a full solution for the velocity and the temperature are obtained using the Newton Raphson numerical method. We extend the work in Akyildiz *et al.* [2] to include the temperature profiles for the fluid.

## An Ellis fluid

The flow of an Ellis fluid has also been the subject of research over the years. Sundaram *et al.* [105] investigated the heat transfer of an Ellis fluid flowing between parallel plates and in a circular pipe respectively. The results revealed that when the Nusselt number decreases, the fluid temperature rises significantly. Park *et al.* [86] investigated heat transfer and pressure drop between parallel channels and the results revealed that the power law index influences the transition from Newtonian to non−Newtonian rheological behaviour. Steller [103] investigated a generalised slit flow of an Ellis fluid flowing between parallel plates and coaxial cylinders. The results illustrated that the most significant discrepancies between predictions of the power law and Ellis models appear if the rheological properties of the fluid are strongly non−Newtonian. Fomin *et al.* [34] used an Ellis model to investigate non−Newtonian rimming flow on a horizontal rotating cylinder. The results revealed that an Ellis fluid exhibits Newtonian behaviour near the free surface and power law fluid behaviour near the surface of a rotating cylinder. In Chapter 4, we investigate the flow of a power law fluid between parallel plates, with special focus on the effect of the parameters of an Ellis model, such as the power law index, on the resulting velocity and temperature profiles of the fluid. In order to manage the modulus sign we follow the

procedure used by Myers [76] and extend his work to include the temperature profiles for the fluid.

### The temperature dependent viscosity model

The temperature dependent viscosity models also received considerable attention from researchers. Ghaly *et al.* [37] investigated the effect of variable viscosity, chemical reaction, and heat and mass transfer on a laminar flow along a horizontal plate. The results illustrated that as the variable viscosity parameter increases, the velocity increases whilst the temperature decreases. The effect of variable viscosity in chemical reactions, such as heat and mass transfer on a laminar flow along parallel plates has been investigated by Saddiqui *et al.* [99]. The results revealed that the velocity and temperature increase when the temperature variation parameter increases. The results in [99] are in agreement with [37]. In Chapter 5, the effect of the temperature dependent viscosity model on the velocity and temperature of the fluid will be studied. The work in this chapter is summarised in the paper by Myers, Charpin and Tshehla, see [77]. Firstly, the case where the flow is driven solely by the shear force will be studied and then a numerical method will be applied to investigate a full solution.



## 1.5.3 Surface tension driven flow

Surface tension is defined as the surface energy per unit area of the surface, see [83, 85, 93]. Surface tension is a key fluid property in applications such as coating, adhesives, and surfactants and it is also of fundamental importance in thin film applications including draining and painting, see [73, 75, 112]. The most commonly used application of surface tension driven flow is the spreading of a thin liquid drop under gravity, which is well established in literature, see [6, 18, 57, 71, 72]. Surface tension for most fluids is a decreasing function with increasing temperature, see [13, 49, 83]. Due to this temperature

dependence, a temperature gradient along the surface can drive the fluid motion. For this reason we again use the energy equation to solve for the temperature of the fluid. Zhao *et al.* [118] investigated thin film fluids with high surface tension as a driving mechanism. Myers [75] points out that thin film flows driven by surface tension, describes diverse physical situations, such as bubble flow, fluid motion on heat exchanger, soapfilms and contact lens motion. Moriarty *et al.* [73] assessed the spreading of thin liquid film with small surface tension and the results showed that in a region local to the front of a drop, where the surface tension is large, surface tension forces are significant, see [81, 108, 113] for examples. Eres *et al.* [31] formulated a theoretical and numerical method to describe the instability and long time evolution of both gravity driven and surface tension driven thin coating films. The results showed that for conditions of a perfect wetting with the substrate downstream of the moving front covered with a thin layer, predicted nonlinear profiles which are oscillatory agree well with published experiments and literature, see also [112] for a similar solution. In the present contribution, in Chapter 6, we investigate the fluid flow in which surface tension and gravity are the driving forces. We use a similar procedure as detailed in [73, 75, 112] to investigate the resulting film height and extend the work to investigate the effect of both driving forces on the resulting velocity and temperature profiles. We further investigate the effect of reduced Reynolds and reduced Péclet numbers using a first order approximation technique.



## 1.6 Goal of study and thesis outline

The aim of this study is to investigate the flow of thin film fluids with variable viscosity. In particular this study will focus on:

- Flow of variable viscosity fluids with a free surface.
- Flow of variable viscosity fluids between parallel plates.

- Surface tension driven flow.

Flow of variable viscosity fluids is an important area in day-to-day operations and has a wide variety of applications especially in industry as discussed in the previous sections, see [84]. Developing proper mathematical models for these types of fluids is essential for production and equipment design. In Chapter 2 lubrication theory will be briefly discussed, and the appropriate boundary conditions for the governing equations for flow with a free surface and between parallel plates are also given. In this chapter, the foundation for mathematical modelling of thin film fluids will be given. In Chapters 3 and 4 shear rate dependent viscosity models, namely the power law, Carreau and Ellis models, will be studied for both flows with a free surface and between parallel plates. Chapter 5 concerns the temperature dependent viscosity model, again for flows with a free surface and between parallel plates. In Chapter 6, the surface tension driven flow and the first order correction for lubrication theory will be studied. The major results and future work will be discussed in the concluding Chapter 7.

# Chapter 2

# Thin film flow

## 2.1 Introduction

The aim of this chapter is to define the appropriate governing equations for flows both with a free surface and between parallel plates. In most fluid applications, the continuity, Navier−Stokes and energy equations may be used to model the film. In this study, the fluid film is assumed to be thin so that lubrication theory may be applied. The equations governing the flow may often consist of a single nonlinear partial differential equation formulated in terms of the local thickness of the fluid film, [69, 84, 116]. A thin film is generally one in which the characteristic height $H$ (in the $y$-direction) is assumed to be smaller than the length scale $L$ (in the $x$-direction), see [78]. Lubrication theory may then be used to make the governing equations tractable. We will discuss the details for lubrication theory in § 2.3. In many practical applications, the continuity and Navier−Stokes equations are sufficient to describe the flow, see [1, 10, 82]. However, in certain situations, the fluid is subjected to high shear rates and external heating. This may have a significant effect on the fluid properties, such as the viscosity. For this reason the standard flow equations are coupled to the heat equation.

The flow regime considered in this study is laminar. Laminar flow is a type of flow in which the individual fluid particles travel smoothly along the streamline without crossing to the neighbouring particles, [27, 66]. This type of flow is normally characterised by a low

Reynolds number ($Re < 2000$, the ratio of inertia forces to viscous forces, see § 2.3 for more information). In § 2.2, the flow configurations are discussed and the general equations governing the flow are also introduced. The conditions valid for lubrication theory are discussed followed by non−dimensional analysis in § 2.3. The non−dimensional analysis is carried out to show how the governing equations can be reduced in line with lubrication theory. This is a vital procedure because it provides us with the insight as to how the relative magnitude of various terms which are less important can be neglected, see [115]. This provides scalar differential equations which are more tractable and can be solved analytically or numerically depending on the type of fluid under investigation. In this chapter we investigate standard models for a Newtonian fluid (water), for flow with a free surface in § 2.4, followed by Couette−Poiseuille flow between parallel plates in § 2.5. This will lay a solid foundation for non−Newtonian fluid models in the subsequent chapters.



## 2.2 Model derivation

In this section the governing equations for the flow are derived. Before the governing equations are introduced, typical flow configurations are shown, for flow with a free surface followed by the flow between parallel plates.

### Fluid flow with a free surface

Fig. 2.1 displays a two-dimensional laminar flow with a free surface. The geometric representation depicts an infinitely wide channel of typical length scale $L$ in the $x$ direction and height $H$ in the $y$ direction. The fluid flows down a plane inclined at an angle $\beta$ and the dominant driving force for the flow is gravity, denoted $g$. The ambient temperature is denoted $T_a$, the fluid temperature is denoted $T$ and the temperature at the bottom surface is denoted $T_s$.

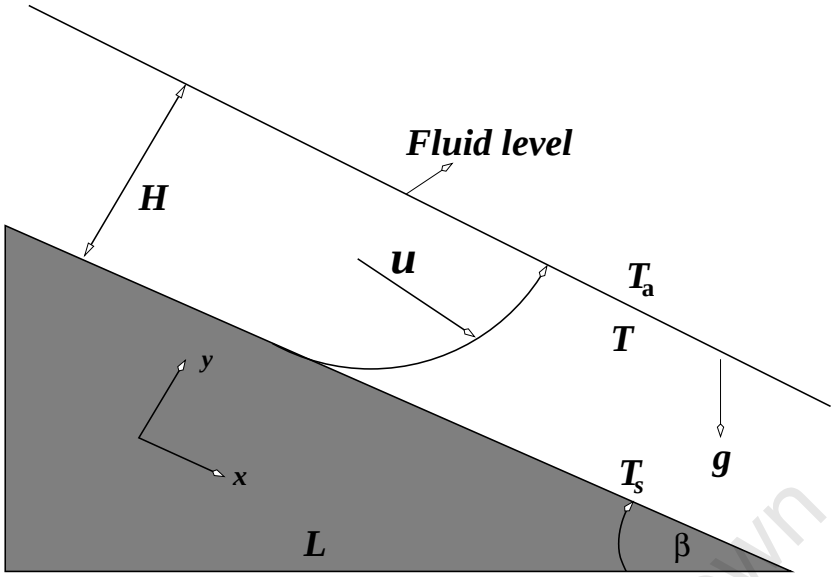


Figure 2.1: Free surface flow geometrical representation.



### Fluid flow between parallel plates

The mathematical formulation and assumptions for flow between parallel plates is now given. In Fig. 2.2 two plates are held apart at a distance $H$. The independent variables $x$, $y$ and $L$ denote the horizontal distance along the plates, the vertical distance and the typical length scale, respectively. The plates are considered to be impermeable and the no-slip condition applies at the plates. The pressure and shear driven cases are combined and, for the pressure driven case both plates are fixed. For the shear driven case the upper plate is moving at the speed $U$ relative to the lower plate. The upper plate is held at temperature $T_u$ and the lower plate at temperature $T_l$. The equations governing the flow are now discussed.

## Governing equations

In general, the fluid dynamics equations for an incompressible fluid are:

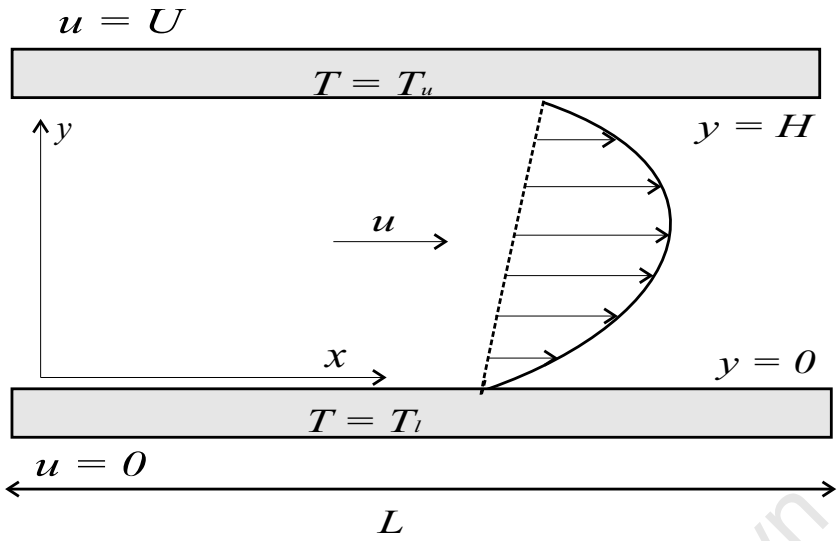


Figure 2.2: Configuration for flow between parallel plates.

## Continuity equation:

The continuity equation is written as,

$$\nabla \cdot \mathbf{u} = 0 \, . \tag{2.2.1}$$

Equation (2.2.1) represents mass conservation. It states that the mass fluxes entering a control volume, balance the outgoing mass fluxes when there are no mass sources or sinks.

## Navier−Stokes equation:

The Navier−Stokes equation is written as,

$$\rho \left( \frac{\partial \mathbf{u}}{\partial t} + (\mathbf{u} \cdot \nabla)\, \mathbf{u} \right) = - \nabla p + \rho \mathbf{g} + \nabla \cdot (\mu \nabla \mathbf{u}) \ , \tag{2.2.2}$$

where $\mathbf{g} = (g \sin\beta, g \cos\beta, 0)$. The Navier−Stokes equation relates the sum of forces acting on a fluid element and its acceleration or rate of change of momentum in the direction of the resultant force.

### Energy equation:

The energy equation is written as,

$$\rho c_p \left( \frac{\partial T}{\partial t} + (\mathbf{u} \cdot \nabla) T \right) = \left[ \frac{\partial p}{\partial t} + (\mathbf{u} \cdot \nabla) p \right] + \nabla \cdot (\kappa \nabla T) + \Phi \ , \tag{2.2.3}$$

where,

$$\Phi = \mu \left[ 2 \left( \frac{\partial u}{\partial x} \right)^2 + 2 \left( \frac{\partial v}{\partial y} \right)^2 + \left( \frac{\partial u}{\partial y} + \frac{\partial v}{\partial x} \right)^2 \right] \ .$$

Equation (2.2.3) describes the conservation of energy, which states that the sum of work and heat added to a system increases the more energy it contains. The dynamic viscosity, viscous dissipation function, heat capacity, density, thermal conductivity and pressure are denoted by $\mu$, $\Phi$, $c_p$ $\rho$, $\kappa$ and $p$ respectively. The Navier−Stokes equations are combined with the continuity and energy equations to solve for the flux $Q$, the velocity $u$ and the temperature $T$ of the fluid. All the notation is listed in the nomenclature section. In the next section, lubrication theory is discussed.

## 2.3 Lubrication theory

Lubrication theory was first established by Reynolds in 1886, see [116], and was first used to describe motion for thin films in bearings [1]. Later, lubrication theory was extended to study other problems which involve thin films in general, such as free surface flow, see [1, 82]. The lubrication approximation is based on the fact that the inertia (and some of the viscous) terms in the governing equations may be neglected. The condition for lubrication theory are valid provided, [1, 55, 82, 84]:

- The square of the aspect ratio, $\varepsilon^2$, is small, that is $\varepsilon^2 \ll 1$, and is defined as the ratio of the film height and length scales where $\varepsilon = H/L$.

- the reduced Reynolds number ($Re = UL/\nu$, is the ratio of inertial forces to viscous forces, $U$ is the velocity scale and $\nu$ is the kinematic viscosity) is small, that is,

$\varepsilon^2 Re \ll 1$, see [55, 84] for example. Note that it is not necessary for the Reynolds number to be small, but the reduced Reynolds number $\varepsilon^2 Re$ to be small.

Equations (2.2.1)−(2.2.3) governing the flow are now non−dimensionalised.

### 2.3.1 Non−dimensional equations

Non−dimensionalisation helps to determine the terms which are dominant and those which can be neglected, and this therefore simplifies the problem. The governing equations in two-dimensions are examined in this section and for a constant viscosity. It is not scaled out since this parameter will be allowed to vary in subsequent chapters, except in Chapter 6 where we investigate a Newtonian fluid considering the effect of surface tension on the resulting flow profiles. The variables are scaled in the following manner:

$$x = Lx' \ , \quad y = Hy' \ , \quad u = Uu' \ , \quad v = Uv' \ , \quad t = \frac{L}{U}t' \ ,$$
$$\mu = \mu_0 \mu' \ , \qquad T = T_0 + \Delta T_0 T' , \qquad p = Pp' = \frac{\mu_0 UL}{H^2}p' \ ,$$

where all quantities with prime denote non−dimensional parameters. The pressure scale $P = \mu_0 UL/H^2$ is standard for lubrication theory. The reference viscosity and the temperature difference are denoted by $\mu_0$ and $\Delta T_0$, respectively. To simplify notation, the primes are omitted from now on. The governing Equations (2.2.1)−(2.2.3) may be non−dimensionalised to give:

**Continuity equation:**

$$\frac{\partial u}{\partial x} + \frac{\partial v}{\partial y} = 0 \ . \tag{2.3.4}$$

**Navier−Stokes equation:**

$$\varepsilon^2 Re \left( \frac{\partial u}{\partial t} + u\frac{\partial u}{\partial x} + v\frac{\partial u}{\partial y} \right) = - \frac{\partial p}{\partial x} + 1 + 2\varepsilon^2 \frac{\partial}{\partial x}\left( \mu \frac{\partial u}{\partial x} \right) + \frac{\partial}{\partial y}\left[ \mu \left( \frac{\partial u}{\partial y} + \varepsilon^2 \frac{\partial v}{\partial x} \right) \right] \ . \tag{2.3.5}$$

$$\varepsilon^4 Re\left(\frac{\partial v}{\partial t}+u\frac{\partial v}{\partial x}+v\frac{\partial v}{\partial y}\right) = -\frac{\partial p}{\partial y}+\varepsilon\cot\beta+2\varepsilon^2\frac{\partial}{\partial y}\left(\mu\frac{\partial v}{\partial y}\right) + \varepsilon^2\frac{\partial}{\partial x}\left[\mu\left(\frac{\partial u}{\partial y}+\varepsilon^2\frac{\partial v}{\partial x}\right)\right] . \quad (2.3.6)$$

**Energy equation:**

$$\varepsilon^2 Pe\left(\frac{\partial T}{\partial t}+u\frac{\partial T}{\partial x}+v\frac{\partial T}{\partial y}\right)=\varepsilon^2\frac{\partial^2 T}{\partial x^2}+\frac{\partial^2 T}{\partial y^2}+PrEc\left(\frac{\partial p}{\partial t}+u\frac{\partial p}{\partial x}+v\frac{\partial p}{\partial y}\right)+\Phi\ , \quad (2.3.7)$$

where,

$$\Phi = Br\mu\left[2\varepsilon^2\left(\frac{\partial u}{\partial x}\right)^2+2\varepsilon^2\left(\frac{\partial v}{\partial y}\right)^2+\left(\frac{\partial u}{\partial y}+\varepsilon^2\frac{\partial v}{\partial x}\right)^2\right] .$$

The Péclet number $Pe = \rho c_p UL/\kappa$ represents the ratio of convective heat transport to the conductive heat transport and the Brinkman number $Br = \mu_0 U^2/\kappa\Delta T_0$ represents the ratio of heat dissipation to fluid conduction. The Prandtl number $Pr = \mu_0 c_p/\kappa$ denotes the ratio of diffusivity for momentum to thermal diffusivity. The Eckert number $Ec = U^2/c_p T_0$ denotes the ratio of kinetic energy to thermal mass. The velocity scale $U = \rho g H^2 \sin\beta/\mu_0$ is determined by the balance between viscous drag and gravitational force on an element in the free surface case, and for flow between parallel plates the externally applied force (pressure drop down the plates) or shear force and drag in the plates. The parameter values may vary widely depending on the particular industrial application or the models under investigation. We present the governing equations such that for purely gravity driven flow, the pressure gradient is neglected and the equations are solved for flow with a free surface. For flow between parallel plates, the pressure gradient and the applied shear force drives the flow and the gravitational force is neglected. Typical parameter values are estimated as follows for a Newtonian fluid (water) flow with a free surface as given in Table 2.1:

From Table 2.1 we can show that the non−dimensional numbers have the following mag-

| Symbol | Name | Typical value | Unit |
|---|---|---|---|
| $c_p$ | Specific heat | $4.18 \times 10^3$ | J kg$^{-1}$ |
| $H$ | Channel height | $10^{-3}$ | m |
| $L$ | Channel length | 0.01 | m |
| $P$ | Pressure scale | $10^3$ | Pa |
| $Pe = \rho c_p UL/\kappa$ | Peclet number | $10^4$ | |
| $Re = \rho UL/\mu_0$ | Reynolds number | 20-2000 | |
| $\Delta T_0$ | Temperature variation | 20 | °C |
| $\beta$ | Inclination angle | 15° | |
| $\varepsilon$ | Aspect ratio of the flow | $10^{-4}$ | |
| $\kappa$ | Thermal conductivity | 0.5 | J ms$^{-1}$ |
| $\mu_0$ | Typical viscosity | $1 \times 10^{-3} - 0.5$ | kg m$^{-1}$s$^{-1}$ |
| $\rho$ | Fluid density | $10^3$ | kg m$^{-3}$ |

Table 2.1: Typical parameter values for Newtonian fluid (water), see [22, 23, 46].

nitude:

$$U = \rho g H^2 \sin 15°/\mu_0 \approx 2.5 \text{ m/s}\,, \qquad Pe \approx 1 \times 10^4,$$
$$PrEc = \mu_0 U^2/\kappa T_0 \approx 5 \times 10^{-4}\,, \qquad Re \approx 20 - 2 \times 10^3.$$

Despite the fact that the Péclet and the Reynolds numbers are large, the reduced quantities $\varepsilon^2 Pe \approx 1 \times 10^{-4}$ and $\varepsilon^2 Re \approx 2 \times 10^{-5}$ are small and so these terms may be neglected from the governing equations. In this work the reduced quantity $PrEc \approx 5 \times 10^{-4}$ is sufficiently small, such that these terms are also neglected in the governing equations. The Brinkman number ($Br = \mu_0 U^2/\kappa \Delta T_0$) may be close to unity and so this term is retained. When $\Delta T_0 \to 0$, the Brinkman number becomes increasingly large and will have a significant effect on the resulting flow profiles. For flow between parallel plates, Myers *et al.* [77] used a lubrication approximation procedure to show that the magnitude of the reduced Reynolds and Péclet numbers ($\varepsilon^2 Pe, \varepsilon^2 Re \ll 1$) are negligible in their analysis for a variable viscosity fluid flow between parallel plates. So, with a proper scaling for Equations (2.2.1)−(2.2.3) it can be shown that the conditions $\varepsilon^2 Pe, \varepsilon^2 Re \ll 1$ are valid for flow between parallel plates. However, it is important to note that Chapter 6 focuses on

the contributions of the correction terms ($\varepsilon^2 Re$ and $\varepsilon^2 Pe$) on the resulting flow profiles. The reduced governing equations valid for both flows with a free surface and between parallel plates may be written as:

$$\frac{\partial u}{\partial x} + \frac{\partial v}{\partial y} = 0 \ . \tag{2.3.8}$$

$$-\frac{\partial p}{\partial x} + \frac{\partial}{\partial y}\left(\mu \frac{\partial u}{\partial y}\right) + 1 = 0 + \mathcal{O}(\varepsilon^2, \varepsilon^2 Re) \ . \tag{2.3.9}$$

$$-\frac{\partial p}{\partial y} = 0 + \mathcal{O}(\varepsilon, \varepsilon^2, \varepsilon^4 Re) \ . \tag{2.3.10}$$

$$\frac{\partial^2 T}{\partial y^2} + \mu Br \left(\frac{\partial u}{\partial y}\right)^2 = 0 + \mathcal{O}(\varepsilon^2, \varepsilon^2 Pe) \ . \tag{2.3.11}$$

The equations governing the flow may be solved, subject to their appropriate boundary conditions. In the following section the boundary conditions are described.

### 2.3.2 Boundary conditions

The velocity and the temperature profiles may be determined after the boundary conditions associated with Equations (2.3.8)−(2.3.11) are stated.

- **At the free surface**: A no slip boundary condition is applied at the bottom and at the free surface the shear stress is zero, see Fig. 2.1 for the flow configuration,

$$u = v = 0 \quad \text{at} \quad y = 0 \ , \qquad \left(\frac{\partial u}{\partial y}\right)\Big|_{y=h} = 0 \ . \tag{2.3.12}$$

  The free surface is at $y = h$. The temperature at the bottom surface is constant and top of the fluid is imposed by the air and the substrate respectively,

$$T = 0 \quad \text{at} \quad y = 0 \ , \qquad \left(\frac{\partial T}{\partial y}\right)\Big|_{y=h} = Bi(T - 1) \ , \tag{2.3.13}$$

  where $Bi = HK_c/k$ is the Biot number and denotes heat transfer coefficient to thermal conductivity [3, 6]. The parameters $k$ and $K_c$ denote the thermal conductivity and heat transfer coefficient respectively. The fluid at the free surface is exposed

to the ambient temperature. Hence, a cooling condition is applied. The boundary conditions on $p$ are:

$$p = 0 \quad \text{at} \quad y = h \ . \tag{2.3.14}$$

The boundary conditions valid for flow between parallel plates will follow below.

- **Between parallel plates**: At $y = 0$, the temperature is zero and the surface is fixed and impermeable:

$$T = 0 \quad \text{at} \quad y = 0 \ , \quad u = v = 0 \quad \text{at} \quad y = 0 \ . \tag{2.3.15}$$

At $y = 1$, the temperature is constant, the surface is impermeable and moves with constant velocity $U$, see Fig. 2.2,

$$T = 1 \quad \text{at} \quad y = 1 \ , \quad u = U = 1 \quad \text{at} \quad y = 1 \ . \tag{2.3.16}$$

To find the pressure between the plates the following conditions are imposed,

$$p = p_0 \quad \text{at} \quad x = x_0 \ , \tag{2.3.17}$$

where $p_0$ is the pressure and $x_0$ is the position of the fluid.

The governing equations and their appropriate boundary conditions will be used in the subsequent sections to solve for the flux, velocity, pressure and temperature profiles of the fluid. In the next section, a simple laminar flow of a Newtonian fluid (water) is investigated for flow with a free surface with a constant viscosity.

## 2.4 Free surface flow

In this section we investigate the flow of a Newtonian fluid with a free surface. The velocity, flux and temperature profiles are derived using the reduced Navier−Stokes and energy equations subject to their appropriate boundary conditions. The velocity profile

is determined by integrating Equation (2.3.9) with respect to $y$, subject to the boundary conditions (2.3.12). This gives,

$$u = \frac{y}{2}\Big(2h - y\Big) \ , \tag{2.4.18}$$

where we have used the fact that $\partial p/\partial x = 0$ to write Equation (2.4.18) since Equation (2.3.10) shows that the pressure $p$ is a function of $x$ only and also considering the boundary conditions (2.3.14). The velocity profile is a standard parabola and a similar expression can be found in [1, 23, 116]. The flux is given by integrating Equation (2.4.18) from 0 to $h$,

$$Q = \int_0^h u dy = \frac{h^3}{3} \ . \tag{2.4.19}$$

Equation (2.4.19) provides a solution for the flow rate. The equation governing the temperature may be obtained by combining Equations (2.3.11) and (2.4.18) to give,

$$\frac{\partial^2 T}{\partial y^2} = -Br(h-y)^2 \ . \tag{2.4.20}$$

Integrating Equation (2.4.20) twice with respect to $y$ and applying the boundary conditions (2.3.13) yields,

$$T = -\frac{Br}{12}\left[(h-y)^4 - h^4\left(1 - \frac{Bi}{(Bi\ h-1)}y\right)\right] + \left(\frac{Bi}{(Bi\ h-1)}\right)y \ . \tag{2.4.21}$$

The first term in Equation (2.4.21) shows that the temperature is quartic in $y$. In order to investigate the behaviour of the velocity, flux and temperature profiles, Equations (2.4.18), (2.4.19) and (2.4.21) are now plotted for various flow controlling parameters.

The parabolic profile for Equation (2.4.18) is shown in Fig. 2.3 with $h = 1$. In this figure the velocity increases across the layer and reaches its maximum at the top of the fluid layer, where $u = 0.325$ at $y = 1$. In Fig. 2.4, the temperature profile representing Equation (2.4.21) is shown. The Biot and the Brinkman numbers are given by $Bi = 0.3$ and $Br = 0.3$, so that both the Biot and the Brinkman numbers are of the same magnitude.

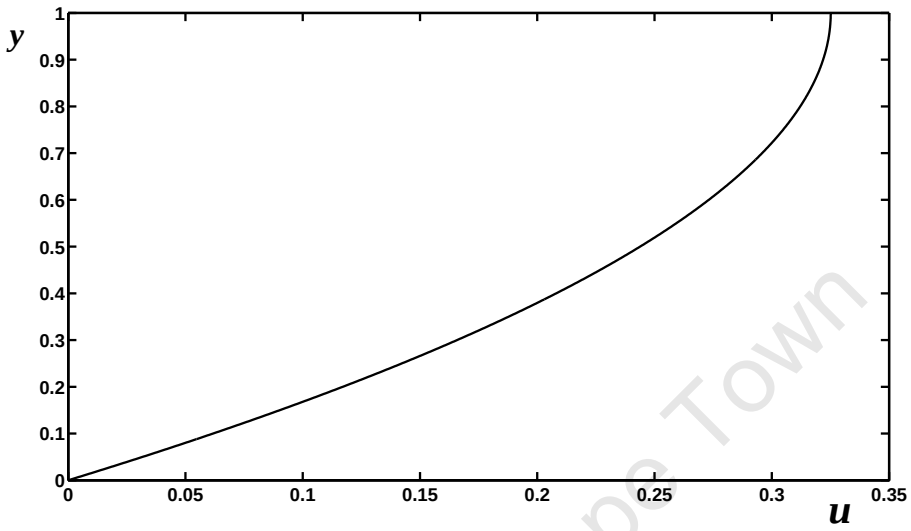


Figure 2.3: The velocity profile for Equation (2.4.18): Boundary conditions (2.3.12).

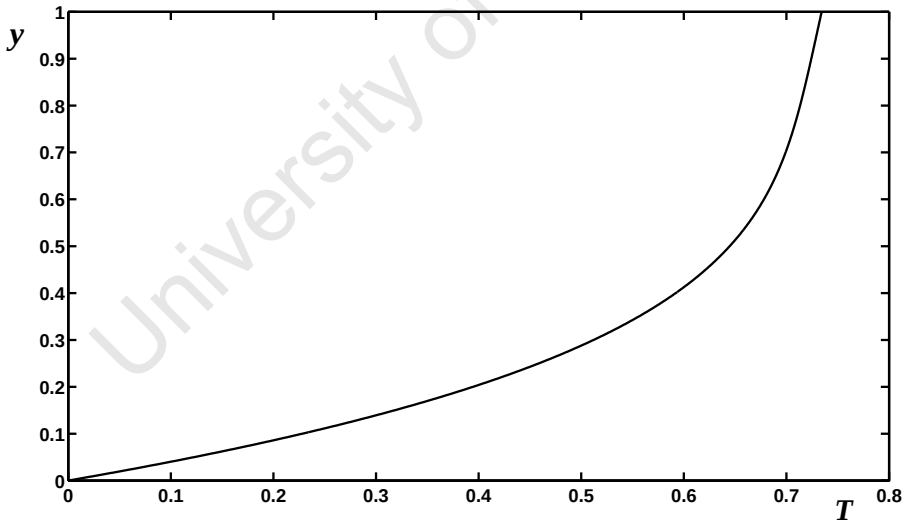


Figure 2.4: The temperature profile for Equation (2.4.21): Boundary conditions (2.3.13).

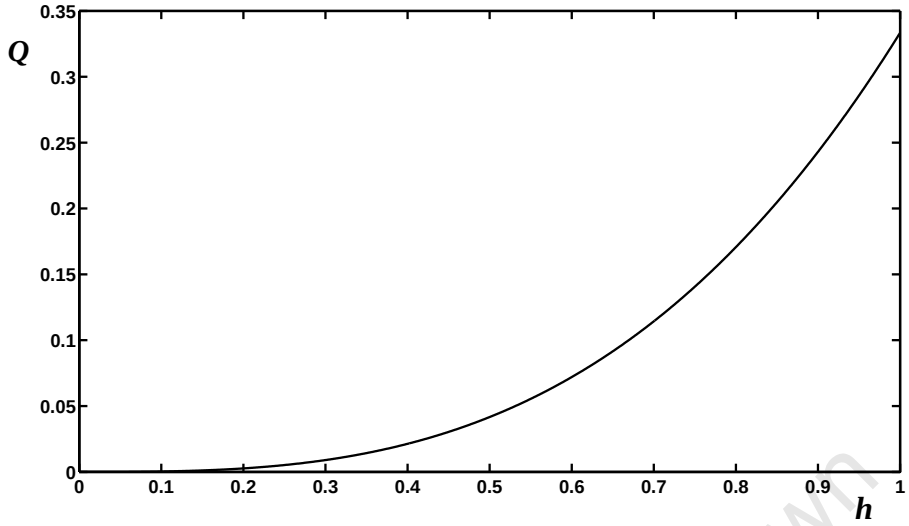


Figure 2.5: The flow rate profile for Equation (2.4.19).



The temperature of the fluid increases across the fluid layer to its maximum at the free surface. The increase in fluid temperature is due to heat generation in the fluid by the viscous force. Fig. 2.5 shows the flow rate and its maximum value is $Q = 0.35$ at $h = 1$.

In industrial applications, the Brinkman number must be found by using experimental data. However, several authors often use the approximation of the temperature profiles using the Brinkman number in the region $0 \leq Br \leq 20$, see [101, 115] for example. We will also use these theoretical values for $Br$ in order to investigate its effect on the resulting temperature profiles. Six temperature profiles given by Equation (2.4.21) are shown in Fig. 2.6. Each plot corresponds to different values of the Brinkman numbers $Br = 0.2, 4, 10, 15, 20$ and 25 for curves (a) through to (f). The temperature of the fluid increases across the layer to the maximum temperature at the top. When $Br$ increases, the temperature of the fluid increases. This shows that the temperature rise due to viscous heat dissipation is significant when $Br$ increases. Heat dissipation is caused by the fluid which flows inside the layer and is in contact with the boundary which in turn produces mechanical work which is transformed into heat [23].

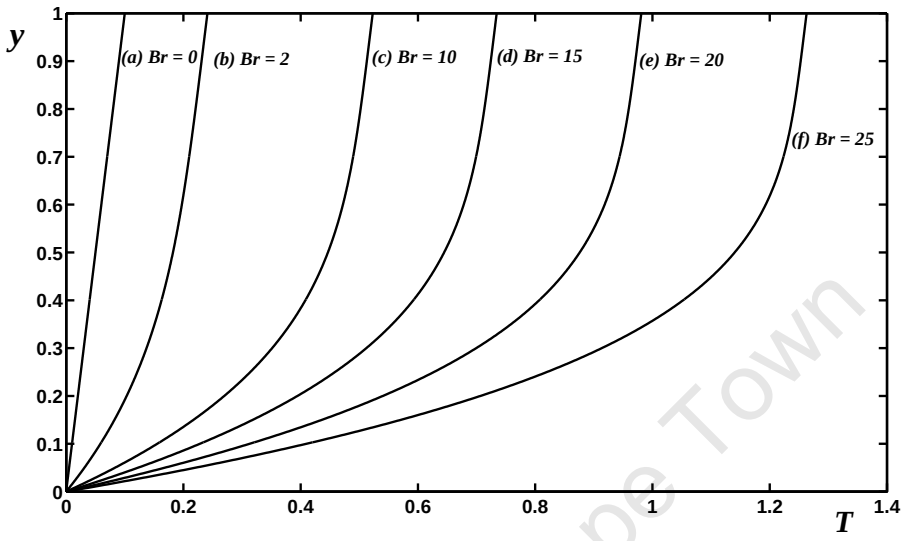


Figure 2.6: The effect of $Br$ on Equation (2.4.21): Boundary conditions (2.3.13).

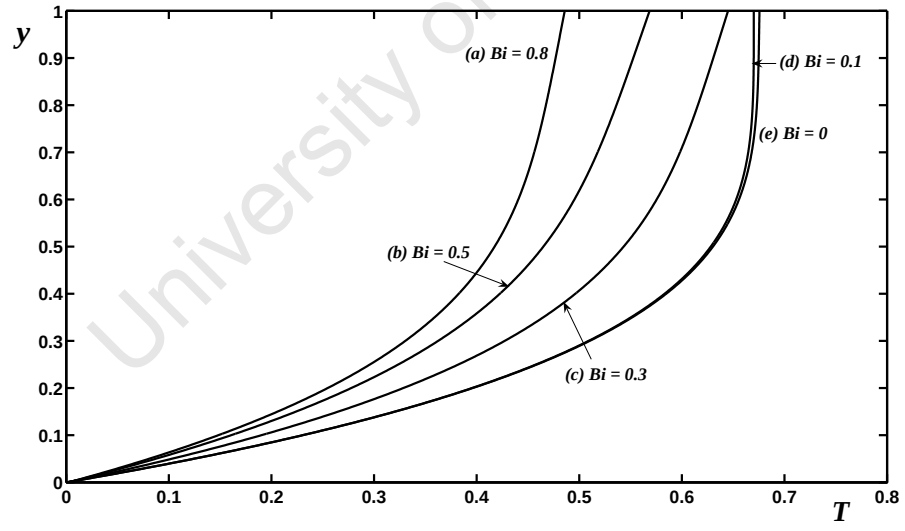


Figure 2.7: The effect of $Bi$ on Equation (2.4.21): Boundary conditions (2.3.13).

The effect of the Biot number on the temperature profiles is investigated. The importance of the Biot number is that it helps to understand the influence of the atmosphere temperature on the flow system. When the Biot number tend to infinity (that is, $k \to \infty$), then both the atmosphere temperature and the fluid temperature reaches equilibrium and $Bi \sim 0$. However, when the Biot number decreases ($k \to 0$) the fluid loses its temperature to the atmosphere and this process will have a major influence on the temperature variation of the fluid. An increase in the Biot number indicates that more heat is lost from the fluid to the atmosphere (hence cooling the fluid). When the Biot number decreases, a reduction in heat transferred to the atmosphere occurs and the fluid gets hotter [51]. In Fig. 2.7 shows the temperature profiles for different values of the Biot numbers, namely $Bi = 0, 0.1, 0.3, 0.5$ and $0.8$ and these curves are extracted from Fig. 2.6. The fluid temperature increases across the fluid layer as $Bi$ decreases due to reduction in the heat transferred to the atmosphere. The figure clearly demonstrates that the fluid temperature rises with decreasing values of the Biot number and the temperature profiles flatten out at the free surface, as $Bi$ decreases and when $Bi = 0$, the resulting profiles shows that temperature gradient at the free surface is zero, as expected from the boundary conditions.

### 2.4.1 Conclusion

Laminar flow of a Newtonian fluid (water) has been investigated for flow with a free surface and a constant height. The velocity of the fluid increases nonlinearly across the channel to its maximum velocity at the top layer. The temperature of the fluid increases across the layer due to heat generation by the viscous force. The effect of the flow controlling parameters such as the Brinkman and the Biot numbers were also investigated. The results show that when $Br$ increases the temperature of the fluid rises, due to viscous heat dissipation. The temperature of the fluid also increases across the layer to its maximum when $Bi$ decreases. The temperature profiles flatten at the free surface, which is a result of heat conducted from fluid to the atmosphere.

## 2.5 Couette-Poiseuille flow

In this section, the pressure gradient and applied shear forces are considered to be the main driving forces for the fluid. Therefore, we neglect all the gravitational forces associated with Equation (2.3.9). Couette flow is caused by the movement of one boundary. Poiseuille flow occurs when both plates are fixed and the pressure gradient drives the flow, see [22, 23] for example. The assumption in this work is that the two plates are completely filled with fluid and the flow regime is laminar and the gap between them is given by $H$ as shown in Fig. 2.2. For illustration purposes the velocity $U$ is not scaled out in this section and it will take the value 0 or 1 depending on whether the top plate is stationary or moving (i.e., $U = 0$ for pressure gradient driven flow or $U = 1$ for shear driven flow).

The velocity and temperature profiles are determined from (2.3.9) and (2.3.11) respectively. Integrating Equation (2.3.9) twice with respect to $y$ and applying the boundary conditions (2.3.15) and (2.3.16) yields,

$$u = \frac{p_x}{2}\Big(y^2 - y\Big) + Uy \ , \tag{2.5.22}$$

where $p_x = \partial p/\partial x$ and $p$ is independent of $y$ from Equation (2.3.10). The first term on the right hand side is the standard parabola for the pressure driven flow. The second term is a classical straight line for shear driven flow. This expression may be found in [23]. An expression for the flux $Q$ is given by,

$$Q = \int_0^1 u dy = \frac{1}{2}(U - \frac{p_x}{6}) \ . \tag{2.5.23}$$

For a constant flux, we can determine the pressure from Equation (2.5.23) as,

$$\frac{\partial p}{\partial x} = 6(U - 2Q) \ . \tag{2.5.24}$$

For incompressible fluids, the flux must be constant [76]. This is shown in Equation (2.5.23) where the flux also depends on the pressure gradient. Therefore, from the boundary conditions (2.3.17) we can deduce that the pressure is known at either end of the

plates. Now for a constant flux, we can show that the second order pressure gradient $p_{xx}$ is zero everywhere, by differentiating Equation (2.5.24) once with respect to $x$. Integrating Equation (2.5.24) and applying the boundary conditions (2.3.17) yields the pressure as,

$$p = p_0 + 6(U - 2Q)(x - x_0) \approx \Delta p = 6(U - 2Q)(x - x_0) \ , \tag{2.5.25}$$

where $\Delta p = p - p_0$ represents the pressure drop. Equation (2.5.25) shows that the pressure is linear. To determine the temperature profile, Equations (2.3.11) and (2.5.22) are combined to give,

$$\frac{\partial^2 T}{\partial y^2} = -Br \left[ \frac{{p_x}^2}{4} \left( 4y^2 - 4y + 1 \right) + 2U p_x y - U p_x + U^2 \right] \ . \tag{2.5.26}$$

Integrating Equation (2.5.26) twice with respect to $y$ and applying the boundary conditions (2.3.15) and (2.3.16) leads to,

$$\begin{aligned} T = y - \left[ \frac{BrU^2}{2} \Big( y^2 - y \Big) \right] - \left[ \frac{BrUp_x}{6} \Big( 2y^3 - 3y^2 + y \Big) \right] \\ - \left[ \frac{Br{p_x}^2}{12} \Big( 2y^4 - 4y^3 + 3y^2 - y \Big) \right] \ . \end{aligned} \tag{2.5.27}$$

The first term on the right hand side is linear, which arises due to the applied heating. The second term appears due to the shear driven flow. The third term occurs due to the combination of the pressure and shear rate. The last term shows that the temperature is quartic in $y$.

Three curves representing velocity profiles corresponding to Equation (2.5.22) are shown in Fig. 2.8. Curve (a) with $U = 1$ and $p_x = 0$ represents a linear profile for the shear driven flow; as expected the velocity increases linearly from $u = 0$ at $y = 0$ at the lower boundary to $u = 1$ at $y = 1$ at the upper boundary. The effect of the applied shear force is demonstrated in this curve where the maximum velocity appears at the moving plate. Curve (b) with $U = 0$ and $p_x = -5$ represents the velocity profile for the pressure driven flow. This is a parabolic curve with its maximum velocity appearing at the centre of the

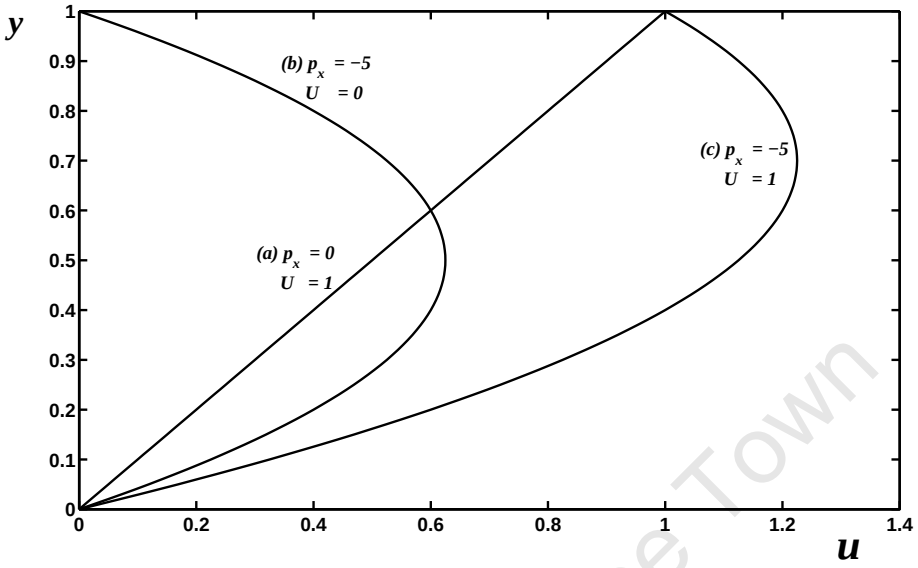


Figure 2.8: The velocity profiles for the pressure/shear driven flow for Equation (2.5.22): Boundary conditions (2.3.15) and (2.3.16).

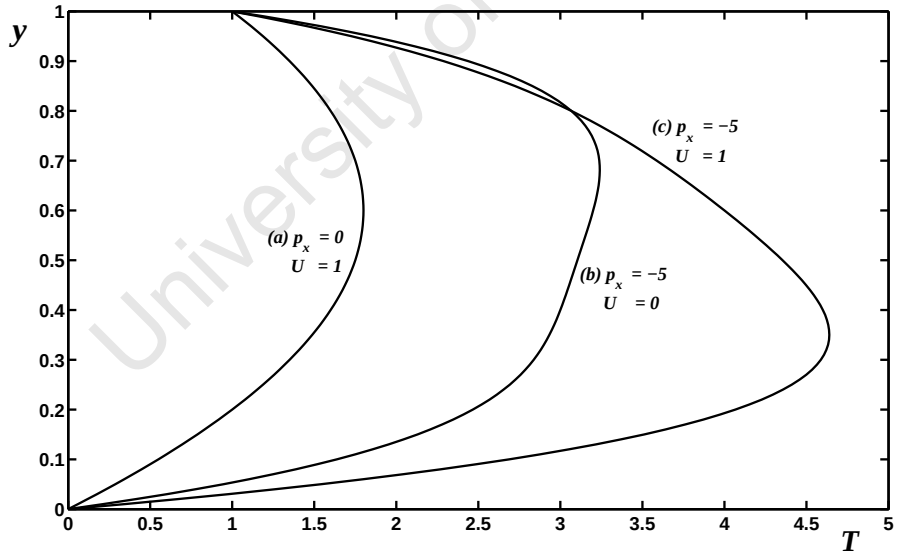


Figure 2.9: The temperature profiles for the pressure/shear driven flow, $Br = 0.3$ for Equation (2.5.27): Boundary conditions (2.3.15) and (2.3.16).

plates, due to the lack of the applied shear force. It is important to note that the negative sign shows that the pressure gradient decreases in the direction of the flow. Curve (c) with $U = 1$ and $p_x = -5$ is the combination of both the shear and pressure driven flow. The velocity of the fluid increases to its maximum point near the moving plate. In this case, both the pressure gradient as well as the applied shear force, where the maximum velocity occurs, depend on which one dominates the flow.

Three temperature profiles, corresponding to Equation (2.5.27) are shown in Fig. 2.9 with $Br = 0.3$. Curve (a) represents the shear driven case with $U = 1$ and $p_x = 0$, and the temperature of the fluid increases to its maximum near the centre of the plates. The curve shows that heat generation is higher at the centre of the plates. Curve (b) represents the pressure driven case with $U = 0$ and $p_x = -5$. The temperature of the fluid increases to its maximum near the top plate, due to heat generated by the applied shear force resulting from the movement of the top plate. Curve (c) represents a combination of both the pressure and shear rate cases. The maximum temperature of the fluid occurs near the bottom plate, which shows that heat generation is more pronounced at the bottom plate.

In real situations, there are numerous other flows in engineering systems such as parallel plates flow, pipe flow measurements and pumps for which the pressure gradient effect is important [22, 23]. The importance of the pressure gradient is shown in Equation (2.5.22). The curvature of the velocity profile in this equation is directly dependent on the pressure gradient $p_x$. If $p_x = 0$, a linear profile is retrieved as shown in Fig. 2.8. The question is what happens when $p_x < 0$ and $p_x > 0$? Therefore, the effect of $p_x$ on the velocity profiles resulting from Equation (2.5.22) and the temperature profile in Equation (2.5.27) is investigated.

Seven curves representing the velocity profiles for Equation (2.5.22) are shown in Fig. 2.10, in the region $-5 \leq p_x \leq 5$. Curve (d) with $p_x = 0$ shows a linear profile increasing across the plates to its maximum at the top plate. When $p_x < 0$ the fluid velocity increases

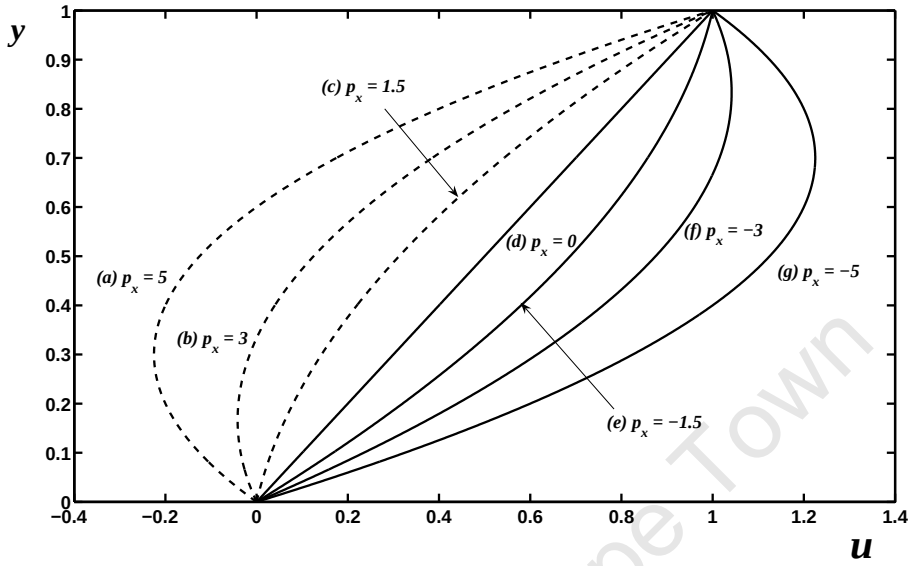


Figure 2.10: The velocity profiles for the pressure driven flow $U = 1$ for Equation (2.5.22): Boundary conditions (2.3.15) and (2.3.16).

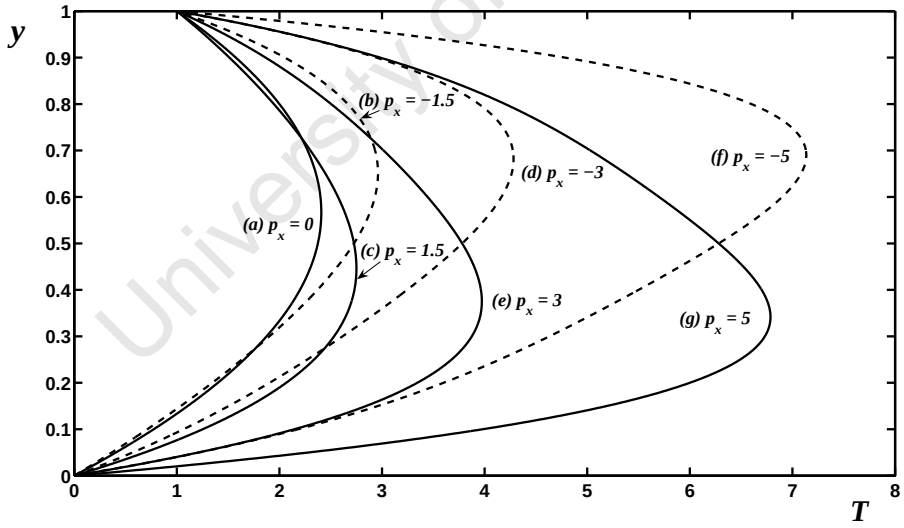


Figure 2.11: The temperature profiles for the pressure driven flow, $U = 1$, $Br = 0.3$ for Equation (2.5.27): Boundary conditions (2.3.15) and (2.3.16).

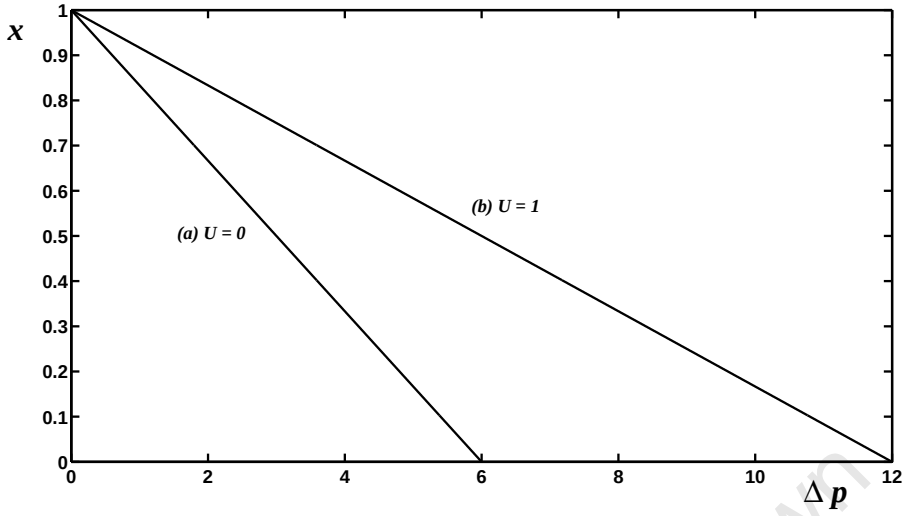


Figure 2.12: The profiles for the pressure drop corresponding to Equation (2.5.25).



significantly in the direction of the flow, with maximum values for the velocities occurring near the top plate, as shown in curves (e) to (g). This is a result of the applied shear force which becomes significant when the pressure gradient decreases in the direction of the flow. For $p_x > 0$, in curves (a) to (c), we observe what is commonly known as the reversed flow eddies. These reversed flow eddies are caused by the drastic changing of the applied drag force (sometimes called the resistance force) acting in the fluid. Of interest is also curve (c) with $p_x = 1.5$, for which the shear stress at the lower plate is zero. For $p_x > 1.5$, there is back flow which shows that flow separation is unbounded at the lower plate. The maximum velocity of the fluid occurs near the bottom plate, when the pressure gradient increases from 0 to 5. The effect of $p_x$ on the temperature profiles is illustrated in Fig 2.11. When $p_x = 0$, a parabola is observed in curve (a) with its maximum temperature at the centre of the plates. This shows that heat generation due to the presence of the pressure gradient is high at the centre of the plates. When $p_x < 0$ the maximum temperature appears near the bottom plate as shown in curves (c), (e,) and (g). As the pressure gradient decreases, the maximum temperature is more pronounced near the bottom plate because heat generation is higher near the bottom plate and the

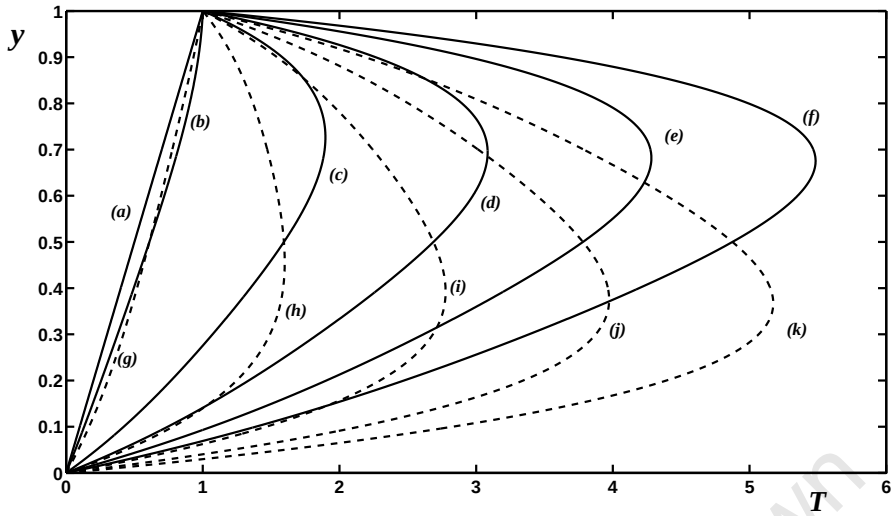


Figure 2.13: The temperature profiles corresponding to Equation (2.5.27), with $U = 1$, $p_x = 3$ and $p_x = -3$: Boundary conditions (2.3.15) and (2.3.16).

rise in temperature of the fluid at the bottom plate is observed. The opposite is true for $p_x > 0$ and the temperature profiles are shown in curves (b), (d) and (g). The maximum temperature appears near the top plate which is a result of heat generation by the applied shear force. Of interest is that when $p_x > 0$, the maximum temperature values are slightly higher than their counterparts when $p_x < 0$. For example if we consider curves (f) and (g), their maximum temperatures are $T = 7.4$ at $y = 0.72$ and $T = 6.8$ at $y = 0.35$ respectively. This shows that the temperature difference between the two curves is 0.6.

Two curves for the pressure drop are shown in Fig 2.12. Other parameters are given by $Q = 0.3, x_0 = 1$. Curve (b) with $U = 1$ shows a linear profile with its maximum value at the bottom, which is double the value of curve (a), which is an obvious case resulting from Equation (2.5.25).

The effect of the Brinkman number is shown in Fig. 2.13. In this figure curve (a) with $Br = 0$, a linear profile from $T = 0$ at $y = 0$ to $T = 1$ at $y = 1$, as expected from Equation (2.5.27), is observed. Curves (b) through to (f) correspond to different values of $Br$ with $p_x = 3$ and curves (g) to (k) correspond to the same Brinkman numbers with $p_x = -3$.

In curves (g) to (k) when $Br$ increases with $p_x < 0$, the maximum temperature is more pronounced at the bottom plate and the temperature of the fluid increases significantly as $Br$ increases. The opposite of this scenario is shown in curves (g) through to (k) where the maximum temperature of the fluid is more pronounced near the top plate. In this figure we can deduce that when $p_x < 0$, heat generation due to the viscous heating term is significantly high near the bottom plate and the opposite is true for $p_x > 0$. The maximum temperature for the values of $p = 3$ are higher compared to the case where $p_x = -3$. For example, curve (g) with $Br = 25$ is 4% higher than curve (k).

### 2.5.1 Conclusion

The Newtonian fluid flow between parallel plates has been investigated. The driving forces for the flow are the applied shear force and the pressure gradient. The velocity profile for the applied shear force occurs at the top plate. The velocity profiles for the combination of both applied shear force and the pressure gradient, appears near the moving plate, probably because the dominant driving force might be the applied shear force caused by the movement of the upper plate. For the pressure driven case the maximum velocity of the fluid occurs at the centre of the plates. The effect of the pressure gradient on the resulting velocity profiles was further explored and the results show that when the pressure gradient is zero, a linear profile is observed. When the pressure gradient is negative the velocity profile increases in the direction of the flow. However, when pressure gradient is positive a reverse flow is observed and the maximum velocity occurs outside the boundaries as the pressure gradient increases. The maximum temperature profiles for the applied shear force occurs at the top plate. For the pressure driven case a parabolic profile is observed with its maximum values appearing at the centre of the plates. When the pressure gradient is zero a parabolic temperature profile is shown resulting from the shear driven case. For a negative pressure gradient all maximum temperatures occur near the bottom plate whilst the opposite is true when the pressure gradient is positive.

Linear profiles for the pressure drop are also shown. The effect of the Brinkman number on the resulting temperature profiles shows a significant increase in the fluid temperature, when $Br$ increases. In particular, for the case where the pressure gradient is positive, the maximum temperature is significantly higher near the top plate.

## 2.6 General conclusion

In Chapter 2, the foundation of mathematical modelling of thin film fluids for flow with a free surface and flow between parallel plates has been laid. Lubrication theory has been introduced and the governing equations were reduced to simpler equations. The flow of a Newtonian fluid has been investigated using the lubrication approximation of the Navier−Stokes and energy equations. Graphical results have been discussed. In the subsequent Chapters 3, 4, and 5 the viscosity will be allowed to vary. However, in Chapter 6 surface tension driven flow with a constant viscosity is investigated. In the following chapter, shear rate dependent viscosity models will be investigated for flow with a free surface.

# Chapter 3

# Fluid flow with a free surface

## 3.1 Introduction



The aim of this chapter is to introduce mathematical models for non−Newtonian fluids. In particular, the shear rate dependent viscosity models introduced in Chapter 1, namely the power law, the Carreau and the Ellis models are investigated for flow with a free surface. The work in this chapter is organised as follows:

In § 3.2, the power law fluid is investigated. We follow the analysis by Myers [76], where we assume that for free surface purely gravity driven flow the velocity gradient ($\partial u/\partial y > 0$) is positive everywhere, hence we neglect the modulus sign in Equation (1.4.2). We extend the work from [76] to include the temperature profiles.

In general, the flow equations resulting from the Carreau model cannot be solved analytically as discussed in Chapter 1 and so the Newton−Raphson numerical method is used to gain a full solution. However, an asymptotic technique which allows certain parameters to be perturbed for analytical solution is used. We impose a non−dimensional parameter $l$ (the ratio of the product of the characteristic time and the velocity force to the film height) in the Carreau model, which is considered to satisfy $l \ll 1$. The other approach for analytical progress is obtained when the power law index $n = 0$ and $n = 2$. These sets of analytical solutions are very important and will give us the option of having more

results to compare with the numerics. This will be carried out in § 3.3.

An Ellis fluid is investigated in § 3.4 and the resulting governing equations allow for analytical progress. We again consider a purely gravity driven flow and let ($\partial u/\partial y > 0$) so that the modulus sign in Equation (1.4.4) can be neglected. The applications of these non−Newtonian fluids models to thin film flow are investigated in § 3.5 for standard materials.

## 3.2 Power law fluid

In this section the power law fluid is now investigated. The power law model is non−dimensionalised to give,

$$\mu = K\left(\frac{\partial u}{\partial y}\right)^{n-1} , \tag{3.2.1}$$

where $K = m(U/H)^{n-1}$. Setting $n = 1$ and $K = \mu$, the Newtonian case is retrieved, for $n < 1$ represents shear thinning fluid and $n > 1$ represents shear thickening fluid. Combining Equations (2.3.9) and (3.2.1), and integrating once with respect to $y$ and applying the boundary conditions, (2.3.12) leads to,

$$\frac{\partial u}{\partial y} = \left(\frac{1}{K}\right)^{\frac{1}{n}} (h-y)^{\frac{1}{n}} . \tag{3.2.2}$$

Integrating Equation (3.2.2) with respect to $y$ and applying the boundary conditions (2.3.12) gives,

$$u = \frac{n}{(n+1)}\left(\frac{1}{K}\right)^{\frac{1}{n}} \left[h^{\frac{n+1}{n}} - (h-y)^{\frac{n+1}{n}}\right] . \tag{3.2.3}$$

Equation (3.2.3) provides a solution for the velocity profile. This equation correspond to Equation 6 in Myers [76] in his analysis for applications of non−Newtonian models to thin film flow. Miladinova *et al.* [70] investigated the flow of a thin layer of a power law liquid falling on an inclined plate and Equation (3.2.3) corresponds to their Equation 13. The flux along the fluid layer is given by integrating Equation (3.2.3) from 0 to $h$,

$$Q = \int_0^h u dy = \frac{n}{(n+1)}\frac{(3n+1)}{(2n+1)}\left(\frac{1}{K}\right)^{\frac{1}{n}} h^{\frac{2n+1}{n}} . \tag{3.2.4}$$

Equation (3.2.4) provides the solution for the flux. Combining Equations (2.3.11) and (3.2.2) gives,

$$\frac{\partial^2 T}{\partial y^2} = -K^{\frac{1}{n}} Br\Big(h-y\Big)^{\frac{n+1}{n}} \ . \tag{3.2.5}$$

Integrating Equation (3.2.5) twice with respect to $y$ and applying the boundary conditions (2.3.13) yields,

$$\begin{aligned} T &= \frac{(n^2 K^{\frac{1}{n}} Br)}{(2n+1)(3n+1)} \left[ h^{\frac{3n+1}{n}} \left( 1 - \frac{Bi\ y}{(Bi\ h-1)} \right) - (h-y)^{\frac{3n+1}{n}} \right] \\ &\quad + \frac{Bi\ y}{(Bi\ h-1)} \ . \end{aligned} \tag{3.2.6}$$

Equation (3.2.6) provides the solution for the temperature profile. The effect of the power law index on the viscosity in Equation (3.2.1), the velocity, the flow rate and the temperature profiles is investigated.

The values of the power law index $n$ used in practice are generally the experimental data which may be obtained in several references, [9, 25, 61, 76]. Hassanien [44] and Shang *et al.* [97] presented their theoretical results for the power law fluid with the power law index $n$ in the region between $0.1 < n < 2$. We will carry a similar analysis for a general case where the values of the power law index $n$ lies in the region $0.1 < n < 3$.

Typical results from Equation (3.2.1) are now discussed. In our analysis we will discuss the behaviour of the fluid for both $n < 1$ and $n > 1$ in which case the value of $n = 1$ represents a Newtonian fluid. Fig. 3.1 shows the plot of viscosity versus shear rate with the power law index in the region $0.1 \leq n \leq 3$. The figure shows that when $n$ ranges between 0.1 and 0.5 the fluid viscosity decreases when the shear rate increases, giving raise to what is known as shear thinning behaviour. The opposite is true for $n > 1$ and this behaviour is known as shear thickening fluid as briefly discussed in Chapter 1. Shang *et al.* [97] displayed the viscosity versus shear rate graph for the shear thinning fluid which showed a decrease in fluid viscosity for $n < 1$. Barnes *et al.* [9] showed the viscosity versus shear rate on a log scale for blood with $n = 0.75$ which also shows that

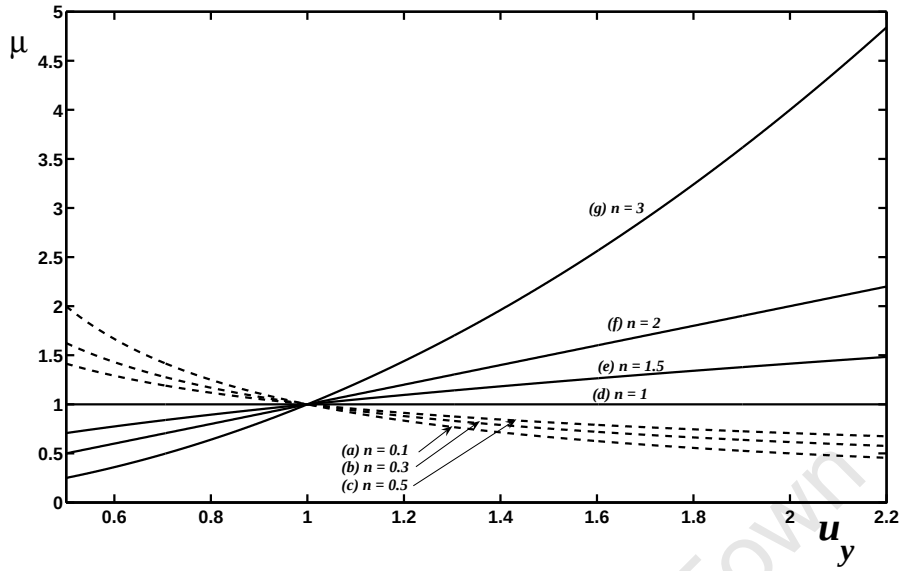


Figure 3.1: The viscosity versus shear rate for different values of $n$ for Equation (3.2.1).

the viscosity decreases as the shear rate increases. Our results are in agreement with some of the results presented in the literature, see also [9, 25].

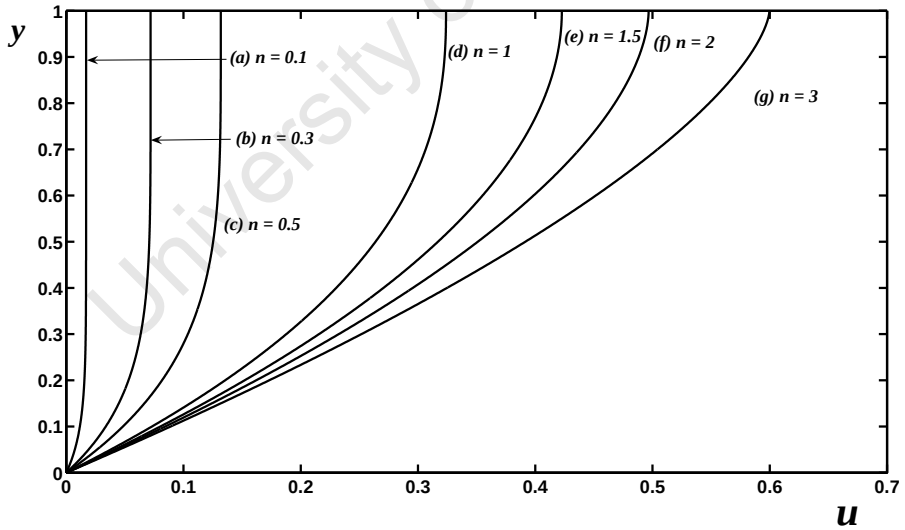


Figure 3.2: The velocity profiles for Equation (3.2.3): Boundary conditions (2.3.12).

The effect of increasing the power law index is shown in Fig. 3.2, which represents the velocity profiles for Equation (3.2.3). Curves (a) to (g) display different velocity profiles

with different power law indices and $K = 1$. The Newtonian case is retrieved in curve (d) with $n = 1$. The figure shows that the maximum velocity of the fluid, which occurs at the free surface, is higher for shear thickening fluids than for shear thinning fluids. The same trend has been observed in Wafo Soh *et al.* [101], in which their velocity profiles for shear thickening fluids were greater than the velocity profiles for shear thinning fluids. This is an indication that the net driving force (presumably gravitational force) for the fluid is higher for shear thickening fluids, which results in a high velocity profile for shear thickening fluids.

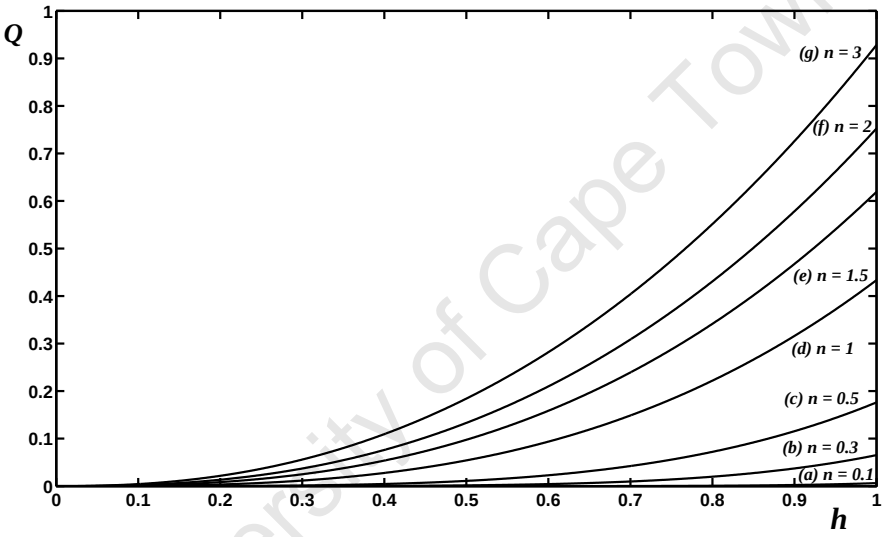


Figure 3.3: The flow rate versus height for different values of $n$ corresponding to Equation (3.2.4).



Flow rate computed from Equation (3.2.4) is shown in Fig. 3.3, plotted with different values of the power law index. The figure illustrates that when $n$ increases the flux increases in the layer and the flow rate is higher.

Fig. 3.4 displays the temperature distribution for the power law fluid characterised by different power law indices, as shown in curves (a) through to (g) with $Bi = Br = 0.3$ and $K = 1$. These curves correspond to Equation (3.2.6). The temperature of the fluid increases significantly for $n > 1$, which is in agreement with the results obtained in

Hassasiem [44], and for $n < 1$ an increase in the fluid temperature is less pronounced. The maximum temperature of the fluid occurs at the free surface and the maximum value for the temperature is higher for the dilatant fluids with $n > 1$ than for the pseudoplastic fluids with $n < 1$. The equivalent Newtonian temperature profile is displayed in curve (d) with $n = 1$. In this case the maximum temperature for a Newtonian fluid is much higher than for the shear thinning fluids. This is due to the action of the viscous force, which results in an increase in heat generation and it is significantly higher for shear thickening fluids.

Fig. 3.5 shows the effect of a variation of the Brinkman number for both pseudoplastic and dilatant fluids respectively. These figures correspond to six different values of $Br$, namely $Br = 0, 2, 10, 15, 20$ and 25. The dotted dashed lines in curves (a) through to (h) represent the temperature profiles with corresponding values to these Brinkman numbers with $n = 0.5$ and the solid lines with $n = 1.5$. It is observed in this figure that when $Br$ increases the temperature of the fluid increases significantly. Increasing $Br$ results in viscous heat dissipation effect. The increase is more pronounced for the dilatant fluid as shown as curves (c), (g), (i), (j) and (k), which illustrate that these fluids respond more rapidly to viscous heat dissipation effect than the pseudoplastic fluid in curves (b), (d), (e), (f) and (h) respectively. It is important to note that curve (a) with $Br = 0$ is common for both cases where $n = 0.5$ and $n = 1.5$, this curve displays a typical linear profile for the temperature of the fluid, which increases across the layer to the maximum temperature at the top layer. In curve (h) with $Br = 25$ the maximum temperature as $T = 1.62$ at $y = 1$ compared to curve (k) with the same Brinkman number and the maximum temperature is given by $T = 3.33$ and $y = 1$ which is 50% higher. Our results are in agreement with the numerical results obtained by Wafo Soh *et al.* [101]. However, temperature profiles shown in this work are significantly higher due to our choice for the Brinkman number ranging between $0 \leq Br \leq 25$ as compared to their range of $2 \leq Br \leq 8$.

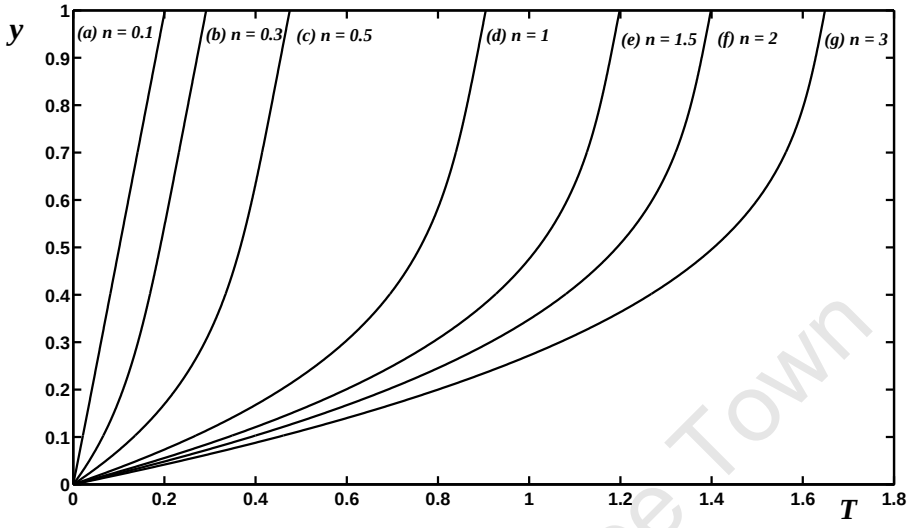


Figure 3.4: The temperature profiles for Equation (3.2.6): Boundary conditions (2.3.13).

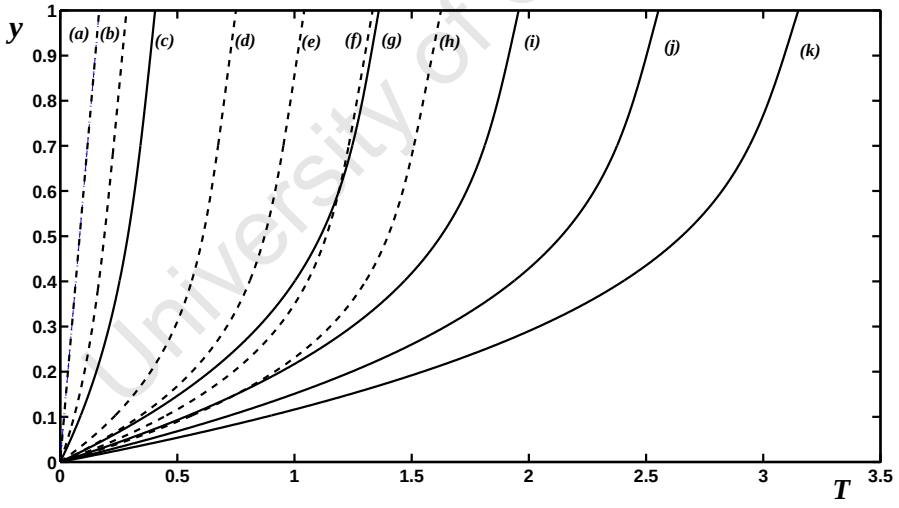


Figure 3.5: The effect of $Br$ on the resulting temperature profiles with $n = 0.5$ dotted dashed lines, $n = 1.5$ solid lines, corresponding to Equation (3.2.6): Boundary conditions (2.3.13).

### 3.2.1 Conclusion

Laminar flow of a power law fluid with a free surface has been investigated. The flow rate, the velocity and the temperature have been plotted and discussed quantitatively. In conclusion, the effect of the power law index plotted for the viscosity versus shear rate with different values of the power law index, shows that when $n < 1$ the fluid viscosity decreases when the shear rate increases, giving raise to what is known as shear thinning behaviour and the opposite is true for $n > 1$. Setting $n = 1$ a Newtonian fluid is retrieved. The resulting flow profiles illustrate that for shear thinning fluids $n < 1$, the velocity and temperature profiles are lower than the Newtonian case. For the case $n \geq 1$ the velocity and temperature of the fluid are slightly greater than the shear thinning fluids with $n < 1$. In general, both the velocity and temperature of the fluid increases across the layer when $n$ increases. The results for the flow rate shows that as the power law index increases from 0.1 to 3, the flux increases in the layer and the flow rare is higher, the higher the flow rate. The Brinkman number $Br$ is also investigated and the results show that as $Br$ increases, the temperature increases due to heat dissipation. In this case the temperature profiles were plotted with fixed values $n = 0.5$ representing shear thinning fluids and $n = 1.5$ for shear thickening fluids. The temperature profiles for shear thickening fluids was found to be significantly higher than that for shear thinning fluids. This illustrates that shear thickening fluids react quickly to heat generation which rises the temperature when the Brinkman number increases.

## 3.3 The flow of a Carreau fluid

The aim of this section is to analyse a non−Newtonian fluid obeying the Carreau model. The non−dimensional form of the Carreau model in Equation (1.4.3) is,

$$\mu = \left(1 + l\left(\frac{\partial u}{\partial y}\right)^2\right)^{\frac{n-1}{2}} , \tag{3.3.7}$$

where $l \approx (\lambda U/H)$. Combining Equations (2.3.9) and (3.3.7), and integrating with respect to $y$, and applying the boundary conditions (2.3.12) gives,

$$\left(1 + l\left(\frac{\partial u}{\partial y}\right)^2\right)^{\frac{n-1}{2}} \frac{\partial u}{\partial y} = (h - y) \ . \tag{3.3.8}$$

Equation (3.3.8) cannot be solved analytically. However, the case where $l \ll 1$ is considered first to allow for analytical progress. Our interest at this stage is to obtain the maximum upper bound for $l$. We will use the experimental data for Hydroxylethycellulose solution flowing in a 5mm thick layer as listed in Table 1 of Myers [76]. The other parameters are given by $\lambda \approx 0.0664$, $\rho g \sin\beta \approx 1000$ and the reference viscosity is given by $\mu_0 = 0.22$. The velocity scale is calculated to be $U = 0.0227$ m/s. Using the above parameter values we can calculate the value of $l \approx 0.3015$. In the following analysis for $l \ll 1$, we will consider the value of $l = 0.3$ as a maximum upper bound for the approximation of the resulting flow profiles. However, it is important to note that, for different fluids, the maximum upper bound for $l$ will be different. We carry our investigation for hydroxylethycellulose solution with its maximum upper bound as calculated above. The asymptotic results are obtained by first considering the values for $l \ll 1$. We further determine the analytical solutions for $n = 0$ representing shear thinning fluids and $n = 2$ for shear thickening fluids. The solutions obtained will be compared with the numerical solution.

## Solution for $l \ll 1$

The velocity is now written in a series form,

$$u = u_0 + l u_1 \ , \tag{3.3.9}$$

where $u_1$ is the first order correction term. Substituting Equation (3.3.9) into (3.3.8) and expanding, leads to,

$$\frac{\partial u_0}{\partial y} + \frac{n-1}{2} l \left(\frac{\partial u_0}{\partial y}\right)^3 + l\left(\frac{\partial u_1}{\partial y}\right) = (h-y) \ . \tag{3.3.10}$$

Integrating the leading order terms gives,

$$u_0 = \frac{y}{2}\Big(2h - y\Big) \ . \tag{3.3.11}$$

Equation (3.3.11) is a standard parabola and can be obtained in several references, see [1, 79] for example. The $l$ correction terms satisfies,

$$\frac{\partial u_1}{\partial y} + \frac{n-1}{2}\left(\frac{\partial u_0}{\partial y}\right)^3 = 0 \ . \tag{3.3.12}$$

Equation (3.3.12) corresponds to Equation (3.10) in [80]. This is solved using the imposed boundary condition $u_1(0) = 0$ to give,

$$u_1 = \frac{(1-n)}{8}\Big[(y-h)^4 - h^4\Big] \ . \tag{3.3.13}$$

To order $l$ the velocity may then be written,

$$u = u_0 + l u_1 = \frac{y}{2}\Big(2h - y\Big) + l\frac{(1-n)}{8}\Big[(y-h)^4 - h^4\Big] \ . \tag{3.3.14}$$

The flux is given by integrating Equation (3.3.14) from 0 to $h$,

$$Q = \int_0^h u dy = \frac{1}{3}h^3 + \left(\frac{l(n-1)}{10}\right) h^5 \ . \tag{3.3.15}$$

Equation (3.3.15) provides the solution for the flow rate. Equations (2.3.11) and (3.3.7) are coupled to give,

$$\frac{\partial^2 T}{\partial y^2} = -Br\left(\frac{\partial u}{\partial y}\right)^2 \left[1 + l\left(\frac{\partial u}{\partial y}\right)^2\right]^{\frac{n-1}{2}} \ . \tag{3.3.16}$$

Equation (3.3.16) must be solved numerically to obtain the full solution. We now follow a similar procedure used to determine the velocity profile to obtain the solution for the temperature profile, that is, the case where $l \ll 1$. Now the temperature can be written in series form,

$$T = T_0 + lT_1 \ , \tag{3.3.17}$$

and combining Equations (3.3.16) and (3.3.17) gives,

$$\frac{\partial^2 T_0}{\partial y^2} + l\frac{\partial^2 T_1}{\partial y^2} = -Br\left[\left(\frac{\partial u_0}{\partial y}\right)^2 + \frac{(n-1)l}{2}\left(\frac{\partial u_0}{\partial y}\right)^4 + 2l\left(\frac{\partial u_0}{\partial y}\right)\left(\frac{\partial u_1}{\partial y}\right)\right] \ . \tag{3.3.18}$$

Integrating the leading order terms with respect to $y$ and applying the boundary conditions (2.3.13) yields,

$$T_0 = \frac{Br}{12}\left(h^4\left(1 - \frac{Bi}{(Bi\ h-1)}y\right) - (h-y)^4\right) + \left(\frac{Bi}{(Bi\ h-1)}\right)y \ . \tag{3.3.19}$$

The first order correction terms is,

$$\frac{\partial^2 T_1}{\partial y^2} = -Br\left[\frac{(n-1)}{2}\left(\frac{\partial u_0}{\partial y}\right)^4 + 2\left(\frac{\partial u_0}{\partial y}\right)\left(\frac{\partial u_1}{\partial y}\right)\right] \ . \tag{3.3.20}$$

Coupling Equations (3.3.12) and (3.3.20) gives,

$$\begin{aligned}\frac{\partial^2 T_1}{\partial y^2} &= -Br\left[\frac{(n-1)}{2}\left(\frac{\partial u_0}{\partial y}\right)^4 - (n-1)\left(\frac{\partial u_0}{\partial y}\right)^4\right] \\ &= \frac{3Br(1-n)}{2}\left(\frac{\partial u_0}{\partial y}\right)^4 \ .\end{aligned} \tag{3.3.21}$$

The boundary conditions for $T_1$ satisfy,

$$T_1(0) = 0 \ , \quad \left.\frac{\partial T_1}{\partial y}\right|_{y=h} = Bi\ T_1 \ . \tag{3.3.22}$$

The expression for $T_1$ is therefore,

$$T_1 = \frac{Br(1-n)}{10}\left[(h-y)^6 - h^6 + \left(\frac{Bi}{(Bi\ h-1)}\right)y\right] \ , \tag{3.3.23}$$

and so the final temperature profile becomes,

$$\begin{aligned} T &= T_0 + lT_1 \\ &= \frac{Br}{12}\left(h^4\left(1-\frac{Bi}{(Bi\ h-1)}y\right)-(h-y)^4\right)+\frac{Bi\ y}{(Bi\ h-1)} \\ &\quad +\frac{lBr(1-n)}{10}\left[(h-y)^6-h^6+\frac{Bi\ y}{(Bi\ h-1)}\right] . \end{aligned} \tag{3.3.24}$$

Equation (3.3.24) provides the solution for the temperature profile. We now proceed to determine the velocity, the flow rate and the temperature profiles when $n = 0$.

## Solution for $n = 0$

In order to obtain the solution for the velocity profile for $n = 0$, Equation (3.3.8) is now written,

$$\left(1+l\left(\frac{\partial u}{\partial y}\right)^2\right)^{-\frac{1}{2}}\frac{\partial u}{\partial y}=(h-y)\ . \tag{3.3.25}$$

For purely gravity driven flow, Equation (3.3.25) gives,

$$\frac{\partial u}{\partial y}=\frac{(h-y)}{\sqrt{1-l(h-y)^2}}\ . \tag{3.3.26}$$

Note Equation (3.3.26) is valid only for all $l \ll 1$, this choice of $l$ is reflected in the scaling for $U$ in which gravitational force is the dominant driving force for the flow. Integrating Equation (3.3.26) and applying the boundary conditions (2.3.12) yields,

$$u=\frac{1}{l}\left(\sqrt{1-l(h-y)^2}-\sqrt{1-lh^2}\right)\ . \tag{3.3.27}$$

Equation (3.3.27) gives the solution for the velocity profile. The flux is given by integrating Equation (3.3.27) from 0 to $h$,

$$Q=\int_0^h u dy=\frac{1}{2\sqrt[3]{l}}\arctan\left(\frac{\sqrt{l}\ h}{\sqrt{1-lh^2}}\right)-\left(\frac{\sqrt{l-lh^2}}{2l}\right)h\ . \tag{3.3.28}$$

Equation (3.3.28) provides the solution for the flow rate. To determine the solution for temperature profiles, Equations (2.3.11), (3.3.7) and (3.3.26) are combined to give,

$$\frac{\partial^2 T}{\partial y^2} = -\frac{Br(h-y)^2}{\left[1 + l\frac{(h-y)^2}{(1-l(h-y)^2)}\right]^2} \ . \tag{3.3.29}$$

Integrating Equation (3.3.29) and applying the boundary conditions (2.3.13) gives,

$$\begin{aligned} T \quad &= -Br\left[\frac{l^2}{56}y^8 - \frac{l^2 h}{7}y^7 + \frac{1}{30}\left(15l^2h^2 - 2l\right)y^6\right] \\ &+Br\left[\frac{1}{5}\left(5h^3l^2 + 2hl\right)y^5 - \frac{1}{12}\left(12lh^2 + 15h^4l^2 + 1\right)y^4\right] \\ &-Br\left[\frac{1}{3}\left(4h^3l - 3h^5l^2 - h\right)y^3 + \frac{1}{2}\left(h^2 - 2h^4l + h^6l^2\right)y^2\right] \\ &+\frac{BrBi}{(Bi\ h-1)}\left[\frac{l^2h^8}{8} - \frac{h^6l}{3} + \frac{h^4}{4}\right]y - \frac{Br}{(Bi\ h-1)}\left[\frac{l^2h^7}{7} - \frac{2h^5l}{5} + \frac{h^3}{3}\right]y \\ &+\frac{Bi}{(Bi\ h-1)}y \ . \end{aligned} \tag{3.3.30}$$

Equation (3.3.30) gives the solution for the temperature profile. In the following subsection, we proceed to determine the velocity, flux and the temperature profiles for $n = 2$.

## Solution for $n = 2$

The velocity profile for the case $n = 2$ is now determined. Equation (3.3.8) is written,

$$\left(1 + l\left(\frac{\partial u}{\partial y}\right)^2\right)^{\frac{1}{2}}\frac{\partial u}{\partial y} = (h-y) \ . \tag{3.3.31}$$

Equation (3.3.31) gives,

$$\left(\frac{\partial u}{\partial y}\right)^2 = \frac{-1 \pm \sqrt{1 + 4l(h-y)^2}}{2l} \ . \tag{3.3.32}$$

For purely gravity driven flow, $(\partial u/\partial y) > 0$. Thus Equation (3.3.32) can be expanded to the order $\mathcal{O}(l^2)$ to give,

$$\frac{\partial u}{\partial y} = \frac{1}{2}\left[2(h-y) - l(h-y)^3\right] \ . \tag{3.3.33}$$

Integrating Equation (3.3.33) and applying the boundary conditions (2.3.12) yields,

$$u = \frac{1}{8}\left[4y\,(2h - y) + l\,(h - y)^4\right] \ . \tag{3.3.34}$$

The flux is given by integrating Equation (3.3.34) from 0 to $h$,

$$Q = \int_0^h u dy = \frac{h^3}{3} + \frac{l\ h^5}{40} \ . \tag{3.3.35}$$

Equations (2.3.11) and (3.3.32) are combined and expanded to give,

$$\frac{\partial^2 T}{\partial y^2} = -Br\left[(h - y)^2 - l(h - y)^4\right] - \frac{Brl}{2}\left[(h - y)^2 - l(h - y)^4\right]^2 \ . \tag{3.3.36}$$

Rearranging the terms to the order $\mathcal{O}(l^2)$ in Equation (3.3.36), integrating and applying the boundary conditions (2.3.13) gives,

$$\begin{aligned} T \quad &= -\frac{Br}{2}\left[\frac{1}{6}(h - y)^4 - \frac{l}{30}(h - y)^6\right] - \frac{Bi\ Br}{2(Bi\ h - 1)}\left[\frac{h^4}{6} - \frac{lh^6}{30}\right] y \\ &\quad + \frac{Br}{2}\left[\frac{h^4}{6} - \frac{lh^6}{30}\right] + \frac{Bi}{(Bi\ h - 1)} y \ . \end{aligned} \tag{3.3.37}$$

Equation (3.3.37) gives the solution for the temperature profile when $n = 2$.

The presentation of the results is organised as follows. The effect of the flow controlling parameters, such as, the power law index $n$ and $l$ are varied to illustrate the behaviour of the fluid viscosity. These flow controlling parameters are again used to investigate their effect on the flow rate, the velocity and the temperature profiles. The effect of $l$ when $n = 0$ and $n = 2$ on the resulting flow profiles is also investigated. Note that in the limit as $l \to 0$, the Newtonian results is recovered as expected, for the $n = 0$ case.

Fig. 3.6 represents plotted curves of the viscosity versus shear rate and the profiles correspond to different values of $l$, namely $l = 0, 0.1, 0.2$ and $0.3$ with $n = 0.5$. Curves (a) to (c) show that when $l$ increases the viscosity of the fluid decreases as the shear rate increases. The Newtonian behaviour is shown in curve (d) with $l = 0$ which shows that the viscosity is constant as the shear rate increases. For $n > 1$, the viscosity of the fluid increases as the shear rate increases when $l$ increases and this is displayed in curves (e) to

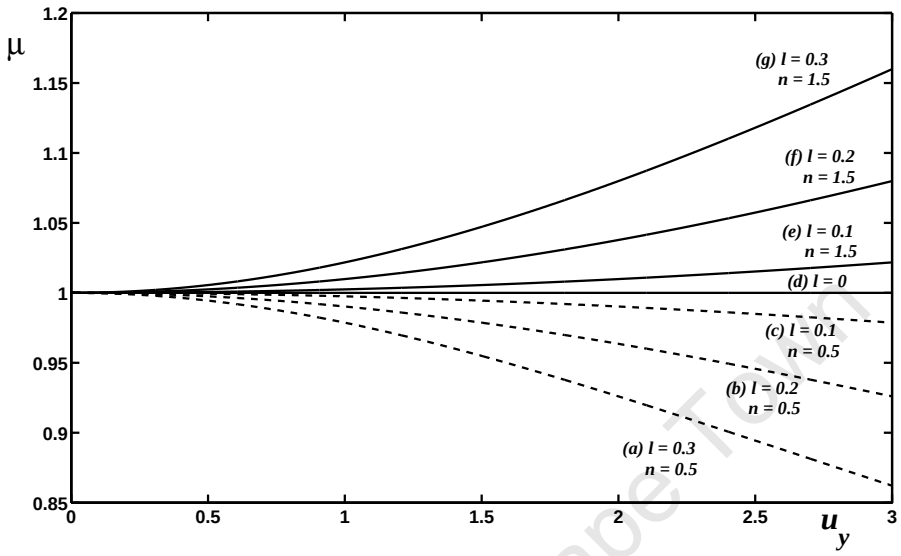


Figure 3.6: Viscosity versus shear rate for various values of $l$ with $n = 0.5$ and $n = 1.5$.

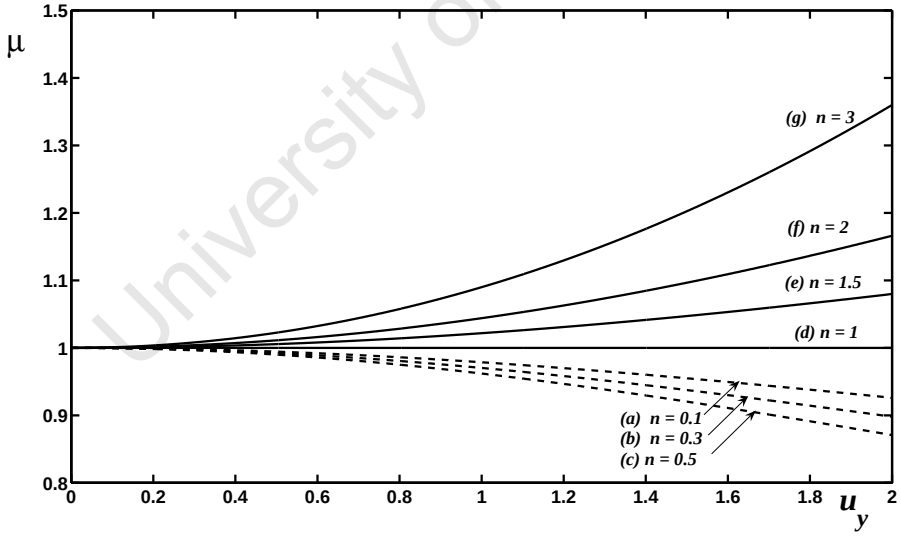


Figure 3.7: Viscosity versus shear rate for power law index $n$ with $l = 0.3$.

(g). The effect of the power law index is shown in Fig. 3.7 with $l = 0.3$. The Newtonian fluid (with $n = 1$) is shown in curve (d) which shows that the viscosity is constant when the shear rate increases. When $n < 1$ the viscosity of the fluid decreases as the shear rate increases and the opposite of this behaviour is shown in curves (e) to (g). When $n$ increases from 1.5 to 3 the viscosity increases as the shear rate increases. Machac *et al.* [60] investigated a terminal falling velocity of a spherical particle using a Carreau model and their results also showed that the fluid viscosity decreases when the power law index increases and their results are in agreement with our results as shown in Fig. 3.7.

The flow rate is displayed in Fig. 3.8 with different values of $l$, namely $l = 0.1, 0.2, 0.3$ and $n = 0.5$ for shear thinning fluids. It is important to note that when $n > 1$ we have more or less a similar behaviour of the flow rate. It is observed from the figure that when $l$ increases we have different levels of the flow rate. Fig. 3.9, displays the flow rate with different values of $n$ and $l = 0.3$. Again in this case when $n$ increases we observe different levels of the flow rate. These two figures show that when either $l$ or $n$ increases, the flux increases in the layer and the flow rate is higher.

The velocity profiles corresponding to Equation (3.3.14) are plotted in Fig. 3.10 with $n = 0.5$ and Fig. 3.11 with $n = 1.5$ respectively. The figures plotted have different values of $l$ and the film height is fixed at $h = 1$. In Fig. 3.10, for $l = 0$, the Newtonian velocity profile is retrieved in curve (a). When $l$ increases the viscosity of the fluid decreases for shear thinning fluids and the velocity increases as the resistance force to the flow decreases with its maximum occurring at the top layer. In Fig. 3.11, with $n \geq 1.5$, the curves illustrate that when $l$ decreases the velocity of the fluid decreases. When the parameter $l$ decreases the fluid viscosity decreases for shear thickening fluids (see Fig. 3.6) and the velocity increases accordingly. This show that the less viscous is the fluid the higher the flow.

Figs. 3.12 and 3.13 shows the temperature profiles for Equation (3.3.24). The temperature

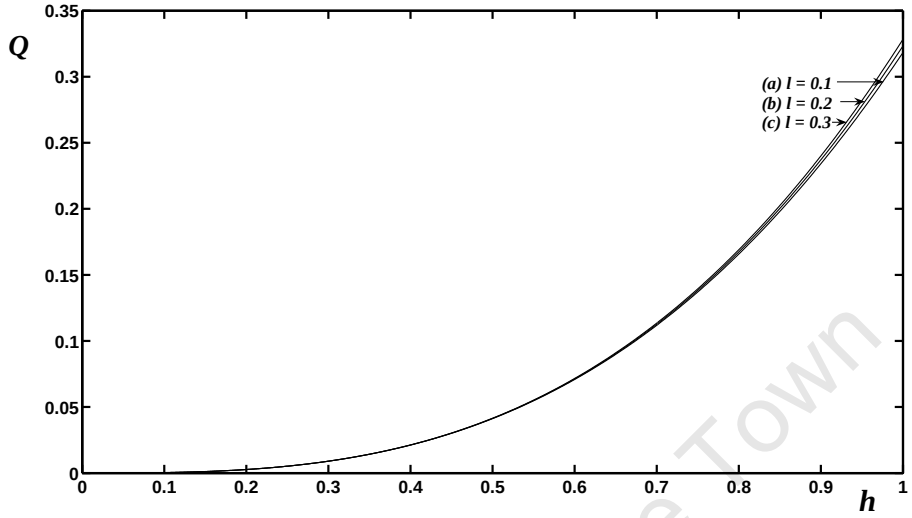


Figure 3.8: The flux versus height for Equation (3.3.15) with different values of $l$ and $n = 0.5$.

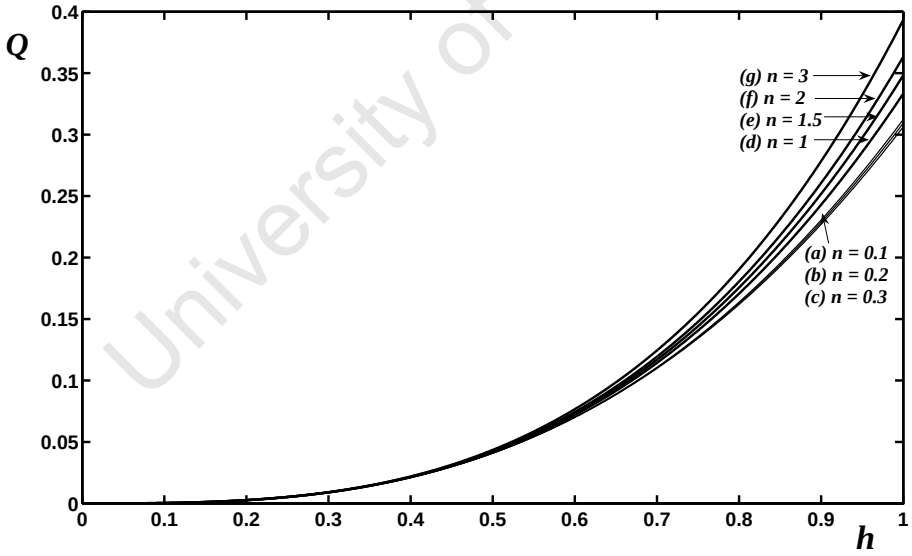


Figure 3.9: The flux versus height for Equation (3.3.15) with different values of $n$ and $l = 0.3$.

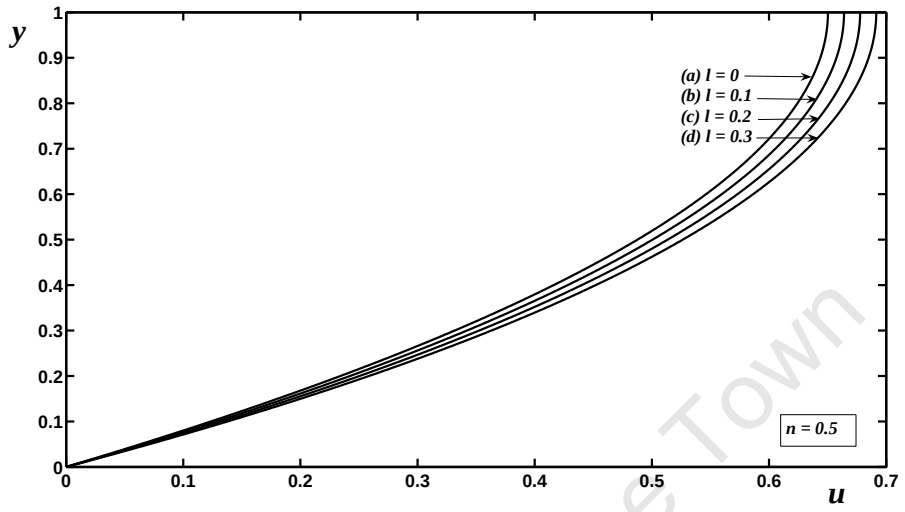


Figure 3.10: The velocity profiles for Equation (3.3.14) with various values of $l$ and $n = 0.5$: Boundary conditions (2.3.12).

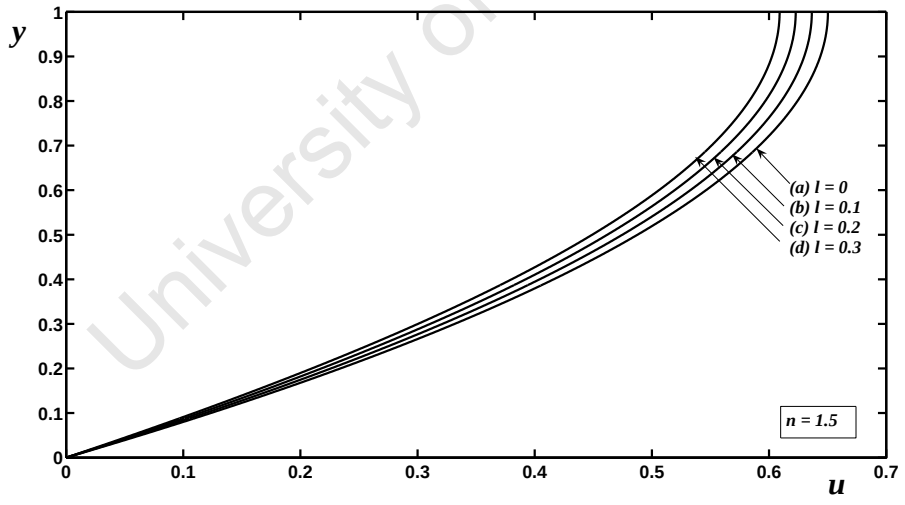


Figure 3.11: The velocity profiles for Equation (3.3.14) with various values of $l$ and $n = 1.5$: Boundary conditions (2.3.12).

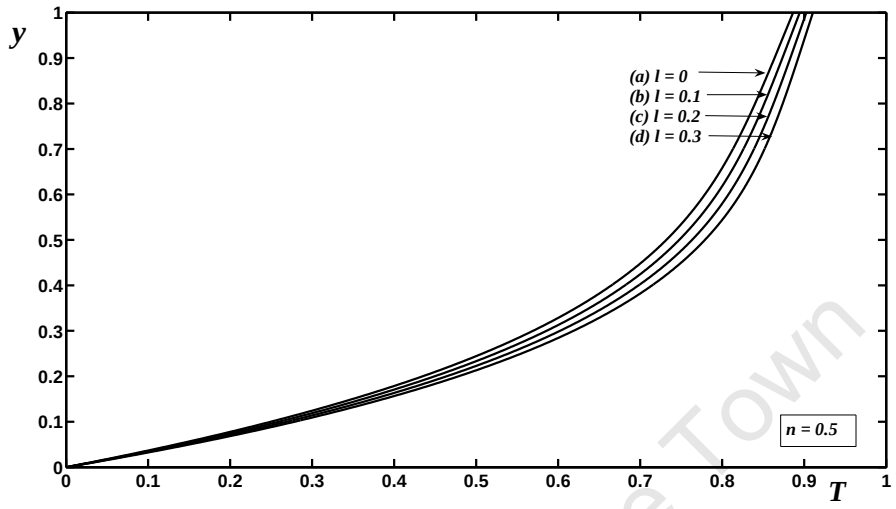


Figure 3.12: The temperature profiles for Equation (3.3.24) with various values of $l$ and $n = 0.5$: Boundary conditions (2.3.13).

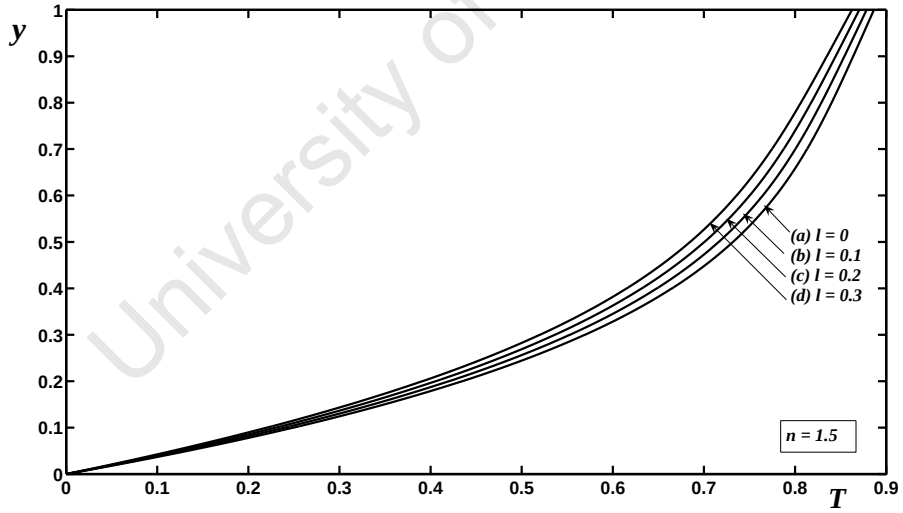


Figure 3.13: The temperature profiles for Equation (3.3.24) with various values of $l$ and $n = 1.5$: Boundary conditions (2.3.13).

profiles are plotted with different values of $l$, $n = 0.5$ and $n = 1.5$. The other parameters are given by $Bi = 0.3$ and $Br = 0.3$ for all these figures. In each figure the temperature profiles are plotted with different values of $l$ similar to those used in Figs. 3.10 with $n = 0.5$ and 3.11 with $n = 1.5$ respectively. In Fig. 3.12 the fluid temperature increases when the non−dimensional parameter $l$ increases, for shear thinning fluids. This shows that heat generation as a result of the viscous term is high when $l$ increases. In Fig. 3.13 the temperature of the fluid for shear thickening fluids is contrary to the curves displayed in Fig. 3.12. The temperature of the fluid increases when $l$ decreases. Heat generation by the viscous term in curves (a) to (d) is higher when the parameter $l$ decreases.

The velocity profiles are now investigated for various power law indices. Equation (3.3.14) is plotted for several values of $n$ between $0.1 \leq n \leq 3$ and $l = 0.3$, in Fig. 3.14. The figure shows that when $n$ decreases, the velocity of the fluid increases across the layer to their maximum values at the free surface. For $n < 1$, the velocity of the fluid increases gradually whilst for $n > 1$ the gap between the fluid velocity is more pronounced with the maximum value for the velocity profile in curve (g) approximately half of the maximum value for the velocity in curve (a). It is shown in this figure that when $n < 1$, the resistance force to the flow for shear thinning fluids is less as $n$ decreases, and the fluid velocity increases significantly. In Fig. 3.15 the temperature profiles corresponding to Equation (3.3.24) are plotted for the same parameter values as in Fig. 3.14, the Brinkman number is fixed at $Br = 0.3$ and the Biot number is also fixed at $Bi = 0.3$. All these curves are similar in shape and the fluid temperature increases to their maximum temperatures at the top layer. In this case when $n < 1$ again we observe the fluid temperature increasing gradually and for $n > 1$ the gap between the temperature profiles is more pronounced and the fluid temperature increases as $n$ decreases. This figure illustrates that the temperature of the fluid increases due to viscous heat generation.

The velocity profiles corresponding to Equation (3.3.27) are now plotted for different values of $l$ with $n = 0$. In Fig. 3.16 curves (a) to (d) are shown and the velocity of the

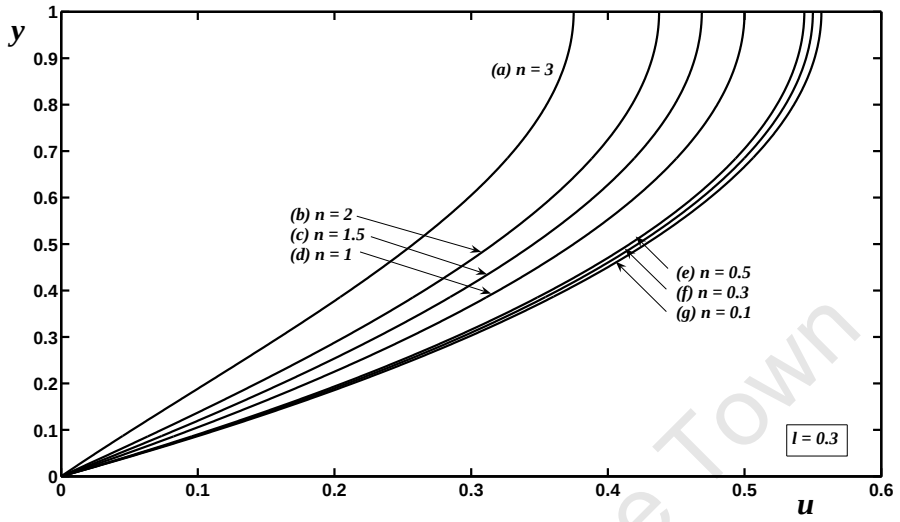


Figure 3.14: The velocity profiles corresponding to Equation (3.3.14) with $l = 0.3$: Boundary conditions (2.3.13).

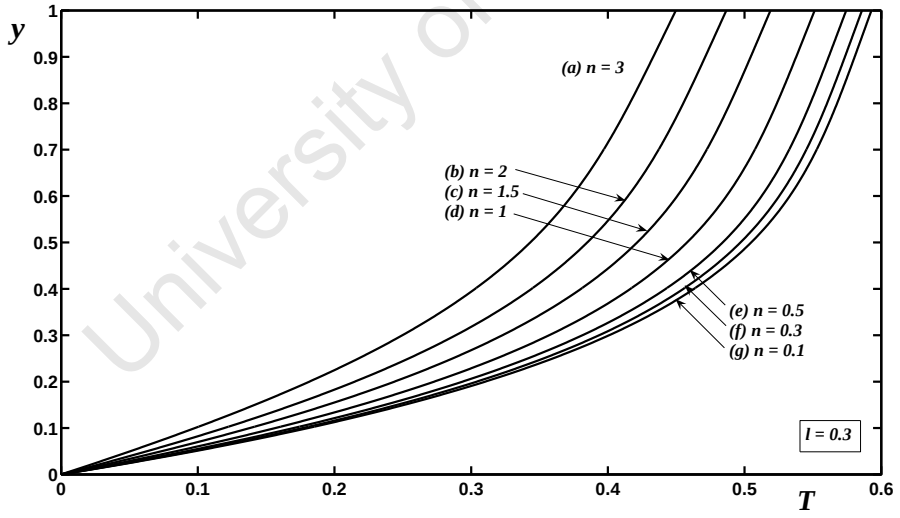


Figure 3.15: The temperature profiles corresponding to Equation (3.3.24) with $l = 0.3$: Boundary conditions (2.3.13).

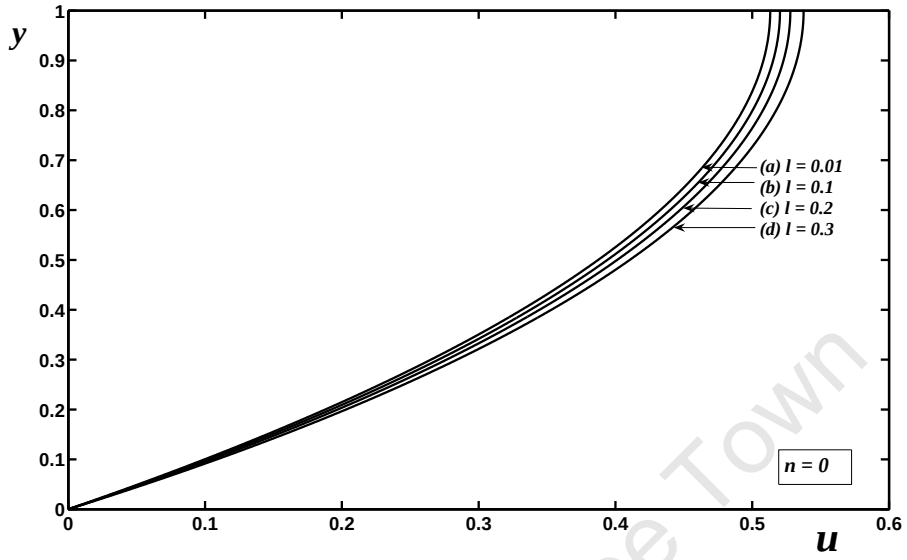


Figure 3.16: The velocity profiles corresponding to Equation (3.3.27) with different values of $l$ and $n = 0$: Boundary conditions (2.3.12).

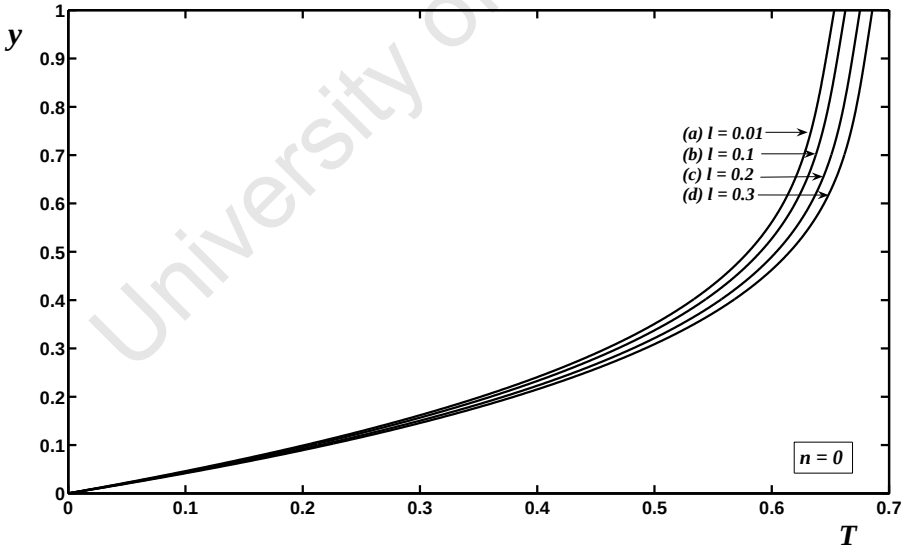


Figure 3.17: The temperature profiles corresponding to Equation (3.3.30) with different values of $l$ and $n = 0$: Boundary conditions (2.3.13).

fluid increases and the gap between them is approximately 2%. The viscosity of the fluid decreases when $l$ increases and subsequently an increase in the fluid velocity is observed due to less resistance force to the flow. The flow rates are shown in Figs. 3.18 and 3.19 (for $n = 2$). The figures illustrate that when $l$ increases, the flux increases in the layer and the flow rate is higher. In Fig. 3.17 the temperature profiles resulting from Equation (3.3.30) are shown. The Brinkman and the Biot numbers are fixed at $Br = Bi = 0.3$ and the values of $l$ are the same as those which are shown in Fig. 3.16. In Fig. 3.17 when $l$ increases, the temperature of the fluid increases and the maximum values for these profiles occurs at the free surface and the gap between the profiles is again 2%. This figure illustrates that the temperature of the fluid increases as $l$ increases due to heat generation by the internal flow processes such as viscous action, which acts to increase the temperature of the fluid.

The velocity profiles corresponding to Equation (3.3.34) are shown in Fig. 3.20 with different values of $l$ and $n = 2$. In this figure the fluid behaviour shows the opposite of the curves as displayed in Fig. 3.16. In curves (a) to (d) the velocity of the fluid increases when the values of $l$ decreases. These curves demonstrate that when $l$ decreases, the velocity increases across the layer, since the viscosity is decreasing and the resistance force to the flow decreases resulting in an increase in the velocity of the fluid. In Fig. 3.21 the temperature profiles corresponding to Equation (3.3.37) are displayed with $Br = Bi = 0.3$ and different values of $l$ as shown in the figure. In this figure again we observe the complete opposite behaviour of shear thinning fluids in Fig. 3.17. In Fig. 3.21 when $l$ decreases, the temperature of the fluid increases. The increase in the fluid temperature is caused by the viscous heat generation, which also act to raise the temperature of the fluid in the layer.

In the following section the velocity and the temperature profiles will be investigated using a numerical method and considering large values of a non−dimensional parameter $l$. We again investigate the effect of the power law index on the resulting flow profiles.

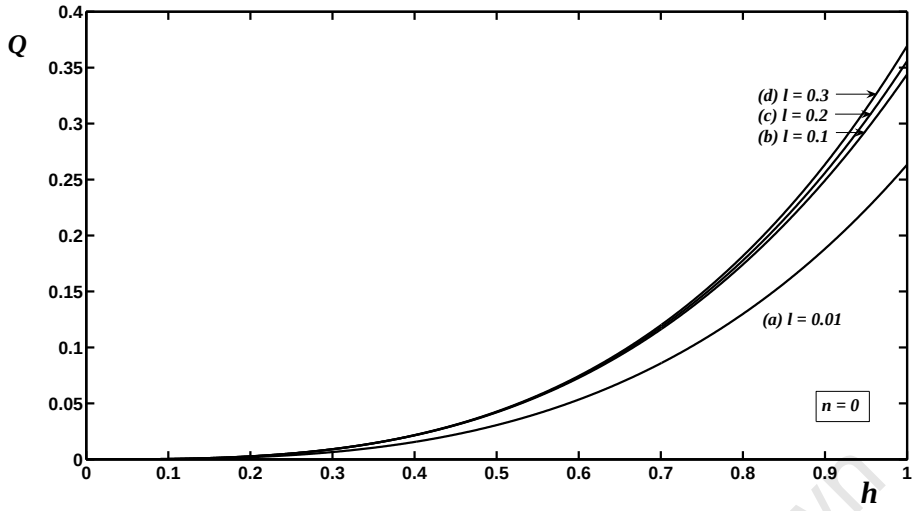


Figure 3.18: The flow rate versus height for Equation (3.3.28) with different values of $l$ and $n = 0$.

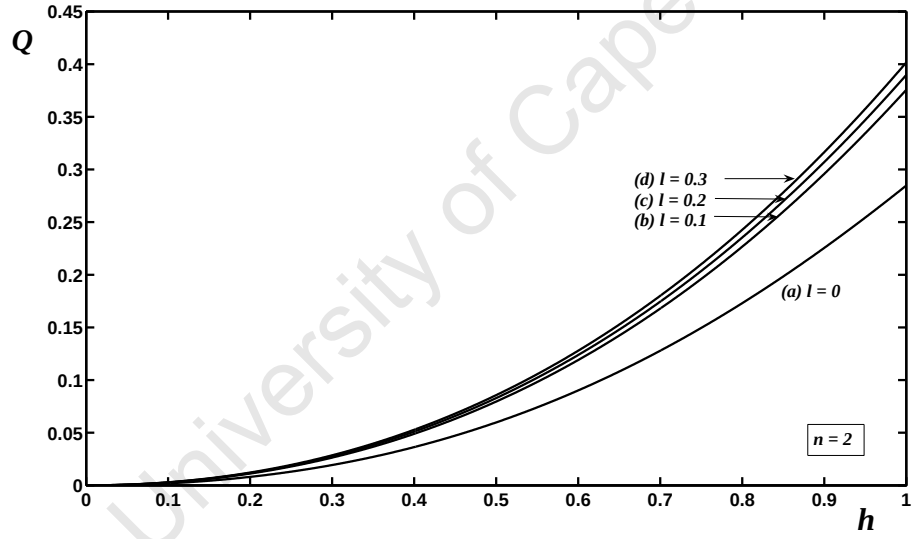




Figure 3.19: The flow rate versus height for Equation (3.3.35) with different values of $l$ and $n = 2$.

### 3.3.1 Numerical scheme for the Carreau model

In the previous section analytical results were obtained for values of $l \ll 1$, $n = 0$ and $n = 2$. A numerical solution valid for all values of $l$ is now introduced. The Newton Raphson method is used to obtain a full solution for the velocity and temperature profiles,

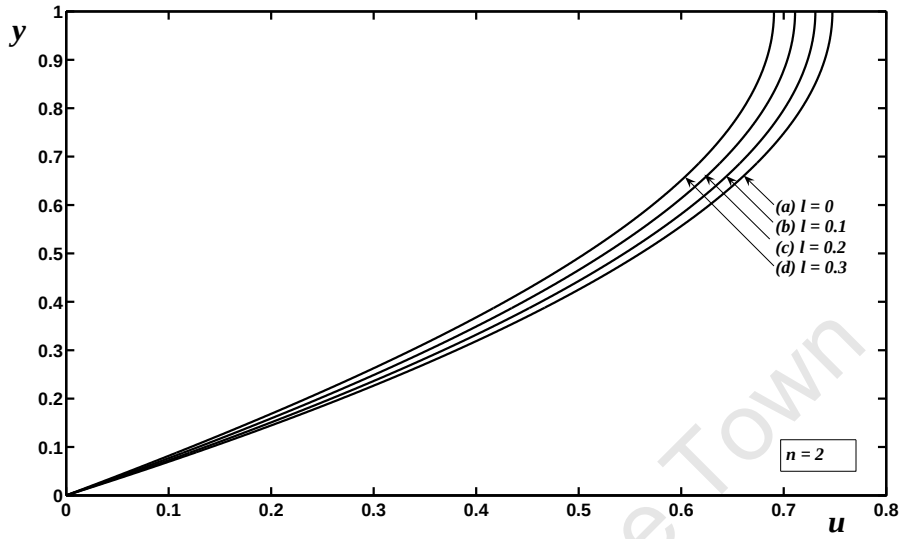


Figure 3.20: The velocity profiles corresponding to Equation (3.3.34) with different values of $l$ and $n = 2$: Boundary conditions (2.3.12).

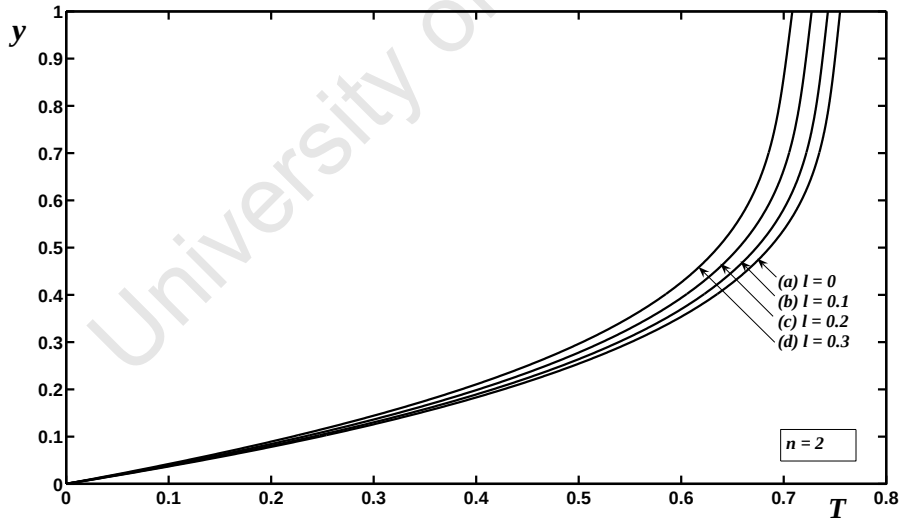


Figure 3.21: The temperature profiles corresponding to Equation (3.3.37) with different values of $l$ and $n = 2$: Boundary conditions (2.3.13).

see [14, 17]. Numerical results are compared with analytical results obtained in the previous section for $l \ll 1$, $n = 0$ and $n = 2$. The analytical results are used as a benchmark to validate the numerical code. Equations (3.3.8) and (3.3.16) may be written,

$$\left(\frac{\partial u}{\partial y}\right)^{\frac{2}{n-1}} + l\left(\frac{\partial u}{\partial y}\right)^{\frac{4}{n-1}} - (h-y)^{\frac{2}{n-1}} = 0\ . \tag{3.3.38}$$

$$\frac{\partial^2 T}{\partial y^2} + Br\left(\frac{\partial u}{\partial y}\right)^2\left[1 + l\left(\frac{\partial u}{\partial y}\right)^2\right]^{\frac{n-1}{2}} = 0\ . \tag{3.3.39}$$

The coupled, non$-$linear partial differential Equations (3.3.38) and (3.3.39) are now solved numerically to obtain a full solution for the velocity $u$ and temperature $T$. The fluid dept is divided into two $j$ cells of step size $\triangle y$. The values of $u$ and $T$ in the $i^{th}$ cell are denoted by $u_i$ and $T_i$ respectively. Equation (3.3.38) takes the form,

$$\left(\frac{\partial u}{\partial y}\right)^{\frac{2}{n-1}}\bigg|_{y=y_i} + l\left(\frac{\partial u}{\partial y}\right)^{\frac{4}{n-1}}\bigg|_{y=y_i} = \Big(h - y_i\Big)^{\frac{2}{n-1}}\ , \tag{3.3.40}$$

where $y_i = i\triangle y$ and $\triangle y$ denote the step size between the cells. The space derivative is calculated using Newton's algorithm in every cell. In this case an initial approximation of $u_0$ and $T_0$ is generated in order to obtain the next approximation value. The boundary conditions give the initial iteration, that is, $u_0 = 0$ at $y = 0$ and $T_0 = 0$ at $y = 0$. We solve for $(\partial u/\partial y)$ and then calculated $u$ throughout the layer, and the velocity may be calculated using the standard integration method,

$$u_{i+1} = u_i + \triangle u_y.\left(\frac{\partial u}{\partial y}\right)\bigg|_{y=y_i}\ , \tag{3.3.41}$$

at $y = y_i$. Finally, Equation (3.3.39) is integrated twice to give the full solution for the temperature profile. The results are now plotted for various values of $l$ and $n$.

We begin our discussion of the numerics by first comparing the analytical solution with a full solution obtained using a numerical code. We use MATLAB to derive the full solution from the governing equations using the Newton Raphson numerical method. We first test our numerical code by comparing the solution resulting from Equations

(3.3.39) and (3.3.40) with $n = 0$ for shear thinning fluids and $n = 2$ for shear thickening fluids. The velocity profiles are plotted from Equations (3.3.14), (3.3.27), (3.3.34) and (3.3.40) for comparison purposes. The temperature profiles are also plotted for Equations (3.3.24), (3.3.30), (3.3.37) and (3.3.39) respectively. For the sake of simplicity, we first compare our numerical code using two small values for the non−dimensional parameter $l$, namely $l = 0.1$ and 0.3. If the analytical results are in agreement with the numerics, we proceed to investigate the numerics for large values of $l$. We proceed again to investigate the behaviour of shear thinning fluids and shear thickening fluids for large values of $l$. The effect of the power law index $n$ on the velocity and temperature profiles is again investigated using the solution obtained numerically.

In Fig. 3.22 the velocity profiles corresponding to Equations (3.3.14), (3.3.27) and (3.3.40) are plotted in curves (a) and (b). In this case the power law index is given by $n = 0$ and $l = 0.1$ and 0.3 as shown in both sets of curves. In set (a), the dash line represents the solution of Equation (3.3.14), the solid line is from the numerics in Equation (3.3.40) and the dash dot line represents the plots for Equation (3.3.27). In set (a) all the curves compare closely and in set (b) all the curves shows a good agreement. Curves (c) to (f) represents the numerical solutions with large values of $l$, namely $l = 1, 3, 7$ and 10. We observe that increasing the values of $l$ results in a significant increase in the fluid velocities. The viscosity of the fluid decreases when $l$ increases, then the fluid velocity increases significantly since the resistance force to flow is diminishing. The convergence of our numerical scheme is obtained within the region $1 \times 10^{-7} \leq \Delta y \leq 1 \times 10^{-9}$. In this range our numerical results do not accept any further grid refinements or changes. The opposite of this behaviour in the velocity of the fluid is shown in Fig. 3.23 with $n = 2$ for shear thickening fluids. The dash dot line is plotted from Equation (3.3.34) and the other curves are as explained above. This figure illustrate that when $l$ decreases the velocity of the fluid increases as expected from shear thickening fluid, due to decreasing resistance force to the flow. In this figure the numerical solution compares well with the analytical

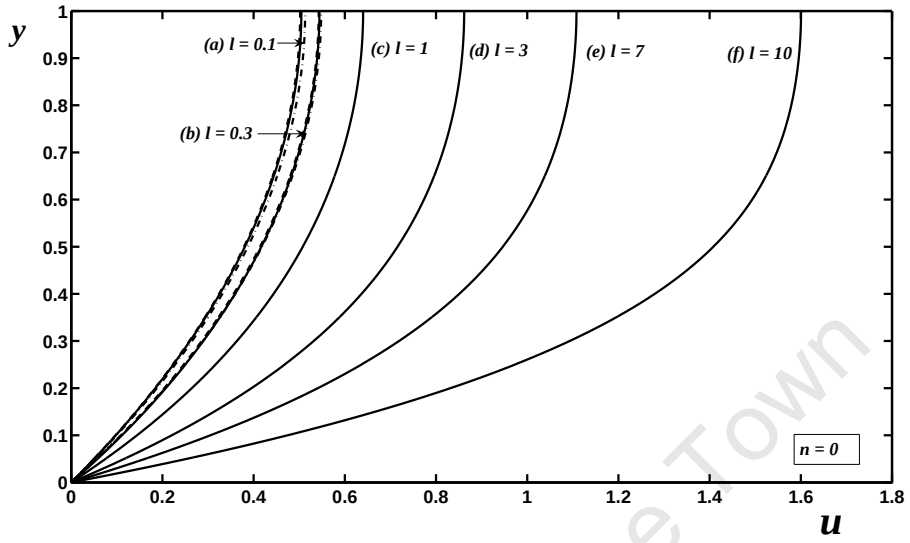


Figure 3.22: The velocity profiles corresponding to Equations (3.3.14), (3.3.27) and (3.3.40) with different values of $l$: Boundary conditions (2.3.12).

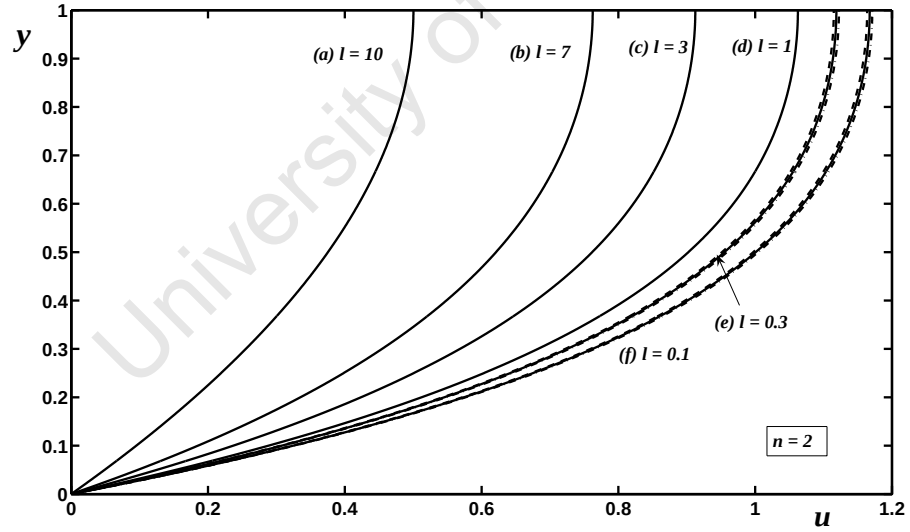


Figure 3.23: The velocity profiles corresponding to Equations (3.3.14), (3.3.34) and (3.3.40) with different values of $l$: Boundary conditions (2.3.12).

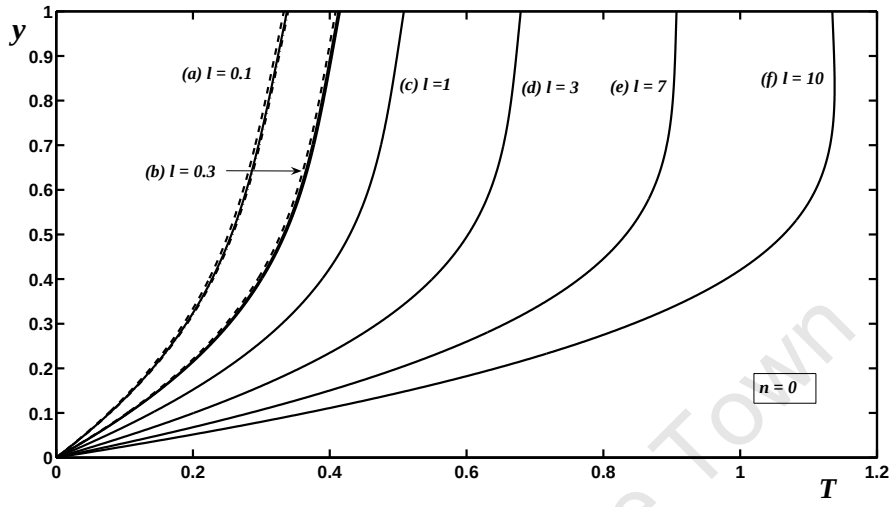


Figure 3.24: The temperature profiles corresponding to Equations (3.3.24), (3.3.30) and (3.3.39) with different values of $l$: Boundary conditions (2.3.13).

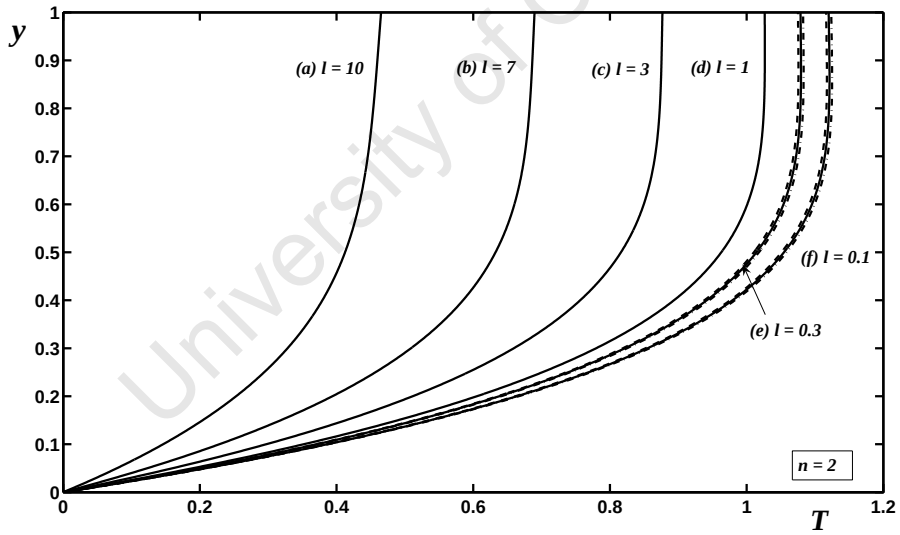


Figure 3.25: The temperature profiles corresponding to Equations (3.3.24), (3.3.37) and (3.3.39) with different values of $l$: Boundary conditions (2.3.13).

solution as shown in curves (e) and (f) for $l = 0.1$ and $l = 0.3$ respectively.

The comparison for the temperature profiles is shown in Fig. 3.24 with $n = 0$ for shear thinning fluids and Fig. 3.25 with $n = 2$ for shear thickening fluids. Fig. 3.24 shows curves corresponding to Equations (3.3.24), (3.3.30) and (3.3.39) with $n = 0$, $Br = Bi = 0.3$ and different values of $l$ as displayed in the figure. For the set of curves (a), the dash line represents the solution for Equation (3.3.24), the solid line is from the numerics in Equation (3.3.39) and the dash dot line represents the solution for Equation (3.3.30). In (b) we again observe that the three curves compare well with the numerics. Curves (c) to (f) show the numerical solution for increasing temperature of the fluid when $l$ increases. The numerical solutions displayed in these curves show maximum temperatures which are greater than the asymptotics as shown previously, since large values for $l$ are considered for the numerical method. Heat is generated in the layer as a result of the action of a viscous force, which causes the collision amongst the fluid molecules and subsequently the temperature of the fluid increases. The opposite of this behaviour of the temperature profiles in Fig. 3.24 is shown in Fig. 3.25. In Fig. 3.25 the dash dot line is plotted from Equation (3.3.37). The temperature increases as the non−dimensional parameter $l$ decreases, with the maximum values for the Newtonian case much higher than for the non−Newtonian fluid with $l = 10$. We again observe that the temperature profiles plotted from the numerics are also in agreement with the analytical solution.

Fig. 3.26 shows the numerical velocity profiles for various values of the power law index $n$ with $l = 0.3$. The fluid velocity for all seven curves increases nonlinearly across the layer to their maximum velocities at the free surface. The results show that the gap between the velocity profiles when $n$ is in the region 0.1 and 0.5 is small and when $n$ is in the region 1 to 3 the gap between the velocity profiles is more pronounced. We observe that the fluid velocity increases when $n$ decreases as a result of the decreasing resistance force to the flow. The Newtonian velocity profile is retrieved in curve (d) with $n = 1$. The velocity profiles resulting from the Carreau model are in agreement with the results shown

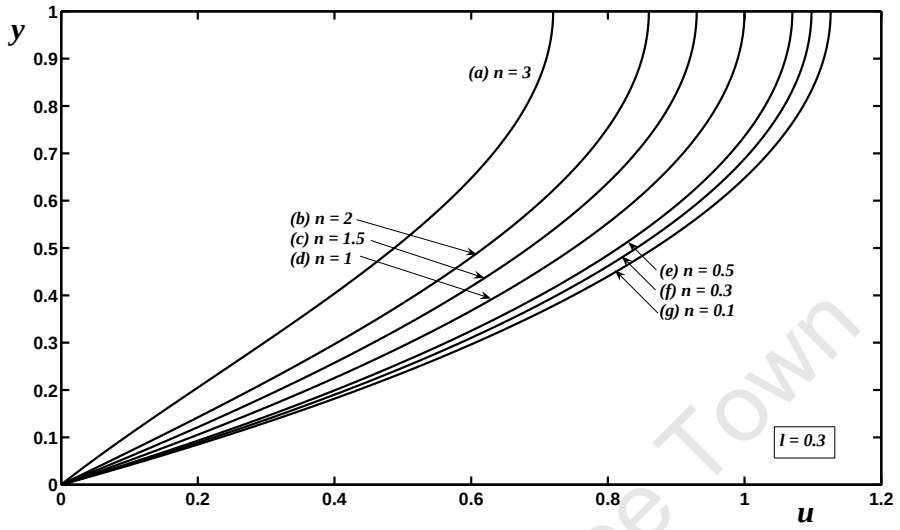


Figure 3.26: The velocity profiles corresponding to Equation (3.3.40) with different values of $n$ and $l = 0.3$: Boundary conditions (2.3.12).

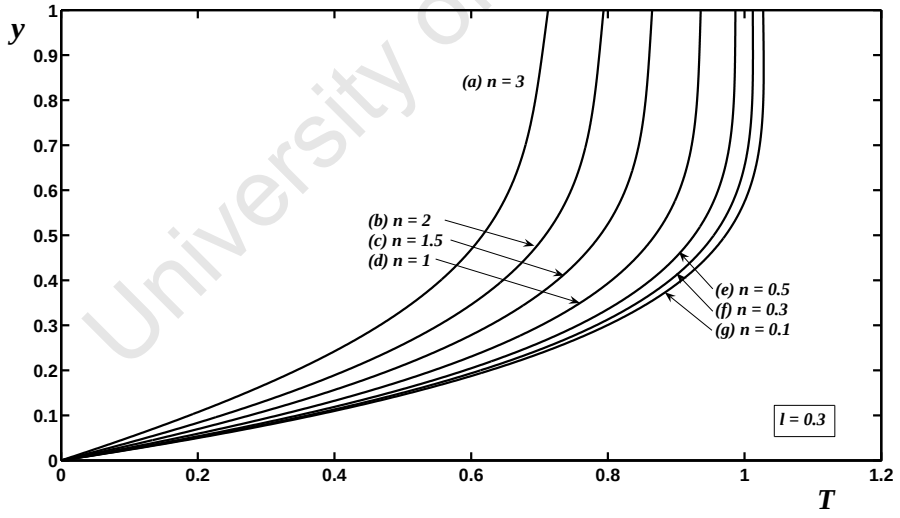


Figure 3.27: The temperature profiles corresponding to Equation (3.3.39) with different values of $n$ and $l = 0.3$: Boundary conditions (2.3.13).

in [76], for shear thinning fluids. However, our velocity profiles show significantly higher maximum values as compared to the profiles in [76], probably due to high shear rates involved in the materials which were investigated. Akyildiz *et al.* [2], used the Runge Kutta method to solve for the velocity profiles for a shear thinning fluid with $n = 0.25$ and the Newtonian fluid with power law index $n = 1$, which is in agreement with our results. Their results revealed that the velocity profile for $n = 0.25$ is slightly higher than the Newtonian case. In Fig. 3.27 the temperature profiles are plotted for the same parameter values of the power law index as shown in Fig. 3.26 with $l = 0.3$ and $Br = Bi = 0.3$. All these temperature curves are similar in shape and the fluid temperatures increase to their maximum levels at the top layer. This shows that the viscous term acts to increase heat generation in the fluid and the temperature of the fluid rises. In the case where $n = 0.1$ and $n = 0.5$, the temperature of the fluid increases gradually as shown in curves (e) to (g), however, in curves (a) through to (d) the gap between the temperature profiles is more pronounced.

### 3.3.2 Conclusion

In this section we have derived the equations governing the flow resulting from the Carreau model. The viscosity versus shear rate were plotted to illustrate the behaviour of the fluid when the flow controlling parameters such as $l$ and the power law index $n$ are varied. The results show that when $l$ increases for shear thinning fluids, the viscosity of the fluid decreases as the shear rate increases and the opposite is true for shear thickening fluids. The viscosity of the fluid decreases with increasing shear rate when the power law index $n > 1$ and the opposite is true for $n < 1$. The effect of the flow controlling parameters on the resulting velocity, flow rate and temperature profiles, were obtained using an analytical and numerical technique. In the case of the flow rates, the results also showed that when either $l$ and $n$ are increasing, the flux increases in the layer and the flow rate is higher. The velocity of the fluid increases significantly when $l$ increases

for $n < 1$ and the opposite is true when $n > 1$. The velocity and temperature profiles increases when the power law index $n$ decreases. The results were extended to include a full solution using the Newton Raphson numerical method for larger values of $l$. The velocity and temperature profiles for small values of $l$ and $n = 0$ were compared and the curves for these profiles are in agreement in particular when $l = 0.3$. Similarly, the results for the velocity and temperature profiles were compared for various values of $l$ with $n = 2$. The results showed good agreement between the analytical results and the numerics, particularly when $l = 0.3$. Therefore, the effect of large values of $l$ on the resulting flow profiles is investigated. The resulting flow profiles shows that the velocity and temperature of the fluid increases significantly when $l$ increases with the power law index $n < 1$ and the opposite is true for $n > 1$. The effect of the power law index $n$ on the resulting flow profiles showed that as $n$ decreases, both the velocity and the temperature of the fluid increases. The numerical solution is preferable since it can be used for larger values of $l$ but the asymptotic solution is useful as a benchmark.

## 3.4 Ellis fluid

The aim of this section is to investigate a fluid obeying the Ellis viscosity model. We consider a purely gravity driven flow such that $\partial u/\partial y > 0$ and the modulus sign in Equation (1.4.4) is neglected. The advantage of using the Ellis model is that it also allows for analytical progress. The Ellis model is non−dimensionalised to give,

$$\frac{1}{\mu} = \left(1 + \phi\left(\mu\frac{\partial u}{\partial y}\right)^{\alpha_1 - 1}\right) . \tag{3.4.42}$$

where $\phi = (\mu_0 U/\tau_1 H)^{\alpha_1 - 1}$. To obtain the velocity, Equations (2.3.9) and (3.4.42) are combined and integrated with respect to $y$, and boundary conditions (2.3.12) are applied to give,

$$\frac{\partial u}{\partial y} = \frac{1}{\mu}(h - y) . \tag{3.4.43}$$

Combining Equations (3.4.42) and (3.4.43), integrating with respect to $y$, and applying the boundary conditions (2.3.12) yields,

$$u = \frac{y}{2}\Big(2h - y\Big) + \frac{\phi}{(\alpha_1 + 1)}\Big[h^{\alpha_1 + 1} - (h - y)^{\alpha_1 + 1}\Big] . \tag{3.4.44}$$

The first term on the right hand side represents a standard parabola for a Newtonian fluid and the second term represents a power law fluid. A similar expression for (3.4.44) is given in [76]. The flux is given by integrating Equation (3.4.44) from 0 to $h$,

$$Q = \int_0^h u dy = \frac{h^3}{3} + \left(\frac{\phi}{(\alpha_1 + 2)}\right) h^{\alpha_1 + 2} . \tag{3.4.45}$$

Equation (3.4.45) gives the solution of the flow rate. Combining Equations (2.3.11) and (3.4.42) leads to,

$$\frac{\partial^2 T}{\partial y^2} = -\frac{Br}{\mu}\Big(h - y\Big)^2 . \tag{3.4.46}$$

Substituting Equation (3.4.42) into Equation (3.4.46), integrating twice with respect to $y$ and applying the boundary conditions (2.3.13) gives,

$$\begin{aligned} T &= -\frac{Br}{12}\left[(h - y)^4 - h^4\left(1 - \frac{Bi}{(Bi\ h - 1)}y\right)\right] + \left(\frac{Bi}{(Bi\ h - 1)}\right) y \\ &\quad - \frac{\phi Br}{(\alpha_1 + 2)(\alpha_1 + 3)}\left[(h - y)^{\alpha_1 + 3} - (h)^{\alpha_1 + 3} - \frac{Bi\ h^{\alpha_1 + 3}}{(Bi\ h - 1)}y\right] . \end{aligned} \tag{3.4.47}$$

The first two terms on the right hand side represent a Newtonian temperature profile and the last term represents the power law temperature profile. In the following discussion of the results, our interest lies with the contribution of the non−dimensional parameter $\phi$ on the resulting flow profiles. The importance of this parameter is shown in Equation (3.4.42), for example, if we consider $\phi = 0$ a Newtonian viscosity is retrieved. However, when $\phi \neq 0$, then the viscosity model is non−Newtonian. The question is how large does the parameter have to be? We consider experimental data listed in [76], to calculate the maximum value possible for $\phi$. For example, if we consider a hydroxylethycellulose flow with a possible height of 0.01 m and other parameters taken from [76] as $\mu_0 = 0.22$, $\tau_1 = 4.93$, $\alpha_1 = 2.073$ and the density given by $\rho = 650$, then we can easily calculate the velocity scale $U = \rho g \sin 15/\mu_0 \approx 0.78$ m/s. This gives $\phi = 3.59$ as the maximum value possible for hydroxylethycellulose. Now we consider the non−dimensional parameter $0 < \phi < 3.59$. It is important to note that hydroxylethycellulose is a shear thickening fluid with $\alpha_1 = 2.073$. Now in the discussion to follow, we consider the values for shear thickening fluids in with $\alpha_1 = 2.073$ with specific reference to hydroxylethycellulose.

Figs. 3.28 and 3.29 show the viscosity versus shear rate behaviour of an Ellis fluid with varying parameter $\phi$, for both shear thinning and shear thickening fluids respectively. In Fig. 3.28 for shear thinning fluid, when $\phi$ increases the fluid viscosity decreases whilst the shear rate increases. The Newtonian case is shown in curve (a) for both figures, which display a constant viscosity as the shear rate increases. Fig. 3.29, with $\alpha_1 = 2.073$ shows an opposite of the behaviour as displayed in Fig. 3.28. It is noteworthy that in Fig. 3.29, the fluid viscosity displays a Newtonian plateau in the lower shear rate region $0 \leq u_y \leq 0.2$ and develops into a power law region and increases significantly as the shear rate increases. Fig. 3.30 with $\phi = 0.3$, displays the viscosity versus shear rate for different parameter values for the power law index $\alpha_1$. For $\alpha_1 < 1$, the viscosity of the fluid decreases when the shear rate increases giving raise to shear thinning behaviour. The constant viscosity is shown in curve (a) with $\alpha_1 = 1$. In the event where $\alpha_1 > 1$ the

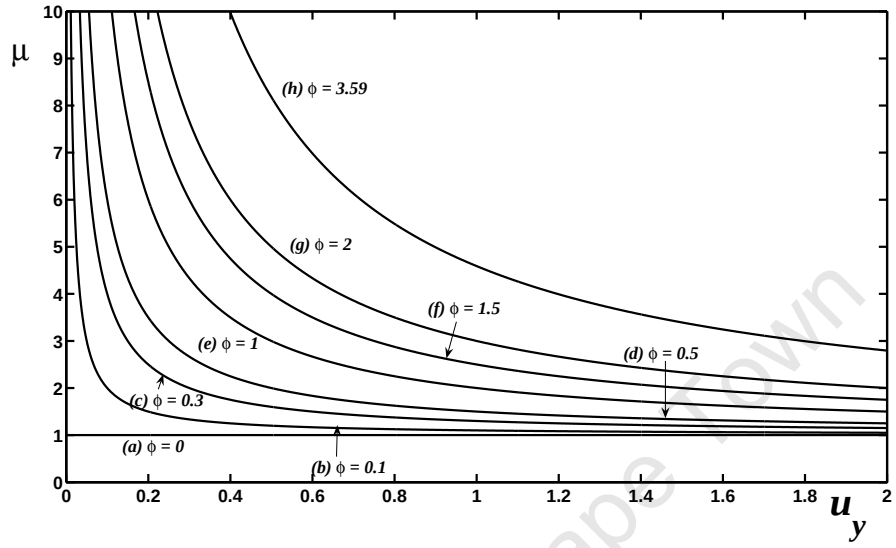


Figure 3.28: Viscosity versus shear rate with different values of $\phi$ and $\alpha_1 = 0.5$.

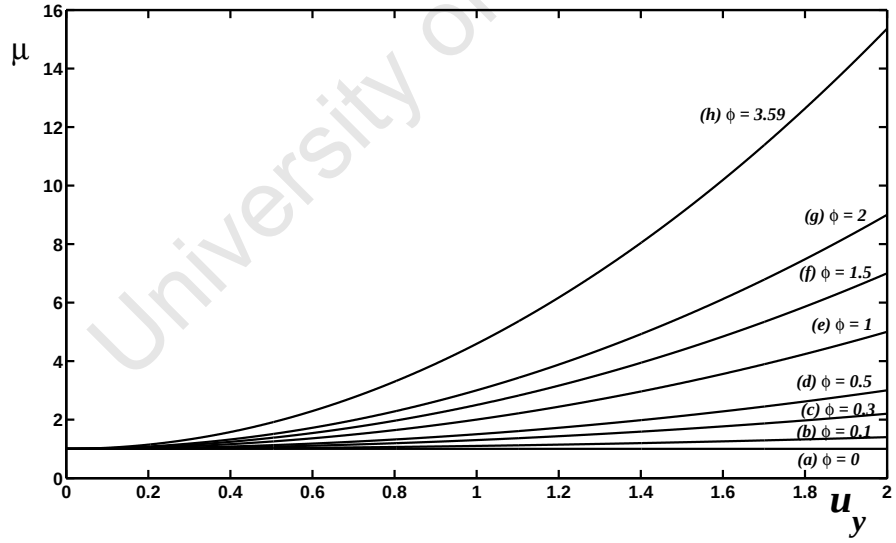


Figure 3.29: Viscosity versus shear rate with different values of $\phi$ and $\alpha_1 = 2.073$.

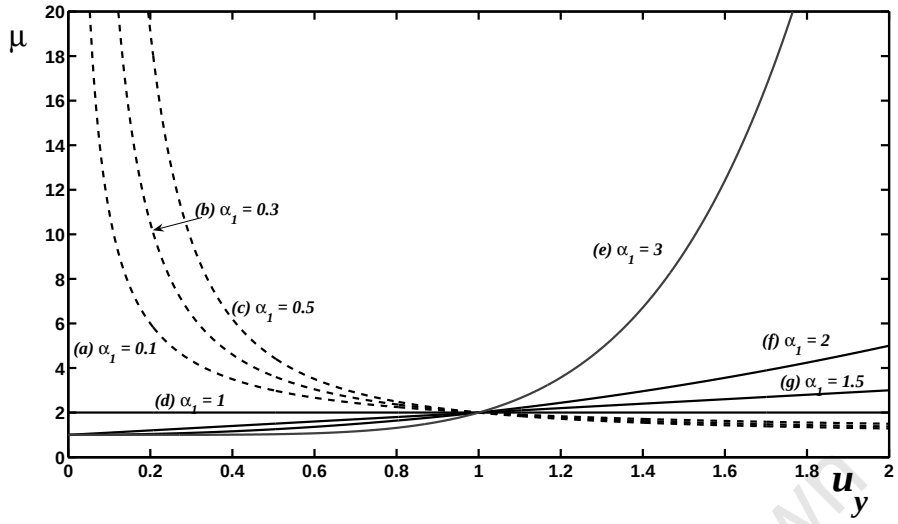


Figure 3.30: Viscosity versus shear rate with different values of $\alpha_1$.

fluid viscosity increases when the shear rate increases which is a typical shear thickening behaviour.

Figs. 3.31 and 3.32 display eight velocity profiles representing Equation (3.4.44) corresponding to different values of $\phi$ in the region $0 \leq \phi \leq 3.59$, with $\alpha_1 = 0.5$ for shear thinning fluid and $\alpha_1 = 2.073$ for hydroxylethycellulose fluid. The Newtonian velocity profile is observed in curve (a) with $\phi = 0$ in both figures. When $\phi$ increases between 0 and 0.5, the velocity of the fluid increases gradually and when $\phi > 1$ a significant increase in the fluid velocity is observed. As shown in Fig. 3.28 with $\alpha_1 = 0.5$ the viscosity of the fluid decreases when $\phi$ increases, while the opposite is true in Fig. 3.29 with $\phi = 2.073$. In Fig. 3.31 as $\phi$ increases, the velocity of the fluid increases as a result of less resistance force to the flow, while in Fig. 3.32 when $\phi$ increases with $\phi = 2.073$, the velocity increases, showing that the more viscous the fluid, the higher the velocity profiles. This is a result of the driving force for the fluid, which is significantly higher when $\phi$ increases with $\alpha_1 > 1$. However, in both figures, that is, Fig. 3.31 and Fig. 3.32, the velocity profiles as shown in Fig. 3.31 are more pronounced as compared to the resulting flow profiles in Fig. 3.32. This shows that a less viscous fluid responds quickly to the driving force of the

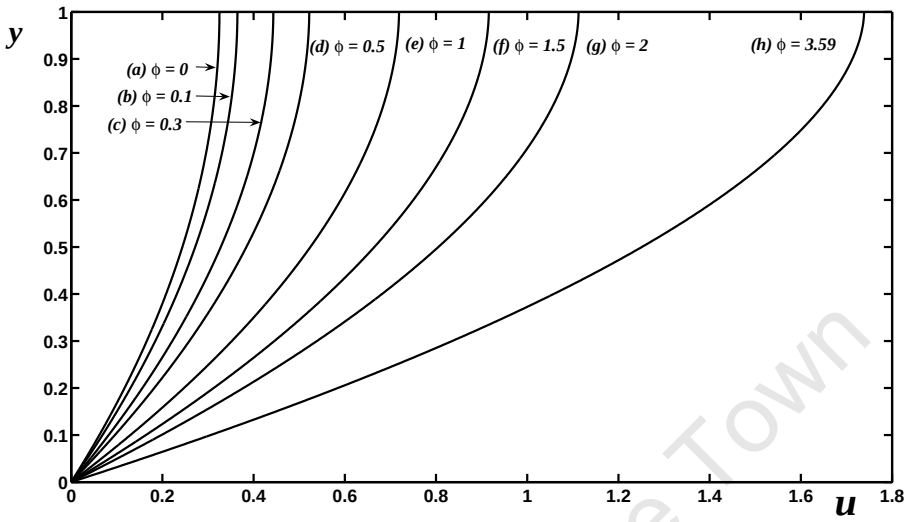


Figure 3.31: The velocity profiles for Equation (3.4.44) with $\alpha_1 = 0.5$: Boundary conditions (2.3.12).

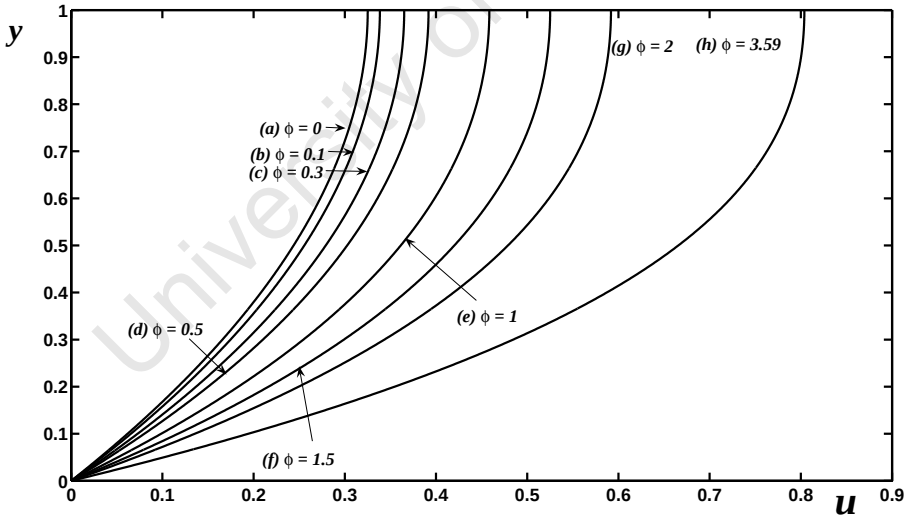


Figure 3.32: The velocity profiles for Equation (3.4.44) with $\alpha_1 = 2.073$: Boundary conditions (2.3.12).

fluid and as a result the flow is faster.

Eight temperature profiles corresponding to Equation (3.4.47) with different values of $\phi$ and $\alpha_1 = 0.5$, $Bi = 0.3$ and $Br = 0.3$ are shown in Fig. 3.33 with $\phi = 0.5$ and Fig. 3.34 with $\phi = 2.073$ for hydroxylethycellulose fluids. The Newtonian temperature profiles are shown in curve (a) with $\phi = 0$ in both figures. The figures show that when $\phi$ increases the temperature of the fluid increases due to heat generation by the viscous action in the fluid. The temperature of the fluid increases significantly when $\phi \geq 1$ which shows that the heat generation by the viscous force is more pronounced when $\phi$ is large. It is noteworthy that for the temperature profiles for $\alpha_1 = 2.073$, the maximum values for the temperature are slightly less than the temperature profiles as shown in Fig. 3.33. This figure again illustrates that less viscous fluids heat up quickly as a result of internal flow processes.

Figs. 3.35 and 3.36 are plots of the flow rates versus the film height representing Equation (3.4.45) with various values of $\phi$ and $\alpha_1$. The figures show that the when $\phi$ and $\alpha_1$ increase, then the flux increases in a layer and the flow rate is higher.

The velocity for different values of the power law index are shown in Fig. 3.37 with $\phi = 3.59$. The viscosity of the fluid decreases for $\alpha_1 < 1$ while the opposite is true for $\alpha_1 > 1$ as in Fig. 3.30. This therefore shows that shear thinning fluids are less viscous and react quickly to the driving force of the fluid and the velocity of the fluid increases significantly as $\alpha_1$ decreases. Fig. 3.38 shows the temperature of the fluid with different values of $\alpha_1$ while other parameters are fixed at $\phi = 3.59$, $Bi = 0.3$ and $Br = 0.3$. The temperature of the fluid increases when $\alpha_1$ decreases. The maximum temperature of the fluid is much more pronounced for $\alpha_1 = 0.1$ which is 50% more than for $\alpha_1 = 3$. This is due to the fact that hydroxylethycellulose fluid is highly viscous and respond slowly to viscous heat generation by the internal flow processes.

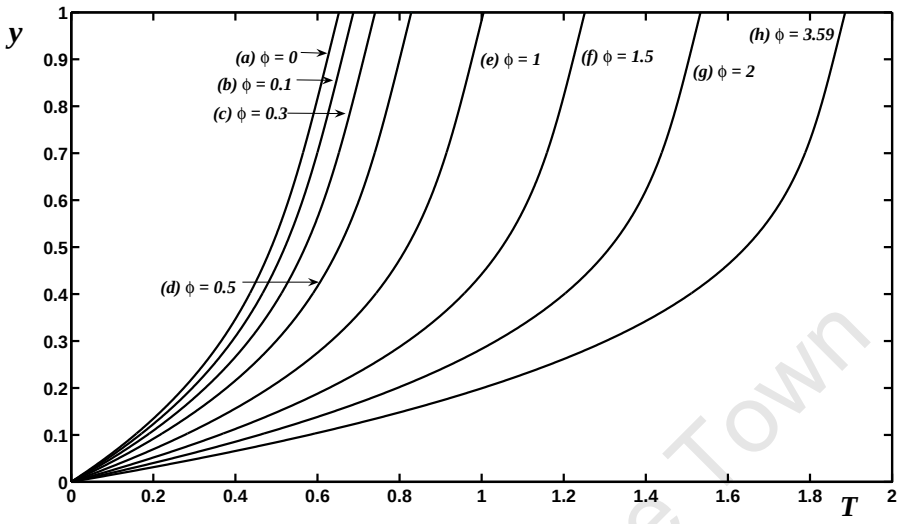


Figure 3.33: The temperature profiles for Equation (3.4.47) with $\alpha_1 = 0.5$: Boundary conditions (2.3.13).

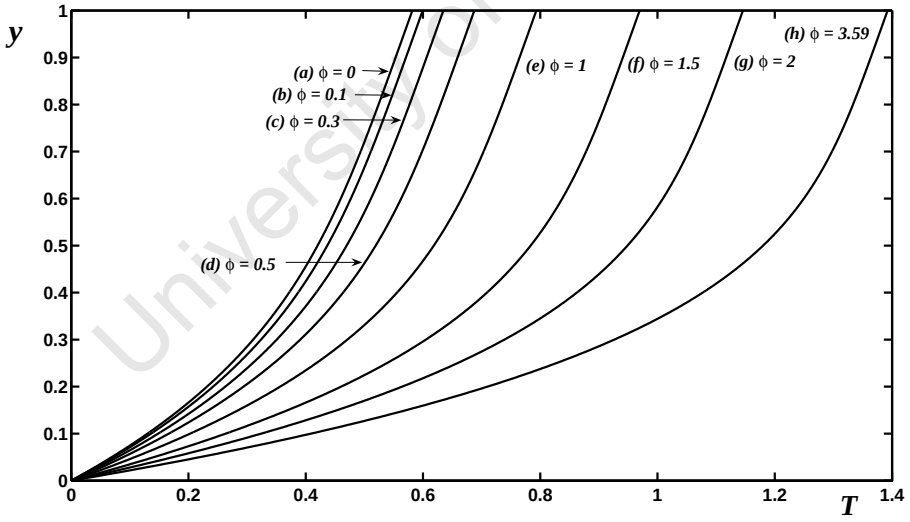


Figure 3.34: The temperature profiles for Equation (3.4.47) with $\alpha_1 = 2.073$: Boundary conditions (2.3.13).

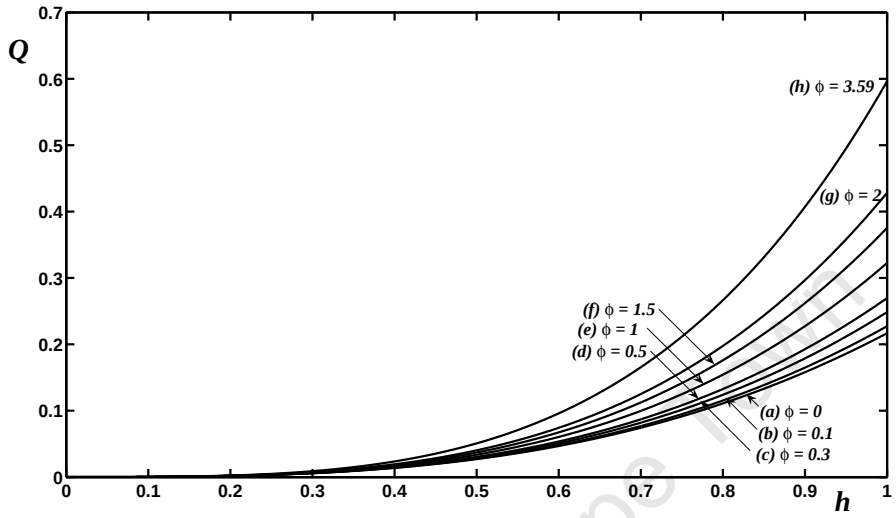


Figure 3.35: The flux versus height for Equation (3.4.45) with different values of $\phi$.

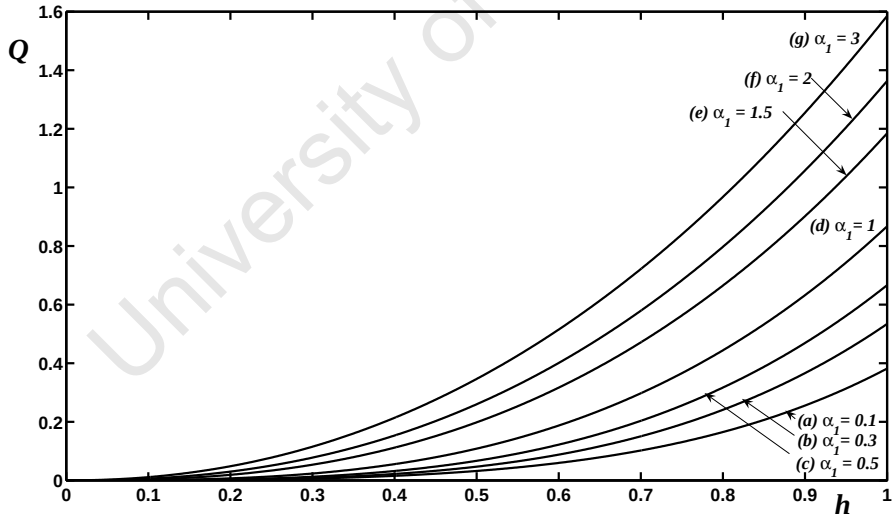


Figure 3.36: The flux versus height for Equation (3.4.45) with different values of $\alpha_1$.

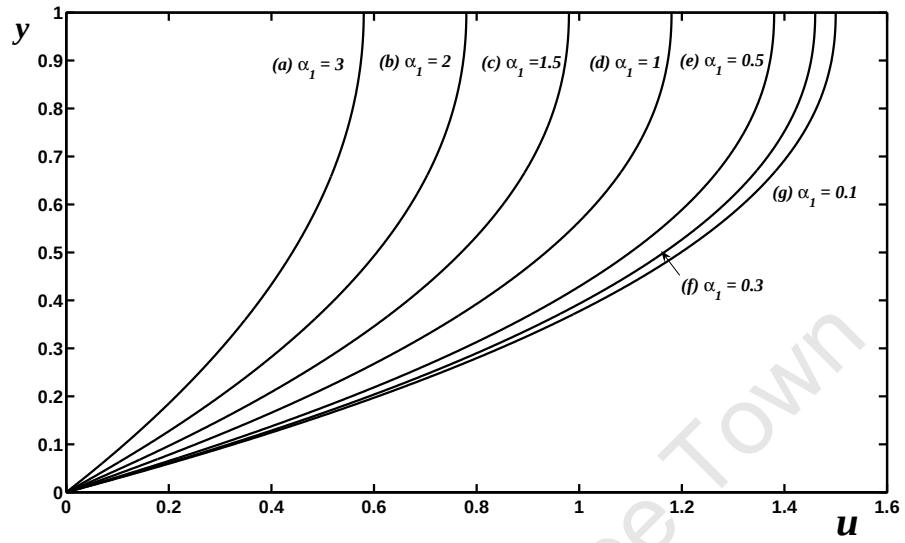


Figure 3.37: The velocity profiles for Equation (3.4.44): Boundary conditions (2.3.12).

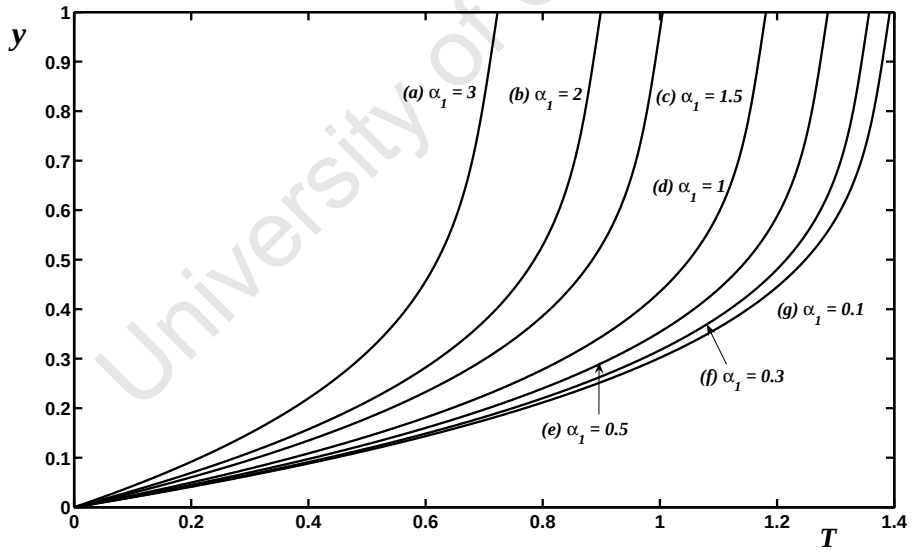


Figure 3.38: The temperature profiles for Equation (3.4.47): Boundary conditions (2.3.13).

### 3.4.1 Conclusion

Laminar flow of an Ellis fluid was investigated. The viscosity versus shear rate were plotted with different values of $\phi$ and the results show that when $\phi$ increases, the viscosity of the fluid decreases as the shear rate increases for shear thinning fluids. The opposite is true for shear thickening fluids. The results for the flow rate showed that when $\phi$ increase for shear thinning fluids, the flux increases in the layer. The velocity and temperature profiles were derived analytically. The results illustrate that the velocity of the fluid increases significantly as $\phi$ increases, due to less resistance force to the flow. The velocity and temperature profiles, for a shear thinning fluid show maximum values at the free surface which are slightly higher than the hydroxylethycellulose fluid. The increases in temperature of the fluid when $\phi$ increases is due to heat generation by the action of the viscous term, which raises the temperature of the fluid as $\phi$ increases. The results show that the velocity and temperature of the fluid increases when the power law index $\alpha_1$ decreases.

## 3.5 Application of viscosity models

The aim of this section is to investigate the applications of the shear rate dependent viscosity models to a thin film flow. We commence our investigation by comparing these models plotted logarithmically on the same set of axis using experimental data for four specific materials namely, aluminum soap, acrylonitrile-butadiene-styrene (ABS) solution, fabric softener, and yoghurt. Experimental data for the parameter values of the shear rate dependent viscosity models for these materials are obtainable in several references, [9, 25, 61, 76]. However, it must be noted that in literature, raw experimental data for aluminum soap, acrylonitrile-butadiene-styrene (ABS) solution, fabric softener, and yoghurt are not readily available. In future it will be of interest to compare this work with raw data from experimental settings, so that a better judgment can be made. Furthermore, comparisons

between theoretical results and actual data will be attempted for the fluxes, velocities and possibly the variation of the temperature of the fluid. This will definitely improve the relevancy of our study to the industrial applications.

The resulting velocity profiles for the shear rate rate dependent viscosity models are compared using the solutions for the velocity profiles as derived in the previous sections. This is a very important exercise to carry out in order to strengthen the previous sections and compare the discrepancies which might occur between theory and experiments. Rheological properties of these materials in industrial applications influences durability and production [119]. This is also again deemed important because in most polymeric materials the challenges are twofold: first the development of accurate rheological models to describe the viscosity versus shear rate relationships; secondly, the efficient analytical and numerical techniques to solve the governing equations, [15, 119].

Table 3.1 gives examples of the parameter values for the four materials considered. The power law, Carreau and Ellis models' parameters for an ABS solution are taken from [25] p. 787 and [61], p. 86. Aluminum soap parameter values from [76] p. 3, and fabric softener from [9] p. 22. Yoghurt parameter values from [9] p. 22 and [61], p. 86. The parameter values for the Ellis model were calculated using the corresponding Carreau model parameter values.



| | Power law | | Carreau model | | | Ellis model | | |
|---|---|---|---|---|---|---|---|---|
| material | $n$ | $K$ | $n$ | $l$ | $\mu_0$ | $\alpha_1$ | $\phi$ | $\mu_0$ |
| ABS | 0.40 | 0.36 | 0.40 | 2.5 | 45 | 0.71 | 3.96 | $1.32 \times 10^4$ |
| Aluminum soap | 0.2 | 68.07 | 0.2 | 1.41 | 89.6 | 5.3 | 69.19 | 89.6 |
| Fabric softener | 0.6 | 10 | 0.4 | 0.11 | 24 | 2.4 | 0.14 | 24 |
| Yoghurt | 0.1 | 34 | 0.1 | 0.26 | 10 | 10 | 0.28 | 10 |

Table 3.1: Power law, Carreau and Ellis models parameter values for various materials, [9, 25, 61, 76].

### 3.5.1 Comparison of the viscosity models for shear thinning fluids

We commence our analysis by comparing these models when plotted on a logarithmic scale for the viscosity versus shear rate using experimental data in Table 3.1. Zhao *et al.* [119] investigated polymer solutions for fabric coating and their results show that the Carreau model is a good fit to experimental data. However, Myers [76] pointed out that the Carreau model may not necessarily give a good fit to experimental data in certain materials. We will follow the analysis by Myers [76] and Zhao *et al.* [119]. In this section we assume that the Carreau model gives a good fit to data for comparison purposes, and use this model as a benchmark for other models. The power law model has been used for the last three decades and it has been trusted to give a good fit to experimental data [9]. It has been pointed out that the power law model may not predict data accurately at lower and higher shear rate regions [25, 76]. We will establish whether this failure of the power law model in the lower and higher shear rates regions can be rectified by using the Carreau and Ellis models for modelling thin films. However, it must be pointed out that the downside of the Ellis fluid is that it may under predict the viscosity at lower shear rate regions [76].

Figs. 3.39 through to 3.42, present the viscosity versus shear rate for an ABS solution, aluminum soap, fabric softener and yoghurt. In all these graphs, the power law model generally fails in the lower shear rate region, since the viscosity for the power law model approaches infinity ($\mu \to \infty$). Fig. 3.39, shows the viscosity versus shear rates for ABS solution. The figure shows that when the viscosity of the fluid increases, the shear rate decreases and the power law model over predicts the data at low shear rate region where $-7 \leq \log u_y \leq -5.5$. The Ellis model and Carreau model are constant in this region showing Newtonian behaviour and subsequently separate when the shear rate increases. At high shear rate regions the models predict similar profiles. In Figs. 3.40 and 3.41 for

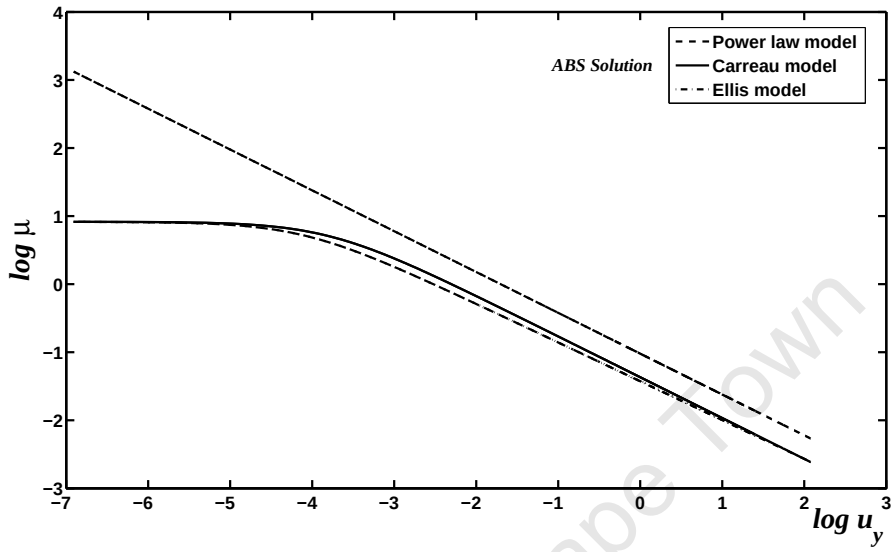


Figure 3.39: Shear rate versus viscosity for ABS solution.

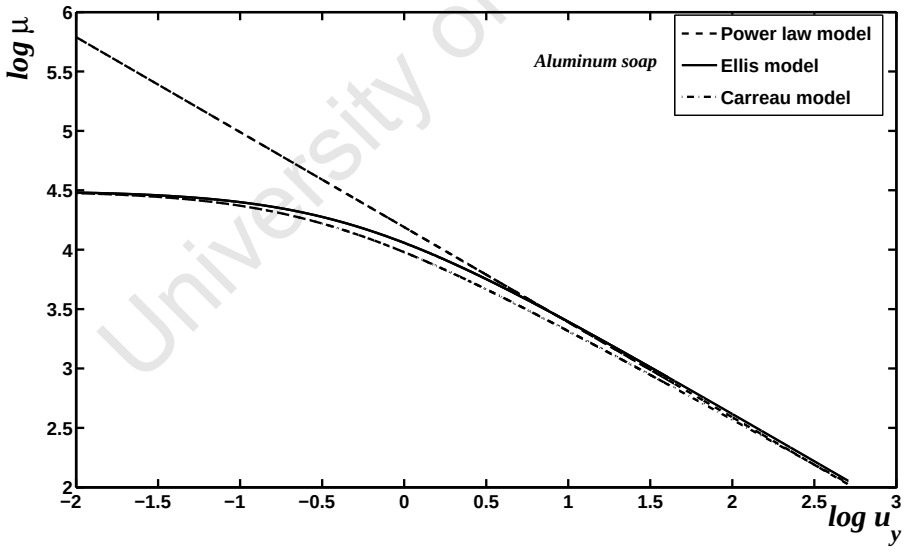


Figure 3.40: Shear rate versus viscosity for aluminum soap.

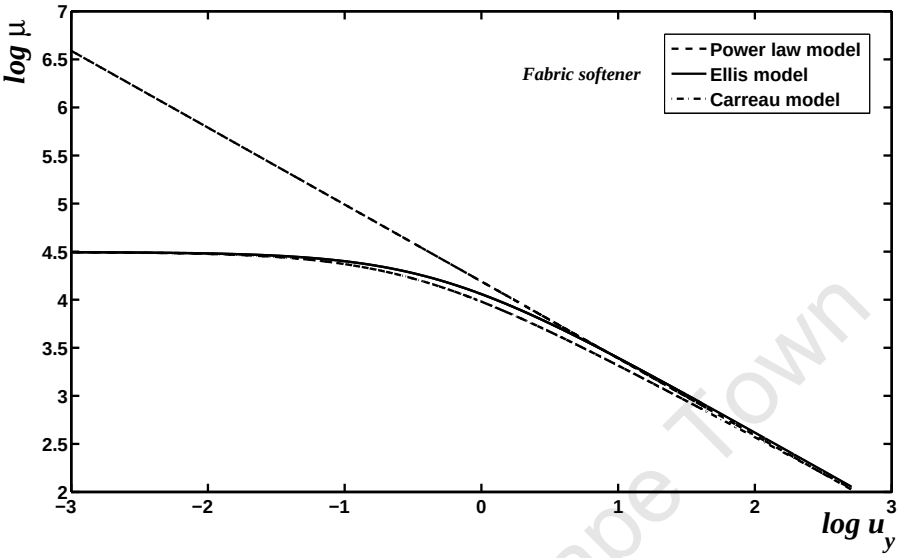


Figure 3.41: Shear rate versus viscosity for fabric softener.

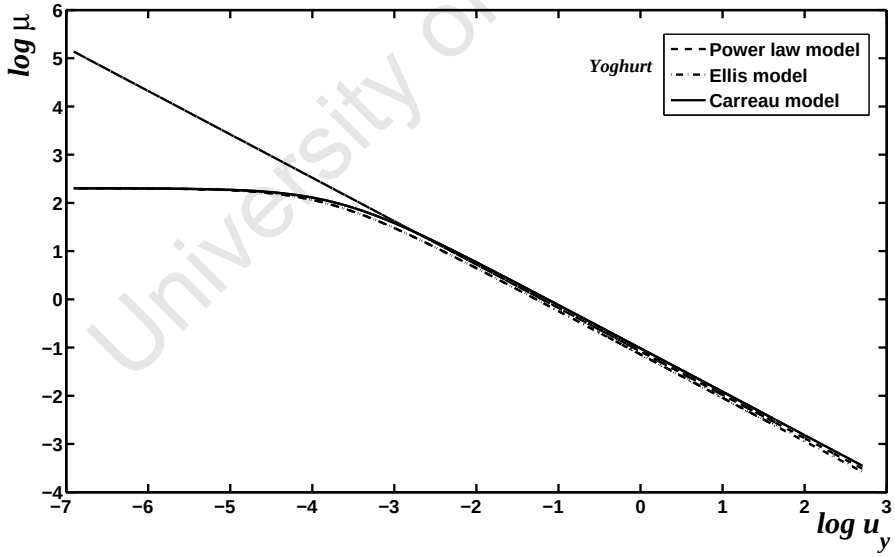


Figure 3.42: Shear rate versus viscosity for yoghurt.

aluminum soap and fabric softener, we have more or less similar predictions of the data by the three models. In these figures again we observe that at the low shear rate region the power law model over predicts the resulting profiles and consequently all the models predict similar profiles when the shear rate increases. In Fig. 3.42 for yoghurt we have again the power law model over predicting the results at the lower shear rate region where $-7.2 \leq \log\, u_y \leq -5.2$ while at high shear rate regions the predicted profiles are in good agreement with the other models. In general, the Carreau model showed a good fit to data, in certain cases also comparing fairly well with the Ellis model. It is clear from all the materials that the power law model generally fails at low shear rate regions. It is important to consider these dynamics when modelling these types of fluids for industrial applications.

Figs. 3.43 to 3.46 show the velocity profiles for the power law, Carreau, Ellis and Newtonian models given by Equations (2.4.18), (3.2.3), (3.3.40) and (3.4.44). The velocity profiles are plotted using the values of the parameters as listed in Table 3.1. Comparison of the velocities predicted by each model on each material is now discussed.

In Fig. 3.43 the velocity profiles predicted by the Newtonian, power law, Carreau and Ellis models for an ABS solution are shown. The Carreau and Ellis models lead to similar velocity profiles with their maximum velocity occurring at the free surface. The power law model in comparison with the Carreau and Ellis models gives a bad prediction with its maximum velocity value at the free surface approximately half of the predicted velocity profiles by the Carreau and Ellis models. This is caused by the high viscosity as predicted in Fig. 3.39 for an ABS solution. In Fig. 3.43 the Newtonian maximum velocity profile is low compared to the velocity profiles predicted by the other three non−Newtonian models. In Fig. 3.44, the velocity profiles predicted for alunimum soap show that the Carreau and Ellis models compare closely whilst the power law gives a terrible prediction of the velocity profiles. In this figure the maximum value for the velocity profile for the power law model is even less than the Newtonian case. The maximum velocity for the

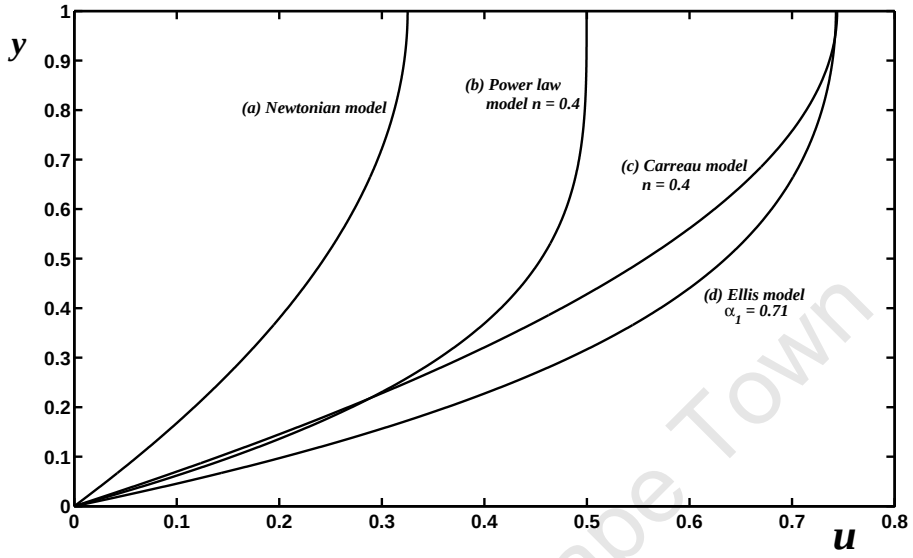


Figure 3.43: The velocity profiles for ABS polymer solution: Boundary conditions (2.3.12).

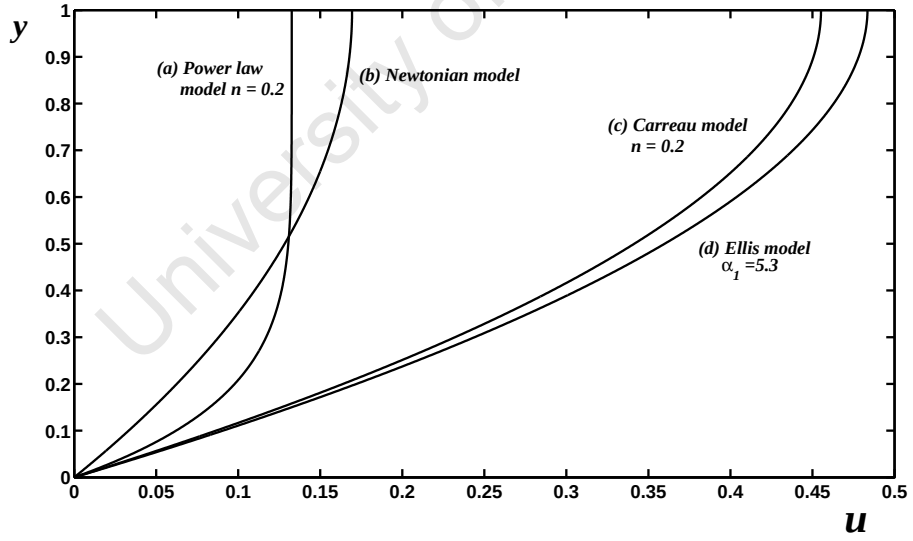


Figure 3.44: The velocity profiles for aluminum soap: Boundary conditions (2.3.12).

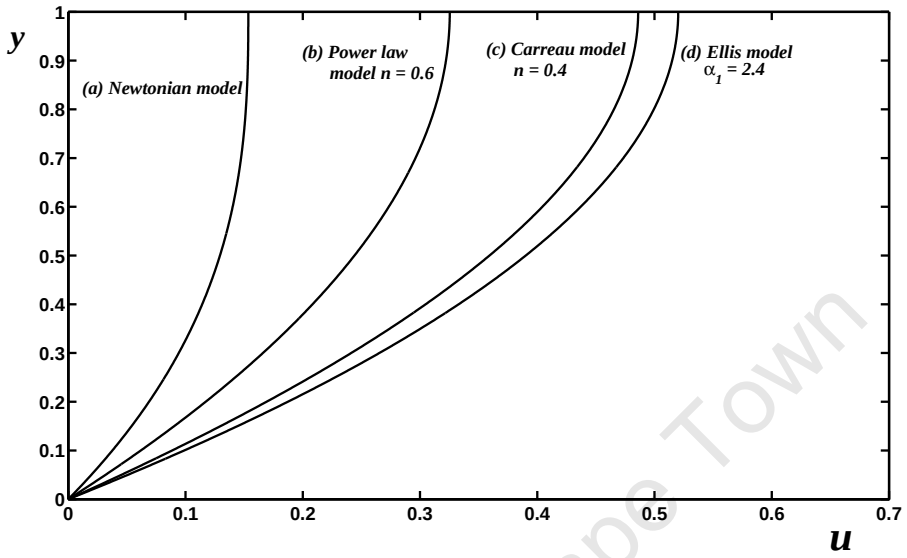


Figure 3.45: The velocity profiles for fabric softener: Boundary conditions (2.3.12).

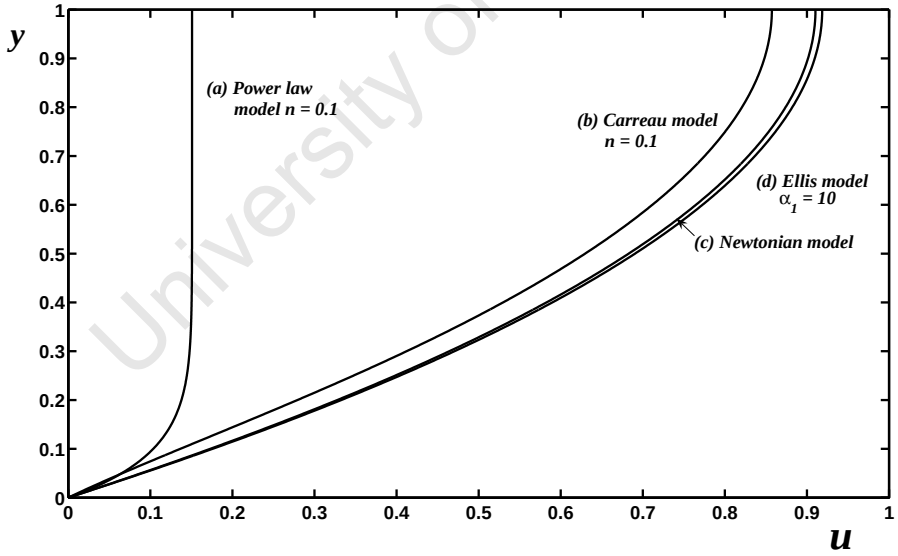


Figure 3.46: The velocity profiles for yoghurt: Boundary conditions (2.3.12).

Ellis model is approximately 80% higher than the power law model, obviously due to high viscosity in the fluid, see Fig. 3.40. In Fig. 3.45 for fabric softener the velocity profiles predicted by the Carreau and Ellis models are in agreement. The power law model with $n = 0.6$ shows the velocity profile with its maximum value which is higher than the Newtonian case. In Fig. 3.46, for yoghurt, the power law model with $n = 0.1$ gives a terrible predicted velocity profile as compared to the Newtonian, Carrea and Ellis velocity profiles. It is interesting to note again that the Newtonian velocity profile compares fairly well with the Ellis velocity profile and it is also greater than the Carreau model. In general, the disagreement between the Carreau and Ellis models in certain fluids such as fabric softener and yoghurt is probably caused by the adjustments of the parameter values in the Ellis model calculated using the equivalent values in the Carreau model. In this case the Carreau and the Ellis models generally are in good comparison while the power law fluid predicted bad results due to high presence of high viscosity in the fluids.

### 3.5.2 Comparison of the viscosity models for shear thickening fluids

In this section, we further the investigation for shear thickening fluids. In particular, the shear rate dependent viscosity models are compared using the parameter values for Coal Water Slurry (CWS) and Styrene Butadiene Styrene polyblock copolymers (SBS). Note that due to the complex nature of the shear thickening fluids, they are less used in practice. Therefore, it is difficult to obtain experimental data recorded in literature for fluids with power law index greater than unity. In the this analysis we will consider the two materials which we could find recorded in literature. The parameter values for CWS is obtainable in Goudoulas *et al.* [39], p. 84 for the Carreau model and Liu *et al.* [58], p. 831 for the power law model. The parameter values for SBS are taken from Gonzalez-Leon *et al.* [38], p. 8040 and Kim *et al.* [53], p. 482 for the power law model and for the Carreau model the parameter values are obtained from Stastna *et al.* [102],

p. 206. The parameter values for the Ellis model were calculated using the corresponding Carreau model parameter values, as explained in the previous section. The parameter values are listed in Table 3.2 below.

| | Power law | | Carreau model | | | Ellis model | | |
|---|---|---|---|---|---|---|---|---|
| material | $n$ | $K$ | $n$ | $l$ | $\mu_0$ | $\alpha_1$ | $\phi$ | $\mu_0$ |
| CWS | 1.56 | 0.00112 | 1.484 | 0.611 | 4.73 | 2.674 | 0.614 | 3.73 |
| SBS | 1.55 | $3.27 \times 10^6$ | 1.955 | 6.812 | 166.964 | 3.512 | 6.814 | 146.634 |

Table 3.2: Power law, Carreau and Ellis models parameter values for two materials, [38, 39, 53, 58, 102].

Figs. 3.47 and 3.48 show a comparison of the viscosities predicted by the above model in Table 3.2 and parameter values for CWS and SBS. Both these figures show that the viscosity of the fluid increases as the shear rate increases displaying a shear thickening behaviour. The power law model is shown to under predict the viscosity. In case of CWS for high shear rates the power law model agrees with the Ellis and Carreau models and the opposite is true for SBS. Figs. 3.49 and 3.50 show the velocity profiles predicted for the Newtonian, power law, Carreau and Ellis fluids. The velocity profiles for the power law, Carreau, Ellis and Newtonian models plotted from Equations (2.4.18), (3.2.3), (3.3.40) and (3.4.44). In both figures the Carreau and Ellis models shows more or less similar profiles. The agreement between the two is mainly due to the fact that some parameter values for the Ellis models were calculated using the Carreau model. The predicted profiles for both Carreau and Ellis fluids are higher than the Newtonian and power law models. In the case of CWS the profiles predicted by the power law fluid is less than the Newtonian case. This is in agreement with the previous suggestion that the power law model gives less accuracy as compared to the other models.



### 3.5.3 Conclusion

In conclusion, the shear rate dependent viscosity models have been investigated using

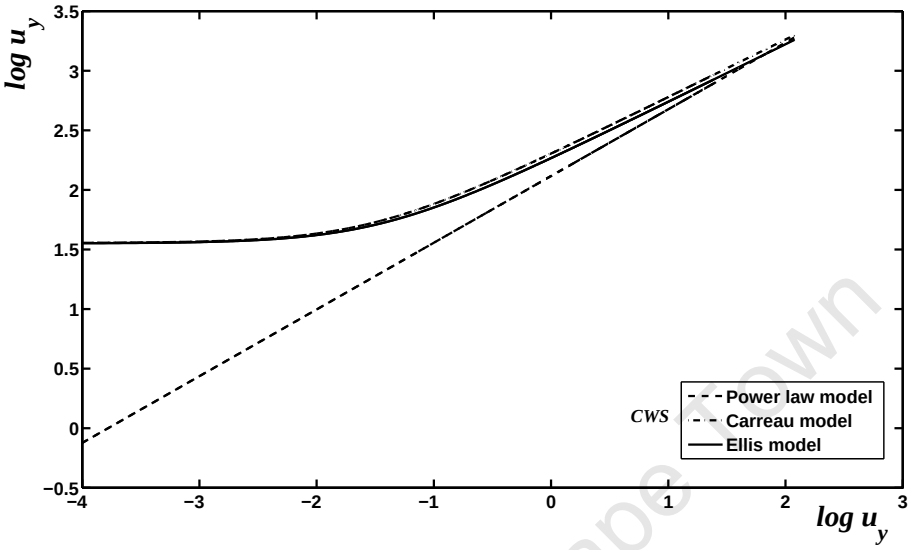


Figure 3.47: Shear rate versus viscosity for CWS.

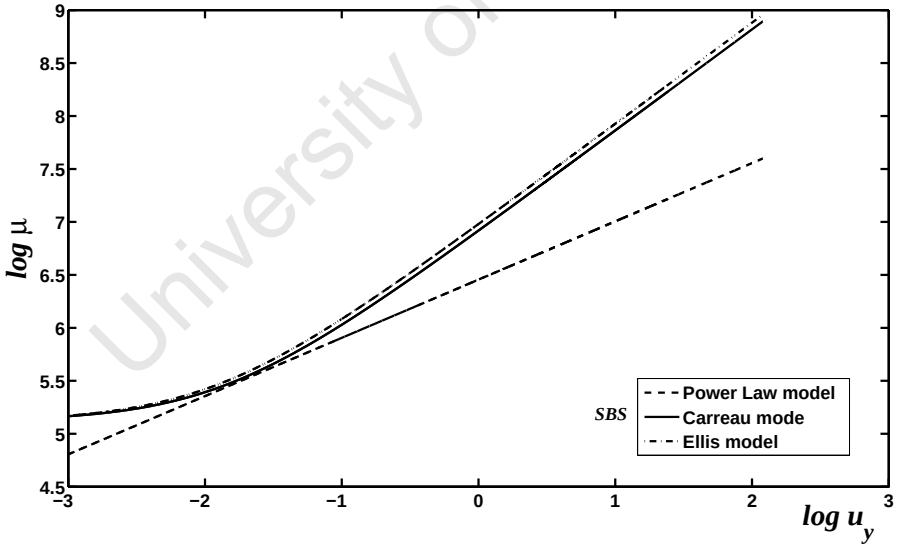


Figure 3.48: Shear rate versus viscosity for SBS.

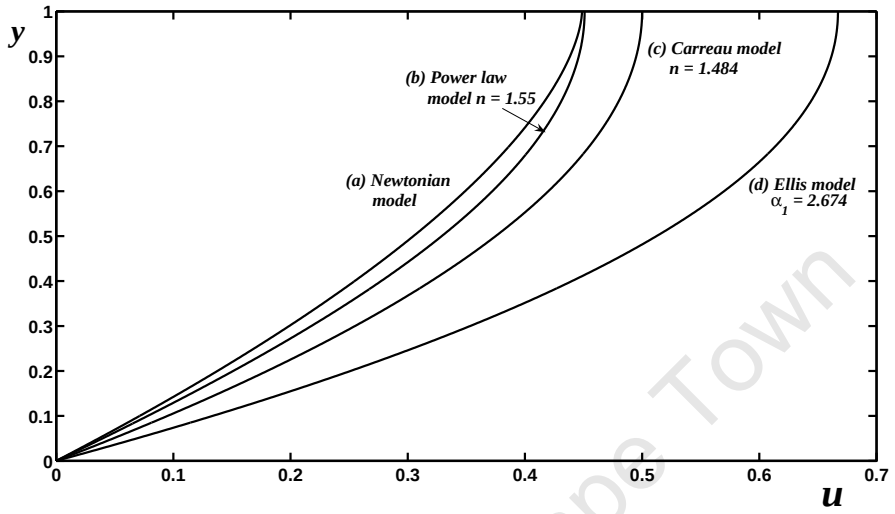


Figure 3.49: The velocity profiles for CWS Boundary conditions (2.3.12).

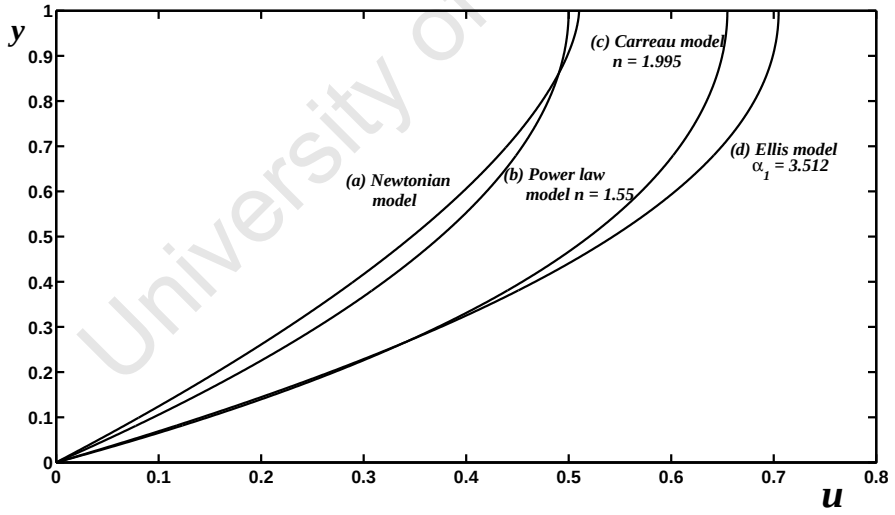


Figure 3.50: The velocity profiles for SBS: Boundary conditions (2.3.12).

different materials, namely, ABS solution, aluminum soap, fabric softener and yoghurt for shear thinning fluids. Furthermore, the models were investigated for shear thickening fluids using CWS and SBS materials. The power law model has been shown to be far from ideal when modelling thin film fluids with low shear rates. This suggests that great care should be taken when modelling thin films using the power law, particularly at low shear rate ranges. This challenge can be overcome by using either the Carreau or Ellis model. The comparisons of the shear rate dependent viscosity models on the plot of the viscosity versus the shear rate, showed that in a low shear rate region the power law gives inaccurate results for certain materials. However, at high shear rate ranges, the power law model also gave a good fit to data on certain materials, with specific reference to yoghurt. This therefore suggests that the power law model is useful in situations where the fluid is subjected to high shear rates, which is in agreement with the results shown by Myers [76]. At low shear rate regions the two models showed Newtonian behavour, but did not coincide with Newtonian transitions to a power law behaviour at high shear rate regions. The velocity profiles were compared with the inclusion of the Newtonian model. The resulting velocity profiles illustrated that the Carreau and Ellis models led to similar results, which suggests that these types of models are appropriate for thin film flows. The power law model again gave inaccurate velocity profiles as compared to the velocity profiles predicted by the Carreau and Ellis models for both shear thinning and shear thickening fluids. Over the years the power law model has been used to model thin films flows and one of the obvious reasons is its simplicity and it allows for analytical progress on the resulting governing equations. Now in this section we showed that when modelling non−Newtonian fluids, the power law model generally fails to predict the flow accurately in low shear rate regions. This model which has been trusted over the years can be supplemented by the Carreau and Ellis models. The Ellis model has been shown to compare fairly well with the Carreau model.

# Chapter 4

# Fluid flow between parallel plates

## 4.1 Introduction



In Chapter 3, we investigated the flow of shear rate dependent variable viscosity models for flow with a free surface. This therefore, provided us with the motivation to extend the investigation to the flow of these variable viscosity models between parallel plates. In this chapter, our main focus is on the variable viscosity models, that is, the power law, the Carreau and the Ellis models for flow between parallel plates. The major driving forces for the fluid are those of the applied shear force caused by the movement of the upper plate and the pressure gradient. These models are used to describe the dynamic viscosity of both shear thinning and shear thickening fluids. We are particularly interested in the effect of flow controlling parameters such as the power law index, non−dimensional parameters $l$, $\phi$ and the Brinkman number, on the resulting flow profiles.

In § 4.2 the power law model is investigated first, which allows for analytical progress. In this case great care must be taken with the modulus sign. We follow the analysis by Myers [76] and Ross [94]. However, we will not copy their results for the following reasons: Ross [94] solved the resulting flow profiles without removing the modulus sign in order to account for backward flow. Myers [76] used a proper procedure in handling the modulus sign, however the heat equation was not coupled to the Navier−Stokes equations and the

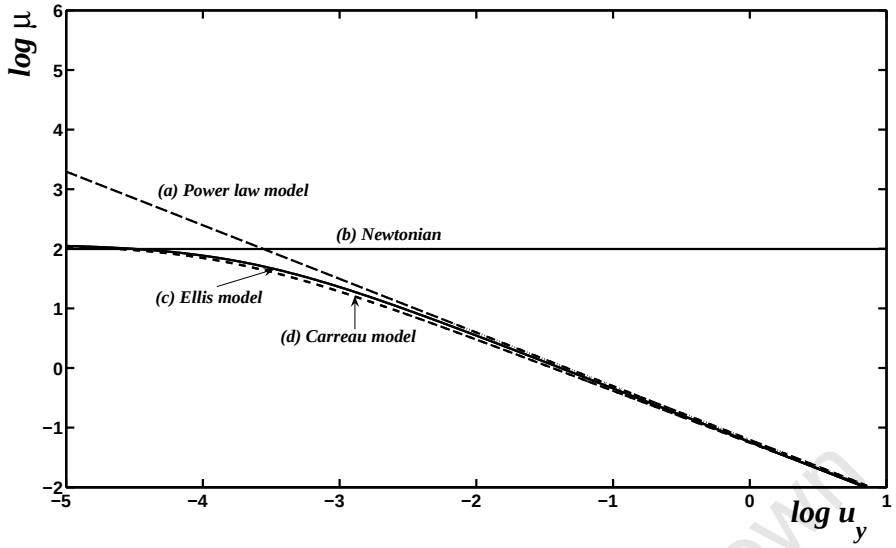


Figure 4.1: The viscosity versus shear rate for blood.



boundary conditions considered were different to ours. We will extend the results in [76] to include the energy equation in order to account for the temperature of the fluid.

In § 4.3, we investigate the flow of Carreau fluid. The governing equations resulting from the Carreau model require a numerical technique to obtain full solution. We again use asymptotic approximation to determine the velocity, flux and temperature profiles and analytical results are derived when $n = 0$ and $n = 2$. The Newton Raphson method is used again to find the full solution using a similar procedure as shown in § 3.3 and we will highlight the differences.

Analytical results for an Ellis fluid are derived in § 4.4 and again we will follow the procedure as detailed in [76]. The main results obtained for these models are discussed quantitatively in each section.

For comparison purposes the four shear rates dependent viscosity models are shown in Fig. 4.1 for blood and the data is obtained in Myers [76] Table 1. The Newtonian case is shown with a constant viscosity and the profile is adjusted by using a factor of two so that the Carreau, Ellis and Newtonian models begin at the same point. For low shear

rates in the region $-5 < \log u_y < -4.2$ the Newtonian, Carreau and Ellis models predict similar profiles, while the power law model is different with viscosity tending to infinity at vanishing shear rates. However, when the shear rate increases the three models namely the power law, the Carreau and the Ellis models predict similar viscosity profiles, in which the viscosity decreases as the shear rate increases. We begin our investigation for flow between parallel plates with the power law fluid in the next section.

## 4.2 The power law fluid

This work has been summarised in the paper by Tshehla, Myers and Charpin, see [111] p. 421-431, which is published in an accredited conference proceedings. Note that the book was edited by M. Rahman and C. A. Brebbia. The applied viscosity law is,

$$\mu = K \left| \frac{\partial u}{\partial y} \right|^{n-1}, \tag{4.2.1}$$

where $K = m(U/H)^{n-1}$ is a constant, $n$ is the power law index. Integrating Equation (2.3.9) gives the following velocity gradient,

$$\mu \frac{\partial u}{\partial y} = p_x \left( y - h_m \right) \ , \tag{4.2.2}$$

where $p_x = (\partial p/\partial x) < 0$, and $h_m$ is the point at which $(\partial u/\partial y) = 0$. To avoid the difficulty with the modulus sign, a simpler method is used, in which case we take a different route to the one used by Ross *et al.* [94]. The procedure which we follow in order to obtain the resulting flow profiles is also physically realistic as pointed out by Myers [76]. However, the method that is used by [94] is recommended for a situation where a backward flow is encountered in an investigation. In this case, the situation where there is at most one turning point for the velocity and temperature profiles is considered. This gives two cases: First case, the velocity increases across the plates until it reaches the maximum say at $(y = h_m)$ and then decreases to the top plate due to the boundary conditions. Note this condition is valid for situations where there is a greater balance between the applied shear

force and the pressure gradient. Otherwise, when the applied shear force drives the flow, the velocity may reach its maximum at the top plate. In this case the condition $y = h_m$ may not be defined. Now for $y \leq h_m$ then $(\partial u/\partial y) \geq 0$, and for $y \geq h_m$ then $(\partial u/\partial y) \leq 0$. The velocity profile is found by combining Equations (4.2.1) and (4.2.2), integrating with respect to $y$ and applying the boundary conditions (2.3.15) and (2.3.16). For $y \leq h_m$ the velocity profile is,

$$u_1 = \left(-\frac{p_x}{K}\right)^{\frac{1}{n}} \frac{n}{n+1}\left(h_m^{\frac{n+1}{n}} - (h_m - y)^{\frac{n+1}{n}}\right) , \tag{4.2.3}$$

and when $y \geq h_m$, the velocity profile becomes,

$$u_2 = \left(-\frac{p_x}{K}\right)^{\frac{1}{n}} \frac{n}{n+1}\left((1-h_m)^{\frac{n+1}{n}} - (y-h_m)^{\frac{n+1}{n}}\right) + 1 . \tag{4.2.4}$$

Equations (4.2.3) and (4.2.4) define the velocity profile. The constant $h_m$ is found by requiring continuity $u_1 = u_2$ at $y = h_m$ that is,

$$\begin{aligned} u(h_m) &= \left(-\frac{p_x}{K}\right)^{\frac{1}{n}} \frac{n}{n+1} h_m^{\frac{n+1}{n}} \\ &= \left(-\frac{p_x}{K}\right)^{\frac{1}{n}} \frac{n}{n+1}\left((1-h_m)^{\frac{n+1}{n}}\right) + 1 . \end{aligned} \tag{4.2.5}$$

Equation (4.2.5) provide the solution for the constant term $h_m$ which is non$-$linear and it requires the numerical method. We use the Newton method to obtain the values of $h_m$. The flux between the plates is given by $Q = Q_1 + Q_2$ where,

$$Q_1 = \int_0^{h_m} u dy = \frac{n^2}{(n+1)(2n+1)}\left(-\frac{p_x}{K}\right)^{\frac{1}{n}} h_m{}^{\frac{2n+1}{n}} . \tag{4.2.6}$$

$$Q_2 = \int_{h_m}^{1} u dy = (1-h_m)\left[1 + \frac{n^2}{(n+1)(2n+1)}\left(-\frac{p_x}{K}\right)^{\frac{1}{n}} (1-h_m)^{\frac{n+1}{n}}\right] . \tag{4.2.7}$$

Adding Equations (4.2.6) and (4.2.7) we obtain the expression for the flux in terms of the pressure gradient,

$$Q = \frac{n^2}{(n+1)(2n+1)}\left(-\frac{p_x}{K}\right)^{\frac{1}{n}} \left[h_m{}^{\frac{2n+1}{n}} + (1-h_m)^{\frac{2n+1}{n}}\right] + (1-h_m) . \tag{4.2.8}$$

For incompressible fluids the flux must be constant [76] and Equation (4.2.8) clearly shows that the flux is constant. To determine the temperature profile for the case $y \leq h_m$, Equations (2.3.11), (4.2.1) and (4.2.2) are combined to give,

$$\frac{\partial^2 T_1}{\partial y^2} = -Br \left(-\frac{p_x}{K}\right)^{\frac{n+1}{n}} \left(h_m - y\right)^{\frac{n+1}{n}} . \tag{4.2.9}$$

Integrating Equation (4.2.9) with respect to $y$, applying boundary conditions (2.3.15) and continuity condition $\partial T_1/\partial y = 0$ at $y = h_T$ gives the temperature profile as,

$$T_1 = -\frac{Br\ n^2}{(2n+1)} \left(-\frac{p_x}{K}\right)^{\frac{n+1}{n}} \left[\frac{1}{(3n+1)} \left((h_m - y)^{\frac{3n+1}{n}} - h_m^{\frac{3n+1}{n}}\right) - (h_m - h_T)^{\frac{2n+1}{n}}\, y\right] , \tag{4.2.10}$$

where the value of $h_m$ is defined by Equation (4.2.5). Similarly, the temperature profile for the case $y \geq h_m$ is found by solving,

$$\frac{\partial^2 T_2}{\partial y^2} = -Br \left(-\frac{p_x}{K}\right)^{\frac{n+1}{n}} \left(y - h_m\right)^{\frac{n+1}{n}} . \tag{4.2.11}$$

Integrating Equation (4.2.11) with respect to $y$, applying boundary conditions (2.3.16) and $\partial T_2/\partial y = 0$ at $y = h_T$, yields,

$$\begin{aligned} T_2 = &-\frac{Br\ n^2}{(2n+1)(3n+1)} \left(-\frac{p_x}{K}\right)^{\frac{n+1}{n}} \left[(y - h_m)^{\frac{3n+1}{n}} - (1 - h_m)^{\frac{3n+1}{n}}\right] \\ &+\frac{Brn}{(2n+1)} \left(-\frac{p_x}{K}\right)^{\frac{n+1}{n}} \left[(h_T - h_m)^{\frac{2n+1}{n}}\, y - (h_T - h_m)^{\frac{2n+1}{n}}\right] + 1 , \end{aligned} \tag{4.2.12}$$

where $h_m$ is given by Equation (4.2.5). Equations (4.2.10) and (4.2.12) give the solution for the temperature profile. The continuity condition is given by $T_2 = T_1$ at $y = h_T$.

$$\begin{aligned} T(h_T) &= -\frac{Br\ n^2}{(2n+1)} \left(-\frac{p_x}{K}\right)^{\frac{n+1}{n}} \left[\frac{1}{(3n+1)} \left((h_m - h_T)^{\frac{3n+1}{n}} - h_m^{\frac{3n+1}{n}}\right) - (h_m - h_T)^{\frac{2n+1}{n}}\, h_T\right] \\ &= -\frac{Br\ n^2}{(2n+1)(3n+1)} \left(-\frac{p_x}{K}\right)^{\frac{n+1}{n}} \left[(h_T - h_m)^{\frac{3n+1}{n}} - (1 - h_m)^{\frac{3n+1}{n}}\right] \\ &\quad +\frac{Brn}{(2n+1)} \left(-\frac{p_x}{K}\right)^{\frac{n+1}{n}} \left[(h_T - h_m)^{\frac{2n+1}{n}}\, h_T - (h_T - h_m)^{\frac{2n+1}{n}}\right] + 1 . \end{aligned} \tag{4.2.13}$$

Equation (4.2.13) provides the solution of the constant $h_T$ which is non−linear and it must be solved numerically.

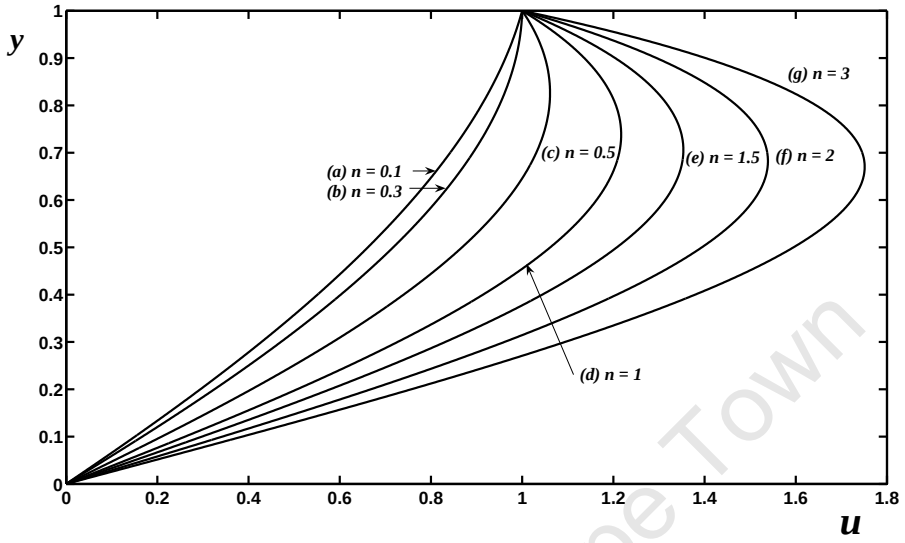


Figure 4.2: The velocity profiles for Equations (4.2.3) and (4.2.4): Boundary conditions (2.3.15) and (2.3.16).

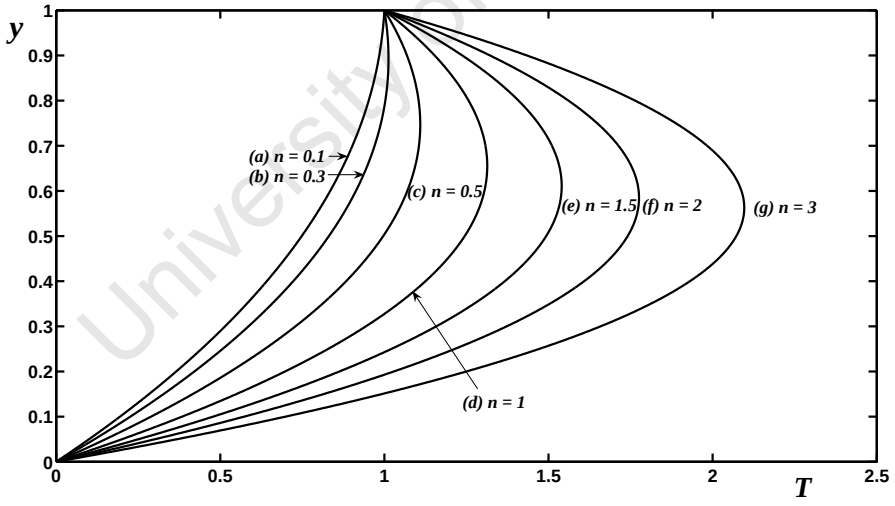


Figure 4.3: The temperature profiles for Equations (4.2.10) and (4.2.12): Boundary conditions (2.3.15) and (2.3.16).

Fig. 4.2 shows the effect of progressively increasing power law index in the region $0.1 \leq n \leq 3$ and $K = 1$ and $p_x = -1.5$. These curves were plotted by using Equations (4.2.3) and (4.2.4). The predicted velocity profiles for curves (a) to (c) increase gradually as $n$ increases to 0.5. The viscosity of the fluid decreases with increasing values of $n < 1$ and increases with values of $n > 1$. The Newtonian case is observed in curve (d) and its maximum velocity for the Newtonian fluid occurs near the moving plate. The shear thickening fluids are displayed in curves (e) through to (g) with $n > 1$. The viscosity for the shear thickening fluids increases as the value of $n$ increases. The applied shear force by the movement of the upper plate presumably dominates the flow since the maximum values for the velocity profiles occur near the top plate. The competition between the applied shear force and the pressure gradient act to increase the velocity of the fluid and it is higher for shear thickening fluids.

Fig. 4.3 displays the temperature profile for Equations (4.2.10) and (4.2.12), characterised by different values for $n$. The Brinkman number and the pressure gradient are fixed at $Br = 0.3$ and $p_x = -1.5$ respectively. The temperature of the fluid predicted by using the values of $n > 1$ are higher than the values of $n < 1$. The Newtonian temperature profile is displayed in curve (d) with $n = 1$ and the maximum temperature for the Newtonian case appears also near the top plate. In curves (e) to (g) the temperature of the fluid increases significantly as the power law index increases. Due to the boundary conditions at the top plate, the fluid temperature decreases to $T = 1$ at $y = 1$. The competition between the applied shear force and the pressure gradient act to increase heat generation and the temperature of the fluid rises. These results are in agreement with Fig. 9 shown in [33]. The temperature profiles were plotted using the numerical method and the results show that the temperature of the fluid between the plates rises as $n$ increases.

Fig. 4.4 shows the effect of a progressively increasing Brinkman number with $p_x = -1.5$. These curves are extracted from Fig. 4.3 curve (b). Each curve corresponds to different values of $Br$, namely $Br = 0, 2, 10, 15, 20$ and 25. Curves (b), (d), (e), (g) and (h) are

plotted for different values of $Br$, that is, 2 to 25 with $n = 0.5$ while curves (c), (f), (i), (j) and (k) are plotted for the same increasing values of the Brinkman numbers with $n = 1.5$. In curve (a) a linear profile is observed and the fluid temperature increases across the layer to a maximum temperature which occurs at $T = 1$ at $y = 1$. This is a common curve for both cases where $n = 0.5$ and $n = 1.5$. Increasing $Br$ results in increased viscous generation effect. For the curves plotted with values of $n = 1.5$, the temperature of the fluid is significantly higher than the cases where $n = 0.5$. This shows that shear thickening fluids respond quicker to the increase in heat generation effect.

### 4.2.1 Conclusion

In conclusion, the velocity and temperature profiles were plotted for different values of the power law index. Generally, the obvious case is that the power law index $n$ influences the flow characteristics of the predicted velocity and temperature profiles of the fluid. The corresponding Newtonian profiles are obtained when the power law index $n = 1$. As

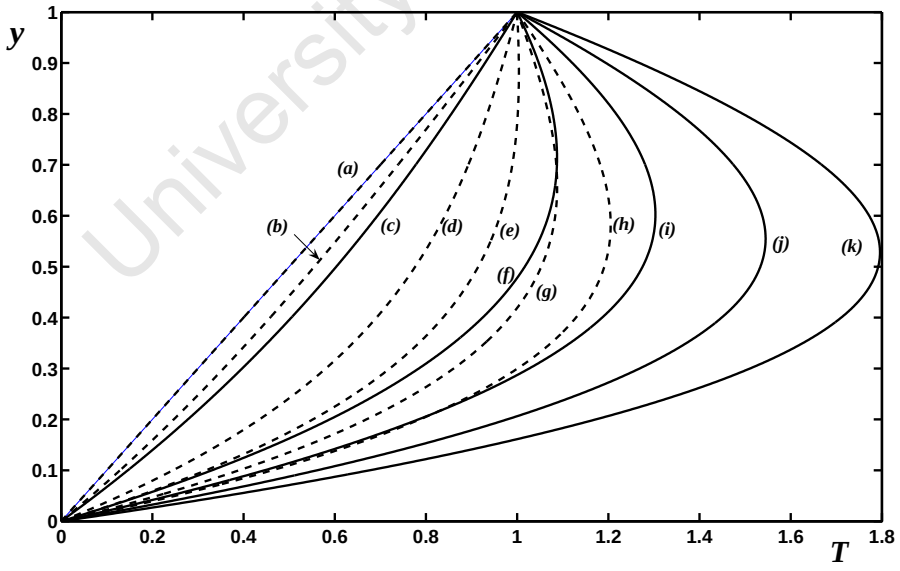


Figure 4.4: The effect of $Br$ for Equations (4.2.10) and (4.2.12) with $n = 0.5$ and $P_x = -1.5$: Boundary conditions (2.3.15) and (2.3.16).

$n$ increases, both the velocity and temperature of the fluid increase slightly with $n < 1$, however the profiles are more pronounced when $n > 1$. The effect of the Brinkman number on the temperature of the fluid showed an increase in the maximum temperature as $Br$ increases. The increase in the fluid temperature is more pronounced for shear thickening fluids due to the high heat dissipation effect.

## 4.3 The Carreau model

The flow of the Carreau model between parallel plates is now investigated. The model is given by Equation (3.3.7). We follow similar procedures as detailed in § 3.3. We first find an analytical solution for the velocity, flux and temperature profiles when $l \ll 1$, followed by analytical solution for $n = 0$, $n = 2$ and subsequently full solutions for the velocity and temperature profiles are obtained using a numerical method.

### Solution for $l \ll 1$

The velocity profile can be derived by coupling Equations (2.3.9) and (3.3.7) resulting in,

$$\frac{\partial}{\partial y}\left(\left(1 + l\left(\frac{\partial u}{\partial y}\right)^2\right)^{\frac{n-1}{2}} \frac{\partial u}{\partial y}\right) = p_x \ . \tag{4.3.14}$$

Equation (4.3.14) cannot be solved analytically, and consequently in § 4.3.1, a numerical solution is found. However, the case $l \ll 1$ will be considered first, where an asymptotic solution can be found. We use a similar procedure as detailed in § 3.3 and the upper bound for a non−dimensional parameter $l = 0.3$. The velocity may be written in series form,

$$u = u_0 + l u_1 \ . \tag{4.3.15}$$

Coupling Equations (4.3.14) and (4.3.15) leads to,

$$\frac{\partial}{\partial y}\left(\frac{\partial u_0}{\partial y}\right) + l\frac{\partial}{\partial y}\left(\frac{(n-1)}{2}\left(\frac{\partial u_0}{\partial y}\right)^3 + l\left(\frac{\partial u_1}{\partial y}\right)\right) = p_x \ , \tag{4.3.16}$$

up to $\mathcal{O}(l^2)$. The leading order terms gives the Newtonian velocity profile as,

$$u_0 = \frac{p_x}{2}\left(y^2 - y\right) + y \ , \tag{4.3.17}$$

and the $l$ correction is given by,

$$\frac{\partial}{\partial y}\left(\left(\frac{\partial u_1}{\partial y}\right) + \frac{n-1}{2}\left(\frac{\partial u_0}{\partial y}\right)^3\right) = 0 \ . \tag{4.3.18}$$

Solving Equation (4.3.18) subject to the imposed boundary conditions for $u_1$, that is,

$$u_1 = 0 \quad \text{at} \quad y = 0 \ , \quad u_1 = 0 \quad \text{at} \quad y = 1 \ , \tag{4.3.19}$$

gives the velocity profile for $u_1$ as,

$$\begin{aligned} u_1 &= \frac{n-1}{8p_x}\left[\left(\frac{p_x}{2}(2y-1)+1\right)^4 + \left(\left(1-\frac{p_x}{2}\right)^4 - \left(1+\frac{p_x}{2}\right)^4\right)y \right. \\ &\quad \left. - \left(1-\frac{p_x}{2}\right)^4\right] \ . \end{aligned} \tag{4.3.20}$$

The final velocity profile is,

$$\begin{aligned} u &= \frac{p_x}{2}\left(y^2 - y\right) + y + \frac{l(n-1)}{8p_x}\left[\left(\frac{p_x}{2}(2y-1)+1\right)^4 \right. \\ &\quad \left. + \left(\left(1-\frac{p_x}{2}\right)^4 - \left(1+\frac{p_x}{2}\right)^4\right)y - \left(1-\frac{p_x}{2}\right)^4\right] \ . \end{aligned} \tag{4.3.21}$$

The flux is obtained by integrating Equation (4.3.21) to give,

$$\begin{aligned} Q &= \int_0^1 u dy \\ &= \frac{1}{2}\left(1-\frac{p_x}{2}\right) + \frac{(n-1)}{8p_x}\left[\left[\frac{1}{5p_x}\left(\left(1+\frac{p_x}{2}\right)^5 - \left(1-\frac{p_x}{2}\right)^5\right)\right]\right. \\ &\quad \left. - \frac{1}{2}\left[2\left(1-\frac{p_x}{2}\right)^4 - \left(1+\frac{p_x}{2}\right)^4\right]\right] \ . \end{aligned} \tag{4.3.22}$$

Equation (4.3.22) shows that the flow rate is constant and also depends on the pressure gradient. The temperature profile is obtained by coupling Equation (2.3.11) and Equation (3.3.7) to give,

$$\frac{\partial^2 T}{\partial y^2} = -Br\left(\frac{\partial u}{\partial y}\right)^2\left[1 + l\left(\frac{\partial u}{\partial y}\right)^2\right]^{\frac{n-1}{2}} \ . \tag{4.3.23}$$

A similar procedure used to obtain the velocity profile is employed to get the solution for the temperature profiles. Expanding $T$ in terms of $l$, the temperature may be written in series form,

$$T = T_0 + lT_1 \ , \tag{4.3.24}$$

and Equation (4.3.23) becomes,

$$\frac{\partial^2 T_0}{\partial y^2} + l\frac{\partial^2 T_1}{\partial y^2} = -Br\left[\left(\frac{\partial u_0}{\partial y}\right)^2 + \frac{l(n-1)}{2}\left(\frac{\partial u_0}{\partial y}\right)^4 + 2l\left(\frac{\partial u_0}{\partial y}\frac{\partial u_1}{\partial y}\right)\right] + \mathcal{O}(l^4) \ . \tag{4.3.25}$$

The leading order terms gives the temperature profile as,

$$\begin{aligned} T_0 \ = \ & -\frac{Br}{24p_x^2}\left[\left(\frac{p_x}{2}(2y-1)+1\right)^4 - \left(\left(1+\frac{p_x}{2}\right)^4 - \left(1-\frac{p_x}{2}\right)^4\right)y \right. \\ & \left. - \ \left(1-\frac{p_x}{2}\right)^4\right] + y \ , \end{aligned} \tag{4.3.26}$$

and the first order perturbation is,

$$\frac{\partial^2 T_1}{\partial y^2} = -Br\left[\frac{(n-1)}{2}\left(\frac{\partial u_0}{\partial y}\right)^4 + 2\left(\frac{\partial u_0}{\partial y}\right)\left(\frac{\partial u_1}{\partial y}\right)\right] \ . \tag{4.3.27}$$

Substituting Equation (4.3.18) into Equation (4.3.27) gives,

$$\frac{\partial^2 T_1}{\partial y^2} = -Br\left[\frac{(n-1)}{2}\left(\frac{\partial u_0}{\partial y}\right)^4\right] \ . \tag{4.3.28}$$

Integrating Equation (4.3.28) combined with Equation (4.3.17) subject to the imposed boundary conditions for $T_1$, that is,

$$T_1 = 0 \quad \text{at} \quad y = 0 \ , \quad T_1 \ = 0 \quad \text{at} \quad y = 1 \ , \tag{4.3.29}$$

gives the temperature profile as,

$$\begin{aligned} T_1 \ = \ & -\frac{Br(n-1)}{60p_x^2}\left[\left(\frac{p_x}{2}(2y-1)+1\right)^6 - \left(\left(1+\frac{p_x}{2}\right)^6 - \left(1-\frac{p_x}{2}\right)^6\right)y \right. \\ & \left. - \ \left(1-\frac{p_x}{2}\right)\right] \ . \end{aligned} \tag{4.3.30}$$

The final temperature profile is therefore,

$$\begin{aligned} T &= T_0 + lT_1 \\ &= -\frac{Br}{24p_x^2}\left[\left(\frac{p_x}{2}(2y-1)+1\right)^4 - \left(\left(1+\frac{p_x}{2}\right)^4 - \left(1-\frac{p_x}{2}\right)^4\right)y \right. \\ &\quad \left. - \left(1-\frac{p_x}{2}\right)^4\right] + y - \frac{Br\ l\ (n-1)}{60p_x^2}\left[\left(\frac{p_x}{2}(2y-1)+1\right)^6 \right. \\ &\quad \left. - \left(\left(1+\frac{p_x}{2}\right)^6 - \left(1-\frac{p_x}{2}\right)^6\right)y - \left(1-\frac{p_x}{2}\right)\right] . \end{aligned} \tag{4.3.31}$$

We now proceed to find the analytical solution for the velocity, flux and temperature profiles for $n = 0$.

## Solution for $n = 0$

In order to determine the solution for the velocity profile, Equation (4.3.14) is integrated once to give,

$$\left(\frac{\partial u}{\partial y}\right)\left[1 + l\left(\frac{\partial u}{\partial y}\right)^2\right]^{\frac{2}{n-1}} = p_x(y - h_i) . \tag{4.3.32}$$

For $n = 0$, Equation (4.3.32) is written,

$$\frac{\partial u}{\partial y} = \pm\frac{px\,(y-h_i)}{\sqrt{1 - lp_x^2(y-h_i)^2}} . \tag{4.3.33}$$

For $(\partial u/\partial y) \geq 0$, $y \leq h_i$ and Equation (4.3.33) is integrated once and the boundary conditions (2.3.15) are applied to give,

$$u_1 = \frac{1}{lp_x}\left[\sqrt{1 - lp_x^2(h_i - y)^2} - \sqrt{1 - lp_x^2 h_i^2}\right] , \tag{4.3.34}$$

and when $(\partial u/\partial y) \leq 0$, $y \geq h_i$ and Equation (4.3.34) is integrated once and applying the boundary conditions (2.3.16) gives,

$$u_2 = \frac{1}{lp_x}\left[\sqrt{1 - lp_x^2(1-h_i)^2} - \sqrt{1 - lp_x^2(y-h_i)^2}\right] + 1 . \tag{4.3.35}$$

The velocity profile is obtained by combining Equations (4.3.34) and (4.3.35). The constant $h_i$ is obtained by requiring the continuity condition $u_1 = u_2$ at $y = h_i$, which gives,

$$\begin{aligned} u(h_i) &= \frac{1}{lp_x}\left[1 - \sqrt{1 - lpx^2 h_i^2}\right] \\ &= \frac{1}{lp_x}\left[\sqrt{1 - lpx^2(1-h_i)^2} - 1\right] + 1 \ . \end{aligned} \tag{4.3.36}$$

Equation (4.3.36) is solved numerically using the Newtons method and substituted into Equations (4.3.34) and (4.3.35) to find the solution for the velocity profiles. The flux is given by $Q = Q_1 + Q_2$ where,

$$Q_1 = \int_0^{h_m} u dy = \frac{\arctan\left(\frac{p_x\sqrt{l}\ h_i}{\sqrt{1-lp_x^2h_x^2}}\right)}{2l^{\frac{3}{2}}p_x^2} - \frac{\sqrt{1-p_x^2h_i^2}\ h_i}{2lp_x} \ , \tag{4.3.37}$$

$$Q_2 = \int_{h_m}^{1} u dy = \frac{3\sqrt{1-p_x^2(1-h_i)^2}}{2lp_x}(1+h_i) - \frac{\arctan\left(\frac{p_x\sqrt{l}\ (1-h_i)}{\sqrt{1-lp_x^2(1-h_x)^2}}\right)}{2l^{\frac{3}{2}}p_x^2} \ . \tag{4.3.38}$$

Adding Equations (4.3.37) and (4.3.38) we obtain the expression for the flux,

$$\begin{aligned} Q = \quad & \frac{\arctan\left(\frac{p_x\sqrt{l}\ h_i}{\sqrt{1-lp_x^2h_x^2}}\right)}{2l^{\frac{3}{2}}p_x^2} - \frac{\sqrt{1-p_x^2h_i^2}\ h_i}{2lp_x} \\ & + \frac{3\sqrt{1-p_x^2(1-h_i)^2}}{2lp_x}(1+h_i) - \frac{\arctan\left(\frac{p_x\sqrt{l}\ (1-h_i)}{\sqrt{1-lp_x^2(1-h_x)^2}}\right)}{2l^{\frac{3}{2}}p_x^2} \ . \end{aligned} \tag{4.3.39}$$

Equation (4.3.39) shows that the flux is constant. The temperature profile is found by setting $n = 0$ in Equation (4.3.23) to give,

$$\frac{\partial^2 T}{\partial y^2} = -\frac{Brp_x^2(y-h_i)^2}{\left[1 + l\frac{p_x^2(y-h_i)^2}{(1-lp_x^2(y-h_i)^2)}\right]^2} \ . \tag{4.3.40}$$

Integrating Equation (4.3.40) with respect to $y$ and applying the imposed boundary conditions $\partial T_1/\partial y = 0$ at $y = h_{T1}$ and (2.3.15) yields,

$$\begin{aligned} T_1 &= Brp_x^2\left[\frac{{p_x}^2 l^2}{56}(h_{T1}^7 y - y^8) + \frac{{p_x}^4 l^2 h_i}{7}(h_{T1}^6 y - y^7) + \frac{{p_x}^4 l}{15}(h_{T1}^5 y - y^6)\right] \\ &\quad + Brp_x^2\left[\frac{{p_x}^3 l h_i}{5}(5h_i^2 l - 2)(h_{T1}^4 y - y^5) + \frac{{p_x}^2}{12}(15h_1^4 l^2 - 12lh_i^2 + 1)(h_{T1}^3 y - y^4)\right] \\ &\quad + Brp_x^2\left[\frac{p_x h_i}{3}(3{h_i}^4 l^2 - 4l{h_i}^2 + 1)(h_{T1}^2 y - y^3) + \frac{h_i^2}{2}({h_i}^4 l^2 - 2lh_i^2 + 1)(h_{T1} y - y^2)\right] . \end{aligned} \tag{4.3.41}$$

Similarly, for $y \geq h_i$, Equation (4.3.40) is integrated and applying the boundray conditions (2.3.16) gives,

$$\begin{aligned} T_2 &= -Brp_x^2\left[\frac{{p_x}^2 l^2}{56}\left((y^8 - h_{T1}^7 y) - (1 - h_{T1}^7)\right) + \frac{{p_x}^4 l^2 h_i}{7}\left((y^7 - h_{T1}^6 y) - (1 - h_{T1}^6)\right)\right. \\ &\quad \left. + \frac{{p_x}^4 l}{15}\left((y^6 - h_{T1}^5 y) - (1 - h_{T1}^5)\right) - \frac{{p_x}^3 l h_i}{5}(5h_i^2 l - 2)\left((y^5 - h_{T1}^4 y) - (1 - h_{T1}^4)\right)\right] \\ &\quad - Brp_x^2\left[\frac{1}{12}(15h_1^4 l^2 - 12lh_i^2 + 1)\left((y^4 - h_{T1}^3 y) - (1 - h_{T1}^3)\right)\right. \\ &\quad \left. + \frac{p_x h_i}{3}(3{h_i}^4 l^2 - 4l{h_i}^2 + 1)\left((y^3 - h_{T1}^2 y) - (1 - h_{T1}^2)\right)\right] \\ &\quad - Brp_x^2\left[\frac{h_i^2}{2}({h_i}^4 l^2 - 2lh_i^2 + 1)\left((y^2 - h_{T1} y) - (1 - h_{T1})\right)\right] + 1 . \end{aligned} \tag{4.3.42}$$

The constant $h_{T1}$ is found by using the continuity condition $T_1 = T_2$ at $y = h_{T1}$ to give,

$$\begin{aligned} T(h_{T1}) &= -Brp_x^2\left[\frac{{p_x}^2 l^2}{56}\left(1 - h_{T1}^7\right) + \frac{{p_x}^4 l^2 h_i}{7}\left(1 - h_{T1}^6\right)\right] \\ &\quad - Brp_x^2\left[\frac{{p_x}^4 l}{15}\left(1 - h_{T1}^5\right) - \frac{{p_x}^3 l h_i}{5}(5h_i^2 l - 2)\left(1 - h_{T1}^4\right)\right] \\ &\quad + Brp_x^2\left[\frac{1}{12}(15h_1^4 l^2 - 12lh_i^2 + 1)\left(1 - h_{T1}^3\right)\right] \\ &\quad + Brp_x^2\left[\frac{p_x h_i}{3}(3{h_i}^4 l^2 - 4l{h_i}^2 + 1)\left(1 - h_{T1}^2\right)\right] \\ &\quad + Brp_x^2\left[\frac{h_i^2}{2}({h_i}^4 l^2 - 2lh_i^2 + 1)\left(1 - h_{T1}\right)\right] + 1 . \end{aligned} \tag{4.3.43}$$

Equation (4.3.43) is solved numerically to obtain the solution for the constant $h_{T1}$ and $h_i$ is defined by Equation (4.3.36). We now proceed to find the solution for the velocity, flux and temperature profiles for the case $n = 2$.

## Solution for $n = 2$

The velocity profile obtained by setting $n = 2$ in Equation (4.3.32) is written,

$$\left(\frac{\partial u}{\partial y}\right)^2 = \frac{-1 \pm \sqrt{1 + 4lp_x^2(y - h_j)^2}}{2l} \ . \tag{4.3.44}$$

The integration of Equation (4.3.44) depends on the sign of the velocity gradient and the form of the solution. For a simple form of a solution, we consider the positive velocity gradient to the order of $\mathcal{O}(l^2)$ and the terms in Equation (4.3.44) are rearranged to give,

$$\frac{\partial u}{\partial y} = \pm\frac{1}{2}\left[2p_x\left(y - h_j\right) - l{p_x}^2(y - h_j)^3\right] \ , \tag{4.3.45}$$

where $\pm$ appear as a result of the square of the velocity gradient in Equation (4.3.44). Now for $(\partial u/\partial y) \geq 0$, $y \leq h_j$, and Equation (4.3.45) is integrated once and we apply the boundary conditions (2.3.15) to give,

$$u_1 = \frac{p_x}{8}\left[4y\left(2h_j - y\right) + l{p_x}^2\left((hj - y)^4 - {h_j}^4\right)\right] \ , \tag{4.3.46}$$

and when $(\partial u/\partial y) \leq 0$, $y \geq h_j$ and the velocity is now written,

$$u_2 = \frac{p_x}{8}\left[4\left(y\left(y - 2h_j\right) - \left(1 - 2h_j\right)\right) - l{p_x}^2\left((y - hj)^4 - (1 - h_j)^4\right)\right] + 1 \ . \tag{4.3.47}$$

The velocity profile is obtained by combining Equations (4.3.46) and (4.3.47). The constant $h_j$ is obtained by requiring that $u_1 = u_2$ at $y = h_j$, which gives,

$$\begin{aligned} u(h_j) &= \frac{{p_x}^2 h_j^2}{2}\left(1 - \frac{lp_x^2}{4}\right) \\ &= \frac{p_x^2}{8}\left[lpx^2\left(1 - h_m\right)^4 - \left(4{h_j}^4 - 2h_j + 1\right)\right] + 1 \ . \end{aligned} \tag{4.3.48}$$

The flux is given by $Q = Q_1 + Q_2$ where,

$$Q_1 = \int_0^{h_m} u dy = \frac{p_x {h_j}^3}{3} + \frac{l p_x^3 {h_j}^5}{40} \ . \tag{4.3.49}$$

$$Q_2 = \int_{h_m}^{1} u dy = \frac{p_x}{12}\left[2(1-3h_j) - 3l{p_x}^3(1-h_j)^5 + 4{h_j}^3\right] \ . \tag{4.3.50}$$

Adding Equations (4.3.49) and (4.3.50) we obtain the expression for the flux in terms of the pressure gradient,

$$Q = \frac{p_x {h_j}^3}{3} + \frac{l p_x^3 {h_j}^5}{40} + \frac{p_x}{12}\left[2(1-3h_j) - 3l{p_x}^3(1-h_j)^5 + 4{h_j}^3\right] \ . \tag{4.3.51}$$

Setting $n = 2$ in Equation (4.3.23) and expanding this equation to the order $\mathcal{O}(l^2)$, gives the second order temperature gradient as,

$$\frac{\partial^2 T}{\partial y^2} = -Br\left[p_x^2(y-h_j)^2 - l p_x^4 (y-h_j)^4\right] \ . \tag{4.3.52}$$

For $y \leq h_j$, Equation (4.3.52) is integrated twice with respect to $y$ and applying the imposed boundary conditions $\partial T_1/\partial y = 0$ at $y = h_{T2}$ and (2.3.15) gives,

$$\begin{aligned} T_1 &= -Br\left[\frac{{p_x}^2}{12}\left(4y(h_j - h_{T2})^3 - \left((h_j-y)^4 - h_j^4\right)\right)\right] \\ &\quad + \frac{Br\ l p_x^4}{60}\left[\left(6y(h_j-h_{T2})^5 - \left((h_j-y)^6 - h_j^6\right)\right)\right] \ , \end{aligned} \tag{4.3.53}$$

where $h_j$ is determined by Equation (4.3.48). Similarly, for $y \geq h_j$, Equation (4.3.52) is integrated twice with respect to $y$ to give,

$$\begin{aligned} T_2 &= -Br\left[\frac{{p_x}^2}{4}\left[(y-h_j)^4 - (1-h_j)^4 - 4\left((h_{T2}-h_j)^3 y - (h_{T2}-h_j)^3\right)\right]\right] \\ &\quad + \frac{Br\ l p_x^4}{60}\left[\left[(y-h_j)^6 - (1-h_j)^6 - 6\left((h_{T2}-h_j)^5 y - (h_{T2}-h_j)^5\right)\right]\right] + 1 \ , \end{aligned} \tag{4.3.54}$$

The constant $h_{T2}$ is obtained by requiring the continuity condition $T_1 = T_2$ at $y = h_{T2}$ to give

$$\begin{aligned} T(h_{T2}) &= -Br\left[\frac{{p_x}^2}{12}\left(4h_{T2}(h_j - h_{T2})^3 - \left((h_j - h_{T2})^4 - h_j^4\right)\right)\right] \\ &\quad + \frac{Br\ lp_x^4}{60}\left[\left(6h_{T2}(h_j - h_{T2})^5 - \left((h_j - h_{T2})^6 - h_j^6\right)\right)\right] , \\ &= -Br\left[\frac{{p_x}^2}{4}\left[(h_{T2} - h_j)^4 - (1 - h_j)^4 - 4\left(h_{T2}(h_{T2} - h_j)^3 - (h_{T2} - h_j)^3\right)\right]\right] \\ &\quad + \frac{Br\ lp_x^4}{60}\left[\left[(h_{T2} - h_j)^6 - (1 - h_j)^6 - 6\left(h_{T2}(h_{T2} - h_j)^5 - (h_{T2} - h_j)^5\right)\right]\right] \\ &\quad + 1 . \end{aligned} \tag{4.3.55}$$

Equations (4.3.53) and (4.3.54) are coupled to determine the solution for the temperature profiles. The velocity and temperature profiles are now plotted. We investigate the effect of the flow controlling parameters, that is $l$ and $n$, on the resulting flow profiles. We will start our investigation with values of $l \ll 1$ and also proceed to investigate the effect of the power law index on the flow profiles. We again use the maximum upper bound for $l$ to be 0.3 and we follow a similar procedure to obtain the velocity and temperature profiles as detailed in § 3.3.

In Figs. 4.5 and 4.6 four curves each representing the predicted velocity profiles for Equation (4.3.21) are shown. The other parameters are given by $n = 0.5$, $p_x = -1.5$ and $0 \leq l \leq 0.3$. In Fig. 4.5, the velocity profile for a Newtonian case is shown in curve (a) with $l = 0$ and is lower than the velocity profile for the case $l = 0.3$ as expected from shear thinning fluids. When $l$ increases with $n = 0.5$ the velocity of the fluid increases because of the reduced resistance force to the flow. For shear thinning fluids the viscosity decreases with an increase in $l$ and the fluid velocity increases due to less resistance force to the flow. The opposite is true as shown in Fig. 4.6 with $n = 1.5$ for shear thickening fluids. The viscosity of the fluid increases when $l$ increases for shear thickening fluid and subsequently the velocity of the fluid increases as the parameter $l$ decreases, and the combined pressure gradients and applied shear force compete in driving the fluid, so

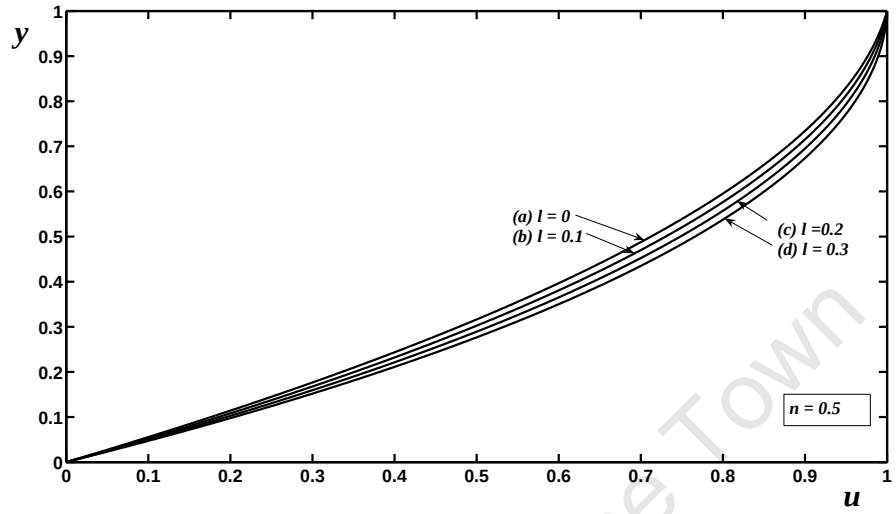


Figure 4.5: The velocity profiles for Equation (4.3.21) with various values of $l$ and $n = 0.5$: Boundary conditions (2.3.15) and (2.3.16).

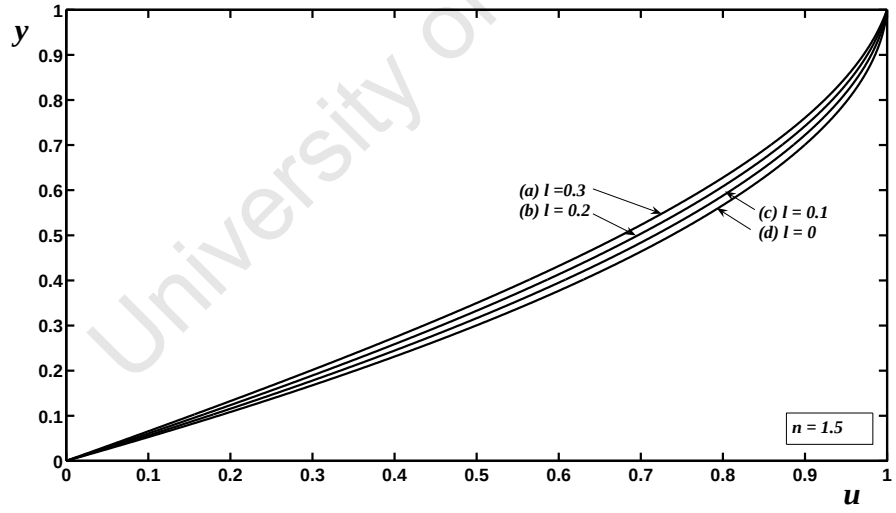


Figure 4.6: The velocity profiles for Equation (4.3.21) with various values of $l$ and $n = 1.5$: Boundary conditions (2.3.15) and (2.3.16).

the maximum values for the velocity profiles occurs at the top plate. These two figures illustrate that the major driving force for the fluid is probably the applied shear force since maximum velocities occur at the top plate.

Figs. 4.7 and 4.8 show the temperature profiles predicted for Equation (4.3.31). Similar parameters as displayed in Figs. 4.5 and 4.6 are used and $Br$ is fixed at $Br = 0.3$. A similar trend as shown in the velocity profiles is observed for the temperature profiles. The temperature of the fluid in curves (a) to (d) increases across the plates to their maximum, which occurs at the top plate in Fig. 4.7. The Newtonian case is retrieved in curve (a). When $l$ increases with $n = 0.5$ the temperature of the fluid increases due to heat generation by the action of both the applied shear force and the pressure gradient. The opposite is true for $n = 1.5$ as displayed in Fig. 4.8 for shear thickening fluids.

The effect of the power law index is shown in Fig. 4.9 for the predicted velocity profiles corresponding to Equation (4.3.21), with $l = 0.3$ and $p_x = -1.5$. The power law indices in the region $0.1 \leq n \leq 3$ for curves (a) through to (g). All the curves are similar in shape and their maximum value occurs at the top plate due to the applied shear force by the movement of the top plate. In curves (e) to (f) their viscosity decreases as the power law index increases, so the velocity increases due to the lower resistance force to the flow. The Newtonian velocity profile is shown in curve (d) with $n = 1$ and the velocity of the fluid increases across the plates to its maximum value at the top plate. In curves (a) through to (c) the gap between the velocity profiles is more pronounced. The velocity of the fluid increases as $n$ decreases from $n = 1.5$ to 3 for shear thickening fluids. The viscosity of the fluid in these curves increases when $n$ increases, which shows that the more viscous the fluid, the lower the flow. Fig. 4.10 show eight curves representing the temperature profiles for Equation (4.3.31) with different values of $n$. Other parameters are similar to those given in Fig. 4.9, and $Br = 0.3$. A similar trend of the flow profiles as in Fig. 4.9 is observed in Fig 4.10. Curves (a) through to (c) display decreasing values of $n$ and the fluid temperature increases across the plates to their maximum temperature at the top

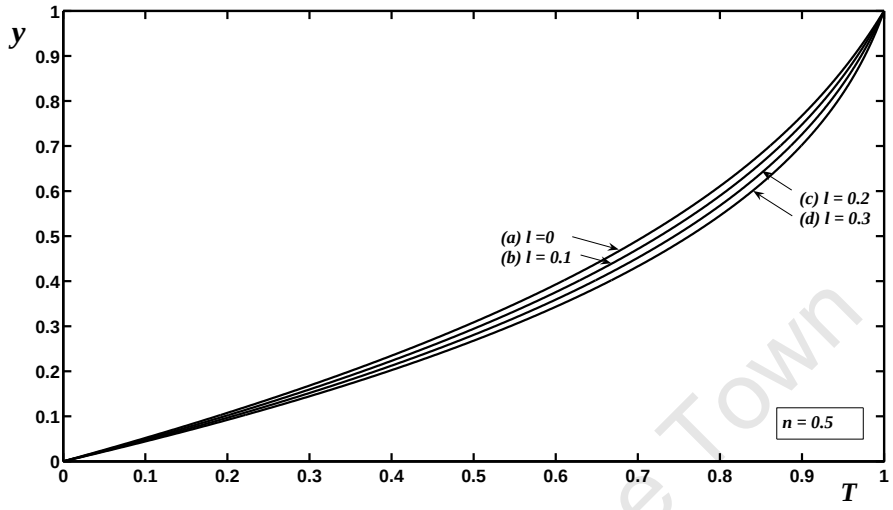


Figure 4.7: The temperature profiles for Equation (4.3.31) with various values of $l$ and $n = 0.5$: Boundary conditions (2.3.15) and (2.3.16).

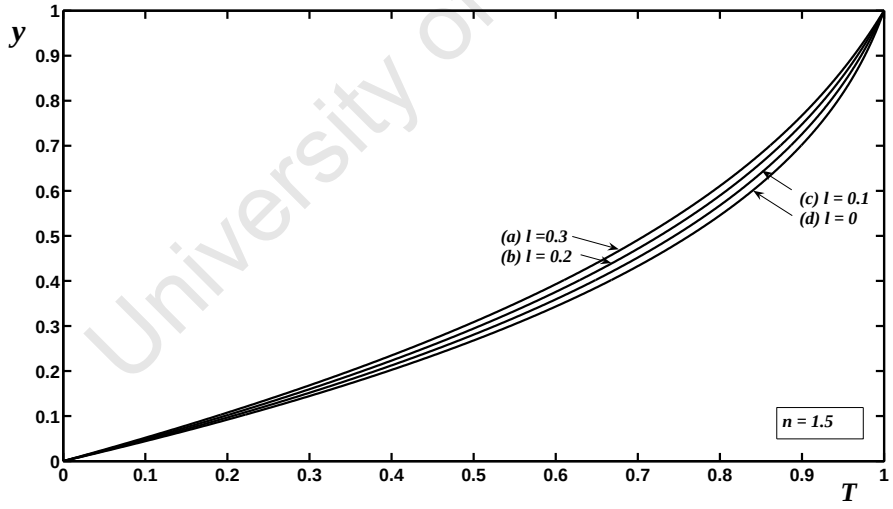


Figure 4.8: The temperature profiles for Equation (4.3.31) with various values of $l$ and $n = 1.5$: Boundary conditions (2.3.15) and (2.3.16).

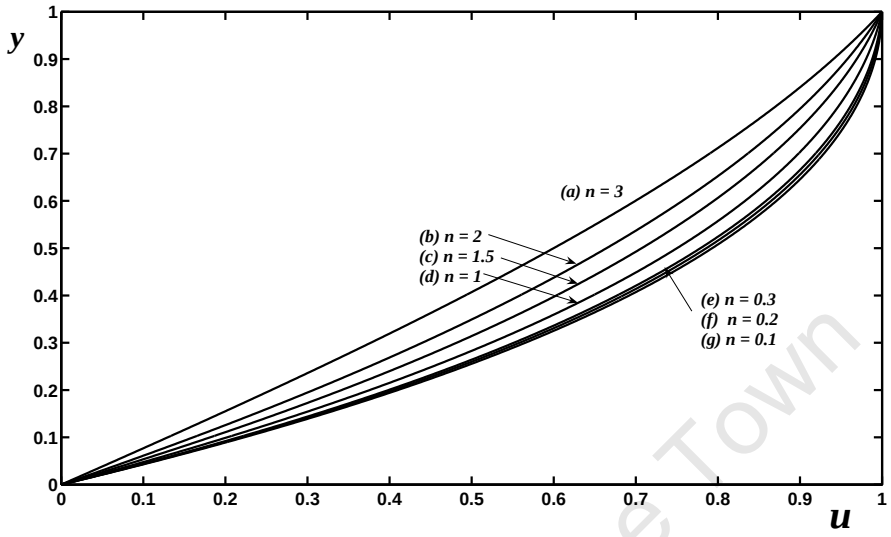


Figure 4.9: The velocity profiles for Equation (4.3.21) with various values of $n$ and $l = 0.3$: Boundary conditions (2.3.15) and (2.3.16).

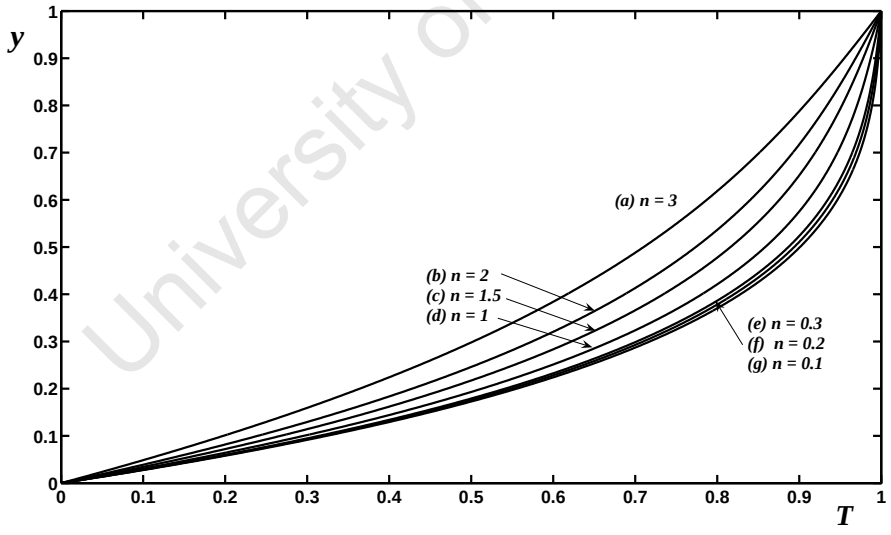


Figure 4.10: The temperature profiles for Equation (4.3.31) with different values of $n$ and $l = 0.3$: Boundary conditions (2.3.15) and (2.3.16).

plate. In curve (d) with $n = 1$, the Newtonian temperature profile is retrieved. As $n$ decreases, the temperature of the fluid increases, since the presence of a pressure gradient and the applied shear force act to create heat generation. Thus the temperature rises due to the internal flow processes and the applied shear force is significant when $n$ decreases.

In Fig. 4.11 the predicted velocity profiles for Equations (4.3.34) and (4.3.35), with different values of $l$, namely $l = 0.01, 0.1, 0.2, 0.3$, $n = 0$ and $p_x = -1.5$ are shown. Curves (a) to (d) increase across the plates to their maximum at the top plate due to the combination of both the pressure gradient and the applied shear force. The velocity profiles in curves (a) through to (d) coincide from $u = 0$ at $y = 0$ to the point $u = 0.48$ at $y = 0.3$ and then the curves separate from this point to their maximum at the top plate. The opposite of this figure is shown in Fig. 4.13 for the case $n = 2$. The curves correspond to Equations (4.3.46) and (4.3.47). In this figure the gap between the velocity profiles is slightly higher as compared to Fig. 4.11. The velocity of the fluid increases as the values of the parameter $l$ decreases as expected from shear thickening fluids. This illustrates that the effect of $l$ is minimal on the velocity profiles when $n = 0$ and the opposite is true when $n = 2$. Fig. 4.12 shows the temperature profiles again with similar values of $l$ as displayed in Fig. 4.11 and the curves correspond to Equations (4.3.41) and (4.3.42). The temperature of the fluid increases gradually to a maximum at the top plate. This also confirms the importance of the power law index $n$. When $l$ increases an increase in the temperature of the fluid is observed due to heat generation by the action of the pressure gradient and applied shear forces. The opposite is true as shown in Fig. 4.14 for shear thickening fluids and the curves correspond to Equations (4.3.53) and (4.3.54).

In the following section we proceed with our investigation for a full solution using a numerical method. We first carry out our investigation by comparing our analytical results with the numerics and subsequently the effect of large values for the parameter $l$ on the resulting flow profiles, are investigated.

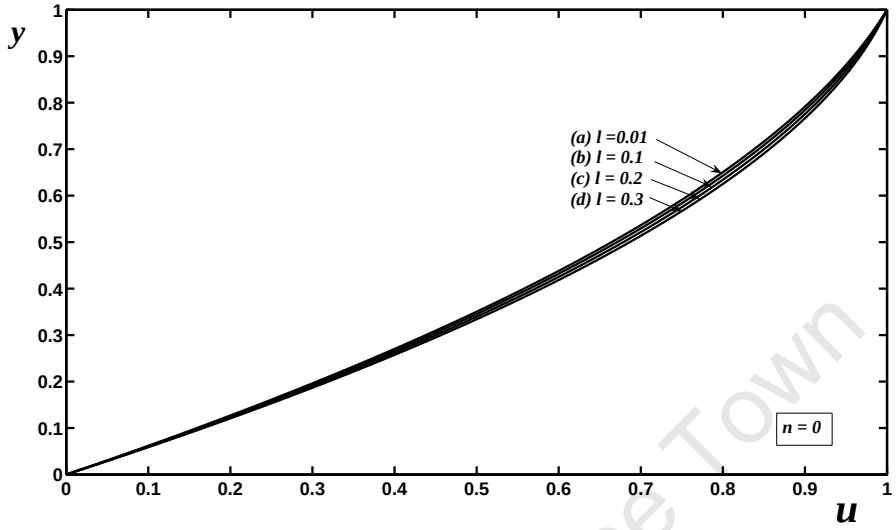


Figure 4.11: The velocity profiles for Equations (4.3.34) and (4.3.35) with various values of $l$: Boundary conditions (2.3.15) and (2.3.16).

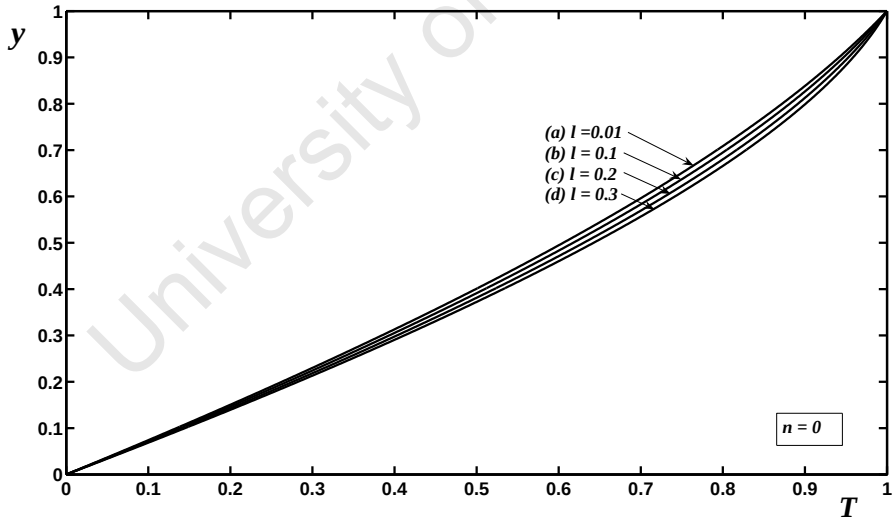


Figure 4.12: The temperature profiles for Equations (4.3.41) and (4.3.42) with various values of $l$: Boundary conditions (2.3.15) and (2.3.16).

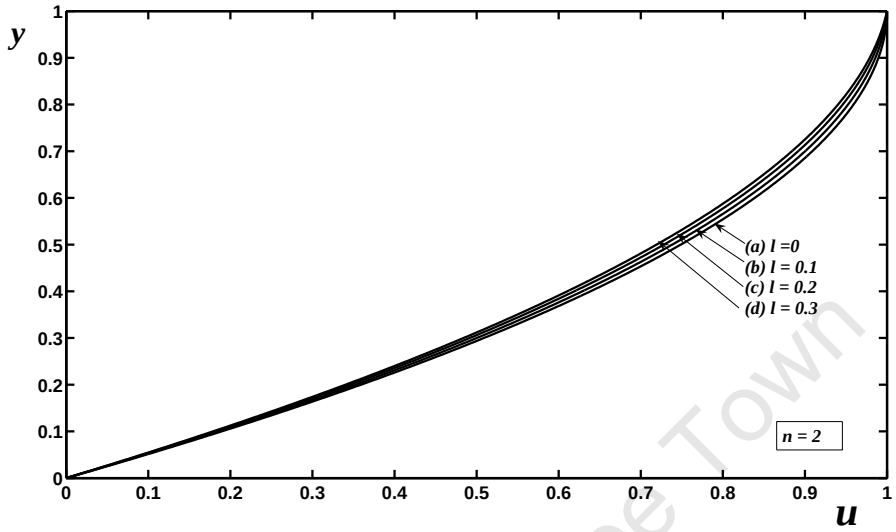


Figure 4.13: The velocity profiles for Equations (4.3.46) and (4.3.47) with various values of $l$: Boundary conditions (2.3.15) and (2.3.16).

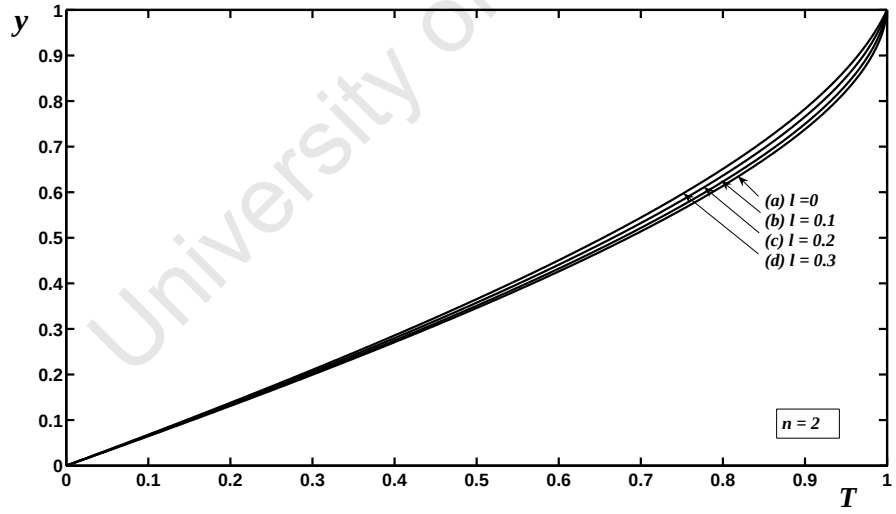


Figure 4.14: The temperature profiles for Equations (4.3.53) and (4.3.54) with various values of $l$: Boundary conditions (2.3.15) and (2.3.16).

### 4.3.1 Numerical solution

A numerical method is used to determine the complete solution of the coupled systems of Equations (4.3.14) and (4.3.23). In the previous section, analytical solutions were obtained for small values of $l$. In this section, large values of $l$ are investigated, but small values of $l$ are first considered to test the reliability of this numerical approach; then the model is extended to investigate the effect of large values of $l$. A procedure similar to that detailed briefly in § 3.3.1 is now employed. Equations (4.3.14) and (4.3.23) are now written in the form,

$$\left(\frac{\partial u}{\partial y}\right)^{\frac{2}{n-1}} + l\left(\frac{\partial u}{\partial y}\right)^{\frac{4}{n-1}} - \left(p_x y + C_1\right)^{\frac{2}{n-1}} = 0 \,, \tag{4.3.56}$$

$$\frac{\partial^2 T}{\partial y^2} + Br\left(\frac{\partial u}{\partial y}\right)^2 \left[1 + l\left(\frac{\partial u}{\partial y}\right)^2\right]^{\frac{n-1}{2}} = 0 \,, \tag{4.3.57}$$

where $C_1$ is the constant of integration. However, the shooting method is used to determine the appropriate value of $C_1$, in which the governing equations satisfy the boundary conditions. In the shooting process, an arbitrary choice of $C_1$ is made to shoot for the target value and the iteration continues until the boundary conditions are satisfied. The velocity and temperature profiles are solved using the Newton Raphson algorithm. Equation (4.3.56) now takes the form,

$$\left(\frac{\partial u}{\partial y}\right)^{\frac{2}{n-1}}\bigg|_{y=y_i} + l\left(\frac{\partial u}{\partial y}\right)^{\frac{4}{n-1}}\bigg|_{y=y_i} - \left(p_x y_i + C_1\right)^{\frac{2}{n-1}} = 0 \,, \tag{4.3.58}$$

The derivative $(\partial u/\partial y)$ is calculated from Equation (4.3.58), and then the velocity profile is solved using,

$$u_{i+1} = u_i + \triangle u_y . \left(\frac{\partial u}{\partial y}\right)\bigg|_{y_i} \,. \tag{4.3.59}$$

The value obtained for the velocity gradient $(\partial u/\partial y)$ is now used in Equation (4.3.57) to solve for $(\partial^2 T/\partial y^2)$. The temperature profile is obtained by integrating Equation (4.3.57) twice with respect to $y$ using the the Newton Raphson method.

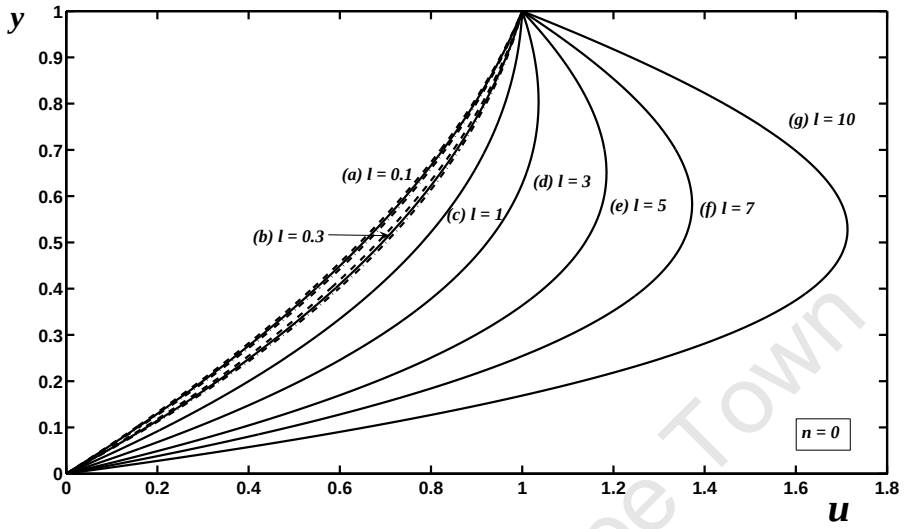


Figure 4.15: The velocity profiles for Equations (4.3.21), (4.3.34), (4.3.35) and (4.3.58): Boundary conditions (2.3.15) and (2.3.16).

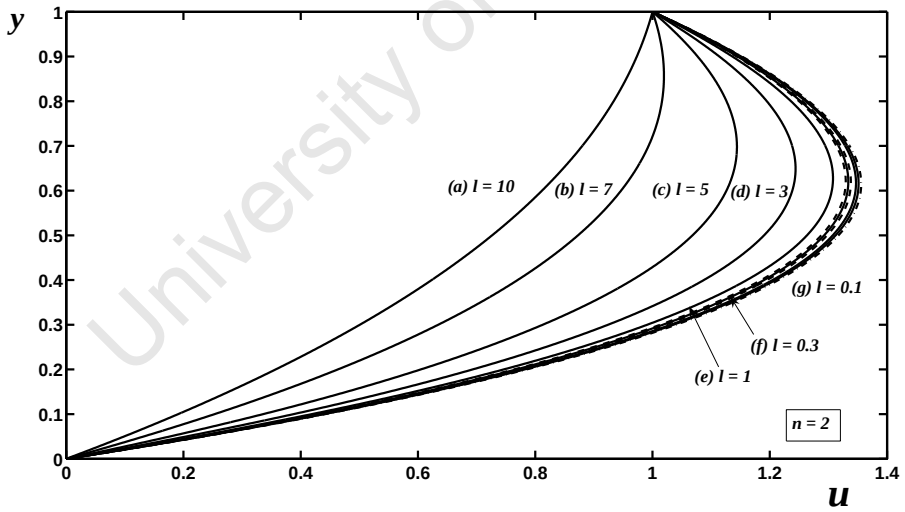


Figure 4.16: The velocity profiles for Equations (4.3.21), (4.3.46), (4.3.47) and (4.3.58): Boundary conditions (2.3.15) and (2.3.16).

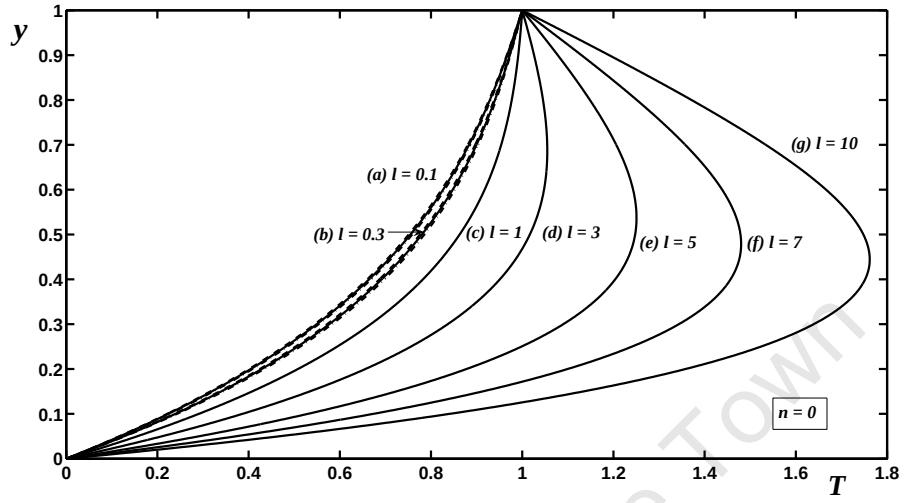


Figure 4.17: The temperature profiles for Equations (4.3.31), (4.3.41), (4.3.42) and (4.3.57): Boundary conditions (2.3.15) and (2.3.16).

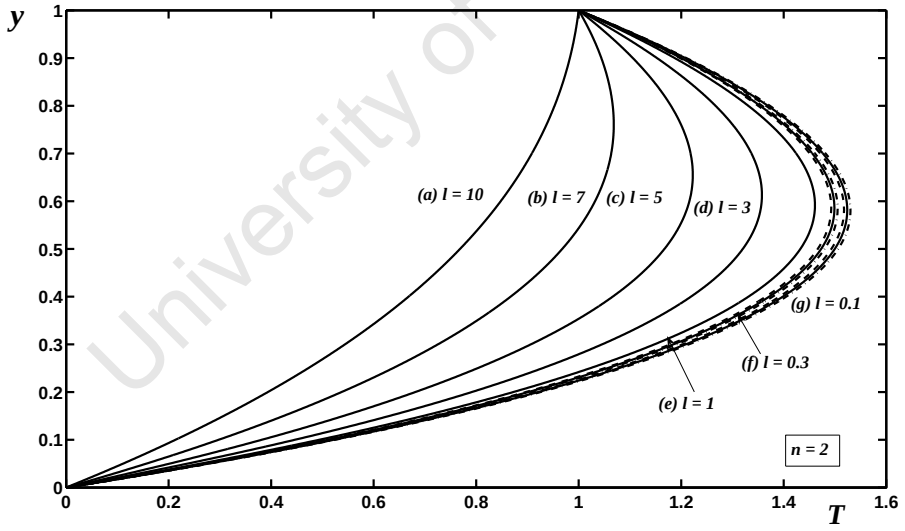


Figure 4.18: The temperature profiles for Equations (4.3.31), (4.3.53), (4.3.54) and (4.3.57): Boundary conditions (2.3.15) and (2.3.16).

In Fig. 4.15 dashed lines represent the velocity profiles corresponding to Equation (4.3.21), dashed dotted lines represent the profiles for Equations (4.3.34) and (4.3.35), and solid lines represent the profiles for Equation (4.3.58). In both sets we have an excellent match of the results predicted by using the analytical, asymptotics and numerical methods. The maximum values for the velocity profiles for curves (a) to (c) occur at the top plate, probably since the dominant driving force for the flow is the applied shear force created by the movement of the upper plate. Competition between the applied shear force and pressure gradient is shown in curves (e) to (g) with maximum values of the fluid appearing near the top plate. The pressure gradient seems to be the dominant driving force for the fluid in curve (g) where the maximum value for the velocity occurs at the centre of the plates. The investigation is extended to larger values of $l$, namely, $l = 1, 3, 5, 7$ and 10 the same way as it is shown in § 3.3. The opposite is displayed in Fig. 4.18 for shear thickening fluids with $n = 2$. The dashed line curve corresponds to Equation (4.3.21), the sold line curve corresponds to Equation (4.3.58) and the dash dotted line to Equation (4.3.46) and (4.3.47). The Newtonian velocity profiles are much higher than the Carreau velocity profiles in curves (a) to (e). This shows that the Newtonian case has less resistance force to the flow as expected, and the fluid flows rapidly as the non−dimensional parameter $l$ decreases from 10 to 0.1. The figure shows that the numerical method gives a better approximation of the velocity profile, since it can be used for larger values of $l$. However, the asymptotics solution can be used as benchmark for the numerical method.

The temperature profiles are shown in Fig. 4.17 and the other parameters are fixed at $Br = 0.3, p_x = -1.5$ and $n = 0$. The dashed curves represent the solution in Equation (4.3.31), the solid lines represent the numerical solution in Equation (4.3.57) and the dash dotted lines represent Equation (4.3.41) and (4.3.42). The temperature profiles in set (b) with $l = 0.3$ show an excellent match in all three curves. The temperature profiles increase significantly as $l$ increases. The maximum values for the temperature profiles occur near the centre for values of $l > 3$ while for curves (a) to (c) their maximum temperature

occurs at the top plate. This shows that when $l$ increases, heat generated by the action of the pressure gradient and the applied shear force, is significantly higher and as a result the temperature profiles are more pronounced at the centre of the plates. In Fig. 4.18 the temperature profiles for the case where the power law index is greater than unity is shown. These curves are the exact opposite of those curves shown in Fig. 4.17 as displayed in Fig. 4.18. As the parameter $l$ decreases a significant increase in the fluid temperature is observed. This shows that when the parameter $l$ decreases, the fluid temperature rises rapidly due to heat generation by the internal flow proceses, and the combination of both the applied shear force and the pressure gradient act to increase heat in the plates.

The velocity profiles corresponding to different values of the power law indices are shown in Fig. 4.19 with $p_x = -1.5$. The maximum velocity for curve (a) occurs at the top plate, which shows the dominant force in driving the fluid is probably the applied shear force. For curves (b) to (g) it occurs near the top plate, which also shows that combination of the applied shear force and pressure gradient competes in driving the fluid. When $n < 1$ the resistance force to the flow decreases, the maximum velocity of the fluid occurs near the top plate. For $n > 1$, shear thickening fluids show that the more viscous the fluid, the more resistance force to the flow and the velocity of the fluid increases gradually as $n$ decreases. The temperature of the fluid is shown in Fig. 4.20 with $Br = 0.3$, $p_x = -1.5$ and $l = 0.3$. The temperature of the fluid increases as $n$ decreases, which shows that heat generation by the internal flow processes is higher when $n$ decreases.



### 4.3.2 Conclusion

In conclusion, the analytical and numerical methods were used to derive the velocity, the flow rate and temperature profiles. In the case of analytical methods three cases were investigated. In particular the situation where $l \ll 1$, and the power law indices $n = 0$ and $n = 2$ allowed for analytical progress. The asymptotic results show that

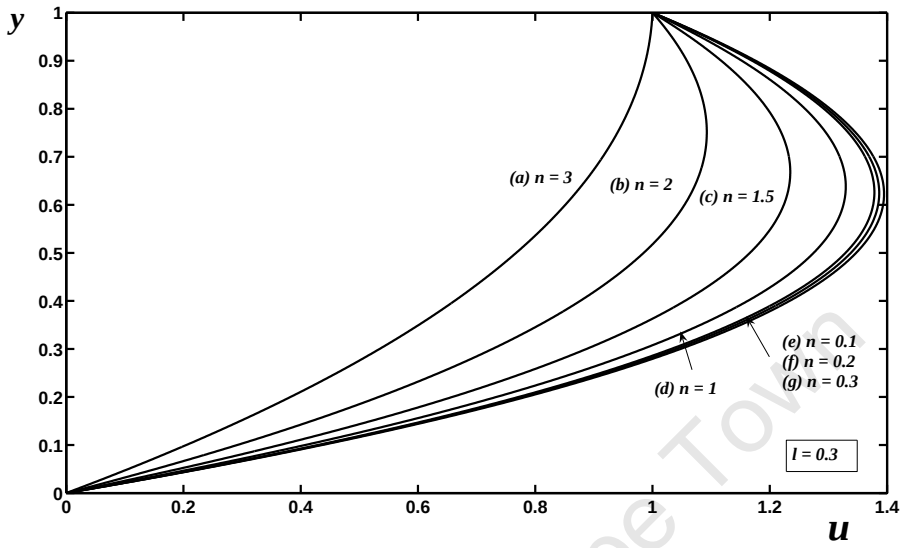


Figure 4.19: The velocity profiles for Equation (4.3.58) with different values of $n$: Boundary conditions (2.3.15) and (2.3.16).

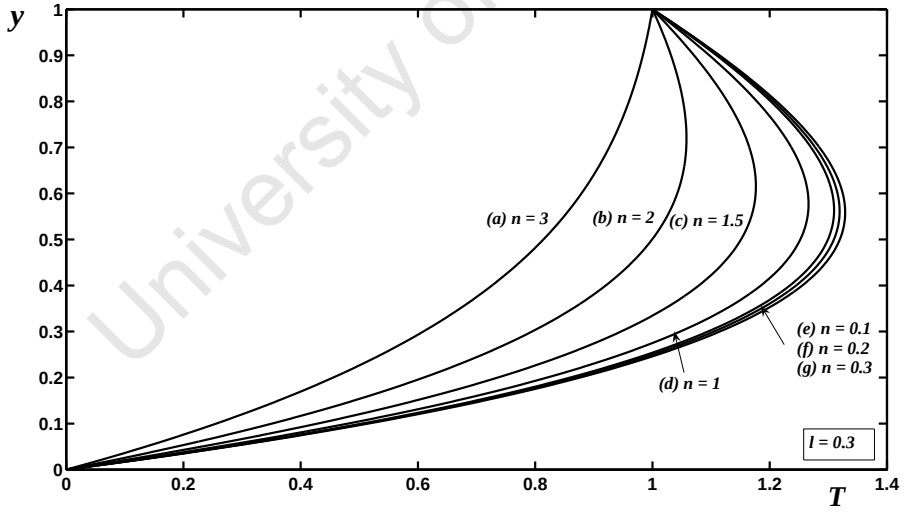


Figure 4.20: The temperature profiles for Equation (4.3.57) with different values of $n$: Boundary conditions ((2.3.15) and (2.3.16).

the velocity and temperature of the fluid increase with increasing values of $l$ for shear thinning fluids and their maximum velocities and temperatures occur at the top plate. The opposite is true for shear thickening fluids, where the fluid velocity and temperature increases when $l$ decreases. In the event where the power law index $n = 0$, the velocity and temperature of the fluid again increases slightly when $l$ increases. The importance of the power law index was also shown since the velocity and temperature profiles appear approximately 0.1% apart when $n = 0$. For the case where the power law index $n = 2$ an improvement of the gap between the velocity and temperature profiles was observed. The velocity and the temperature profiles derived from the analytical methods and the numerical methods were plotted on the same set of axes. The comparison for the three sets of curves showed a perfect match in particular for the resulting velocity and temperature profiles when $l = 0.3$. The effect of large values of $l$ on the resulting flow profiles were further investigated and the results show that the velocity and temperature of the fluid increase significantly as $l$ increases. The opposite is true for the case considered for the power law index greater than unity. The numerical method is preferable since the velocity and the temperature were found to increase significantly when $l$ increases for the case $n = 0$ and the opposite is true for the case $n = 2$. The power law index also shows that the velocity and temperature of the fluid increases as $n$ decreases. The numerical code showed results for the velocity and temperature of the fluids with decreasing values of $n$ which are significantly higher as compared to the analytical case where $l \ll 1$ is considered.



## 4.4 Ellis fluid

The aim of this section is to investigate non−Newtonian fluid flow between parallel plates where the viscosity is defined by the Ellis model. The viscosity model applied is,

$$\frac{1}{\mu} = 1 + \phi \left| \mu \frac{\partial u}{\partial y} \right|^{\alpha_1 - 1}, \tag{4.4.60}$$

where $\phi = (\mu_0 U/\tau_1 H)^{\alpha_1 - 1}$. Integrating Equation (2.3.9) with respect to $y$ gives,

$$\frac{\partial u}{\partial y} = \frac{1}{\mu} p_x \left(y - h_n\right) \ , \tag{4.4.61}$$

where $h_n$ is the value which gives $(\partial u/\partial y) = 0$. To take care of the modulus sign, we carry out a similar procedure as detailed in § 4.2 for a power law fluid. This leads to two cases, $y \leq h_n$ (which gives $(\partial u/\partial y) \geq 0$) and $y \geq h_n$ (which gives $(\partial u/\partial y) \leq 0$). Combining Equations (4.4.60), (4.4.61) and the case $y \leq h_n$, integrating with respect to $y$, and applying the boundary conditions (2.3.15) yields,

$$u_1 = -\frac{p_x}{2}\left({h_n}^2 - (h_n - y)^2\right) + \frac{\phi(-p_x)^{\alpha_1}}{(\alpha_1 + 1)}\left[h_n^{\alpha_1+1} - (h_n - y)^{\alpha_1+1}\right], \tag{4.4.62}$$

provided $\alpha_1 \neq -1$, since the second term in Equation (4.4.62) becomes undefined. For $y \geq h_n$ the velocity profile is now given by,

$$\begin{aligned} u_2 &= \frac{p_x}{2}\Big((y - h_n)^2 - (1 - h_n)^2\Big) \\ &+ \frac{\phi(-p_x)^{\alpha_1}}{(\alpha_1 + 1)}\left[(y - h_n)^{\alpha_1+1} - (1 - h_n)^{\alpha_1+1}\right] + 1 \ . \end{aligned} \tag{4.4.63}$$

Similar expressions for Equations (4.4.62) and (4.4.63) may be found in [76]. Continuity conditions for the velocity, $u_1 = u_2$ at $y = h_n$, determines $h_n$ as,

$$u(h_n) = \frac{p_x}{2}\left({h_n}^2 - (1 - h_n)^2\right) + \frac{\phi(-p_x)^{\alpha_1}}{(\alpha_1 + 1)}\left(h_n^{\alpha_1+1} - (1 - h_n)^{\alpha_1+1}\right) + 1 \ . \tag{4.4.64}$$

Equation (4.4.64) is solved numerically for $h_m$. The flux between the plates is given by $Q = Q_1 + Q_2$ where,

$$Q_1 = \int_0^{h_m} u dy = -\frac{p_x}{3}{h_n}^3 + \frac{\phi\ (-p_x)^{\alpha_1}}{(\alpha_1 + 1)(\alpha_1 + 2)}\ {h_n}^{\alpha_1+2} \ , \tag{4.4.65}$$

and,

$$\begin{aligned} Q_2 &= \int_{h_m}^{1} u dy \\ &= \frac{p_x(1 - h_n)^2}{6}\left((1 - h_n) - 3(1 + h_n)\right) \\ &+ \frac{\phi\ (-p_x)^{\alpha_1}(1 - h_n)^{\alpha_1+1}}{(\alpha_1 + 1)(\alpha_1 + 2)}\left((1 - h_n) - (\alpha_1 + 1)(1 + h_n)\right) + (1 - h_n) \ . \end{aligned} \tag{4.4.66}$$

Adding Equations (4.4.65) and (4.4.66) we obtain the expression for the flux in terms of the pressure gradient,

$$\begin{aligned} Q &= -\frac{p_x}{3}{h_n}^3 + \frac{p_x(1-h_n)^2}{6}\left((1-h_n)-3(1+h_n)\right) \\ &\quad + \frac{\phi\ (-p_x)^{\alpha_1}(1-h_n)^{\alpha_1+1}}{(\alpha_1+1)(\alpha_1+2)}\left({h_n}^{\alpha_1+2}+(1-h_n)-(\alpha_1+1)(1+h_n)\right) \\ &\quad +(1-h_n)\ . \end{aligned} \tag{4.4.67}$$

Equation (4.4.67) provide the solution for the flow rate which is constant. The temperature profile for the case $y \leq h_n$ is derived by combining Equations (2.3.11) and (4.4.60) to give,

$$\frac{\partial^2 T_1}{\partial y^2} = -Br\left[{p_x}^2\left(h_n-y\right)^2 + \phi\ \left(p_x\right)^{\alpha_1+1}\left(h_n-y\right)^{\alpha_1+1}\right]\ . \tag{4.4.68}$$

Integrating Equation (4.4.68) twice with respect to $y$, applying the boundary conditions (2.3.15) and the condition $\partial T_1/\partial y = 0$ at $y = h_{T3}$, yields,

$$\begin{aligned} T_1 &= -\frac{Br{p_x}^2}{12}\left(\left(h_n-y\right)^4-{h_n}^4\right) - \frac{Br{p_x}^2}{3}\left(h_n-h_{T3}\right)^3 y \\ &\quad -\frac{Br\phi(-p_x)^{\alpha_1+1}}{(\alpha_1+2)(\alpha_1+3)}\left[\left(h_n-y\right)^{\alpha_1+3}-{h_n}^{\alpha_1+3}\right] \\ &\quad -\frac{Br\phi(-p_x)^{\alpha_1+1}}{(\alpha_1+2)}\left[\left(h_n-h_{T3}\right)^{\alpha_1+2}y\right]\ . \end{aligned} \tag{4.4.69}$$

For $y \geq h_n$, Equations (2.3.11) and (4.4.60) are combined to give,

$$\frac{\partial^2 T_2}{\partial y^2} = -Br\left[{p_x}^2\left(y-h_n\right)^2 + \phi(-p_x)^{\alpha_1+1}\left(y-h_n\right)^{\alpha_1+1}\right]\ . \tag{4.4.70}$$

Integrating Equation (4.4.70) twice with respect to $y$, applying the boundary conditions (2.3.16) and the condition $\partial T_2/\partial y = 0$ at $y = h_{T3}$, yields,

$$\begin{aligned} T_2 &= -\frac{Br{p_x}^2}{12}\left[\left[\left(y-h_n\right)^4-\left(1-h_n\right)^4\right]-4\left(h_{T3}-h_n\right)^3\left(1-y\right)\right] \\ &\quad -\frac{Br\phi(-p_x)^{\alpha_1+1}}{(\alpha_1+2)(\alpha_1+3)}\left[\left[\left(y-h_n\right)^{(\alpha_1+4)}-\left(1-h_n\right)^{(\alpha_1+3)}\right]\right. \\ &\quad \left.-(\alpha_1+3)\left(h_{T3}-h_n\right)^{(\alpha_1+3)}\left(1-y\right)\right]+1\ . \end{aligned} \tag{4.4.71}$$

The continuity condition is obtained when $T_1 = T_2$ at $y = h_{T3}$ which gives,

$$\begin{aligned} T(h_{T3}) &= -\frac{Brp_x{}^2}{12}\left((h_n - h_{T3})^4 - h_n{}^4\right) - \frac{Brp_x{}^2}{3}(h_n - h_{T3})^3 h_{T3} \\ &\quad -\frac{Br\phi(-p_x)^{\alpha_1+1}}{(\alpha_1+2)(\alpha_1+3)}\left[(h_n - h_{T3})^{\alpha_1+3} - h_n{}^{\alpha_1+3}\right] \\ &\quad -\frac{Br\phi(-p_x)^{\alpha_1+1}}{(\alpha_1+2)}\left[(h_n - h_{T3})^{\alpha_1+2} y_T\right] \\ &= -\frac{Brp_x{}^2}{12}\left[\left[(h_{T3} - h_n)^4 - (1-h_n)^4\right] - 4(h_{T3} - h_n)^3(1 - h_{T3})\right] \\ &\quad -\frac{Br\phi(-p_x)^{\alpha_1+1}}{(\alpha_1+2)(\alpha_1+3)}\left[\left[(h_{T3} - h_n)^{(\alpha_1+4)} - (1-h_n)^{(\alpha_1+3)}\right]\right. \\ &\quad \left. -(\alpha_1+3)(h_{T3} - h_n)^{(\alpha_1+3)}(1 - h_{T3})\right] + 1\ . \end{aligned} \tag{4.4.72}$$

The constant $h_{T3}$ is obtained by substituting Equation (4.4.64) into (4.4.72) and solving the coupled equations numerically. Equations (4.4.69) and (4.4.71) provide the solution for the temperature profile.

Our presentation of results is organised as follows: firstly, we investigate the effect of the parameter $\phi$ on the resulting flow profiles and secondly we investigate the effect of the power law index $\alpha_1$. A similar procedure as detailed in § 3.4 is now followed.

Fig. 4.21 with $\alpha_1 = 0.5$ and Fig. 4.22 with $\alpha_1 = 2.073$ shows the effect of progressively increasing $\phi$, namely, $\phi = 0, 0.1, 0.3, 1, 1.5, 2$ and 3.59 and other parameters are fixed at $K = 1$ and $p_x = -1.5$. Increasing values of $\phi$ indicates an increase in the fluid viscosity as displayed in Fig. 3.29. The velocity profiles represent the solutions in Equations (4.4.62) and (4.4.63). Curves (a) in both figures represent a Newtonian velocity profile with $\phi = 0$ and the velocity of the fluid increases across the plates to its maximum at the top plate. In Fig. 4.21 curves (b) and (c) the fluid velocities are increasing to their maximum velocities which occurs at the top plate. This implies that the most probable driving force for the flow in curves (a) to (c) is the applied shear force. In curves (d) through to (g) the maximum velocity in each curve occurs near the top plate and due to the boundary conditions the fluid velocity decreases to $u = 1$ at $y = 1$ at the top plate.

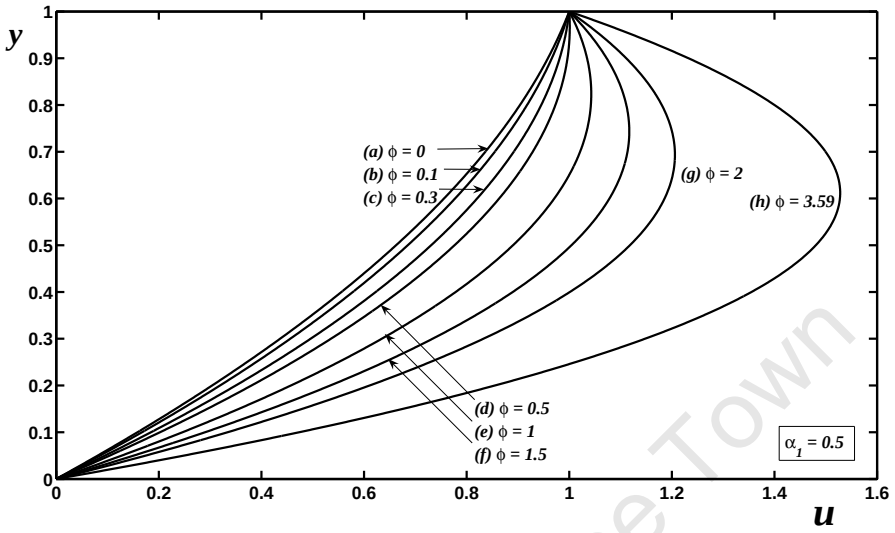


Figure 4.21: The velocity profiles for Equations (4.4.62) and (4.4.63) with $\alpha_1 = 0.5$: Boundary conditions (2.3.15) and (2.3.16).

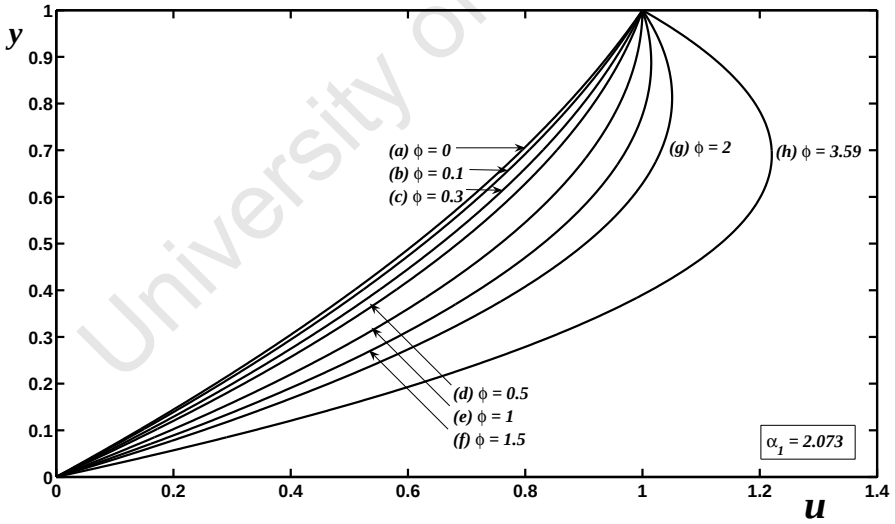


Figure 4.22: The velocity profiles for Equations (4.4.62) and (4.4.63) with $\alpha_1 = 2.073$: Boundary conditions (2.3.15) and (2.3.16).

These curves illustrate that the most probable dominant force in driving the fluid is the applied shear force competing with the pressure gradient. The Ellis fluid velocity profiles are much greater than the Newtonian velocity profile and when the values of $\phi$ increases the velocity of the fluid is greater. A similar trend of the velocity profiles is observed in Fig. 4.22 with $\alpha_1 = 2.073$ for a hydroxylethycellulose fluid. Since the fluid shows a degree of shear thickening, the velocity profiles are less pronounced as compared to the ones in Fig 4.21.

In Figs. 4.23 and 4.24 the corresponding temperature profiles representing Equations (4.4.69) and (4.4.71) are displayed. The other parameters are similar to those given in Fig 4.22 and $Br = 0.3$. The Newtonian temperature profile is retrieved in curves (a) of both figures and again the fluid temperature increases until its maximum at the top plate for curves (a) to (d). In Fig. 4.23 when $\phi$ increases, the temperature of the fluid increases significantly, and the maximum values of the temperature occur towards the centre of the plates. The maximum value for curve (g) and (h) occurs at the centre of the plates. This is due to the heat generation by the internal flow processes, which is higher towards the centre of the plate when $\phi$ is large. However, maximum temperatures in Fig. 4.24 are less pronounced and the two figures illustrate that shear thinning fluids heat up quickly compared to the hydroxylethycellulose fluid.

Eight curves representing the velocity profile in Equations (4.4.62) and (4.4.63) with different values of $0 \leq \alpha_1 \leq 3$ are shown in Fig. 4.25 with $p_x = -1.5$ and $\phi = 0.3$. Curves (a) to (c) show a shear thinning behaviour and since the viscosity of the fluid decreases as $\alpha_1$ increases, the resistance force to the flow decreases and the fluid velocity increases to its maximum at the top plate. The Newtonian case is retrieved in curve (d) with the power law index $\alpha_1 = 1$. Curves (e) through to (g) show the velocity profile with $\alpha_1 = 1.5, 2$ and 3 respectively. The velocity of the fluid increases significantly in the direction of the flow when $\alpha_1$ increases. In this case, the viscosity of the fluid increases as $\alpha_1$ increases and the curves illustrate that the velocity of the fluid flows faster when

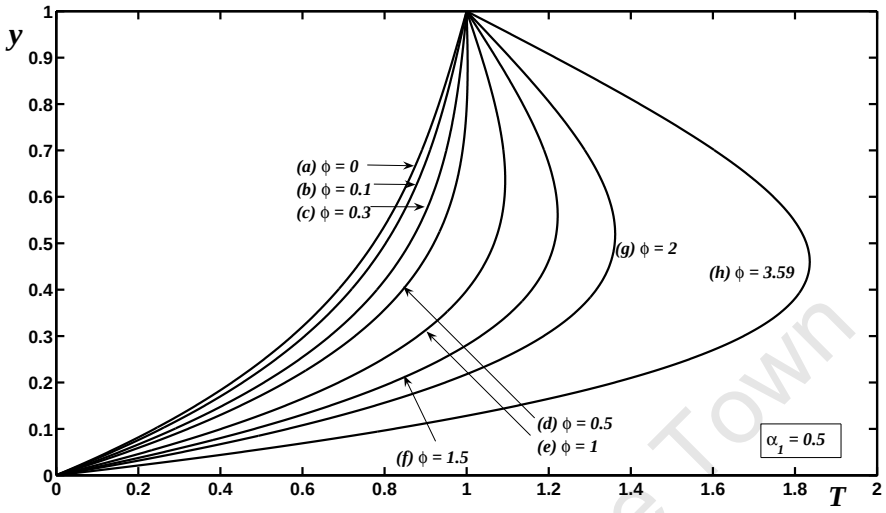


Figure 4.23: The temperature profiles for Equations (4.4.69) and (4.4.71) with $\alpha_1 = 0.5$: Boundary conditions (2.3.15) and (2.3.16).

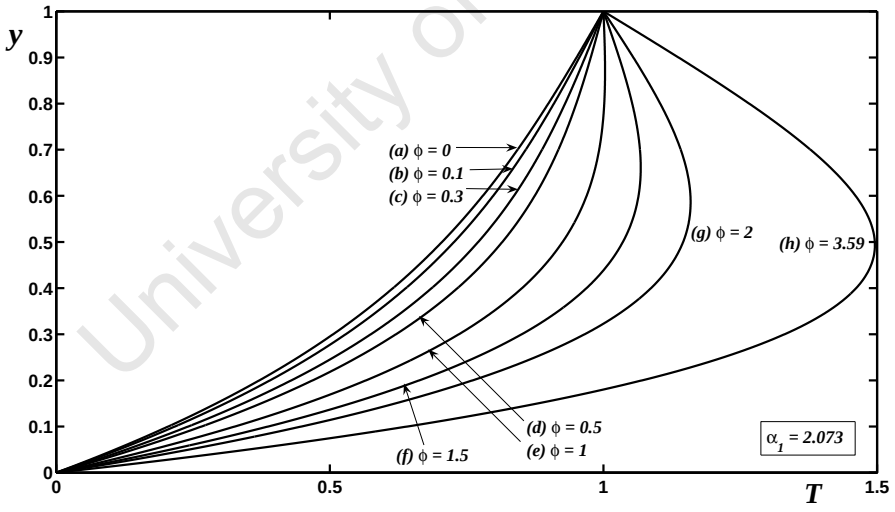


Figure 4.24: The temperature profiles for Equations (4.4.69) and (4.4.71) with $\alpha_1 = 2.073$: Boundary conditions (2.3.15) and (2.3.16).

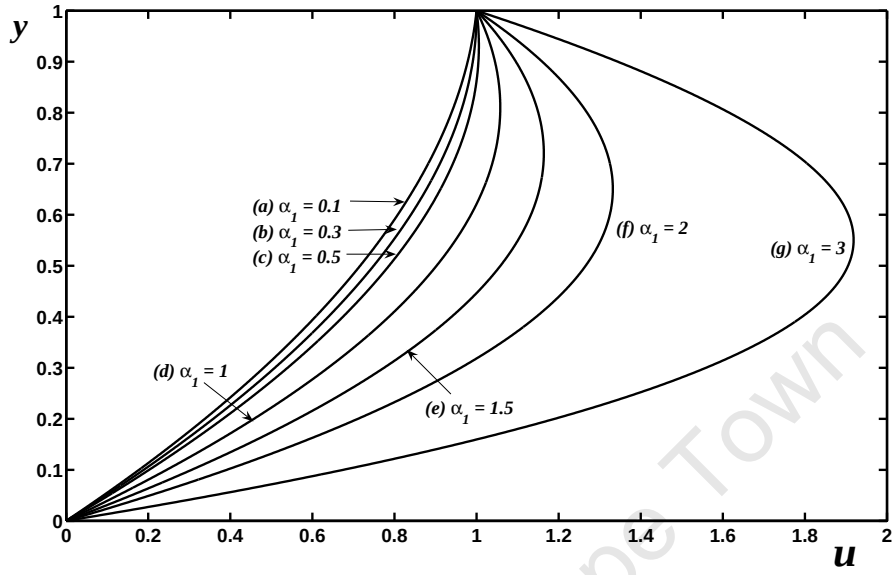


Figure 4.25: The velocity profiles for Equations (4.4.62) and (4.4.63) with various values of $\phi$: Boundary conditions (2.3.15) and (2.3.16).

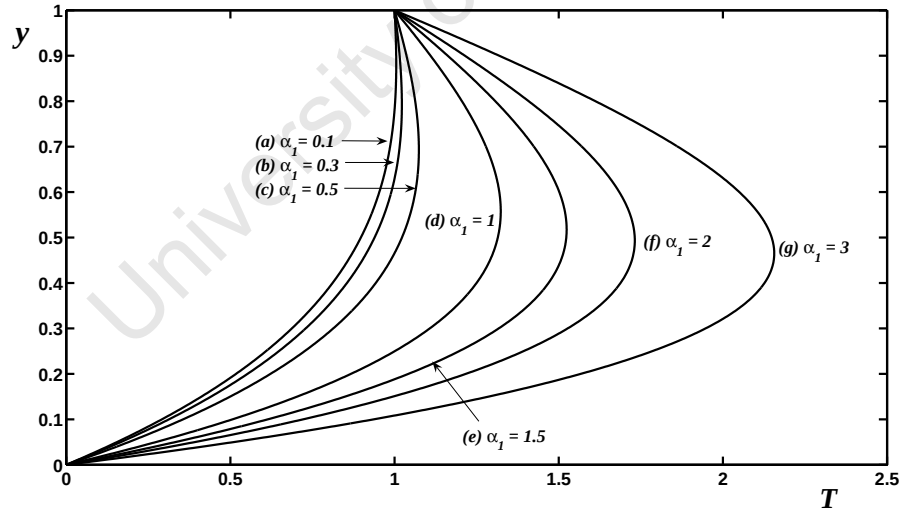


Figure 4.26: The temperature profiles for Equations (4.4.69) and (4.4.71) with various values of $\phi$: Boundary conditions (2.3.15) and (2.3.16).

$\alpha_1$ becomes increasingly large. This shows that the dominant driving force for the fluid is significantly higher when $\alpha$ is large, and the more viscous the fluid, the higher the velocity profiles.

Fig 4.26 shows eight temperature profiles corresponding to the solutions of Equations (4.4.69) and (4.4.71). The other flow controlling parameters are $Br = 0.3$, $\phi = 0.3$ and $p_x = -1.5$. Curves (a) to (c) show the effect of the power law index $\alpha_1 < 1$. These curves increase gradually as $\alpha_1$ increases, which shows that for shear thinning fluids heat generation by action of the both the applied shear force and the pressure gradient raises the fluid temperature. A Newtonian temperature profile is shown in curve (d) again with $\alpha_1 = 1$ which increases to its maximum near the centre of the plates and decreases to the top plate due to the boundary conditions. Curves (e) through to (g) display values $\alpha_1 > 1$ and the temperature of the fluid increase significantly as $\alpha_1$ increases. These curves show that shear thickening fluids responds quickly to heat generation, which is more pronounced towards the centre of the plates, due to the competition between the applied shear force and the pressure gradient which act to generate heat in the plates.



### 4.4.1 Conclusion

In conclusion, the effect of parameters $\phi$ and $\alpha_1$ on the resulting flow profiles were investigated. The velocity and temperature of the fluid increases when $\phi$ increases. The maximum fluid velocity occurs near the top plate for large values of $\phi$ while the maximum temperature of the fluid occurs near the centre of the plates. The maximum fluid velocity for shear thinning fluids is much higher than for shear thickening fluids. This is a result of the applied shear force by the movement of the top plate which seems to dominate the flow when both parameters are large, and for the temperature profiles heat generated by the internal flow processes is high near the centre of the plates. The effect of the power law index $\alpha_1$ on the velocity and temperature profiles showed that the velocity of the fluid

increases significantly for $\alpha_1 > 1$ and the maximum velocities again occur near the top plate. The maximum temperature of the fluid occurs near the centre and the temperature becomes increasingly large when $\alpha_1 > 1$ which shows that shear thickening fluids respond quickly to heat generation as $\alpha_1$ increases.

# Chapter 5

# The temperature dependent viscosity model

## 5.1 Introduction

In Chapter 1, we highlighted that one of the important physical properties which affect viscosity in a typical industrial application is the temperature. This provided our motivation to include the heat equation in our study. Therefore in this chapter, we will focus on the temperature dependent variable viscosity model for flow both with a free surface and flow between parallel plates. The focus is on the effect of temperature on the fluid viscosity. In particular, we investigate the effect of the viscosity model, which assumes that the viscosity decreases exponentially with temperature on the resulting film profiles.

In § 5.2, we will derive the governing equations resulting from the viscosity model for flow with a free surface. The driving force for the flow is assumed to be the gravitational force. In general, the flow equation resulting from this model cannot be solved analytically. However, the model is analysed using an asymptotic technique, when the viscosity variation is gradual and a full solution is obtained using the Runge−Kutta numerical method.

In § 5.3, the flow between parallel plates is investigated. The driving forces for the fluid are considered to be those of the applied shear force caused by the movement of the upper

plate and the pressure gradient. In this section we take advantage of the fact that when the pressure gradient is neglected, some degree of analytical progress is possible for the shear driven case. Finally, we will obtain the full solution of the governing equations using the Runge−Kutta numerical method.

## 5.2 Free surface flow

This work has been summarised in the paper by Tshehla and Myers, see [110]. The viscosity model in Equation (1.4.5), may be written in non−dimensional form as,

$$\mu = e^{-\alpha T} \ , \tag{5.2.1}$$

where $\alpha = \theta \Delta T$. Equation (5.2.1) is commonly known as Nahme's exponential law [24] or Reynolds' law [77]. Combining Equations (5.2.1) and (2.3.9), integrating with respect to $y$, and applying the boundary conditions (2.3.12) give the velocity gradient,

$$\frac{\partial u}{\partial y} = (h - y) e^{\alpha T} \ . \tag{5.2.2}$$

Equation (5.2.2) cannot be integrated further to determine $u$, since it involves the temperature $T$ which is unknown. Substituting Equations (5.2.1) and (5.2.2) into the reduced energy Equation (2.3.11) gives,

$$\frac{\partial^2 T}{\partial y^2} = -Br \left(h - y\right)^2 e^{\alpha T} \ . \tag{5.2.3}$$

As it stands we cannot make analytical progress in Equation (5.2.3). Therefore, Equations (5.2.2) and (5.2.3) form a coupled system of non−linear partial differential equations which requires a numerical technique to obtain a full solution. However, when the viscosity variation is gradual, that is, $\alpha \ll 1$ and $T \sim \mathcal{O}(1)$, an asymptotic analysis is possible. The question is, how small must the parameter $\alpha$ be? Therefore, the key factor in determining the stage at which $\alpha$ is small, is the magnitude of $\Delta T$, and $\theta$ is the fluid property. In certain industrial applications for lubricating oil, the experimental values for the temperature may

be confined in the region $-50°\text{C} \leq \text{T} \leq 300°\text{C}$, see [9, 95, 115]. Our interest is on large values $\Delta T$, since $\alpha \sim \theta\Delta T$ and typically the fluid property $\theta$ for lubricating oil is less than unity [51]. Now taking the temperature difference $\Delta T \sim 200°\text{C}$ and $\theta \sim 0.00242$, see [54] p. 31, it can easily be shown that $\alpha \sim 0.5$ for a lubricating oil. It is important to note that for different values of $\theta$ and $\Delta T$, the results will obviously yield a different value of $\alpha$, depending on the fluid under investigation. The velocity and temperature may then be expanded in a series form,

$$u = u_0 + \alpha u_1 \ , \tag{5.2.4}$$

$$T = T_0 + \alpha T_1 \ , \tag{5.2.5}$$

where $u_0$, $T_0$, $u_1$ and $T_1$ represent the leading order terms and the first order perturbation terms in $\alpha$. Substituting for $T$ into Equation (5.2.3) yields,

$$\frac{\partial^2 T_0}{\partial y^2} + \alpha \frac{\partial^2 T_1}{\partial y^2} = -Br\,(h-y)^2 - \alpha T_0 Br\,(h-y)^2 \ . \tag{5.2.6}$$

The leading order and $\mathcal{O}(\alpha)$ terms from Equation (5.2.6) are,

$$\frac{\partial^2 T_0}{\partial y^2} = -Br(h-y)^2 \ , \tag{5.2.7}$$

$$\frac{\partial^2 T_1}{\partial y^2} = -BrT_0(h-y)^2 \ . \tag{5.2.8}$$

Integrating Equation (5.2.7) with respect to $y$ and applying the boundary conditions (2.3.13) yields,

$$T_0 = \frac{Br}{12}\left[h^4\left(1 - \frac{Bi}{(Bi\ h-1)}y\right) - (h-y)^4\right] + \left(\frac{Bi}{(Bi\ h-1)}\right)y \ . \tag{5.2.9}$$

The corresponding boundary conditions for $T_1$ are,

$$T_1 = 0 \qquad \text{at} \quad y = 0 \ , \qquad \left(\frac{\partial T_1}{\partial y}\right)\bigg|_{y=h} = Bi\ T_1 \ . \tag{5.2.10}$$

Combining Equations (5.2.8) and (5.2.9), integrating with respect to $y$, applying the boundary conditions (5.2.10) yields,

$$\begin{aligned} T_1 &= \frac{Br^2}{12}\left[\frac{1}{56}(h-y)^8 - \frac{1}{60}\left(5(h-y)^4 + \frac{h^4\ Bi}{(Bi\ h-1)}(10y^3h^2 - 10y^4h + 3y^5)\right)\right] \\ &+\frac{Br^2}{12}\left[\frac{Bi}{(Bi\ h-1)}\left(\frac{h^8}{12(Bi\ h-1)} - \frac{h^9\ Bi}{20(Bi\ h-1)}\right)y + \frac{11h^8}{168}\right] \\ &+\frac{Bi}{(Bi\ h-1)}\Big(10y^3h^2 - 10y^4h + 3y^5\Big) + \frac{Bi}{(Bi\ h-1)^2}\left(\frac{h^8}{12} - \frac{h^9\ Bi}{20}\right)y \ . \end{aligned} \tag{5.2.11}$$

The final temperature profile is obtained by combining both Equations (5.2.9) and (5.2.11) to give,

$$\begin{aligned} T = &-\frac{Br}{12}\left[(h-y)^4 - h^4\left(1 - \frac{Bi}{(Bi\ h-1)}y\right)\right] + \left(\frac{Bi}{(Bi\ h-1)}\right)y \\ &+\frac{\alpha Br^2}{12}\left[\frac{1}{56}(h-y)^8 - \frac{h^4}{12}(h-y)^4 + \frac{Bi\ h^4}{12(Bi\ h-1)}\big(8(h-y)^3\right. \\ &\left.-y(h-y)^4\big)\right] + \frac{Bi\ Br}{48(Bi\ h-1)}\Big[4(h-y)^3 - y(h-y)^4\Big] \\ &+\frac{\alpha Br^2}{12}\left[\frac{1}{56}(h-y)^8 - \frac{1}{60}\left(5(h-y)^4 + \frac{h^4\ Bi}{(Bi\ h-1)}(10y^3h^2 - 10y^4h + 3y^5)\right)\right] \\ &+\frac{\alpha Br^2}{12}\left[\frac{Bi}{(Bi\ h-1)}\left(\frac{h^8}{12(Bi\ h-1)} - \frac{h^9\ Bi}{20(Bi\ h-1)}\right)y + \frac{11h^8}{168}\right] \\ &+\frac{\alpha Bi}{(Bi\ h-1)}\Big(10y^3h^2 - 10y^4h + 3y^5\Big) + \frac{\alpha Bi}{(Bi\ h-1)^2}\left(\frac{h^8}{12} - \frac{h^9\ Bi}{20}\right)y \ . \end{aligned} \tag{5.2.12}$$

Equation (5.2.12) provides the solution for the temperature profile when $\alpha \ll 1$. Similarly, a solution for the velocity profile can be derived. Combining Equations (5.2.2) and (5.2.4) gives,

$$\frac{\partial u_0}{\partial y} + \alpha\frac{\partial u_1}{\partial y} = (h-y) + \alpha T_0(h-y) \ . \tag{5.2.13}$$

The leading order and $\mathcal{O}(\alpha)$ terms are therefore,

$$\frac{\partial u_0}{\partial y} = (h-y) \ , \tag{5.2.14}$$

$$\frac{\partial u_1}{\partial y} = T_0(h-y) \ . \tag{5.2.15}$$

Equation (5.2.14) gives the Newtonian velocity profile. To obtain $u_1$, Equations (5.2.9) and (5.2.15) are combined to give,

$$\begin{aligned}\frac{\partial u_1}{\partial y} &= -\frac{Br}{12}\left[(h-y)^5 - h^4(h-y) + \frac{Bi\ h^4}{(Bi\ h-1)}y\Big(h-y\Big)\right] \\ &\quad + \frac{Bi}{(Bi\ h-1)}y\Big(h-y\Big)\ . \end{aligned} \tag{5.2.16}$$

Integrating Equation (5.2.16) with respect to $y$ and applying the boundary condition $u_1(0) = 0$, leads to,

$$\begin{aligned}u_1 &= \frac{Br}{72}\left[(h-y)^6 - 6\left(\frac{yh^4}{2}(2h-y) - \frac{Bi\ y^2}{6(Bi\ h-1)}(3h-2y)\right) - h^6\right] \\ &\quad + \frac{Bi\ y^2}{6(Bi\ h-1)}\Big(3h-2y\Big)\ . \end{aligned} \tag{5.2.17}$$

The Newtonian velocity profile for Equations (2.4.18) and (5.2.17) are combined to give the final velocity profile as,

$$\begin{aligned}u &= \frac{y}{2}\Big(2h-y\Big) + \frac{\alpha\ Br}{72}\left[(h-y)^6 - 6\left(\frac{yh^4}{2}(2h-y) - \frac{Bi\ y^2}{6(Bi\ h-1)}(3h-2y)\right) - h^6\right] \\ &\quad + \frac{Bi\ y^2}{6(Bi\ h-1)}\Big(3h-2y\Big)\ . \end{aligned} \tag{5.2.18}$$

Equation (5.2.18) provides the solution for the velocity profile. The flux is given by integrating Equation (5.2.18) from 0 to $h$,

$$Q = \int_0^h u dy = \frac{h^3}{3} + \frac{19\alpha\ Brh^7}{14}\ . \tag{5.2.19}$$

Equation (5.2.19) gives the solution of the flow rate. The analytical solution obtained using the asymptotic technique will be compared with the numerical solution in § 5.2.1. This comparison is vital for validating our numerical solution that will be developed using the Runge−Kutta method. The results for the temperature, velocity and the flux are discussed including the viscosity variation with temperature.

Fig. 5.1 displays the viscosity variation versus the temperature and Fig. 5.2 shows the flow rate. The temperature of the fluid is considered in the region 0°C ≤ T ≤ 70°C. In

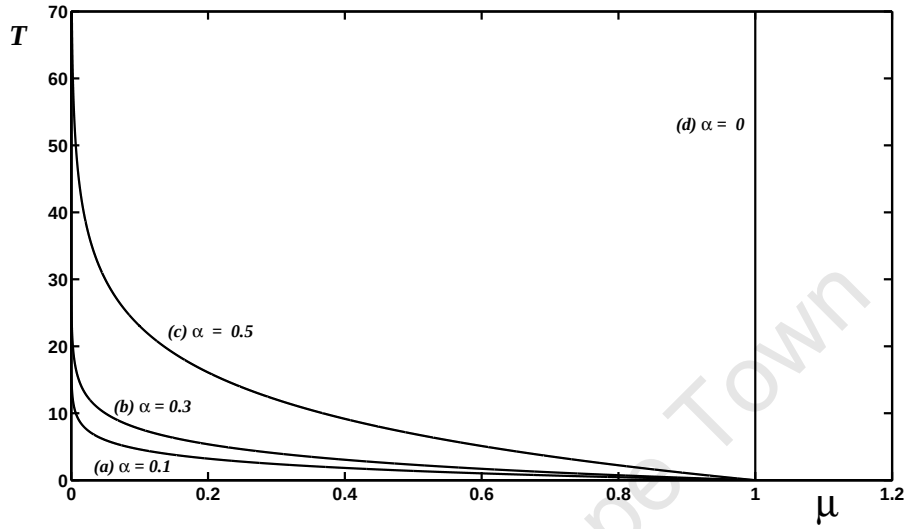


Figure 5.1: The viscosity versus temperature for Equation (5.2.1).

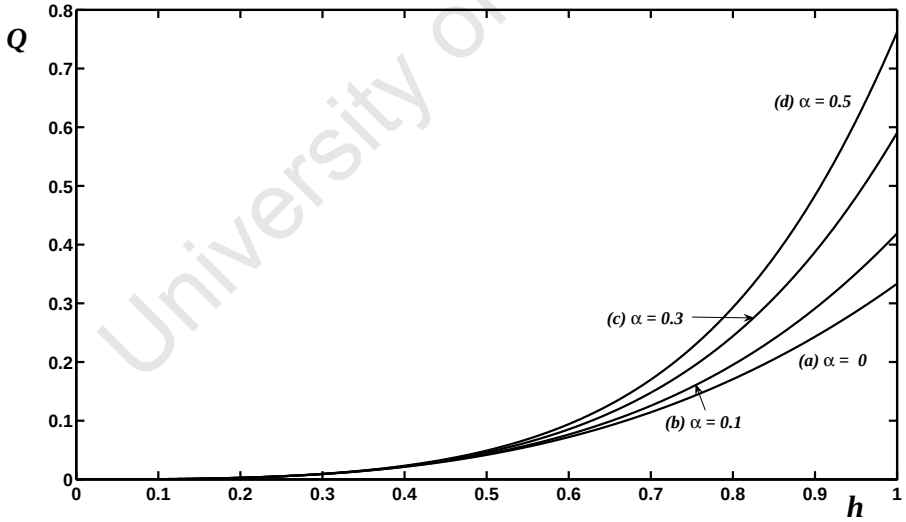


Figure 5.2: The flow rate for Equation (5.2.19).

Fig. 5.1, the Newtonian case is retrieved in curve (d), which is constant. It is clearly shown in the figure that when $\alpha$ increases from 0.1 to 0.5, the viscosity decreases exponentially when the fluid temperature increases. This figure shows that the viscosity is sensitive to temperature and confirms the definition of viscosity dependence on temperature, which states that the viscosity of fluids decreases with increasing temperature [61]. Fig. 5.2 displays the flow rate with different values of $\alpha$. When $\alpha$ increases from 0 to 0.5, the flux increases in the layer and the flow rate is higher.

Fig. 5.3 shows the temperature profiles corresponding to Equation (5.2.12). The results are calculated for the case $Bi = Br = 0.3$, so that the Biot and the Brinkman numbers are of the same magnitude. Different values of $\alpha$ were considered in order to investigate its effect on resulting flow profiles. We start our investigation with a simple case where $\alpha = 0$ for a Newtonian fluid to a maximum of $\alpha = 0.5$ for a lubricating oil. Curves (a), (b), (c) and (d) display four different values of $\alpha$. When $\alpha$ increases, the temperature of the fluid increases due to heat generation by the internal friction caused by the collision of the fluid particles. The Newtonian case is retrieved in curve (a) with $\alpha = 0$. In Fig. 5.4, four curves representing the velocity profiles for Equation (5.2.17) are plotted. These profiles correspond to different values of $\alpha$ as shown in Fig. 5.3. The figure shows that the velocity of the fluid increases when $\alpha$ increases. This is a result of the resistance force to the flow which decreases as $\alpha$ increases. Curve (a) displays a Newtonian velocity profile with $\alpha = 0$, and the fluid velocity increases across the fluid layer to the maximum point at the top, due to the effect of the gravitational forces and lack of resistance force to the flow.



### 5.2.1 The Runge−Kutta numerical scheme

The coupled non−linear partial differential Equations (5.2.2) and (5.2.3) for the velocity and the temperature profiles are solved numerically using the fourth order Runge−Kutta

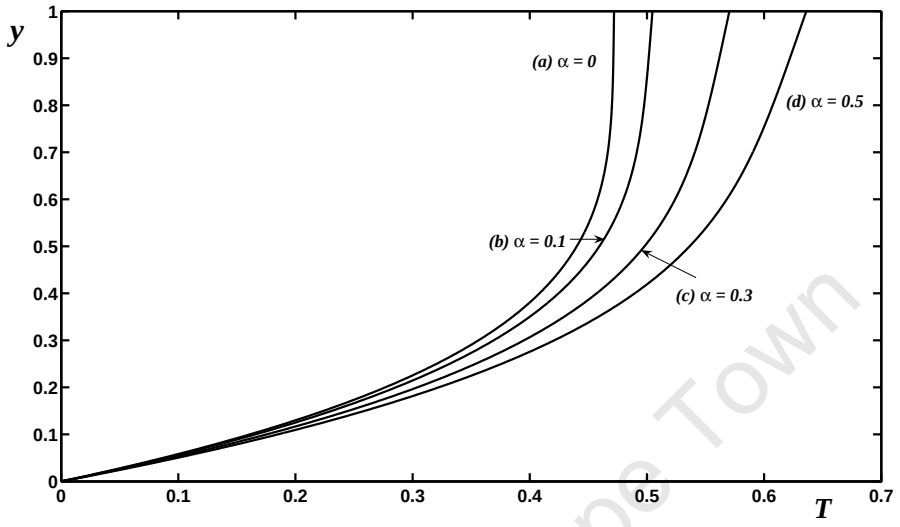


Figure 5.3: The temperature profiles for Equation (5.2.12): Boundary conditions (2.3.13).

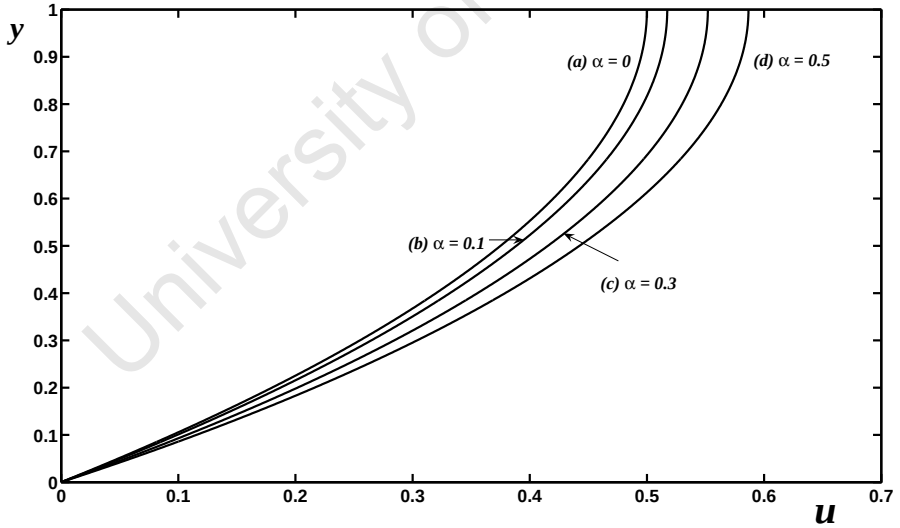


Figure 5.4: The velocity profiles for Equation (5.2.18): Boundary conditions (2.3.12).

integration scheme. The temperature profile must be calculated first and then substituted into the velocity equation to obtain the solution for the velocity profile. Setting $t_1 = T$ and $t_2 = \partial T/\partial y$, Equation (5.2.3) can be written as a system of two first order equations in $t_1$ and $t_2$ of the form,

$$\frac{\partial}{\partial y}\begin{bmatrix} t_1 \\ t_2 \end{bmatrix} = \begin{bmatrix} t_2 \\ -Br\,(h-y)^2\, e^{\alpha t_1} \end{bmatrix} . \tag{5.2.20}$$

This system can be written in vector form,

$$\frac{\partial \mathbf{t}}{\partial y} = F(\mathbf{t}, y) , \tag{5.2.21}$$

where $\mathbf{t} = (t_1, t_2)$. The solutions for this system of differential equations are obtained subject to two point boundary conditions (2.3.12) and (2.3.13). The Runge−Kutta method requires an initial value, and the initial value for the temperature $t_1$ is taken as the boundary condition at $y = 0$. The corresponding initial value for $t_2$ is randomly chosen. It is important to note that the best numerical results largely depend on a good guess for the initial condition, see [29, 30]. Once these initial values are chosen we employ the Runge−Kutta method to solve for the temperature. When the iterative process for the Runge−Kutta scheme terminates, the derivative for the temperature $t_2$ at the free surface is eventually corrected using the given boundary conditions (2.3.13). The set of parameters $\alpha$, $Bi$ and $Br$ are coupled to the system of differential equations and we solve our equations using a small step size for $\Delta y$. The velocity gradient is given by,

$$\frac{\partial u}{\partial y} = (h-y)e^{\alpha t_1} . \tag{5.2.22}$$

Once the temperature profile is calculated, the velocity profile is computed from Equation (5.2.22) using the finite difference scheme,

$$u_{n+1} = u_n + \Delta u_y . \left(\frac{\partial u}{\partial y}\right)\Bigg|_{(y_i,t_i)} . \tag{5.2.23}$$

The results for the asymptotic and numerical methods are now discussed.

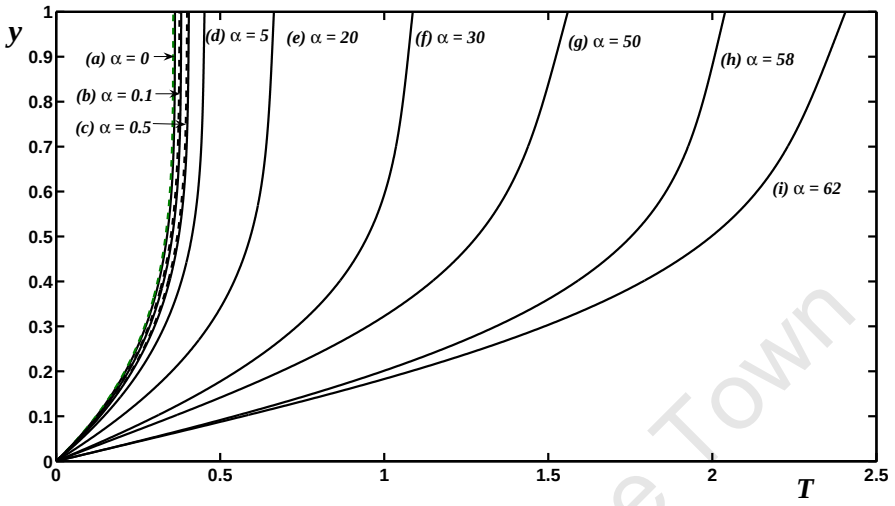


Figure 5.5: The temperature profiles for Equations (5.2.12) and (5.2.20): Boundary conditions (2.3.13).

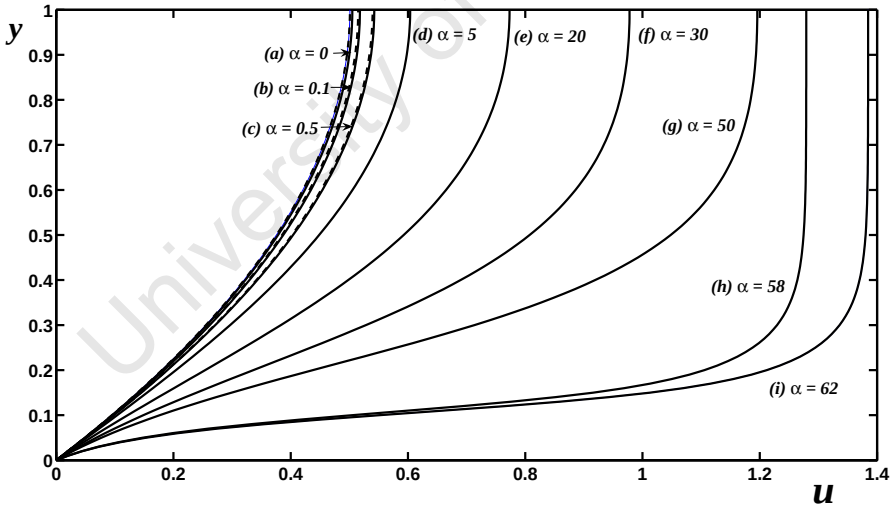


Figure 5.6: The velocity profiles for Equation (5.2.18) and (5.2.22): Boundary conditions (2.3.12).

We now proceed with our analysis for the comparison of the asymptotic and numerical solutions given in Equations (5.2.12) and (5.2.20) for the temperature profiles and in Equations (5.2.18) and (5.2.22) for the velocity profiles. We begin our investigation with the Newtonian case when $\alpha = 0$ for the asymptotic and numerical solutions. In Figs. 5.5 and 5.6 the temperature and velocity profiles are plotted, and in each figure, the dotted lines represent the profiles from the asymptotic solution and solid lines for the numerical solution. For the sake of visibility, we choose $\alpha = 0, 0.1$ and $\alpha = 0.5$ for the set of curves in (a) through to (c) in both Figs. 5.5 and 5.6, and other parameters are given by $Bi = Br = 0.3$, so that they have the same magnitude. The two curves for the temperature and velocity profiles coincide particularly for the cases where $\alpha = 0.1$ and 0.5. This shows that our numerical results are in good agreement with the asymptotic. Large values for $\alpha$ are shown in curves (d) through to (i) from $\alpha = 5$ to 62 for the temperature profiles in Fig. 5.5. The velocity gradient in Equation (5.2.2) increases exponentially with temperature which eventually feeds back into Equation (5.2.3) through the viscous heating term. The Newtonian temperature profile is shown in curve (a) and an increasing temperature of the fluid to the maximum temperature at the top layer is shown. This curve is the same as the one which is shown in Fig. 5.3 curve (a). It is observed that the temperature of the fluid increases significantly as $\alpha$ increases. The velocity profiles are displayed in Fig. 5.6. Curves (a) through to (i) correspond to different values of $\alpha$ as displayed in the figure, and other flow controlling parameters are the same as those which are given in Fig. 5.5. The velocity of the fluid for all these curves increases across the fluid layer to their respective maximum velocities at the top layer. Again in this case, when $\alpha$ increases, the velocity of the fluid increases due to less resistance force to the flow. Curve (a) also shows the Newtonian velocity profile, which is similar to the one that is shown in Fig. 5.4, curve (a). It is important to note that the values of $\alpha$ were randomly chosen to test the reliability and the breakdown in the numerical scheme. The values for large $\alpha$ were tested up to 62. The results showed that for values of $\alpha > 50$ a change

in the flow structure is observed. For example, in Fig. 5.6 curves (h) and (i) shows different flow behaviour as compared to curves (a) through to (g). Since the viscosity of the fluid decreases exponentially when $\alpha$ increases, this therefore causes the fluid to behave like a Newtonian fluid when $\alpha = 58$ and 62. The temperature of the fluid increases significantly for values of $\alpha = 58$ and 62 as shown in curve (h) and (i). Elbashbeshy *et al.* [29] analysed the effect of temperature dependent viscosity on heat transfer over a continuous moving surface. The full solutions for the velocity and temperature profiles were obtained using the fourth order Runge−Kutta numerical scheme. The viscosity was taken for water and air. The viscosity does not vary exponentially with temperature in their investigation. Their results indicate that when the viscosity variation parameter increases for water, the temperature of the fluid increases slightly, which is in agreement with our results. However, in their investigation the velocity of the fluid decreases when the viscosity variation parameter increases.

The effect of the Biot number on the resulting temperature and velocity profiles is investigated. The importance of the Biot number is discussed in detail in § 2.4. Because of the strong feedback between the Navier−Stokes and the energy equations, the Biot number will have a major influence on the resulting velocity and temperature profiles. Using the parameters listed in the previous section, it can easily be shown that $Bi = 7.692 \sim 8$. We again begin with a simple analysis for $Bi = 0$ to a maximum of $Bi = 8$ calculated for lubricating oil. The curves for the temperature profiles are shown in Fig. 5.7 with different values of the Biot numbers, namely, $Bi = 0, 0.01, 1, 4$ and 8. The fluid temperature increases across the fluid layer to its maximum temperature at the free surface as $Bi$ decreases due to reduction in the heat transferred to the surrounding environemnt. The figure clearly demonstrates that the fluid temperature rises with decreasing values of the Biot number and the temperature profiles flatten out at the free surface, as $Bi$ decreases, and when $Bi = 0$ the temperature profile shows that the temperature gradient at the free surface is zero. Khaled *et al.* [51] investigated the rate of heat and entropy transfer to

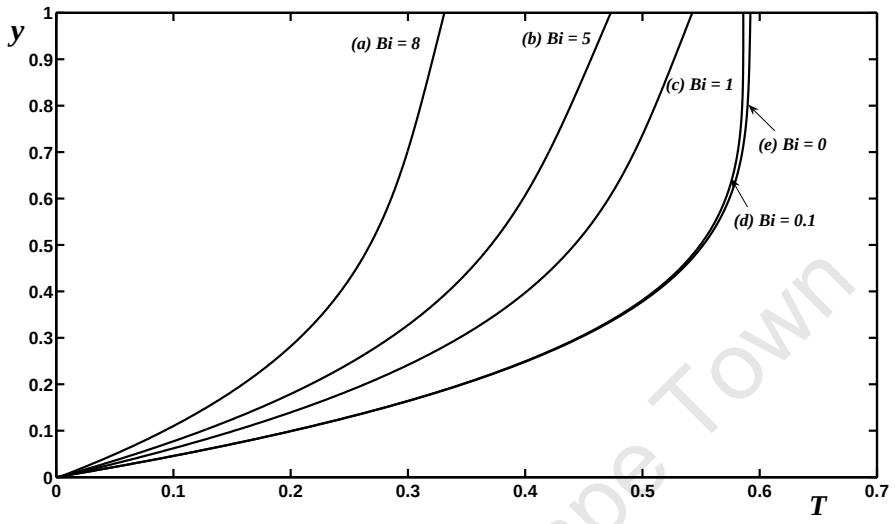


Figure 5.7: The temperature profiles for Equation (5.2.20): Boundary conditions (2.3.13) .

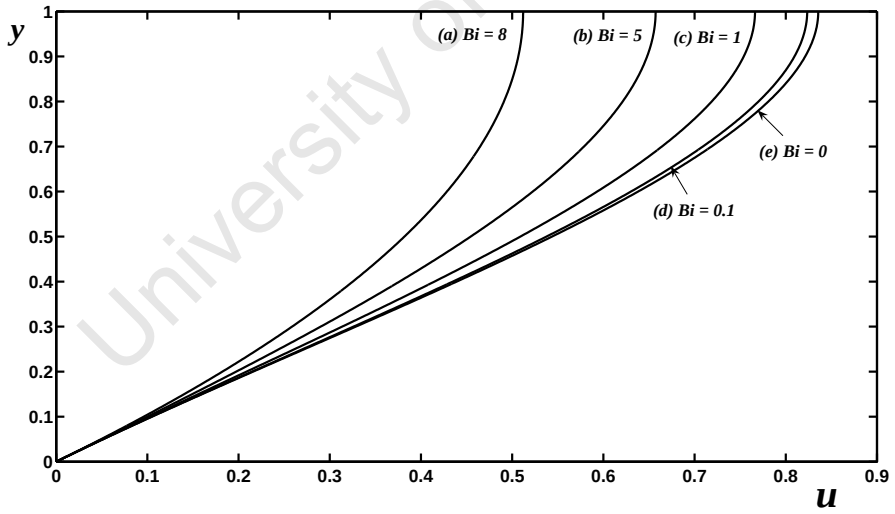


Figure 5.8: The velocity profiles for Equation (5.2.22): Boundary conditions (2.3.12) .

the slab wall and the results showed that the dimensionless temperature in the slab wall increases as $Bi$ decreases, which is in agreement with our findings. The corresponding velocity profiles are shown in Fig. 5.8 with different values of the Biot numbers. The fluid velocity increases across the layer to its maximum at the free surface as the Biot number decreases. This is a result of the resistance force to the flow which decreases as $Bi$ decreases.

The effect of the Brinkman number is displayed in Figs. 5.9 and 5.10 for the temperature and velocity profiles. Other parameters are given by $\alpha = 0.3$ and $Bi = 0.3$. Using the values listed in the previous section the Brinkman numbers are given by $Br = 0$ for the Newtonian case to 0.5 as shown in Fig. 5.9. We have the Newtonian case displayed in curve (a) in each figure with a constant viscosity. Increasing $Br$ results in increased viscous heat dissipation effect. The temperature of the fluid increases significantly when $Br$ increases. In Fig. 5.10, when $Br$ increases, the fluid heats up quickly and the viscosity of the fluid drops, and the flow is faster. As a result, the fluid velocity increases significantly in the direction of the flow.



### 5.2.2 Conclusion

A steady gravity driven flow of a temperature dependent variable viscosity model was investigated. The results were obtained using an asymptotic technique and the fourth order Runge−Kutta integration scheme. We used experimental values for lubricating oil to determine the value of $\alpha$ for the asymptotic approximation terms. The results illustrated that when the non−dimensional temperature variation parameter increases, an increase in the fluid velocity and temperature is observed. Furthermore, the effect of the flow controlling parameters such as the Biot and the Brinkman numbers were investigated. In the case of a Biot number, the temperature of the fluid increases significantly when the Biot number decreases due to heat lost from the fluid to the surrounding environment,

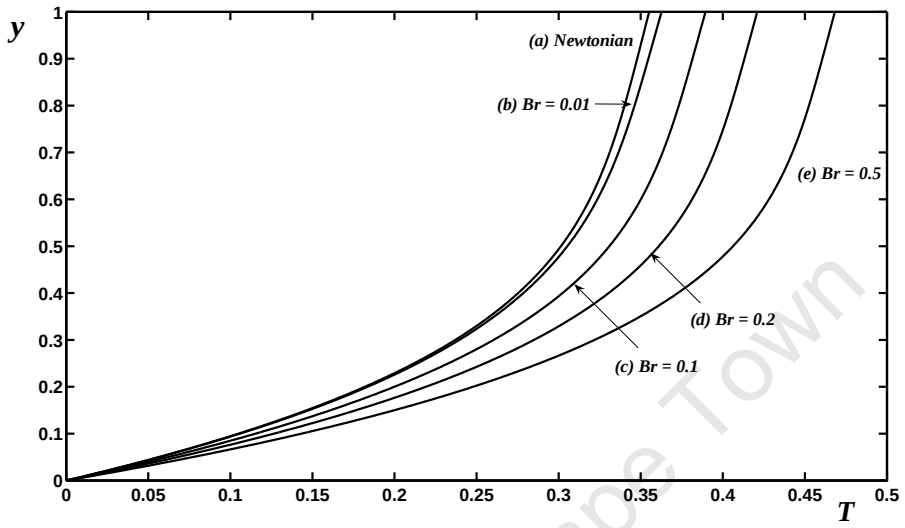


Figure 5.9: The temperature profiles for Equation (5.2.20): Boundary conditions (2.3.13).

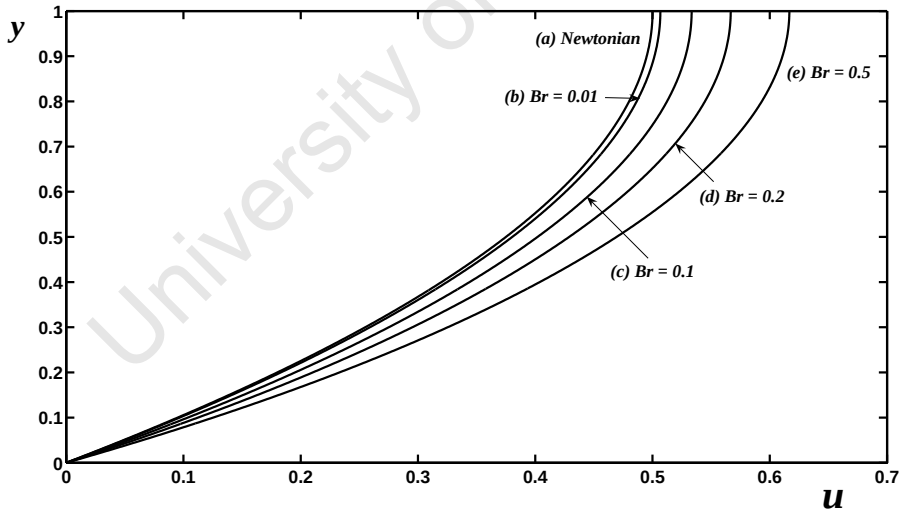


Figure 5.10: The velocity profiles for Equation (5.2.22): Boundary conditions (2.3.12).

and as a result, the fluid temperature flattens out at the free surface. The velocity of the fluid increases as the Biot number decreases, due to less resistance force to the flow. The numerical results were compared with the asymptotics. The Newtonian cases for both the temperature and velocity of the fluid are retrieved when $\alpha$ is zero, and the results showed good agreement when $\alpha = 0.1$ and 0.5 respectively. When $\alpha$ increases, the temperature and the velocity of the fluid increases significantly. However, when $\alpha = 58$, a change in the flow structure is observed from the velocity profiles. Since the viscosity of the fluid decreases exponentially when $\alpha$ increases, the prediction of the velocity profiles shows a different flow structure. This therefore causes the fluid to behave like a Newtonian fluid, in particular when $\alpha \geq 58$. The Brinkman number $Br$ was also investigated, and the results showed that as $Br$ increases, the temperature due to heat dissipation and the velocity of the fluid increased significantly due to the resistance force to the flow, which decreases when $Br$ increases.

## 5.3 Flow between parallel plates

In this section, the effect of a temperature dependent viscosity model on the laminar flow along parallel plates is investigated. This work has been summarised in the paper by Myers, Charpin and Tshehla, see [77]. When the flow is solely shear driven at the top plate a degree of analytical progress is possible, see [11, 23, 35]. This investigation is carried out in § 5.3.1. When there is also a pressure gradient driving the flow, the system must be solved numerically. This is carried out in § 5.3.2.

In order to obtain the solution for the velocity, Equation (2.3.9) may be integrated once to give,

$$\frac{\partial u}{\partial y} = \frac{1}{\mu}\left(p_x y + A\right) \ , \tag{5.3.24}$$

where $p_x = \partial p/\partial x$ and $A$ is a constant of integration. With a constant viscosity the fluid flow decouples from the temperature and Equation (5.3.24) may be integrated immedi-

ately to determine the velocity throughout the plates. The temperature follows easily by combining Equations (5.2.1) with (5.3.24). When the viscosity is not constant this simple analysis cannot be followed through. In the following section we examine a specific case, where the viscosity variation is exponential.

## General analysis

Using the exponential viscosity variation in Equation (5.2.1) the velocity in Equation (5.3.24) may be written:

$$\frac{\partial u}{\partial y} = (p_x y + A)\, e^{\alpha T} \ . \tag{5.3.25}$$

Equation (5.3.25) involves the unknown temperature $T$ and so it cannot be integrated with respect to $y$. The temperature profile may be obtained by substituting Equation (5.3.25) into the energy Equation (2.3.11). This leads to,

$$\frac{\partial^2 T}{\partial y^2} = -Br\,(p_x y + A)^2\, e^{\alpha T} \ . \tag{5.3.26}$$

Note, the temperature Equation (5.3.26) is not coupled to the velocity Equation (5.3.25). Hence Equation (5.3.26) may be solved first and the temperature then substituted into (5.3.25) to determine the velocity. As it stands we cannot make further analytical progress. However, when $p_x = 0$ we can integrate the temperature equation. We will now consider this case before moving on to numerical solutions in the subsequent section.



### 5.3.1 Shear driven flow

When $p_x = 0$, Equations (5.3.25) and (5.3.26) reduce to,

$$\frac{\partial u}{\partial y} = A e^{\alpha T} \ , \tag{5.3.27}$$

$$\frac{\partial^2 T}{\partial y^2} = -Br A^2 e^{\alpha T} \ , \tag{5.3.28}$$

where $BrA^2$ is constant. Fowler [35] obtains the same equation as part of model reactions in industrial processes such as occur in blast furnaces or fluidised bed roasters. Equation (5.3.28) is sometimes known as the Gel'fand equation, see Stuart [104]. Multiplying Equation (5.3.28) by $\partial T/\partial y$ and integrating with respect to $y$ gives,

$$\left(\frac{\partial T}{\partial y}\right)^2 + \chi^2 e^{\alpha T} = \chi^2 e^{\alpha T_m} \implies \frac{\partial T}{\partial y} = \pm\chi\sqrt{e^{\alpha T_m} - e^{\alpha T}}\ , \tag{5.3.29}$$

where

$$\chi = \sqrt{\frac{2BrA^2}{\alpha}}\ ,$$

$\chi$ represents the rate of heat production and $T_m$ is a constant denoting the temperature where $\partial T/\partial y = 0$. The integration now depends on the sign of the temperature gradient and form of the solution. When the temperature gradient is positive, that is, $\partial T/\partial y > 0$ then Equation (5.3.29) may be written,

$$\frac{\partial T}{\partial y} = \chi\sqrt{e^{\alpha T_m} - e^{\alpha T}}\ . \tag{5.3.30}$$

Integrating both sides with respect to $y$ and applying $T(0) = 0$,

$$y \ = \frac{1}{\chi}\int_0^T \frac{dT}{\sqrt{e^{\alpha T_m} - e^{\alpha T}}}\ . \tag{5.3.31}$$

The right hand side of Equation (5.3.31) may be integrated using the substitution $h = \sqrt{e^{\alpha T_m} - e^{\alpha T}}$. Subsequent rearrangement leads to,

$$y = \frac{2}{\alpha\chi}e^{-\frac{\alpha T_m}{2}}\left(\tanh^{-1}\sqrt{1 - e^{-\alpha T_m}} - \tanh^{-1}\sqrt{1 - e^{\alpha(T - T_m)}}\right)\ . \tag{5.3.32}$$

When the maximum temperature occurs within the plates then Equation (5.3.32) satisfies $T(y_m) = T_m$ where,

$$y_m = \frac{2}{\alpha\chi}e^{-\frac{\alpha T_m}{2}}\tanh^{-1}\sqrt{1 - e^{-\alpha T_m}}\ . \tag{5.3.33}$$

If $T$ increases monotonically so that $T(0) = 0, T(1) = 1$ then imposing the upper boundary condition gives an equation for $T_m$,

$$\chi = \frac{2}{\alpha}e^{-\frac{\alpha T_m}{2}}\left(\tanh^{-1}\sqrt{1 - e^{-\alpha T_m}} - \tanh^{-1}\sqrt{1 - e^{\alpha(1 - T_m)}}\right)\ . \tag{5.3.34}$$

In regions where $\partial T/\partial y < 0$ Equation (5.3.30) may be written,

$$\frac{\partial T}{\partial y} = -\chi\sqrt{e^{\alpha T_m} - e^{\alpha T}} \ . \tag{5.3.35}$$

Integrating and imposing $T(y_m) = T_m$ leads to,

$$y = y_m - \frac{2}{\alpha\chi}e^{-\frac{\alpha T_m}{2}} \tanh^{-1}\sqrt{1 - e^{\alpha(T-T_m)}} \ , \tag{5.3.36}$$

where $y_m$ is still specified by Equation (5.3.33). Imposing $T(1) = T_u$, where $T_u = 0$ or 1 depending on whether the upper plate is heated or not, and substituting for $y_m$ via Equation (5.3.36) gives a nonlinear relation for $T_m$,

$$\chi = -\frac{2}{\alpha}e^{-\frac{\alpha T_m}{2}}\left(\tanh^{-1}\sqrt{1 - e^{-\alpha T_m}} - \tanh^{-1}\sqrt{1 - e^{\alpha(T_u - T_m)}}\right) \ . \tag{5.3.37}$$

Equation (5.3.37) shows that there are two possible solution branches, depending on whether the temperature gradient $\partial T/\partial y$ is positive or negative. When $T_u = 0$ the fact that the shear heating is positive requires the temperature to reach a maximum within the plates and a subsequent decrease back to zero. When $T_u = 1$, if shear heating is small, the temperature may increase steadily to reach a maximum value of 1 at $y = 1$. If the shear heating is stronger, the temperature may reach a maximum within the plates and then decrease to 1 at the top plate.



**Positive temperature gradient**

In this first configuration, the temperature is increasing progressively to $T = T_u = 1$ at $y = 1$. Equation (5.3.29) may then be integrated to give,

$$T = T_m + \frac{1}{\alpha}\ln\left\{1 - \tanh^2\left[\tanh^{-1}\left(\sqrt{1 - e^{-\alpha T_m}}\right) - \frac{A\sqrt{\alpha Br}}{\sqrt{2}e^{-\frac{\alpha T_m}{2}}}y\right]\right\} \ . \tag{5.3.38}$$

The constant $T_m$ may be determined via the boundary condition $T(1) = T_u$,

$$T_u = T_m + \frac{1}{\alpha}\ln\left\{1 - \tanh^2\left[\tanh^{-1}\left(\sqrt{1 - e^{-\alpha T_m}}\right) - \frac{A\sqrt{\alpha Br}}{\sqrt{2}e^{-\frac{\alpha T_m}{2}}}\right]\right\} \ . \tag{5.3.39}$$

Note, $T_m$ is the temperature where the temperature gradient is zero. In this case, it will occur outside of the plates, $y > 1$. The solution given by Equation (5.3.38) is valid for small rates of shear heating, which correspond to low Brinkman numbers. As $Br$ increases, the point where $T_m$ occurs moves closer to the plates until, at a critical Brinkman number, say $Br_0$, the temperature gradient is zero at $y = 1$. This may be determined by differentiating Equation (5.3.29) to give,

$$Br_0 = \frac{2e^{-\alpha}}{A^2\alpha}\left[\tanh^{-1}\sqrt{1-e^{-\alpha}}\ \right]^2 . \tag{5.3.40}$$

Combination of the positive and negative temperature gradient analysis will now follow.

**Positive and negative temperature gradient**

This second configuration is applied when $T_u = 1$ and the temperature reaches a maximum value within the plates $T_m$ at $y = y_m$ or when $T_u = 0$. Equation (5.3.29) must be integrated on either side of $y = y_m$.

- When $\partial T/\partial y \geq 0$, so $y \leq y_m$:

$$y = y_m - \frac{\sqrt{2}e^{-\frac{\alpha T_m}{2}}}{A\sqrt{\alpha Br}}\tanh^{-1}\sqrt{1-e^{\alpha(T-T_m)}} . \tag{5.3.41}$$

- When $\partial T/\partial y \leq 0$, $y \geq y_m$:

$$y = y_m + \frac{\sqrt{2}e^{-\frac{\alpha T_m}{2}}}{A\sqrt{\alpha Br}}\tanh^{-1}\sqrt{1-e^{\alpha(T-T_m)}} . \tag{5.3.42}$$

Both equations may be re-arranged to give,

$$T = T_m + \frac{1}{\alpha}\ln\left\{1-\tanh^2\left[\frac{A\sqrt{\alpha Br}}{\sqrt{2}e^{-\frac{\alpha T_m}{2}}}(y_m - y)\right]\right\} . \tag{5.3.43}$$

The constants $y_m$ and $T_m$ may be found using boundary conditions (2.3.15) and (2.3.16). At $y = 0$, $T = 0$,

$$y_m = \frac{\sqrt{2}e^{-\frac{\alpha T_m}{2}}}{A\sqrt{\alpha Br}}\tanh^{-1}\sqrt{1-e^{-\alpha T_m}} . \tag{5.3.44}$$

Substituting for $y_m$ in Equation (5.3.44) shows that the temperature profile in this case is exactly that specified by Equation (5.3.29). Since the temperature is the same as that of the previous section the second boundary condition, $y = 1$, $T = T_u$, must lead to Equation (5.3.39) to determine $T_m$ (although in this case $T_u$ may take the value 0 or 1). This requires determination of the velocity profile.

**Velocity profile**

Combining Equations (5.3.27) and (5.3.38), the equation governing the velocity profile may be written,

$$\frac{\partial u}{\partial y} = Ae^{\alpha T_m}\left[1 - \tanh^2\left(\tanh^{-1}\left(\sqrt{1-e^{-\alpha T_m}}\right) - \frac{A\sqrt{\alpha\ Br}}{\sqrt{2}e^{\frac{-\alpha T_m}{2}}}y\right)\right] . \qquad (5.3.45)$$

Using the boundary conditions $u(0) = 0$, a straightforward integration shows that the velocity profiles across the layer is,

$$u(y) = \frac{\sqrt{2}e^{\frac{\alpha T_m}{2}}}{\sqrt{\alpha\ Br}}\left[\tanh\left(\frac{A\sqrt{\alpha\ Br}}{\sqrt{2}e^{\frac{-\alpha T_m}{2}}}y - \tanh^{-1}\sqrt{1-e^{-\alpha T_m}}\right) + \sqrt{1-e^{-\alpha T_m}}\right] . \qquad (5.3.46)$$

If the flow is driven by the velocity of the upper plate, the value of the constant $A$ is chosen to satisfy $u(1) = 1$,

$$1 = \frac{\sqrt{2}e^{\frac{\alpha T_m}{2}}}{\sqrt{\alpha\ Br}}\left[\tanh\left(\frac{A\sqrt{\alpha\ Br}}{\sqrt{2}e^{\frac{-\alpha T_m}{2}}}y - \tanh^{-1}\sqrt{1-e^{-\alpha T_m}}\right) + \sqrt{1-e^{-\alpha T_m}}\right] . \qquad (5.3.47)$$

The flux is now given by,

$$\begin{aligned} Q \;=\; & -\frac{1}{A\alpha Br}\ln\left[\left(\tanh\left(\frac{A\sqrt{\alpha\ Br}}{\sqrt{2}e^{\frac{-\alpha T_m}{2}}} - \tanh^{-1}\sqrt{1-e^{-\alpha T_m}}\right) - 1\right)\left(\sqrt{1-e^{-\alpha T_m}} - 1\right)\right] \\ & -\frac{1}{A\alpha Br}\ln\left[\left(\tanh\left(\frac{A\sqrt{\alpha\ Br}}{\sqrt{2}e^{\frac{-\alpha T_m}{2}}} - \tanh^{-1}\sqrt{1-e^{-\alpha T_m}}\right) + 1\right)\left(\sqrt{1-e^{-\alpha T_m}} + 1\right)\right] \\ & +\frac{\sqrt{2}e^{\frac{\alpha T_m}{2}}}{\sqrt{\alpha\ Br}}\sqrt{1-e^{-\alpha T_m}} . \end{aligned} \qquad (5.3.48)$$

Equation (5.3.48) shows the solution for the flux. Both the maximum temperature $T_m$ and the constant $A$ must then be calculated using Equations (5.3.39) and (5.3.47) respectively.

A response diagram for the maximum temperature $T_m$ as a function of $Br$ is shown in Fig. 5.11. The following results are calculated for the case $\alpha = A = 1$. To solve this problem the maximum temperature $T_m$ must first be calculated by solving Equation (5.3.39). A similar diagram for the symmetric case, $T_u = 0$, is discussed in Fowler [35]. For values of $Br_0 = 0.274$ there are two possible values of $T_m$. In the corresponding time-dependent situation the lower branch is stable, the upper unstable. For $Br_0 = 0.518$, one maximum temperature is observed and for $Br_0 > 0.518$ the system has no real solution, which implies that there is no steady state solution beyond this point. Fig. 5.11 displays a classical form indicating thermal runaway. This is due to feedback between the temperature and viscosity or shear heating. In this case, as the maximum temperature increases, the viscosity of the fluid decreases exponentially due to the applied shear heating in the plates. The velocity gradient in Equation (5.3.25) increases exponentially with temperature and feeds back into the temperature Equation (5.3.26) through the shear heating term in Equation (2.3.11). This leads to thermal runaway. For sufficiently low values of $Br_0 < 0.274$ the numerical solution of Equation (5.3.39) indicates that the lower values of the maximum temperature $T_m$ occurs outside the parallel plates. The



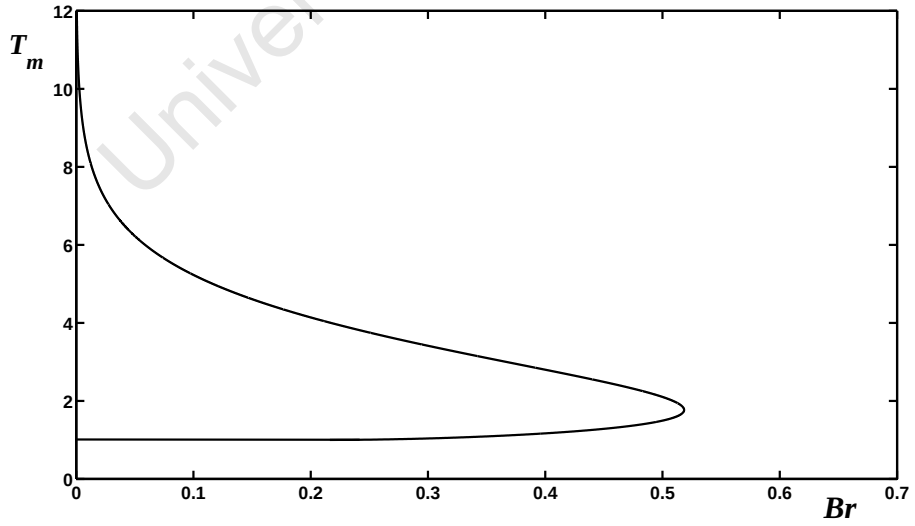


Figure 5.11: The maximum temperature as a function of $Br$, Equation (5.3.37).

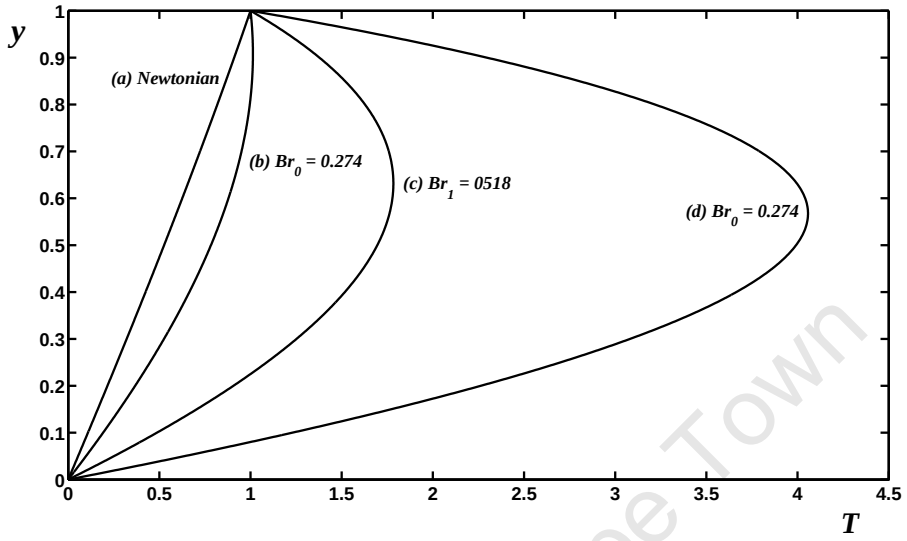


Figure 5.12: The temperature profiles for Equation (5.3.43): Boundary conditions (2.3.15) and (2.3.16).

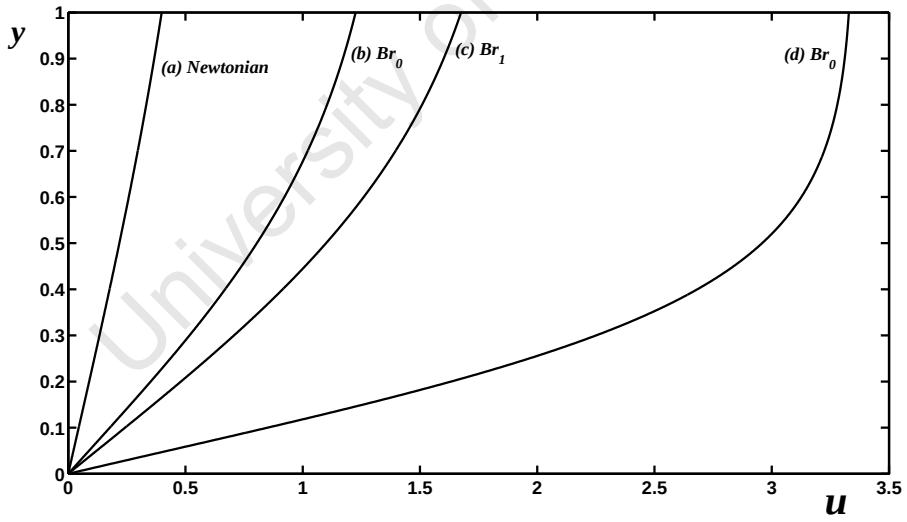


Figure 5.13: The velocity profiles for Equation (5.3.46): Boundary conditions (2.3.15) and (2.3.16).

two physical solutions occur when $T_m$ is determined by the upper branch and when the temperature increases monotonically from 0 to 1 without any maximum.

In Fig. 5.12 four temperature profiles are displayed for Equation (5.3.43). For a Newtonian fluid the viscosity is constant and the temperature increases linearly from 0 to 1. With an exponential viscosity variation with temperature two solutions are shown for the case $Br_0 = 0.274$. The maximum temperatures are $T = 1$ from a lower branch and $T = 4.1$ from the upper branch at $y = 1$, for curves (b) and (d) respectively. These maximum temperatures can be observed in Fig. 5.11. The curve closest to the Newtonian line is the limiting case where $T_m$ occurs at the top plate. Curve (d) shows the solution where $T_m$ is obtained from the upper branch of the curve in Fig. 5.11. The final curve (c) is a single solution corresponding to $Br_1 = 0.518$. This curve displays a single maximum fluid temperature $T_u = 2.1$ at $y = 0.6$, which decreases to the top plate $T = 1$ at $y = 1$. The corresponding curves for the velocity profiles are shown in Fig. 5.13 representing Equation (5.3.46). The Newtonian fluid shows the standard linear velocity profile. The next curve with $Br_0 = 0.274$, shows the velocity increasing non−linearly across the plates to a maximum at $y = 1$ in curves (b) and (d) respectively. Curve (c), with $Br_1 = 0.518$ and $T_m = 2.1$, increases from $u = 0$ at $y = 0$ across the plates to its maximum velocity at the top plate.



### 5.3.2 Numerical solution

In the following section we start by continuing our analysis of the shear driven and the pressure gradient flows. In this case the pressure gradient $p_x \neq 0$. The temperature and velocity must be determined by solving Equations (5.3.25) and (5.3.26) respectively. In addition the constants $T_m$ and $A$ must be found numerically by solving Equations (5.3.39) and (5.3.47) respectively. Substituting for the temperature into Equation (5.3.25) gives an expression for the velocity gradient which is subsequently integrated numerically using

a fourth order Runge−Kutta scheme. When the pressure gradient is non−zero neither the temperature nor the velocity may be computed explicitly. The temperature and velocity profiles are therefore both determined numerically, again with a fourth-order Runge−Kutta scheme. This method is fully detailed in § 5.2.1, however the model is slightly modified to include the shooting method for the constant of integration. The shooting technique is used for the targeted values at the boundaries, see [14, 52] for examples. It is important to note that the best numerical results largely depend on a good guess for the initial condition, see [30].

We now consider the situation where the pressure gradient and the applied shear forces have the same magnitude. Fig. 5.14 with $p_x = -1.5$, shows the variation of the maximum temperature with the Brinkman number. This figure is again similar to Fig. 5.11 and in this case the maximum Brinkman number appears at $Br = Br_1 = 0.925$. In this figure again if we consider the case where $Br_0 = 0.272$, two possible maximum temperatures are observed each one appearing on the lower and upper branches. In Fig. 5.15 the temperature profiles are shown for Newtonian fluids and non−Newtonian fluids with different



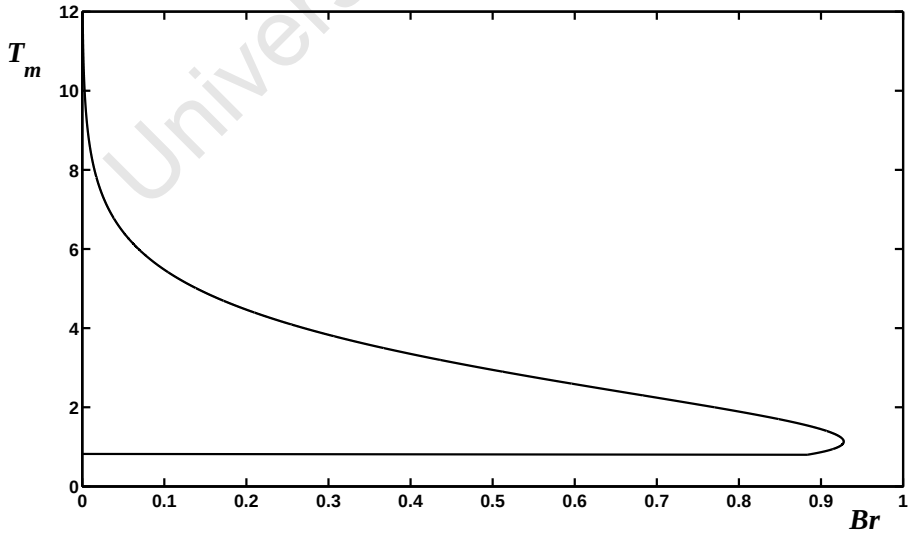


Figure 5.14: The maximum temperature as a function of $Br$, Equation (5.3.37).

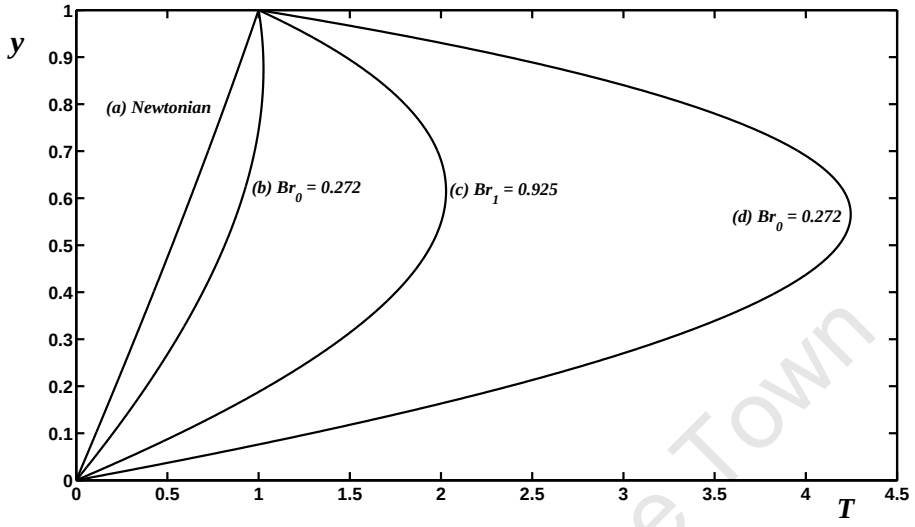


Figure 5.15: The temperature profiles for the numerical solution: Boundary conditions (2.3.15) and (2.3.16).

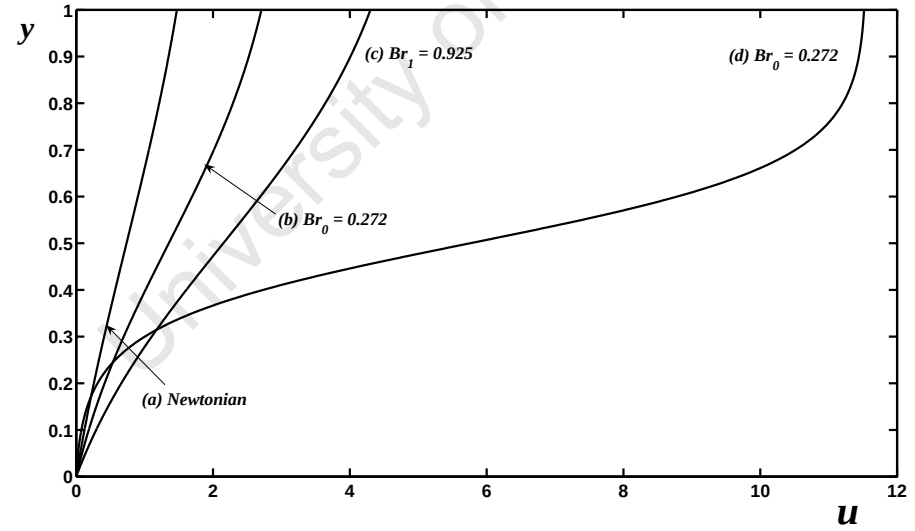


Figure 5.16: The velocity profiles for for the numerical solution: Boundary conditions (2.3.15) and (2.3.16).

values of the Brinkman number. These curves are similar to those observed in Fig. 5.12, however the main difference in this case is that the maximum temperature profiles are slightly higher while the Newtonian profile is the same as in the previous case. The corresponding velocity profiles are shown in Fig. 5.16. The combination of both the applied shear force and the pressure gradient, act to increase the velocity of the fluid. These curves illustrate that the added driving force for the fluid also increases heat generated between the plates and causes the maximum temperature to occur close to the top plate as shown in Fig. 5.14

We now proceed to investigate a general case where the Brinkman number increases progressively from 0 to 25. In Fig. 5.17, the temperature profile is shown with six different values of $Br$ for curves (a) through to (f) respectively. In this case the temperature variation is significantly larger when $Br$ increases. Of course this is caused by the addition of the pressure gradient as a driving force for the fluid and subsequently it increases heat generated between the plates. The maximum temperature for all the cases occurs near the top plate and the Newtonian case with $Br = 0$ is similar to those observed before. The corresponding velocity profiles are shown in Fig. 5.18 which also show increasing profiles with their maximum occurring at $y = 1$. The maximum velocities are more pronounced near the top plate due to the competition between the applied shear force and the pressure gradient in driving the fluid.



### 5.3.3 Conclusion

A model that describes the flow of a thin film fluid with exponential viscosity variation with temperature has been analysed. Two situations are examined; the shear driven flow as well as the combination of pressure gradient and shear driven flow. The variation of the maximum temperature with the Brinkman number is shown and the resulting flow profiles shows two solution branches in which the lower branch is stable and the upper branch

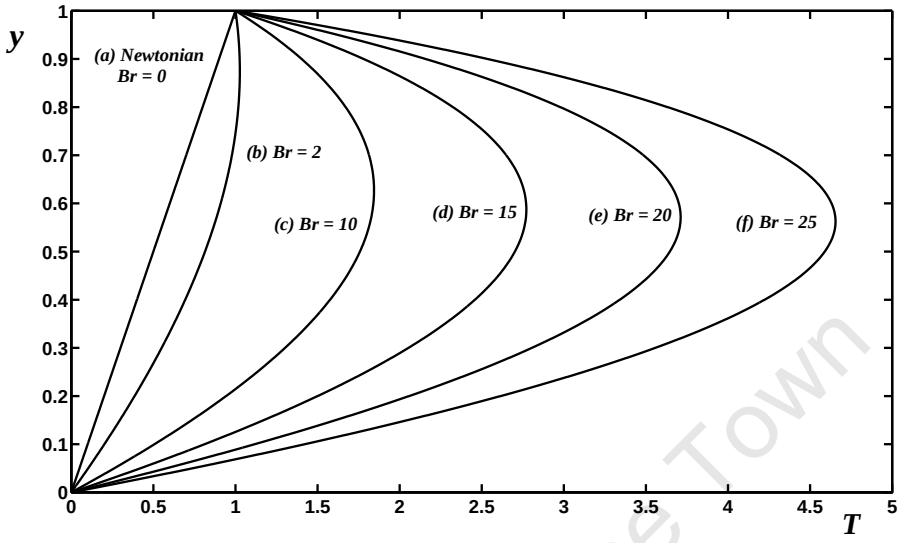


Figure 5.17: The temperature profiles for the numerical solution: Boundary conditions (2.3.15) and (2.3.16).

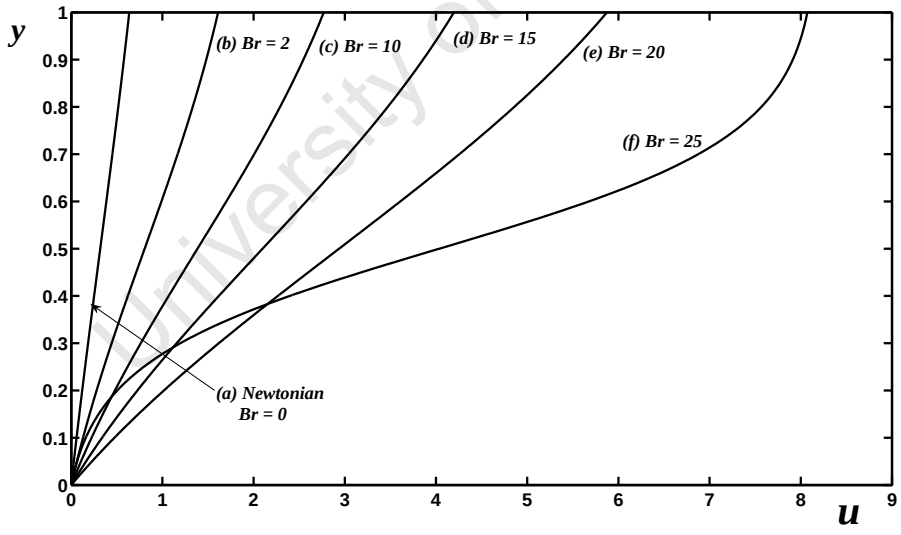


Figure 5.18: The velocity profiles for for the numerical solution: Boundary conditions (2.3.15) and (2.3.16).

unstable. In this case two possible maximum temperatures can be observed one from the lower branch and one from the top branch. The temperature and velocity profiles were plotted using these values for the different Brinkman numbers. The results showed that for a Newtonian case, since the viscosity is constant, a linear profile for the temperature and velocity profiles were observed. For non−Newtonian cases, the maximum temperature and velocity of the fluid occurs near the top plate due to the applied shear force. When both the pressure gradient and the applied shear force drive the flow, the resulting profiles are slightly higher than the case where only the applied shear force drives the flow. This is an obvious case since the addition of the pressure gradient also acts to increase heat generated and also increases the fluid velocity. The combined shear and pressure driven case had to be solved using a numerical technique. The fourth order Runge−Kutta and shooting methods were applied to derive the velocity and temperature profiles. The effect of the Brinkman number was also investigated. The Brinkman number was allowed to vary between 0 and 25, and the results showed that the velocity and the temperature of the fluid increase as $Br$ increases. These profiles showed the effect of the combined pressure gradient and applied shear force by the movement of the upper plate which again act to increase the resulting velocity and temperature of the fluid.

# Chapter 6

# Surface tension driven flow

## 6.1 Introduction

In this chapter, a Newtonian fluid is investigated where the driving forces for the flow are assumed to be those of gravity and surface tension. The work in this chapter is organised as follows: A model for a Newtonian fluid flowing under the influence of a constant surface tension and gravitational forces is derived in § 6.2. In general for industrial applications, surface tension decreases with the increase of the temperature, see [12, 85, 98]. For this reason and also to be consistent with the previous chapters, the heat equation will be used to investigate the effect of temperature on the fluid. We are particularly interested in investigating the effect of including surface tension and gravitational forces on the resulting flow profiles with different film heights.

The model is further extended to investigate the effect of the first order perturbation terms for lubrication theory in § 6.3. The first order perturbation is very important since it includes the correction terms which are neglected when lubrication theory is applied. The advantage of using the first order correction terms is that it increases the degree of accuracy to the resulting flow profiles. The film height $h$, which is assumed to be changing in the direction of the flow, is determined by using a Runge−Kutta numerical scheme. To completely characterise the flow, we now describe the problem geometry.

## 6.2 Derivation of the model

Fig. 6.1 shows a geometrical representation of the problem. In the $y$ direction the height varies from the initial to final fluid levels given by $h_i$ and $h_\infty$ respectively, with a length scale $L$ in the $x$ direction. The flow is inclined at an angle $\beta$ to the horizontal plane, the force of gravity is denoted $g$ and the flux is denoted $Q$. The fluid temperature at the bottom is assumed to be equal to the substrate temperature $T_s$. The atmospheric temperature is denoted $T_a$ and the fluid temperature is given by $T$.

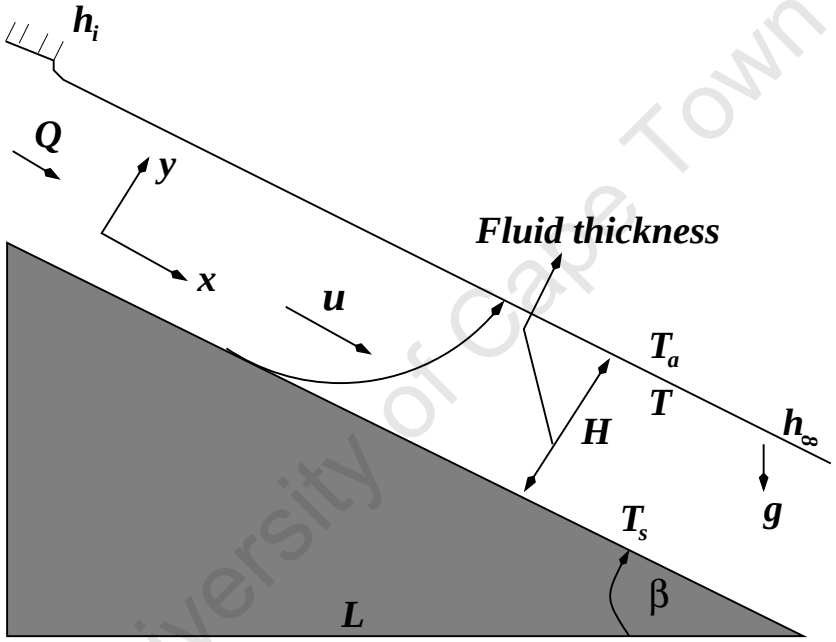


Figure 6.1: Problem configuration for the surface tension driven flow, where $\mathbf{u} = (u, 0)$.



The reduced governing Equations (2.3.8)−(2.3.11) from Chapter 2 are now used in this section. Equation (2.3.9) can be integrated subject to the boundary conditions (2.3.12) to give,

$$u = \frac{(p_x - 1)y}{2}\Big(y - 2h\Big) \ . \tag{6.2.1}$$

This equation will provide the solution for the velocity profiles provided the film height and the pressure gradient are known. A similar expression for Equation (6.2.1) may be

obtained in ÓBrien *et al.* [81] which was used in the analysis for modelling of thin film flows. Following Myers *et al.* [78] and Weidner *et al.* [113], in order to introduce a constant surface tension to our governing equation, we impose the boundary conditions for the pressure at the free surface as follows,

$$p = p_a - Ch_{xx} \quad \text{at} \quad y = h, \tag{6.2.2}$$

where $C = (\sigma\varepsilon^3/\mu U)$ is the inverse capillary number which represents the ratio of surface tension to viscous forces and $\sigma$ denotes the surface tension, see [75]. The second order term $h_{xx}$ represents the change of curvature. Integrating Equation (2.3.10) and applying the boundary conditions (6.2.2) leads to the following expression for the pressure,

$$p = p_a - Ch_{xx} \ . \tag{6.2.3}$$

Differentiating Equation (6.2.3) once with respect to $x$ and substituting for the pressure gradient in Equation (6.2.1) gives the velocity profile as,

$$u = \frac{(Ch_{xxx} + 1)y}{2}\Big(2h - y\Big) \ . \tag{6.2.4}$$

Combining Equations (2.3.11) and (6.2.1) gives a second order ordinary differential equation for $T$,

$$\frac{\partial^2 T}{\partial y^2} = -Br(p_x - 1)^2 (y - h)^2 \ . \tag{6.2.5}$$

Integrating Equation (6.2.5) twice with respect to $y$ and applying the boundary conditions (2.3.13) yields,

$$T = -\frac{Br(Ch_{xxx} + 1)^2}{12}\left[(y-h)^4 - h^4\left(1 - \frac{Bi\ y}{(Bi\ h - 1)}\right)\right] + \left(\frac{Bi}{(Bi\ h - 1)}\right) y \ , \tag{6.2.6}$$

where we have used Equation (6.2.4) to eliminate $p$ in favour of $h$. Equation (6.2.6) gives the solution for the temperature profile provided the inverse capillary number and the film height are known. A numerical scheme is now developed to obtain the solution for the film height.

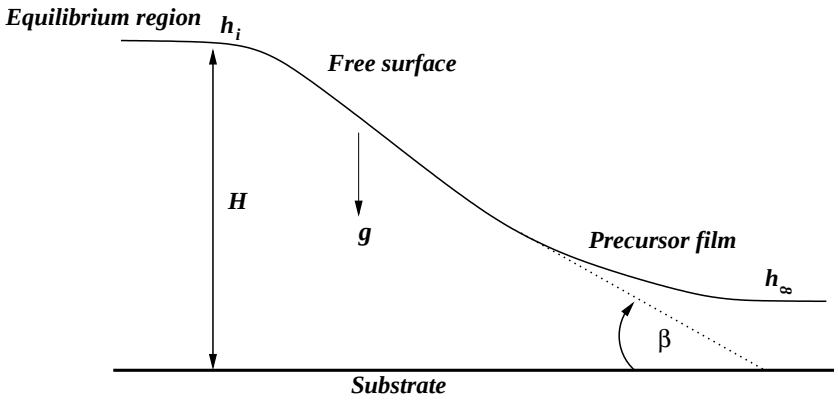


Figure 6.2: Typical film height.

## Numerical solution

We now turn our attention to derive the film height for a thin film inclined at an angle $\beta$ under the influence of gravitational forces and surface tension. The equilibrium region is far behind the precursor film. We consider a very simple flow configuration ahead of a contact line whose thickness is assumed to be constant and is given by $H$, see [81]. Typical flow configuration is shown in Fig. 6.2. This type of flow, which is under the influence of gravitational and surface tension forces, has a wide variety of applications in industrial (surface coating, paints, chemical) and natural processes (tear drop, raindrop on the windowpane) and as a result has been widely studied [75, 81, 108, 112]. In order to determine the solution for the film height $h$, Equation (6.2.4) is used to calculate the flux $Q$. This is determined by,

$$Q = \int_0^h u dy = \frac{h^3}{3}\Big(1 + Ch_{xxx}\Big) \ . \tag{6.2.7}$$

The constant term represents the gravitational force, the $h^3$ term appears due to the viscous force and the third order derivative term appears due to the surface tension [75]. Equation (6.2.7) shows the relationship between the flux and the fluid height $h$ and it is now solved as an initial value problem to show the behaviour of the solution, see [26, 75, 112]. We now follow the analysis developed by Tuck *et al.* [112] for gravity drainage problems to solve for the film height. The film height is in the region $0 \leq h \leq H$.

Let $H = h_\infty$ (where $h_i$ and $h_\infty$ denoted the initial and the final film height, see Figs. 6.1 and 6.2 at the far end of the fluid layer). Now in Equation (6.2.7), $h \to H$ as $x \to \infty$, therefore $h_{xxx} \to 0$ which implies that $Q = H^3/3$ and the expression for $h_{xxx}$ is written,

$$h_{xxx} = \frac{1}{BC}\left(\frac{H^3}{h^3} - 1\right) , \tag{6.2.8}$$

where $x$ and $h$ are scaled out to simplify the problem and $B = H/L^3$. Equation (6.2.8) cannot be solved analytically and so a numerical solution is now considered. It is convenient to set $\xi = -BC^{\frac{1}{3}}x$, such that, when $x \to -\xi$ then $h \to 1$, and then Equation (6.2.8) can be written,

$$h_{\xi\xi\xi} = 1 - \frac{1}{h^3} . \tag{6.2.9}$$

Equation (6.2.9) is similar to Equation (9a) from Troian *et al.* [108] which is used to model fingering instabilities of driven spreading films. A similar expression may be found in Eres *et al.* [31], with our equation corresponding to their Equation (21), which was used to obtain the solution for the fluid film height in coating films. This equation is coupled with the initial condition $h = h_i$ at $\xi = 0$, where $h_i$ represents the maximum fluid height at $\xi = 0$. The solution $h = 1$ satisfies Equation (6.2.9), but not the initial condition $h_i = h_0$ at $\xi = 0$. If we choose the starting point $\xi = \xi_0$, then we can march back by solving Equation (6.2.9) until we reach $h = h_0$. The film height in the equilibrium region is perturbed to provide the starting point for the initial algorithm [75],

$$h = 1 + \vartheta f(\xi) , \tag{6.2.10}$$

where $\vartheta \ll 1$ is the perturbation parameter. The importance of the perturbation parameter $\vartheta$ is that it determines how close to zero the film height can get although $h$ never reaches zero, see Tuck *et al.* [112]. Substituting Equation (6.2.10) into Equation (6.2.9) and linearizing leads to,

$$f_{\xi\xi\xi} \approx 3f , \tag{6.2.11}$$

which is a linear differential equation such that $f$ takes the form $e^{m\xi}$. There are three roots, that is, $m_0 = \omega$, $m_1 = -\frac{\omega}{2} + i\frac{\sqrt[6]{3^5}}{2}$ and $m_2 = -\frac{\omega}{2} - i\frac{\sqrt[6]{3^5}}{2}$, where $\omega = \sqrt[3]{3}$. Equation (6.2.11) has general solution of the form,

$$f = a_0 e^{\omega\xi} + e^{-\frac{\omega}{2}\xi}\left(a_1 \cos\left(\frac{\sqrt[6]{3^5}}{2}\xi\right) + a_2 \sin\left(\frac{\sqrt[6]{3^5}}{2}\xi\right)\right) \ . \tag{6.2.12}$$

Equation (6.2.12) can be expressed in the form,

$$f = a_0 e^{\omega\xi} \ , \tag{6.2.13}$$

where we have used the fact that $a_1 = a_2 = 0$ to write Equation (6.2.13), otherwise the roots become unbounded as $\xi \to \infty$. Now Equation (6.2.10) can be written,

$$h = 1 + \vartheta e^{\omega\xi} \ , \tag{6.2.14}$$

where $a_0$ is absorbed into $\vartheta$, see [75, 112] for example. Equation (6.2.14) is now solved using the Runge−Kutta numerical scheme by setting $y_1 = h$, $y_2 = h_\xi$, and $y_3 = h_{\xi\xi}$, and so Equation (6.2.9) can be written:

$$\begin{bmatrix} y_1' \\ y_2' \\ y_3' \end{bmatrix} = \begin{bmatrix} y_2 \\ y_3 \\ 1 - \frac{1}{y_1^3} \end{bmatrix} \ . \tag{6.2.15}$$

The initial height is given by Equation (6.2.14) and we let $\xi = 0$ to be the starting point. Repeated differentiation of Equation (6.2.14) at $\xi = 0$ gives,

$$y_1(0) = 1 + \vartheta \ , \qquad y_2(0) = \vartheta m \ , \qquad y_3(0) = \vartheta m^2 \ .$$

Since Equation (6.2.15) is autonomous we solve for the film height at the far end and shift the $\xi-$axis to the initial condition where $(\xi, h_0) = (0, 1.001)$ march back to the height where $h_0 = 3$ (the value for $h_0 = 3$ is chosen in order to magnify the results for the film height).

Fig. 6.3 shows the results obtained using the numerical method described above. The film heights are obtained using different values of the parameter $\vartheta$ namely, $\vartheta = 0.001, 0.1, 0.2$

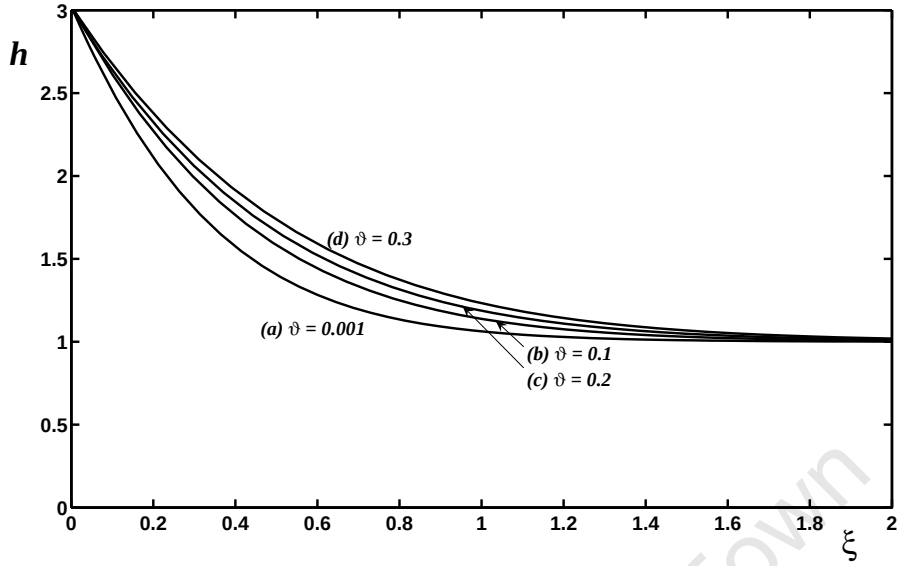


Figure 6.3: The relationship between the fluid height and surface corresponding to Equation (6.2.15).

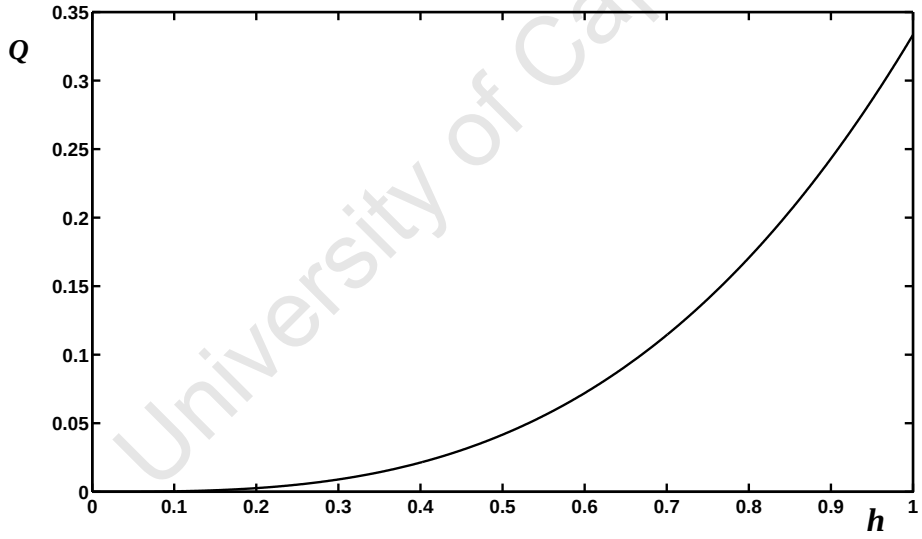


Figure 6.4: The profiles corresponding to Equation (6.2.7) for the flow rate.

and 0.3 for curves (a) through to (d) respectively. As the parameter $\vartheta$ increases from 0.001 to 0.1, an increase in the fluid level is observed, whereas from 0.1 to 0.3 the increase is less pronounced. The curves show that the fluid height decreases significantly in the direction of the flow due to the competition between gravitational and surface tension

forces. In the analysis of Tuck *et al.* [112], they found an oscillatory solution having an infinite number of minima and maxima which occurs due to the inclusion of the second term in Equation (6.2.12). This is the main difference between our results and those presented in [112, 108]. The flow rate is also shown in Fig. 6.4 with $h = 1$ and the figure shows that the maximum value for the flow rate is $Q = 0.34$ at $h = 1$. This curve is the same as the one which is observed in Chapter 2.

The velocity and temperature profiles in Equations (6.2.3) and (6.2.6) respectively are now plotted for different film heights $h$. The $h_{xxx}$ is calculated numerically using Equation (6.2.7) and $h_{xxxx} = -3h_x/h^4$ is also determined numerically.

In Fig. 6.5 four velocity profiles representing the solution of Equation (6.2.3) are displayed. These curves correspond to different values of the fluid height $h = 3, 2, 1.5$ and 1 for curves (a) to (d) respectively. The velocity of each curve increases across the fluid layer to a maximum at the top layer. The curves demonstrate that when $h$ decreases from 3 to 1, the fluid velocity increases significantly as a result of the competition between the gravitational forces and surface tension. Curve (d) represents the velocity profile without the effect of the surface tension, with $h = 1$ and $h_{xxx} = 0$. As expected, the fluid flows rapidly in the absence of the surface tension and the dominating driving force for the flow are the gravitational force.

Fig. 6.6 shows the temperature profiles representing the solution for Equation (6.2.9). Curves (a) to (d) display the temperature of the fluid which increases across the layer to a maximum temperature at the top layer with different film heights as given in the figure. The Brinkman and Biot numbers are fixed at $Br = Bi = 0.3$ respectively. Curves (a) to (c), show the temperature profiles for the fluid which are less pronounced compared to curve (d). The temperature of the fluid rises due to the action of the viscous term caused by the collision of the fluid particles during the flow process, which in turn creates heat. However, when the surface tension terms are excluded as shown in curve (d) the

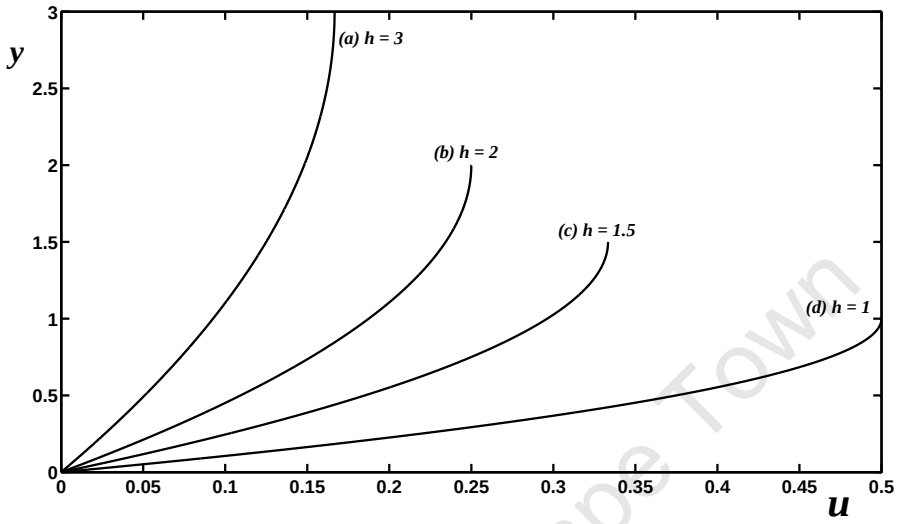


Figure 6.5: The velocity profiles for Equation (6.2.3): Boundary conditions (2.3.12).

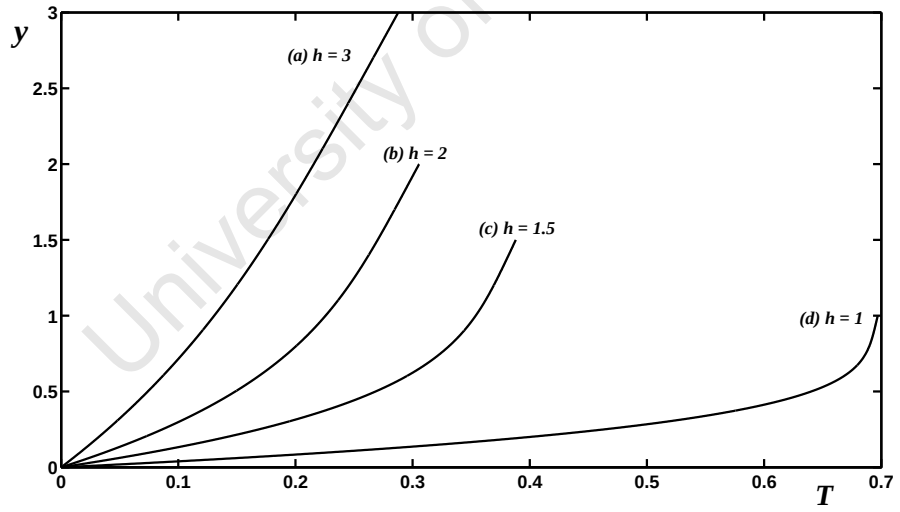


Figure 6.6: The temperature profiles for Equation (6.2.6): Boundary conditions (2.3.13).

temperature of the fluid increases significantly as a result of heat generated by the viscous term.

### 6.2.1 Conclusion

The velocity, flux and temperature profiles for a Newtonian fluid were investigated analytically. However, the film height was solved using a Runge−Kutta numerical method. The resulting velocity profiles were plotted with different values of the film height and the results show that the velocity of the fluid increases in the direction of the flow as the film height decreases due to the competition between gravitational forces and surface tension. For the case where the surface tension force is neglected, the velocity profile is more pronounced since the major driving force for the flow is gravitational forces and the fluid flows faster. The temperature profiles showed similar trends to the velocity profiles. The temperature increases when the film height decreases due to viscous heat generation. The numerical results for the film height decreases as the perturbation parameter increases due to the competition between gravitational and surface tension forces.

## 6.3 First order correction for the lubrication theory

The aim of this section is to investigate the effect of the first order correction terms for the lubrication theory. In this case a general asymptotic method is used which requires non−dimensionalisation of the continuity, Navier−Stokes and energy equations [1]. The appropriate dominant terms in the governing equations are highlighted and the system is solved to investigate the effect of the first order correction terms and surface tension. The essence of lubrication approximation as discussed in Chapter 2 briefly, is that the aspect ratio and the reduced Reynolds number ($\varepsilon^2, \varepsilon^2 Re$) are small. Practically this means that the derivatives in the direction perpendicular to the flow dominate and that inertia terms may be neglected from the Navier−Stokes equations [1, 82]. If we consider the first

order correction, inertia terms may not be neglected. This therefore adds more terms to the Navier−Stokes equations, which implies that the first order correction will be more accurate in predicting the resulting flow profiles. Lubrication analysis which includes inertia terms in the leading order balance, may be complex to solve and may require a numerical solution, see [55, 79]. The same argument is applicable to the energy equation where the heat conduction terms are also added in the governing equation. This discussion will follow towards the end of the section. The reduced Péclet and Reynolds number in this section will play the major role in determining the stage at which the fluid velocity and temperature may become significantly large.



## First order correction terms with a large Reynolds number

In Chapter 2, lubrication assumptions were based on $\varepsilon^2,\ \varepsilon^2 Re,\ \varepsilon^2 Pe \ll 1$, so that terms of $\mathcal{O}(\varepsilon^2, \varepsilon^2 Re,\ \varepsilon^2 Pe)$ were neglected from the governing Equations (2.3.4)−(2.3.7). The viscosity was taken for water in Table 1.1a [23]. The magnitude of these terms were calculated as $\varepsilon^2 \approx 1 \times 10^{-8}$, $Pe \approx 1 \times 10^4$ and $Re \approx 2 \times 10^3$. This shows that neglecting the terms of order $\varepsilon^2 \approx 1 \times 10^{-8}$, $\varepsilon^2 Pe \approx 1 \times 10^{-4}$ and $\varepsilon^2 Re \approx 2 \times 10^{-5}$ led to typical errors of about $10^{-6}\%$, $0.01\%$ and $2 \times 10^{-3}\%$ respectively.

Our interest is now in the contribution of the reduced Reynolds number to the velocity and temperature profiles. If the dynamic viscosity decreases to give $\mu_0 \approx 1 \times 10^{-6}$ and thermal conductivity increases to $\kappa \approx 0.6$, then the magnitude of the Reynolds number gives $Re = 2.5 \times 10^7$, $Pe = 1 \times 10^4$ and we assume that $Br$ is still of order unity. These changes imply that the reduced Reynolds and Péclet numbers are $\varepsilon^2 Re = 0.25 \approx 0.3$, $\varepsilon^2 Pe = 1 \times 10^{-4}$. This new magnitude would lead to typical errors of $\varepsilon^2 Re \approx 30\%, \varepsilon^2 Pe \approx 1 \times 10^{-3}\%$. It is now clear that the magnitude of $\varepsilon^2 Re > (\varepsilon^2 Pe,\ \varepsilon^2)$. Let the reduced Péclet and Reynolds numbers be expressed as $\zeta = \varepsilon^2 Pe$ and $\delta = \varepsilon^2 Re$, such that $(\delta \times \zeta) \approx 4.25 \times 10^{-7} \ll 1$. It follows that $\delta \gg \varepsilon^2, \zeta$, so the terms of $\mathcal{O}(\delta)$ are retained from the equations governing

the flow. This new lubrication assumption will add the inertia terms to Equations (2.3.5). The quantity $\varepsilon PrEc \approx 4 \times 10^{-5} \ll 1$. Therefor, the terms of order $\mathcal{O}(\varepsilon^2, \zeta, PrEc)$ will now be neglected from governing equations. It is important to note the maximum upper bound for the reduced Reynolds number $\delta = 0.3$. The Navier−Stokes Equation (2.3.5) now takes the form:

$$-\frac{\partial p}{\partial x} + \frac{\partial}{\partial y}\left(\mu\,\frac{\partial u}{\partial y}\right) + 1 \;\; = \;\; \delta\left(u\frac{\partial u}{\partial x} + v\frac{\partial u}{\partial y}\right) + \mathcal{O}(\delta^2, \varepsilon^2)\ . \tag{6.3.16}$$

In order to consider the first order perturbation terms for lubrication theory, it is now reasonable to consider asymptotic expansions of the form,

$$u = u_0 + \delta u_1\ , \quad v = v_0 + \delta v_1\ , \quad T = T_0 + \delta T_1\ , \tag{6.3.17}$$

where $u_1$, $v_1$ and $T_1$ are the first order perturbation terms for the velocity and temperature profiles respectively. The following boundary conditions are used for the first order correction term $u_1$,

$$u_1 = 0 \quad \text{at} \quad y = 0\ , \quad \left(\frac{\partial u_1}{\partial y}\right)\bigg|_{y=h} = 0\ . \tag{6.3.18}$$

Substituting the expansion for $u$ into Equation (6.3.16) gives,

$$\frac{\partial}{\partial y}\left(\frac{\partial u_0}{\partial y}\right) + \delta\frac{\partial}{\partial y}\left(\frac{\partial u_1}{\partial y}\right) = p_x - 1 + \delta\left(u_0\frac{\partial u_0}{\partial x} + v_0\frac{\partial u_0}{\partial y}\right)\ . \tag{6.3.19}$$

The leading order terms are,

$$\frac{\partial}{\partial y}\left(\frac{\partial u_0}{\partial y}\right) = p_x - 1\ , \tag{6.3.20}$$

and this leads to a solution in Equation (6.2.1) and the first order correction is,

$$\frac{\partial}{\partial y}\left(\frac{\partial u_1}{\partial y}\right) = \left(u_0\frac{\partial u_0}{\partial x} + v_0\frac{\partial u_0}{\partial y}\right)\ . \tag{6.3.21}$$

Integrating Equation (6.3.21) with respect to $y$ and applying the boundary conditions (6.3.18) will lead to Equation (6.2.4) for $u_0$. The continuity Equation (2.3.8) is then used to determine $v_0$,

$$v_0 = -\frac{\partial}{\partial x}\int_0^y u_0 dy = -p_{xx}\left(\frac{y^3}{6} - \frac{hy^2}{2}\right) + \frac{(p_x - 1)}{2}y^2 h_x\ . \tag{6.3.22}$$

Equation (6.3.22) also provides the solution for $v_0$. Now the velocity gradient at the leading order is,

$$\frac{\partial u_0}{\partial x} = \frac{p_{xx}}{2}\Big(y^2 - 2yh\Big) + \frac{(p_x - 1)}{2}\Big( - 2yh_x\Big) \ . \tag{6.3.23}$$

Combining Equations (6.3.20)−(6.3.23) gives the equation for the first order correction,

$$\frac{\partial}{\partial y}\left(\frac{\partial u_1}{\partial y}\right) = \frac{(p_x - 1)p_{xx}}{6}\Big(y^4 - 4hy^3 + 6h^2y^2\Big) \ . \tag{6.3.24}$$

Integrating Equation (6.3.24) twice with respect to $y$ and applying the boundary conditions (6.3.18) yields,

$$u_1 \ = \ \frac{(p_x - 1)p_{xx}}{180}\Big(y^6 - 6hy^5 + 15h^2y^4 - 36h^5y\Big) \ . \tag{6.3.25}$$

The final velocity profile is,

$$u \ = \ \frac{(p_x - 1)}{2}\Big(y^2 - 2yh\Big) + \frac{\delta(p_x - 1)p_{xx}}{180}\Big(y^6 - 6hy^5 + 15h^2y^4 - 36h^5y\Big) \ . \tag{6.3.26}$$

We eliminate $p$ in favour of $h$ from Equation (6.3.26) by a using similar argument as in Equation (6.2.4) to give,

$$u = \frac{(1 + Ch_{xxx})}{2}\left[\Big(2yh - y^2\Big) + \frac{\delta(Ch_{xxxx})}{90}\Big(y^6 - 6hy^5 + 15h^2y^4 - 36h^5y\Big)\right] \ . \tag{6.3.27}$$

Similarly, substituting the expansion for $T$ in Equation (2.3.11) gives the equation,

$$\frac{\partial^2 T_0}{\partial y^2} + \delta\frac{\partial^2 T_1}{\partial y^2} \ = \ -Br\left[\left(\frac{\partial u_0}{\partial y}\right)^2 + 2\delta\left(\frac{\partial u_0}{\partial y}\right)\left(\frac{\partial u_1}{\partial y}\right)\right] + \mathcal{O}(\delta^2) \ . \tag{6.3.28}$$

The leading order terms with respect to $\delta$ lead to Equation (6.2.6). The $\mathcal{O}(\delta)$ terms satisfy,

$$\frac{\partial^2 T_1}{\partial y^2} = -2Br\left(\frac{\partial u_0}{\partial y}\right)\left(\frac{\partial u_1}{\partial y}\right) \ . \tag{6.3.29}$$

Combining Equations (6.2.1) and (6.3.25) gives,

$$\begin{aligned} T_1 = -\frac{Br(p_x - 1)^2 p_{xx}}{840}\Big[&y^8 - 8hy^7 + 28h^2y^6 - 28h^3y^5 - 56h^5y^3 \\ &+168y^2h^6 - \left(\frac{148h^7}{(Bi\ h - 1)} - \frac{105Bi\ h^8}{(Bi\ h - 1)}\right)y\Big] \ . \end{aligned} \tag{6.3.30}$$

The final temperature profile is given by,

$$\begin{aligned} T &= -\frac{Br(Ch_{xxx}+1)^2}{12}\left[(y-h)^4 - h^4\left(1-\frac{Bi\ y}{(Bi\ h-1)}\right)\right] \\ &\quad + \left(\frac{Bi}{(Bi\ h-1)}\right)y - \delta\frac{Br(Ch_{xxx}+1)^2(Ch_{xxxx})}{840}\Big[y^8 - 8hy^7 + 28h^2y^6 \\ &\quad -28h^3y^5 - 56h^5y^3 + 168y^2h^6 - \left(\frac{148h^7}{(Bi\ h-1)} - \frac{105Bi\ h^8}{(Bi\ h-1)}\right)y\Big] \ , \end{aligned} \tag{6.3.31}$$

where the terms $p_x$ and $p_{xx}$ are eliminated using Equation (6.2.3). The graphical solutions for the velocity profiles will be plotted from Equation (6.3.27) and the temperature profiles from Equation (6.3.31) after the film height has been solved using the numerical method in the subsequent section.

## First order correction with a large Péclet number

The Péclet number in the energy equation has the same prominent role as the Reynolds number in the Navier−Stokes equations, see [1, 82, 92]. We now turn our attention to the contributions of the reduced Péclet number from the energy equation. This will therefore add the heat conduction terms to the equation governing the flow. If we consider a decreasing thermal conductivity term $\kappa \approx 0.01$, then the Péclet number $Pe = \rho c_p UL/\kappa = 2.6 \times 10^7$ and the Reynolds number $Pe = \rho UL/\mu_0 = 2.4 \times 10^3$ by using the values listed in Table 2.1 from Chapter 2. The reduced Péclet and Reynolds numbers gives $\varepsilon^2 Pe = 0.26 \approx 0.3$ and $\varepsilon^2 Re = 2.5 \times 10^{-5}$. The reduced Péclet number will lead to a typical error of about 30% and the reduced Reynolds number to $\varepsilon^2 Re = 2.5 \times 10^{-3}\%$. This shows that the contribution of the reduced Péclet number is higher compared to the reduced Reynolds number. We consider a situation whereby $\varepsilon^2 Pe > \varepsilon^2, \varepsilon^2 Re$ such that the terms of $\mathcal{O}(\zeta)$ are retained from the energy equation and the terms of $\mathcal{O}(\zeta^2, \varepsilon^2, \delta, PrEc)$ are neglected. The Brinkman number is still of order unity and it will be retained from the governing equations. This is made possible by the fact that in Equations (2.3.5) and (2.3.7), the two equations are not fully coupled and there is no direct feedback of the

velocity gradient into the energy equation and we cannot follow a similar procedure as discussed briefly in Chapter 5. Now Equation (2.3.7) takes the form,

$$\frac{\partial^2 T}{\partial y^2} + Br\left(\frac{\partial u}{\partial y}\right)^2 = \zeta\left(u\frac{\partial T}{\partial x} + v\frac{\partial T}{\partial y}\right) + \mathcal{O}(\zeta^2, \varepsilon^2, \delta, PrEc) \ . \tag{6.3.32}$$

The first order perturbation terms are now given by,

$$u = u_0 + \delta u_1 \ , \quad v = v_0 + \delta v_1 \ , \quad T = T_0 + \zeta T_1 \ , \tag{6.3.33}$$

where $u_1$, $v_1$ and $T_1$ are the first order perturbation terms. Substituting the expansion for $T$ in Equation (6.3.32) gives,

$$\frac{\partial^2 T_0}{\partial y^2} + \zeta\frac{\partial^2 T_1}{\partial y^2} = -Br\left(\frac{\partial u_0}{\partial y}\right)^2 + \zeta\left(u_0\frac{\partial T_0}{\partial x} + v_0\frac{\partial T_0}{\partial y}\right) + \mathcal{O}(\zeta^2) \ . \tag{6.3.34}$$

The leading order terms with respect to $\zeta$ leads to Equation (6.2.6). The $\mathcal{O}(\zeta)$ terms satisfy,

$$\frac{\partial^2 T_1}{\partial y^2} = u_0\frac{\partial T_0}{\partial x} + v_0\frac{\partial T_0}{\partial y} \ . \tag{6.3.35}$$

Combining Equations (6.2.4), (6.2.6) and (6.3.22) gives,

$$\begin{aligned}
\frac{\partial^2 T_1}{\partial y^2} = \quad & -\frac{(h_{xxx}+1)^2\ h_{xxxx}\ Br}{72}\Big(3(y-h)^6 - 2(y-h)^4 + \lambda_1\ h^4\ (y-h)^3 \\
& +6h(y-h)^3 - 6\lambda_1 h^6\Big(y - \frac{4h}{3}\Big)\Big) - \frac{(h_{xxx}+1)^3\ h_{xxxx}\ Br}{1728}\Big(18(y-h)^5 \\
& +3h(y-h)^4 + 6\lambda_1 h^4(y-h)^2 - \lambda_1 h^5(y-h)\Big) - \frac{\lambda_1}{12}\Big(2h_{xxxx}(y-h)^3 \\
& -6h_x(h_{xxx}+1)(y-h)^2 - h\ h_x(h_{xxx}+1)(y-h) - 12h_{xxxx}h^2(y-\frac{4h}{3})\Big) \\
& -\frac{(h_{xxx}+1)^2\ h_{xxxx}\ Br}{12}\Big((y-h)^6 + h^2(y-h)^4 - h^4\ (y-h)^2 - h^6\Big) \\
& -\frac{(h_{xxx}+1)^3\ h_{xxxx}\ Br}{6}\Big((y-h)^5 + h^2(y-h)^3 + h^3(y-h)^2 + h^5\Big) \\
& -\frac{\lambda_2\ (h_{xxx}+1)}{2}\Big((y-h)^3 + h(y-h)^2 + h^2 y\Big) \ ,
\end{aligned} \tag{6.3.36}$$

where,

$$\begin{aligned}
\lambda_1 &= \frac{Bi}{(Bi\ h - 1)} \ , \\
\lambda_2 &= \frac{\lambda_1\ Br\ (h_{xxx}+1)\ h_x}{12}\left[h^3\Big(h_{xxx}h + 4(h_{xxx}+1)\Big) + \frac{\lambda_1((h_{xxx}+1)h^4 - 12)}{12}\right] \ .
\end{aligned}$$

We will use the MAPLE program to find the solution for the temperature profile in Equation (6.3.36). Integrating Equation (6.3.36) twice with respect to $y$, and applying the boundary conditions (3.3.22) yields,

$$\begin{aligned}
T_1 = \quad & -\frac{(h_{xxx}+1)^2\ h_{xxxx}\ Br}{12}\Big(\frac{(y-h)^8}{112}-\frac{(y-h)^6}{10}+(y-h)^5\Big(\frac{\lambda_1 h^4}{120}-\frac{h}{20}\Big)\\
& -\frac{\lambda_1\ h^4\ (y^3-4y^2h)}{6}+\Big(\frac{5\lambda_1 h^8}{6(Bi\ h-1)}-\frac{\lambda_1^2 h}{3}\Big)y+\Big(\frac{\lambda_1 h^9}{120}-\frac{h^8}{112}+\frac{3h^6\lambda_1}{20}\Big)y\\
& -\Big(-\frac{\lambda_1 h^9}{120}-\frac{h^8}{112}+\frac{h^6}{20}\Big)\Big)-\frac{(h_{xxx}+1)^3\ h_{xxxx}\ Br}{12}\Big(\frac{(y-h)^7}{336}+\frac{h(y-h)^6}{1440}\\
& +\frac{\lambda_1 h^4(y-h)^4}{288}-\frac{h^5\lambda_1(y-h)^3}{864}+\Big(\frac{\lambda_1 h^8}{216}-\frac{23h^7}{10080}\Big)y-\Big(\frac{\lambda_1 h^8}{216}-\frac{23h^7}{10080}\Big)\Big)\\
& -\lambda_1\Big(\frac{h_{xxxx}}{120}\Big((y-h)^5-20h^2(y^3-4hy^2)\Big)-\frac{h_x(h_{xxx}+1)}{72}\Big(3(y-h)^4\\
& -h(y-h)^3\Big)-\Big(\frac{5h_x h^2}{6(Bi\ h-1)}-\frac{\lambda_1 h_{xxx}}{2}\Big)h^2y+h^4\Big(\frac{h_{xxx}}{120}+\frac{h_x(h_{xxx}+1)}{18}y\Big)\\
& -h^2\Big(\frac{1}{120}-\frac{h_x(h_{xxx}+1)h^2}{36}\Big)\Big)+\bar{T}\ , \qquad (6.3.37)
\end{aligned}$$

where,

$$\begin{aligned}
\bar{T} \ = \ & -\frac{(h_{xxx}+1)^2\ h_{xxxx}\ Br}{12}\Big(\frac{(y-h)^8}{56}+\frac{h^2(y-h)^6}{30}-\frac{h^4(y-h)^4}{12}\\
& -\frac{h^6}{2}y^2+\frac{293h^8}{840}+\Big(\frac{h^7}{(Bi\ h-1)}+\frac{127\lambda_1 h^8}{840}\Big)y\Big)\\
& -\frac{(h_{xxx}+1)^3\ h_{xxxx}\ Br}{6}\Big(\frac{(y-h)^7}{42}+\frac{h^2(y-h)^5}{20}+\frac{h^3(y-h)^4}{12}\\
& +\frac{h^5y^2}{2}-\frac{8h^7}{15}+\Big(\frac{h^6}{2(Bi\ h-1)}+\frac{h^7\lambda_1}{15}\Big)y\Big)\\
& -\frac{\lambda_2\ (h_{xxx}+1)}{2}\Big(\frac{(y-h)^5}{20}+\frac{h(y-h)^4}{12}+\frac{h^3y^2}{2}\\
& +\frac{11h^5}{30}+\Big(\frac{2h^5\lambda_1}{15}-\frac{h^4}{2(Bi\ h-1)}\Big)\Big)\ . \qquad (6.3.38)
\end{aligned}$$

The final temperature profile is given by the following equation,

$$\begin{aligned}
T \ = \ & -\frac{Br(h_{xxx}+1)^2}{12}\left[(y-h)^4+h^4\left(\lambda_1 y-1\right)\right]+\lambda_1 y\\
& -\zeta\Big[T_1+\bar{T}\Big]\ , \qquad (6.3.39)
\end{aligned}$$

where $T_1$ and $\bar{T}$ are defined by Equations (6.3.37) and (6.3.38) respectively. The numerical solution for the film height is now discussed.

## Numerical solution

The flux $Q$ is given by integrating Equation (6.3.26) from 0 to $h$,

$$Q = \int_0^h u dy = (1 + Ch_{xxx}) \left[ \frac{h^3}{3} - \frac{(111Ch_{xxxx})}{1260} h^7 \right] . \tag{6.3.40}$$

Equation (6.3.40) will provide the solution for the flux provided the terms such as $C, h_{xxx}$ and $h_{xxxx}$ are known. The film height may only be solved numerically. However, the series solution of the form,

$$h = h_0 + \delta h_1 , \tag{6.3.41}$$

gives the flux $Q = Q_0 + \delta Q_1$ as follows:

$$\begin{aligned} Q &= \int_0^h (u_0 + \delta u_1)\, dy \\ &= (1 + Ch_{0xxx}) \left[ \frac{{h_0}^3}{3} + \delta \left( \frac{{h_0}^3 Ch_{1xxx}}{3(1 + Ch_{0xxx})} + \left( {h_0}^2 h_1 - \frac{111Ch_{0xxxx}h_0^7}{1260} \right) \right) \right] . \end{aligned} \tag{6.3.42}$$

The leading order terms in Equation (6.3.42) then satisfy,

$$h_{0xxx} = \frac{1}{C} \left( \frac{3Q_0}{h_0^3} - 1 \right) . \tag{6.3.43}$$

Equation (6.3.43) is similar to Equation (6.2.8). A similar procedure as detailed in § 6.2 is used to find the solution for $h_0$. The first order correction term gives the expression for $h_{1xxx}$ in terms of $Q_1$ as,

$$h_{1xxx} = \frac{1}{C} \left[ \frac{111Ch_{0xxxx}h_0^4(1 + Ch_{0xxx})}{420} + \frac{3Q_1}{h_0^3} - \frac{3(1 + Ch_{0xxx})h_1}{h_0} \right] . \tag{6.3.44}$$

In Equation (6.3.44), for $x \to \infty$ we require $h_1 \to 0$ which implies that $Q_1 = 0$, so that $h$ remains unchanged, see [108]. Let $h_1 = y_1$, $h_{1x} = y_2$, $h_{1xx} = y_3$ and $h_{1xxx} = y_3'$ and then Equation (6.3.44) is solved using the following system of equations,

$$\begin{bmatrix} y_1' \\ y_2' \\ y_3' \end{bmatrix} = \begin{bmatrix} y_2 \\ y_3 \\ \frac{111Ch_{0xxxx}h_0^4(1+Ch_{0xxx})}{420\ C} - \frac{1}{C}\frac{3(1+Ch_{0xxx})y(1)}{C\ h_0} \end{bmatrix} . \tag{6.3.45}$$

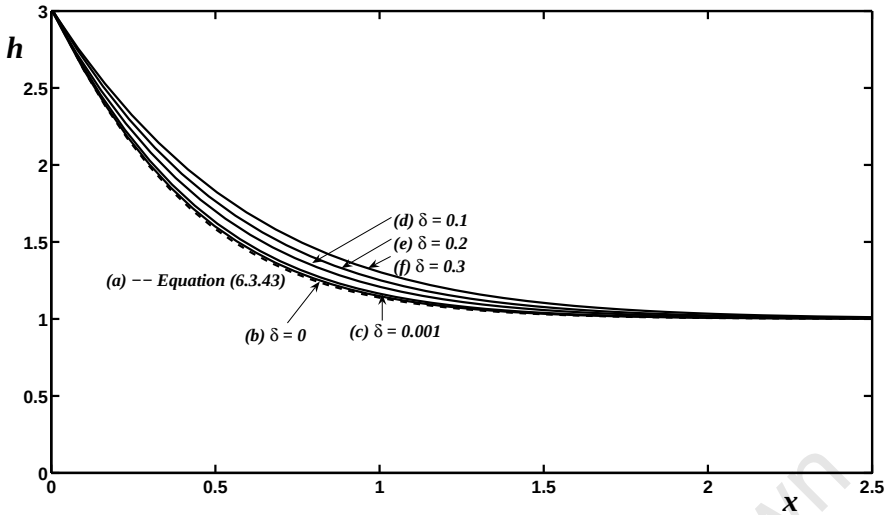


Figure 6.7: The fluid height versus the surface for Equation (6.3.45).

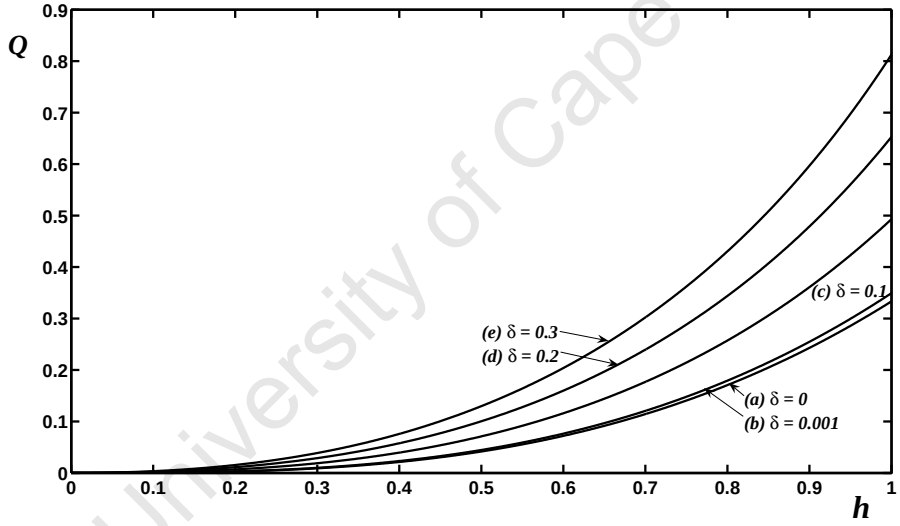




Figure 6.8: The profiles corresponding to Equation (6.3.42) for the flow rate.

The initial conditions as stated in § 6.2 are also used to solve the system of Equations (6.3.45) and a similar procedure will be carried out to find the solution for the film height.

In Fig. 6.7 the fluid height $h$ is displayed with progressively increasing values of the reduced Reynolds number $\delta$, namely $\delta = 0, 0.001, 0.1, 0.2$ and $0.3$ for curves (b) to (d) and curve (a) is plotted by using Equation (6.2.15). The figure represents the solution to

Equations (6.3.43) and (6.3.45) respectively. We have an excellent match of the results as shown in curves (a) and (b) without the effect of the reduced Reynolds number. Similar trends for the film height as shown in Fig. 6.3 are observed. The film height again in this case decreases in the direction of the flow, influenced by the competition between the two main forces which are the gravitational force and the surface tension force. In Fig. 6.8 the flow rate is shown with different values of the reduced Reynolds number. When the parameter $\delta$ increases, the flux increases in the layer and the flow rate is higher.

The velocity and temperature profiles are now plotted with different parameter values for $\delta$, $\zeta$ and the film height.

Fig. 6.9 shows four velocity profiles representing the solution for Equation (6.3.27). The curves display different values of the fluid height $h$ and the reduced Reynolds number is given by $\delta = 0.3$. In this figure, when the film height decreases from 3 to 1, the fluid velocity increases non−linearly across the layer to a maximum velocity at the free surface. The curves show that as the fluid height decreases, the competition between the surface tension and gravitational forces retards the flow and when the surface tension term is neglected, the gravitational force dominates the flow, and so the fluid flows faster as shown in curve (d). In Fig. 6.10 four curves representing the temperature profiles in Equation (6.3.39) are shown. Other parameters are given by $Br = 0.3$, $Bi = 0.3$ and $\delta$ is the same as it appears in Fig. 6.9. These curves are plotted for different film heights as shown in the figure. The curves illustrate that when the parameter $h$ decreases, the fluid temperature increases significantly due to heat generated by the internal flow processes. The fluid particles create heat upon colliding with one another and as a result the fluid temperature increases, particularly when the surface tension terms are neglected. The inclusion of the inertia terms shows a significant increase in the resulting flow profiles both for the velocity and the temperature of the fluid as compared to the curves which were observed in § 6.2. This shows that neglecting the inertia terms in the governing equations may under predict the resulting flow profiles.

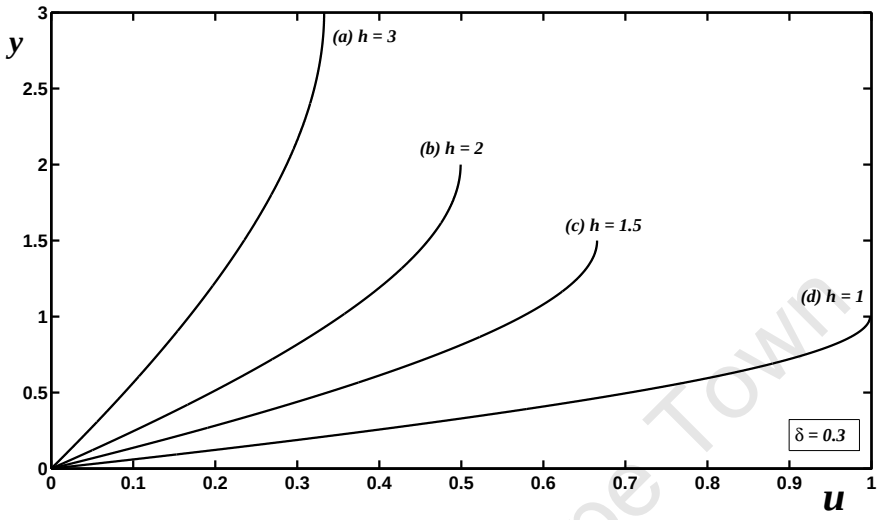


Figure 6.9: The velocity profiles for Equation (6.3.27): Boundary conditions (2.3.12).

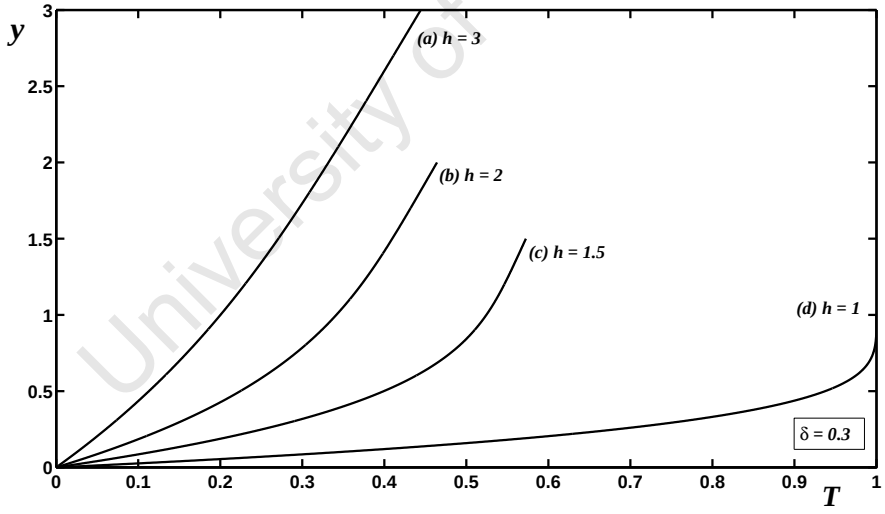


Figure 6.10: The temperature profiles for Equation (6.3.31): Boundary conditions (2.3.13).

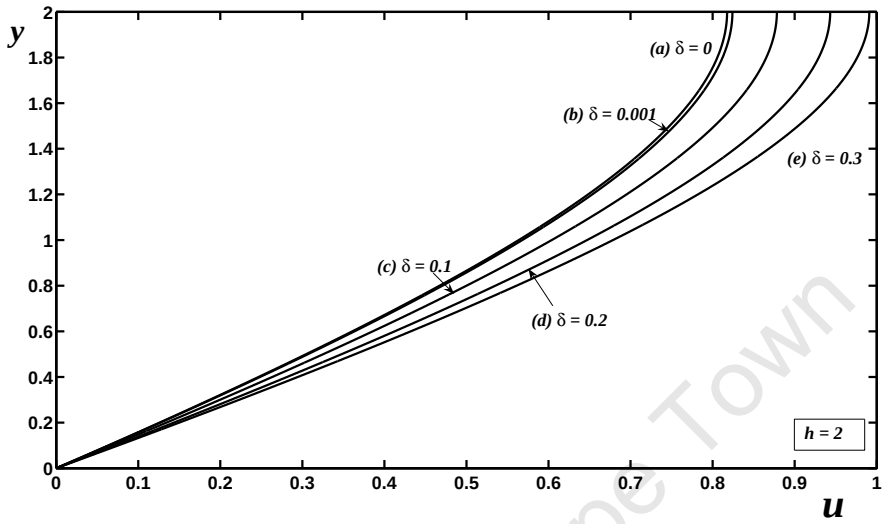


Figure 6.11: The velocity profiles for Equation (6.3.37): Boundary conditions (2.3.12).

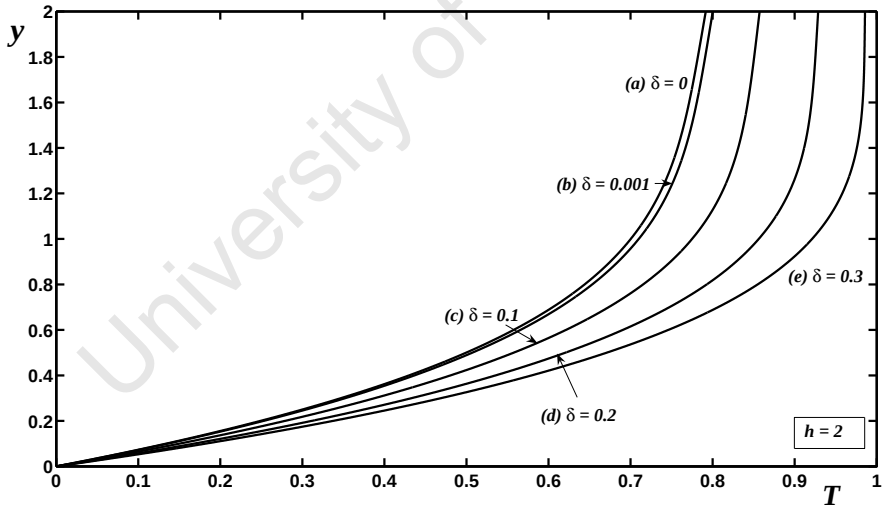


Figure 6.12: The temperature profiles for Equation (6.3.31): Boundary conditions (2.3.13).

Fig. 6.11 displays five velocity profiles with five different values for the reduced Reynolds number as shown in the figure with $h = 2$. All the curves are similar in shape and when $\delta$ increases the velocity of the fluid increases nonlinearly across the fluid layer to a maximum velocity at the free surface. Curve (a) with $\delta = 0$ displays the velocity profile without the effect of the reduced Reynolds number, while curve (b) with $\delta = 0.001$ shows the effect of the reduced Reynolds number which is closer to zero. The two curves compare well and the gap between the profiles is approximately 1%. However, when the parameter $\delta$ increases, its effect is shown in curves (c) through to (e) as the fluid velocity increases and the maximum values of the resulting flow profiles appear approximately 5% apart. The velocity profiles in curves (c) to (e) are more pronounced due to the addition of the correction terms to the flow. For $\delta > 0.3$, our solution will be physically unrealistic and a breakdown in our solution will occur since the maximum value for the reduced Reynolds number is 0.3. The effect of $\delta$ on the temperature profiles is shown in Fig. 6.12. Other parameters are given by $Br = 0.3$ and $Bi = 0.3$ and the values of $\delta$ are similar to those which are in Fig. 6.11. In this case again a trend similar to the velocity profiles, is observed for the temperature profiles. A significant increase in the fluid temperature is observed in curves (c) to (e). When $\delta$ increases the temperature of the fluid increases again as a result of viscous heat generation.

Fig. 6.13 shows four curves for the temperature profile with different values for the film height. These curves are similar to those observed in Fig. 6.10. The other parameters are given by $h = 1, 1.5, 2, 3$, $Bi = 0.3$, $\xi = 0.3$ and $Br = 0.3$. The curves represent the temperature profiles in Equation (6.3.39). When the fluid height decreases an increase in the fluid temperature is observed. The rise in temperature is caused by the internal flow processes. In the case where the surface tension terms are neglected, the temperature of the fluid increases significantly as shown in curve (d). In Fig. 6.14 the effect of the reduced Péclet $\zeta$ is shown. When $\zeta$ increases, the fluid temperature of the fluid increases due to heat generation by the viscous and heat conduction terms. Curve (a)

shows the temperature profile without the effect of the parameter $\zeta$ and it is closer to curve (b) in which $\zeta = 0.001$. The gap between the two curves at the free surface is approximately 0.1%. The maximum temperatures in curves (c) to (e) are much greater than the maximum temperature as displayed in curves (a) and (b). These curves indicate that as $\zeta$ increases, the heat conduction terms also make a greater contribution to heat generated in the layer which in turn increases the fluid temperature significantly.

### 6.3.1 Conclusion

The first order correction terms for the velocity and temperature profiles were obtained using an analytical perturbation method. However, the Runge−Kutta numerical technique was used to derive the fluid height. In general, when the parameter $\delta$ increases from 0 to 0.3, the film height decreases in the direction of the flow due to the effect of the surface tension and gravitational forces. Consequently, both the fluid velocity and fluid temperature increase significantly as the film height decreases. The maximum velocity for the resulting profiles shows a better improvement due to the inclusion of the inertia terms. The effect of the parameter $\delta$ was investigated and the results for the flow rate shows that as $\delta$ increases, the flux increases in the layer, and the flow rate is higher. Its effect on the resulting velocity and temperature profiles illustrates that as $\delta$ increases, the velocity and temperature increases significantly. The effect of the reduced Péclet number $\zeta$ also showed that the temperature of the fluid due to heat generation by the viscous and heat conduction terms, increases significantly when $\zeta$ increases. The Reynolds number displayed significantly greater maximum values for the velocity profiles when $\delta$ lies between 0.1 and 0.3, illustrating the effect of the first order correction terms. Similarly the reduced Péclet number in the region between 0.1 and 0.3 also showed a significant improvement of the temperature profiles as compared to the zeroth order temperature profiles.

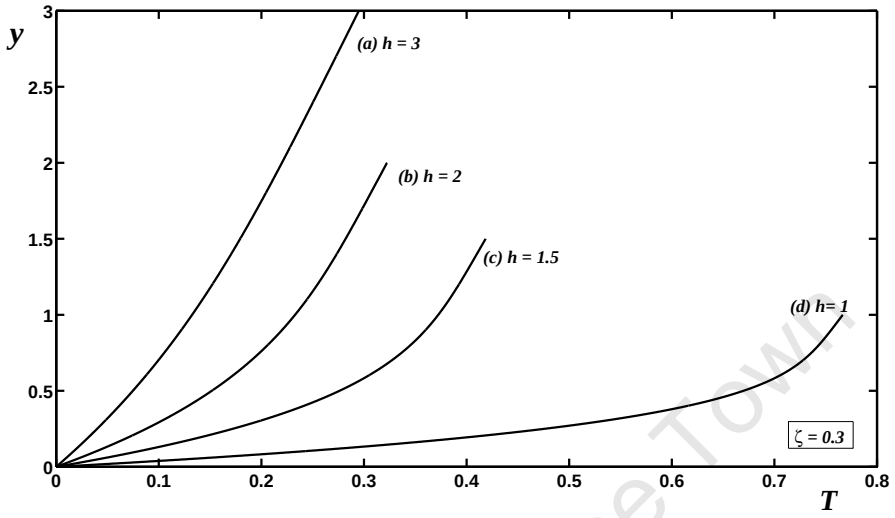


Figure 6.13: The temperature profiles for Equation (6.3.39): Boundary conditions (2.3.13).

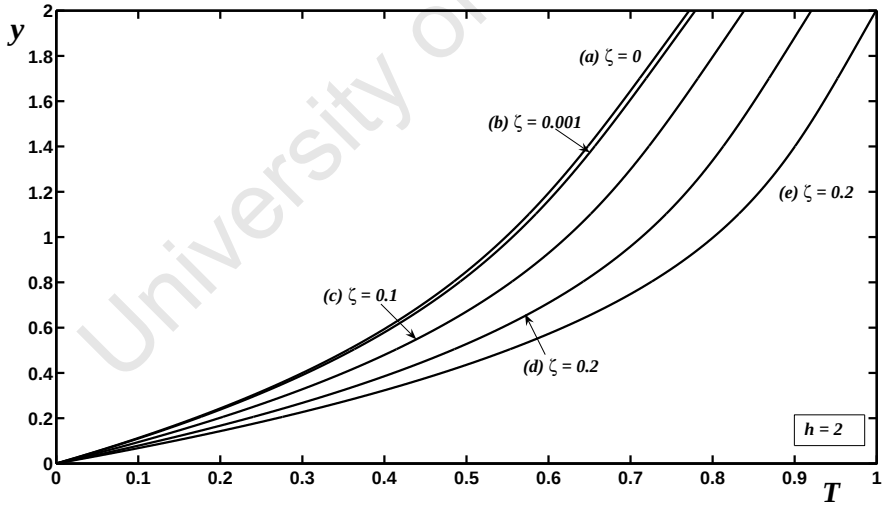


Figure 6.14: The effect of $\zeta$ on the temperature profiles for Equation (6.3.39): Boundary conditions (2.3.13).

# Chapter 7

# Conclusion and further work



In this study the flow of Newtonian and non−Newtonian fluids were investigated using the continuity, Navier−Stokes and energy equations. The main objective was to develop a thin film mathematical model that governs the flow with a free surface and between parallel plates. The governing equations were reduced in line with the lubrication theory, and solved subject to their appropriate governing equations for the flow rate, pressure, velocity and temperature profiles.

To set up the foundation of this work, a simple laminar flow of a Newtonian fluid with a free surface and between parallel plates was investigated in Chapter 2. This chapter successfully laid down the foundation and standard results were obtained for a Newtonian fluid with constant viscosity. The results for flow with a free surface illustrated that the velocity of the fluid increases nonlinearly across the layer to its maximum velocity at a free surface. The temperature of the fluid also increases across the layer due to heat generation by the action of a viscous force. The effect of the flow controlling parameters, that is, the Brinkman and the Biot numbers, were also investigated. The results presented showed that when Brinkman number increases the temperature of the fluid raises, due to viscous heat dissipation. The Biot number also showed that the temperature of the fluid increases across the layer and the temperature profiles flatten at the free surface which is a result of heat lost to the atmosphere. For flow between parallel plates two cases were explored,

that is, the pressure gradient driven case and the applied shear force driven case. When the applied shear force drives the flow, the maximum velocity and temperature of the fluid occur at the top plate. When both the applied shear force and the pressure gradient drives the flow, the resulting velocity profiles for the fluid appear near the moving plate, probably because the dominant driving force might be the applied shear force caused by the movement of the upper plate. The temperature of the fluid increased across the layer with its maximum value occurring near the top plate, since both the pressure gradient and the applied shear force act to increase heat generation. For the pressure driven case the maximum values for the velocity of the fluid occurred at the centre of the plates. The effect of the pressure gradient on the resulting flow profiles was further investigated and the results showed that when the pressure gradient is zero, a linear profile is observed. When the pressure gradient is positive, the velocity profile increased in the direction of the flow while for a negative pressure gradient a reverse flow is observed and the maximum velocity occurs outside the boundaries. The resulting temperature profile for the case where the pressure gradient is zero showed a parabolic profile. For positive pressure gradients the maximum temperatures occurred near the top plate, whilst the opposite is true for negative pressure gradients. The effect of the Brinkman number on the resulting temperature profiles showed a significant increase in the fluid temperature when the Brinkman number becomes increasingly large. In particular, for the cases where the pressure gradient is positive, the maximum temperature is significantly higher near the top plate and the opposite is true for the negative pressure gradient.

In Chapter 3, the shear rate dependent viscosity models, namely the power law model, the Carreau model, and the Ellis model, were applied to a general two-dimensional free surface flow. The power law and Ellis models allowed for analytical progress. In general, the Carreau model required a numerical method to gain full solutions to the governing equations. However, when the viscosity variation is small (that is, $l \ll 1$) an asymptotic technique is used to simplify the governing equations and so an approximate solution

could be found. Furthermore, when the power law index is zero or when $n = 2$, the governing equations allowed for analytical progress. The asymptotic and analytical cases are studied in order to have more results to compare with the numerics.

For the power law model, we investigated first the effect of the power law index. The viscosity versus shear rate was plotted with different values of the power law indices. This showed that when $n < 1$, the fluid viscosity decreased when the shear rate increased, giving rise to a shear thinning behaviour and for $n > 1$ the viscosity of the fluid increased with increasing shear rate also illustrating a shear thickening behaviour, while for $n = 1$ a Newtonian fluid was retrieved. The resulting flow profiles for a shear thinning fluid showed velocity profiles which were lower than the Newtonian case. The velocity profiles were higher for shear thickening fluids than the Newtonian case. This illustrates that the net driving force (presumably the gravitational force) for the fluid is higher for shear thickening fluids, which results in high velocity profiles for a shear thickening fluid. The resulting temperature profiles showed a similar trend to the velocity profiles. The fluid temperature increased significantly for shear thickening fluids and for shear thinning fluids an increase in the fluid temperature is less pronounced. This is a result of the action of the viscous force, which results in an increase in heat generation and it is significantly higher for shear thickening fluids. When the power law index increases from 0.1 to 3, the profiles for the flow rate showed that the flux increased in the layer, the flow rate is higher. The effect of the Brinkman number on the temperature profiles was also investigated and the results showed that when Brinkman number increases, the temperature of the fluid increases due to heat dissipation. The temperature profiles illustrating the effect of Brinkman number were plotted with a fixed value of $n = 0.5$ representing shear thinning fluids and $n = 1.5$ for shear thickening fluids. The temperature profiles for the shear thickening fluids were significantly higher than those for shear thinning fluids. The results illustrated that shear thickening fluids react more quickly to heat dissipation than the shear thinning fluids, in which case the fluid temperature increases when the Brinkman

number increases.

For the Carreau model, an asymptotic approximation was carried out first for $l \ll 1$. Two cases were explored for the power law index, that is, the case where the power law index is equal to zero and the power law index is equal to 2. These allowed for analytical progress. Subsequently a numerical scheme, namely the Newton Raphson algorithm, was developed to solve the full set of the governing equations. The viscosity versus shear rate were plotted to illustrate the behaviour of the fluid viscosity when both the non−dimension parameter $l$ and the power law index $n$ are varied. The results showed that when $l$ increases for shear thinning fluids, the viscosity of the fluid decreases as the shear rate increases. The opposite is true for shear thickening fluids. For the power law index, the viscosity of the fluid decreased with increasing shear rate for shear thickening fluids with $n > 1$ and the opposite is true for shear thinning fluids with $n < 1$. The effect of these flow controlling parameters on the resulting velocity, flow rate and temperature profiles, were obtained. The results for the flow rate showed that when either $l$ or $n$ increased, the flux increased in the layer and the flow rate was higher. The results for the velocity profiles illustrated that the fluid velocity increased significantly when $l$ increases for shear thinning fluids and the opposite is true for shear thickening fluids. When $l$ increases, the viscosity of the fluid decreases as the shear rate increases and the velocity increases as a result of less resistance force to the flow. Similar flow profiles were observed with respect to the temperature. The temperature of the fluid increased when the parameter $l$ increased for shear thinning fluids and the converse is true for shear thickening fluid. The resulting flow profiles illustrating the effect of the power law index on the velocity and temperature profiles showed that both the velocity and the temperature of the fluid increased when the power law index $n$ decreased. The case where $n = 0$ also showed that the velocity and the temperature of the fluid increases when the non−dimensional parameter $l$ increases and the opposite is true for shear thickening fluids. The results obtained using the Newton Raphson numerical method were also compared to the analytical results and larger values

of $l$ were investigated. The results obtained numerically and analytically for the velocity and temperature profiles, were compared for small values of $l$. The curves for the velocity and temperature profiles were in agreement in particular when $l = 0.3$. The effect of large values of $l$ on the resulting flow profiles was investigated and the results showed that the velocity and the temperature of the fluid increased significantly when $l$ increased for shear thinning fluids and the converse holds for shear thickening fluids. The numerical solution is preferable since it can be used for larger values of $l$ but the asymptotic solution is useful as a benchmark. The effect of the power law index on the resulting velocity of the fluid showed that when $n$ decreased, the fluid velocity increased across the layer to its maximum at the free surface due to less resistance force to the flow. The results for the temperature profile also showed that the temperature of the fluid increased as the power law index decreased, due to heat generation by the viscous force.

The Ellis model was investigated analytically to solve for the flow rate, velocity and temperature profiles. These profiles were plotted with different values of the non−dimensional parameter $\phi$ and the power law index $\alpha_1$. The viscosity versus shear rate were plotted with different values of $\phi$ and the results showed that as the parameter $\phi$ increases, the viscosity of the fluid decreases when the shear rate increases for shear thinning fluids and the opposite is true for shear thickening fluids. For the power law index, the fluid viscosity decreases when the shear rate increases for shear thinning fluids, while the converse holds for shear thickening fluids. The flow rate showed that when either $\phi$ or $\alpha_1$ increases, the flux increases in the layer. The results for the velocity profiles illustrate that when $\phi$ increased, the velocity of the fluid increased significantly due to less resistance force to the flow for shear thinning fluids. A similar pattern for the velocity profiles were observed for the shear thickening fluids (hydroxylethycellulose fluid). The profiles illustrated that the more viscous the fluid the higher the velocity profiles. The temperature profiles plotted showed that the fluid temperature increases across the layer when $\phi$ increases, due to heat generation by the action of viscous term. The effect of the power law index on the

resulting velocity and temperature profiles was investigated. The results show that the velocity of the fluid increased when the power law index decreased, with its maximum velocities occurring at the top layer. The velocity profiles for a shear thinning fluid are more pronounced compared to a shear thickening fluid since shear thinning fluids are less viscous and have less resistance force to the flow. The temperature of the fluid increased as the power law index $\alpha_1$ decreased.

The study was then extended to a comparison of the shear rate dependent viscosity models using experimental data. The parameter values for several materials, namely ABS solution, aluminum soap, fabric softener and yoghurt, were obtained from the literature. Furthermore, the models were investigated for shear thickening fluids using CWS and SBS materials. The viscosity versus shear rate for these materials was plotted and the power law model was shown to be far from ideal when modelling thin film fluids, particularly at low shear rates regions. The comparisons of these viscosity models showed that at a low shear rate region, the power law over predicts the materials. However, at a high shear rate range the power law model also gave a good fit to data on certain materials, particularly yoghurt. At low shear rate regions the Carreau and Ellis models showed a Newtonian behavour, but did not coincide with Newtonian transitions to power law behaviour at high shear rate regions. The velocity profiles were also plotted, including the Newtonian model, and compared. The resulting velocity profiles illustrated that the Carreau and Ellis models led to similar results. The power law model again gave inaccurate velocity profiles as compared to the velocity profiles predicted by the Newtonian, Carreau and Ellis models. The power law model generally fails to predict the flow accurately at low shear rate regions, for both shear thinning and shear thickenning fluids. This model which has been trusted over the years can be supplemented by using the Carreau and Ellis models. The Ellis model compared fairly well to the Carreau model.

In Chapter 4, the study of shear rate dependent viscosity models was carried out for flow between parallel plates. The two main driving forces for the flow were the applied shear

force by the movement of the upper plate and the pressure gradient.

For the power law model, the velocity and temperature profiles were plotted for different values of the power law index. The corresponding Newtonian velocity and temperature profiles were obtained when the power law index $n = 1$. When $n$ increases, both the velocity and temperature of the fluid increase slightly, particularly for a shear thinning fluid. However, the velocity and temperature profiles are much higher for shear thickening fluids. The applied shear force by the movement of the upper plate presumably dominates the flow, since the maximum velocity profiles occur near the top plate. For the temperature profiles, the competition between the applied shear force and the pressure gradient acts to increase heat generation and subsequently the temperature of the fluid increases and it is more pronounced for shear thickening fluids. The effect of the Brinkman number on the temperature profiles showed that the temperature of the fluid increased significantly as Brinkman number increased. The maximum temperature for the shear thickening fluid occurred near the top plate, and the results showed that the applied shear force and the pressure gradient act to create heat and so the temperature of the fluid rises.

The flow of a Carreau fluid between parallel plates was also investigated. Three cases were investigated, in particular the situation where viscosity variation is small, that is, $l \ll 1$, the power law index $n = 0$ and $n = 2$. The asymptotic results show that the velocity and temperature of the fluid increased when $l$ increased, for shear thinning fluids and their maximum velocities and temperatures occur at the top plate. The opposite is true for shear thickening fluids, where the fluid velocity and temperature increased as $l$ decreased. The effect of the power law index on the velocity and temperature profiles was also investigated. The results showed that for a shear thinning fluid, the velocity increases gradually with an approximately 0.1% gap between the resulting flow profiles. However, the velocity profiles for shear thinning fluids are significantly higher than for shear thickening fluids. The Newtonian velocity profile is retrieved when $n = 1$. For shear thickening fluids, the gap between the profiles was more pronounced and the velocity of

the fluid increases significantly as $n$ decreases. The temperature of the fluid increases as the power law index increases and so heat generation by the action of the pressure gradient and the applied shear force, is high when $n$ decreases. In the event where the power law index $n = 0$, the velocity and temperature of the fluid again increased evenly when the non−dimensional parameter $l$ increased and the converse hold for the case $n = 2$. The velocity and temperature profiles appeared approximately 0.1% apart when $n = 0$. The velocities profiles derived from the analytical methods and the numerical method, were compared and the profiles were plotted on the same set of axes. Similarly, the temperature profiles were plotted on the same set of axes for comparison purpose. Comparison of the three sets of curves were in good agreement, in particular when $l = 0.3$. Large values of $l$ were further investigated and the resulting flow profiles showed that the velocity and temperature of the fluid increased significantly when $l$ increased. The maximum velocity of the fluid appears near the moving plate for values of $l < 3$ and the maximum velocity occurs near the centre of the plates for $l > 5$. The driving force (probably the pressure gradient) for the fluid is higher towards the centre of the plates as $l$ increases significantly. Similarly, the temperature of the fluid is more pronounced near the centre of the plates for larger values of $l$. This shows that heat generation is more pronounced near the centre of the plates. The opposite is again true for shear thickening fluids with $n = 2$ and as expected, the velocity and temperature of the fluid increases when $l$ decreases. The effect of the power law index on the velocity and temperature profiles was again investigated and the results showed that the velocity and temperature of the fluid increased significantly as $n$ decreased. The Newton−Raphson method was employed to investigate the effect of large values of $l$ on the resulting velocity and temperature profiles. The numerical results showed for the velocity and temperature of the fluids with increasing values of $l$, were significantly higher as compared to the asymptotic case where $l \ll 1$ was considered.

The Ellis model was investigated for flow between parallel plates to illustrate the effect of the non−dimensional parameter $\phi$ and the power law index $\alpha_1$ on the resulting velocity

and temperature profiles. The results showed that the velocity of the fluid increases when the non−dimensional parameter $\phi$ increases with the maximum values occurring near the top plate for values of $\phi > 1$. This is a result of less resistance force to the flow and the fluid velocity is more pronounced for shear thinning fluids as compared to shear thickening fluid (in particular hydroxylethycellulose fluid). This is a result of the applied shear force by the movement of the top plate which seems to dominate the flow. The temperature profile showed that for $\phi > 1$ the temperature of the fluid increases significantly in the direction of the flow with maximum values for the temperature occurring near the top plate. However, for values of $\phi > 2$ the maximum value for the temperature occurs at the centre of the plates for both shear thinning fluids and shear thickening fluids. The increase in the temperature of the fluid is due to the heat generation by the action of the applied shear force and the pressure gradient, which is high near the centre of the plates. The effect of the power law index $\alpha_1$ on the resulting velocity and temperature profiles was shown. The velocity of the fluid increases significantly for shear thickening fluids and their maximum velocities again occur near the top plate. The results for the temperature profiles showed that the maximum temperature of the fluid occurs near the centre and the temperature becomes increasingly large for shear thickening fluids, which illustrated that shear thickening fluids, respond quickly to heat generation as the power law index increases.

In Chapter 5, a model describing the flow of a thin film with exponential viscosity variation with temperature, which is known as the Reynolds equation, was investigated for flows both with a free surface and between parallel plates. Generally, the model required a numerical method to solve for the full solutions of the velocity and temperature profiles.

For flow with a free surface, the resulting governing equation required a numerical method to gain full solution. However, an asymptotic technique was used to gain an analytical solution when the viscosity variation is small. The results were obtained using an asymptotic technique and the fourth order Runge−Kutta integration scheme. Experimental

values for lubricating oil were used to determine the value of $\alpha$ for the asymptotic approximation terms. The viscosity versus temperature showed that when the temperature variation parameter increases, the viscosity of the fluid decreases significantly as the temperature of the fluid increases. The results further showed that when the non−dimensional temperature variation parameter increases, the fluid velocity and temperature increases. The effect of the flow controlling parameters such as the Biot and the Brinkman numbers were again investigated. The temperature profiles illustrating the effect of the Biot number showed that the temperature of the fluid increases significantly when the Biot number decreases, due to heat lost from the fluid to the atmosphere. The temperature profiles flatten out at the free surface as Biot number decreased. Due to less resistance force to the flow, the velocity of the fluid increases as the Biot number decreases. The numerical results were compared with the asymptotics. The Newtonian cases for both the temperature and velocity of the fluid were retrieved when $\alpha$ is zero. The results showed good agreement particularly when $\alpha = 0.1$ and 0.5. When $\alpha$ increases, the temperature and the velocity of the fluid increases significantly. However, when $\alpha = 58$, a change in the flow structure is observed from the velocity profiles. Since the viscosity of the fluid decreases exponentially when $\alpha$ increases, the prediction of the velocity profiles shows a different flow structure. This therefore causes the fluid to behave like a Newtonian fluid, in particular when $\alpha \geq 58$. The effect of a Brinkman number was also investigated. The results showed that when $Br$ increased, the temperature of the fluid increased due to the viscous heat generation term and the velocity of the fluid increased significantly due to less resistance force to the flow.

In addition, two scenarios for flow between parallel plates were studied. Firstly, the model was investigated without the effect of the pressure gradient and so analytical progress was possible. The variation of the maximum temperature with the Brinkman number was shown and the resulting flow profiles displayed the two solution branches in which the lower branch is stable and the upper branch unstable. In this case two possible

maximum temperatures can be observed one from the lower branch and one from the upper branch. The temperature and velocity profiles were plotted using these values for the different Brinkman numbers. The results showed that for a Newtonian fluid the profiles for the temperature and velocity of the fluid are linear, since the viscosity is constant. For non−Newtonian fluids, the maximum temperature of the fluid occurs near the top plate due to the applied shear force by the movement of the upper plate, which acts to create heat generation. The combined shear and pressure driven cases was solved using a numerical technique. The fourth order Runge−Kutta and shooting methods were employed to derive the full solution for the velocity and temperature profiles. When both the pressure gradient and the applied shear force drives the flow, the resulting temperature and velocity profiles were slightly higher than the case where only the applied shear force drives the flow. A general case for the Brinkman number variation was also investigated. The Brinkman number was allowed to vary between 0 and 25, and the results showed that the velocity and the temperature of the fluid increased when $Br$ increased, illustrating the effect of the combined pressure gradient and applied shear force by the movement of the upper plate, which act to increase the resulting velocity and temperature of the fluid.

Chapter 6, considered the effect of both the surface tension and the first order correction terms for the lubrication theory, with different film height. In both cases, the investigation was carried out using an analytical method. However, the relationship between the surface and the fluid height could only be determined numerically and so the Runge−Kutta scheme was developed to achieve this. The resulting velocity profiles were plotted with different values of the film height and the results showed that the velocity of the fluid increases as the film height decreases due to the competition between gravitational and surface tension forces. For the case where surface tension force is neglected, the velocity profile is more pronounced. The temperature profiles showed similar trends to the velocity profiles. The temperature increased when the film height decreased due to viscous heat dissipation. The numerical results for the film height decreased when the perturbation

parameter increased due to the competition between the gravitational and the surface tension forces.

The first order correction terms for lubrication theory were investigated. In general, when the reduced Reynolds number increases from 0 to 0.3 the film height decreases in the direction of the flow due to the effect of the surface tension and gravitational forces. The results for the velocity and temperature profiles showed that the profiles increased when the fluid height decreased. The maximum velocity for the resulting flow profiles showed a better improvement due to the inclusion of the inertia terms. The effect of the reduced Reynolds number on the flow rate showed that as the reduced Reynolds number increased, the flux increases in the layer and the flow rate was higher. The effect of the reduced Reynolds number on the resulting velocity and temperature profiles illustrated that as $\delta$ increased, the velocity and temperature increased significantly. The effect of the reduced Péclet number $\zeta$ was also investigated and the results showed that the temperature of the fluid increased significantly, as $\zeta$ increased. The Reynolds number displayed significantly greater maximum values for the velocity profiles when $\delta$ lies between 0.1 and 0.3 illustrating the effect of the first order correction terms. Similarly the reduced Péclet number in the region between 0.1 and 0.3 also showed a significant improvement of the temperature profiles as compared to the zeroth order temperature profiles.



# Further work

The models and the numerical techniques developed in this work provided considerable insight into the flow behaviour of Newtonian and non−Newtonian fluids for both flows with a free surface and parallel plates. However, this study could be developed further and in the following ways:

- The shear rate dependant viscosity models and the temperature dependant viscosity model may be investigated in a circular pipe to monitor the flow characteristics of

each model. This has a wide range of industrial applications such as pipe lines transporting fuel, oil and water for agricultural purposes. The shear rate dependent viscosity models may become handy to improve durability of equipment and of production.

- The shear rate dependent viscosity models for both flows with a free surface and between parallel plates may be coupled to fluid instability theory. Collaboration work should be carried out with various institutions and companies to investigate the applications of these models in an experimental setting.

- In future, the temperature dependent viscosity model may be improved in a number of directions. Firstly, between parallel plates, the temperature at the plates must be allowed to vary. This is significant when the temperature of the fluid is high. For situations where there are two possible maximum temperatures, the higher value is associated with an unstable solution. This will permit energy dissipation through the boundaries and may change this diagnosis. It will require variation in the $x$-direction, as the surface heats-up. With the current model, this variation was shown to be negligible at the leading order, but may become important with the added heat flow.

- It would be interesting to extend Chapter 6 to investigate the first order correction terms for the lubrication theory between parallel plates and in addition to allow the viscosity of the fluid to vary. This has a wide range of industrial applications such as coating films.

- The shear rate dependent models may be extended using numerical schemes to investigate non−Newtonian fluids, such as Bingham fluids with yield stress, which may increase the applicability of this work significantly.

- The shear rate dependent viscosity models may be extended again using experimen-

tal data to monitor the discrepancy which may occur between theory and experiment. **********

# Bibliography


[1] D. J. Acheson. *Elementary Fluid Dynamics*. Oxford University Press, 1990.

[2] F. T. Akyildiz and K. Vajravelu. Orthogonal cubic spline collocation method for the nonlinear parabolic equation arising in a non-Newtonian flow. *Appl. Math. Comp.*, 189:462–471, 2007.

[3] F. Alhama and J. Zueco. Application of a lumped model to solids with linearly temperature dependent thermal conductivity. *Appl. Math. Modelling*, 31:302–310, 2007.

[4] N. Ali and T. Hayat. Peristaltic motion of Carreau fluid in an asymmetric channel. *Appl. Math. Comp., Article in press*, 193(2):535–552.

[5] H. I. Anderson, S. Fu, T. G. Myers, and C. P. Thompson. UV induced fluorescence and comparative velocity measurement of thin liquid film. $9^{th}$ *Int. Symposium on Flow Visualisation, Heriot-Watt University, Edinburgh*, 31:1–7, 2000.

[6] A. M. Azouni, C. Normand, and G. Pétré. Surface tension driven flows in a thin layer of a water-n-heptanol solution. *J. Colloid Interface Sci.*, 239:509–516, 2001.

[7] S. Bair. A Reynolds-Ellis equation for line contact with shear thinning. *Tribology Int. Elsevier Ldt*, 39:310–316, 2006.

[8] M. T. Balhoff and K. E. Thompson. A macroscopic model for shear thinning flow in packed beds based on network modelling. *Chem. Eng. Sci.*, 61(1):698–719, 2006.

[9] H. A. Barnes, J. F. Hutton, and K. Walters. *An Introduction to Rheology.* Elsevier Sci. Publishers B. V., 1989.

[10] G. K. Batchelor. *An Introduction to Fluid Dynamics.* Cambridge University Press, 2000.

[11] T. Berbernes and D. Eberly. *Mathematical Problems from Combustion Theory*, volume 83. Springer Verlag, Appl. Math. Sci., 1989.

[12] R. B. Bird, W. E. Stewart, and E. N. Lightfoot. *Transport Phenomenon,* $2^{nd}$ *edition.* John Wiley & Sons, 2002.

[13] S. Blairs and M. H. Abbasi. Correlation between surface tension and critical temperatures of the liquid metals. *J. Colloid Interface Sci.*, 304:549–553, 2006.

[14] G. J. Borse. *Numerical Methods with MATLAB.* PWS Publishing Co., 1997.

[15] A. Bourgeat, O. Gipouloux, and E. Marušić-Paloka. Mathematical modelling and numerical simulation of a non-Newtonian viscous flow through a thin filter. *SIAM J. Appl. Math.*, 62(2):597–626, 2001.

[16] J. B. Boxall, I. Guymer, and A. Marion. Transverse mixing in sinuous natural open channels flows. *J. Hydraulic Research*, 41(2):153–165, 2003.

[17] R. L. Burden and J. D. Faires. *Numerical Analysis,* $7^{th}$ *edition.* Thompson Learning, 2001.

[18] K. Casson and D. Jonson. Surface tension driven flow due to the adsorption and desorption of colloidal particles. *J. Colloid Interface Sci.*, 242:279–283, 2001.

[19] R. Chebbi. Laminar flow of power law fluids in the entrance region of a pipe. *Chem. Eng. Sci.*, 57(1):4435–4443, 2002.

[20] C. H. Chen. Marangoni effects on forced convection of power law liquids in a thin film over a stretching surface. *Phys. Letters A*, 370:51–57, 2007.

[21] R. P. Chhabra and J. F. Richardson. *Non-Newtonian Flow in the Process Industries*. Butterworth & Heinemann, 1999.

[22] S. W. Churchill. *Viscous Flows, the Practical Use of Theory*. Butterworth Series in Eng., 1988.

[23] V. N. Constantinescu. *Laminar Viscous Flow*. Springer Verlag, 1995.

[24] A. Costa and G. Macedonio. Viscous heating in fluids with temperature dependent viscosity: implications for magma flows. *Non-linear Processing Geophys.*, 10:545–555, 2003.

[25] H. W. Cox and C. W. Macosko. Viscous dissipation in die flows. *A.I.Ch.E., J.*, 20(4):785–795, 1974.

[26] J. Davis and S. M. Troian. Influence of boundary slip on optimal excitations in thermocapillary driven spreading. *Physical Rev, E*, 70(46309):1–11, 2004.

[27] J. F. Douglas, J. M. Gasiorek, and J. A. Swaffield. *Fluid Mechanics,* $3^{rd}$ *edition*. Longman Group, Ltd, 1998.

[28] T. D. Eastop and A. McConkey. *Applied Thermodynamics for Engineering Technologists,* $3^{rd}$ *edition*. Longman Group, Ldt, 1978.

[29] E. M. A. Elbashbeshy and M. A. A. Bazid. The effect of temperature dependant viscosity on heat transfer over a continuous moving surface. *J. Appl. Phys.*, 33:2716–2721, 2000.

[30] E. M. A. Elbashbeshy and M. A. A. Bazid. The effect of temperature dependant viscosity on heat transfer over a continuous moving surface with variable internal heat generation. *Appl. Math. Comp.*, 153(3):721–731, 2003.

[31] M. H. Eres, L. W. Schwartz, and R. V. Roy. Fingering phenomena for driven coating films. *Phys. Fluids*, 12(6):1278–1295, 2000.

[32] J. Feng and L. G. Leal. Pressure driven channel flows of a model liquid-crystalline polymer. *Phys. Fluids*, 11(10):2821–2835, 1999.

[33] W. Florez, H. Power, and F. Chejne. Multi-domain DRM boundary element method for non-isothermal non-Newtonian Stokes flow with viscous dissipation. *Int. J. Mum. Methods Heat Fluid Flow*, 13(6):736–768, 2003.

[34] S. Fomin, T. Hashida, and J. Watterson. Fundamentals of steady state non-Newtonian rimming flow. *J. non-Newtonian Fluid Mech.*, 111:19–40, 2003.

[35] A. C. Fowler. *Mathematical Models in the Applied Sciences*. Cambridge University Press, 1997.

[36] R. W. Fox, A. T. McDonald, and P. J. Pritchard. *Introduction to Fluid Mechanics, $6^{rd}$ edition*. John Wiley & Sons, 1998.

[37] A. Y. Ghaly and M. A. Seddeek. Chebyshev finite difference method for the effects of chemical reaction, heat and mass transfer on laminar flow along a semi-infinite horizontal plate with temperature dependent viscosity. *Chaos Solutons Fractals*, 19:61–70, 2004.

[38] J. A. Gonzalez-Leon, S. W. Ryu, S. A. Hewlett, S. H. Ibrahim, and A. M. Mayes. Core-Shell polymer nanoparticles for baroplastic processing. *Macromolecules*, 38:8036–8044, 2005.

[39] T. B. Goudoulas, E. F. Kastrinakis, and S. G. Nychas. Rheological aspects of dense lignite water suspensions, time dependence, preshear and solids loading effects. *Rheol Acta*, pages 73–85, 2003.

[40] A. K. Gupta and S. N. Purwar. Melt rheological properties of polypropylene/SEBS (styrene-ethylene butylene-styrene block copolymer) blends. *J. Appl. Polymer Sci.*, 29(1):1079–1093, 1984.

[41] G. K. Gupta. Hydrodynamic stability of the plane poiseuille flow of an electro-rheological fluid. *Int. J. Non-linear Mech.*, 34:589–602, 1999.

[42] R. Haldenwang, P. Slatter, and R. Chhabra. The thin film approximation for laminar flow in open channels for non-Newtonian fluids. $9^{th}$ *Int. Seminar on Paste and Thickened Tailings, Cape Town, South Africa, 31 March - 2 April*, 2004.

[43] J. Harris. *Rheology and non-Newtonian Flow*. Longman Group, Ltd, 1977.

[44] I. A. Hassanien. Flow and heat transfer on a continuous flat surface moving in a parallel free stream of power law fluid. *Appl. Math. Modelling*, 20:779–784, 1996.

[45] G. T. Helleloid. On the computation of viscosity shear rate temperature master curves for polymeric liquids. *Morehead Electronic J. Appl. Math.*, 1:1–11, 2001.

[46] J. P. Holman. *Heat Transfer,* $6^{th}$ *edition*. McGraw-Hill, 1990.

[47] X. Huang and M. H. Garcia. Modelling of non-hydroplaning mud flows on continental slopes. *Marine Geology*, 154:131–142, 1999.

[48] W. S. Jana. *Introduction to Fluid Mechanics*. PWS-KENT, 1993.

[49] M. A. Jaworski and D. N. Ruzic. Facility to study surface tension driven MHD flows in liquid lithium: Solid/Liquid lithium diverter experiments (SLiDE). *Article in press*, pages 1–31, 2006.

[50] G. S. Karamanos and S. J. Sherwin. A high order splitting scheme for the Navier-Stokes equations with variable viscosity. *Appl. Numerical Math.*, 33:455–462, 2000.

[51] A. R. A Khaled. Conduction heat and entropy transfer in a semi infinite medium and wall with a combined periodic heat flux and convective boundary condition. *Int. J. Thermal Sci.*, 47:76–83, 2008.

[52] A. Kharab and R. B. Guenther. *An Introduction to Numerical Methods, a MATLAB Approach.* Charpman & Hall/CRC., 2002.

[53] Y. D. Kim and J. H. Kim. Synthesis of polypyrrole SBS composites and the particle size effect on the electrorheological properties of suspensions. *Synthetic Metals*, 158:479–483, 2008.

[54] D. Knezevic and V. Savic. Mathematical modelling of dynamic viscosity, as a function of temperature and pressure, of mineral oil for hydraulic systems. *Mech. Eng.*, 4(1):27–34, 2006.

[55] L. G. Leal. *Laminar Flow and Convective Transport Processes.* Butterworth & Heinemann, 1992.

[56] O. Levenspiel. *Engineering Flow and Heat Exchange.* Plenum Press, 1984.

[57] A. S. Lexmond and C. W. M. van der Geld. The effect of plate thickness, surface tension and fluid flow on detachment of drops from a plate. *Experimental Thermal Fluid Sci.*, 29:813–819, 2005.

[58] M. Liu and Y. F. Duan. Resistance properties of coal water slurry flowing through local piping fittings. *Experimental Thermal Fluid Sci.*, 33:828–837, 2009.

[59] P. A. Longwell. *Mechanics of Fluid Flow.* McGraw-Hill, 1966.

[60] I. Machać, B. Šiška, and R. Teichman. Fall of non-spherical particles in a Carreau model liquid. *Chem. Eng. Processing*, 41:577–584, 2002.

[61] C. W. Macosko. *Rheology, Principles, Measurements, and Applications.* VCH. Publishers, 1994.

[62] R. N. O. Magno, E. N. Macêdo, and J. N. N. Quaresma. Solutions for the internal boundary layer equations in simultaneously developing flow of power law fluids within parallel plates channels. *Chem. Eng. J.*, 87:339–350, 2002.

[63] M. A. A. Mahmoud. Variable viscosity effects on hydromagnetic boundary layer flow along a continuously moving vertical plate in the presence of radiation. *Appl. Math. Sci.*, 17(1):799–814, 2007.

[64] S. Mahmud and R. A. Fraser. Thermodynamic analysis of flow and heat transfer inside channel with two parallel plates. *Exergy Int. J.*, 2:140–146, 2002.

[65] C. R. M. Maia, J. B. Aparecido, and L. F. Milanez. Heat transfer in laminar flow of non-Newtonian fluids in ducts of elliptical section. *Int. J. Thermal Sci.*, 45:1066–1072, 2006.

[66] B. S. Massey. *Mechanics of Fluids,* $6^{th}$ *edition.* Chapman & Hall, 1989.

[67] M. Massoudi and T. X. Phuoc. Flow of a generalised second grade non-Newtonian fluid with variable viscosity. *Continum Mechanics Thermodynamics, Springer-Berli/Heidelberg*, 16(6):529–538, 2004.

[68] T. G. Mezger. *The Rheology Handbook.* Vincentz Verlag, 2002.

[69] S. Middleman. *An Introduction to Fluid Dynamics.* John Wiley & Sons, 1998.

[70] S. Miladinova, G. Lebon, and E. Toshev. Thin film flow of a power law liquid falling down an inclined plate. *J. non-Newtonian Fluid Mech.*, 122:69–78, 2004.

[71] E. Momoniat. Axisymmetric spreading of a thin drop under gravity and time-dependent non-uniform surface tension. *J. Math. Anal. Appl.*, 322:41–50, 2006.

[72] E. Momoniat, T. G. Myers, and S. Abelman. New solutions for surface tension driven spreading of a thin film. *Int. J. Non-linear Mech.*, 40:523–529, 2005.

[73] J. A. Moriarty, L. W. Schwartz, and E. O. Tuck. Unsteady spreading of thin liquid films with small surface tension. *Phys. Fluids*, 3(5):733–742, 1991.

[74] B. R. Munson, D. F. Young, and T. H. Okiishi. *Fundamentals of Fluid Mechanics, $3^{rd}$ edition.* John Wiley & Sons, 1998.

[75] T. G. Myers. Thin films with high surface tension. *SIAM Rev*, 40(3):441–462, 1998.

[76] T. G. Myers. Application of non-Newtonian models to thin film flow. *Physical Rev, E*, 72(1):1–11, 2005.

[77] T. G. Myers, J. P. F. Charpin, and M. S. Tshehla. The flow of a variable viscosity fluid between parallel plates with shear heating. *Appl. Math. Modelling*, 30:799–815, 2006.

[78] T. G. Myers, H. X. Liang, and B. Wetton. The stability and flow of a rivulet driven by interfacial shear and gravity. *Int. J. Non-linear Mech.*, 39(8):1239–1249, 2004.

[79] T. G. Myers and M. Lombe. The importance of the coriolis force on axisymemetric horizontal rotating thin film flows. *Chem. Eng. Processing*, 45:90–98, 2006.

[80] A. E. El Naby, E. E. M. El Misery, and M. F. A. El Kareen. Effects of a magnetic field on trapping through peristaltic motion for generalized newtonian fluid in channel. *Physica A*, 367:79–92, 2006.

[81] S. B. G. ÓBrien and L. W. Schwartz. Theory and modelling of thin film flows. *Encyclopedia Surface Colloid Sci.*, pages 5283–5297, 2002.

[82] H. Ockendon and J. R. Ockendon. *Viscous Flow.* Cambridge University Press, 1995.

[83] R. M. Olson. *Essentials of Engineering Fluid Mechanics, $3^{rd}$ edition.* Happer & Row, 1973.

[84] A. Oron, S. H. Davis, and S. G. Bankoff. Long scale evolution of thin liquid films. *Rev, Modern Phys. American Phys. Society*, 69(3):931–980, 1997.

[85] S. J. Palmer. The effect of temperature on surface tension. *Phys. Education*, 11(2):119–120, 1976.

[86] S. Park and D. R. Lee. Investigation of heat transfer and pressure drop between parallel channels with pseudoplastic and dilatant fluids. *J. Appl. Polymer Sci.*, 89:3601–3608, 2003.

[87] A. Pinarbasi and M. Imal. Viscous heating effects on the linear stability of poiseuille flow of an inelastic fluid. *J. non-Newtonian Fluid Mech.*, 127:67–71, 2005.

[88] A. Pinarbasi and A. Liakopoulos. The role of variable viscosity in the stability of channel flow. *Int. Comm. Heat Mass Transfer*, 22(6):837–847, 1995.

[89] B. K. Rao. Heat transfer to falling power law fluid film. *Int. J. Heat Fluid Flow*, 20:429–436, 1999.

[90] A. J. Raudkivi and R. A. Callander. *Advanced Fluid Mechanics*. Edward Arnold Publishers, Ltd, 1975.

[91] J. Rayner. *Basic Engineering Thermodynamics,* $4^{th}$ *edition*. Longman Sci., & Technical, 1987.

[92] B. Reisfield, S. G. Bankoff, and S. H. Davis. The dynamics and stability of thin liquid films spin coating: Films with unit-order and large peclet numbers. *J. Appl. Phys.*, 70(10):5267–5277, 1991.

[93] G. P. Roberts, H. A. Barnes, and P. Carew. Modelling the flow of very shear thinning liquids. *Chem. Eng. Sci.*, 56:5617–5623, 2001.

[94] A. B. Ross, S. K. Wilson, and B. R. Duffy. Blade coating of power law fluid. *Phys. Fluids*, 11(5):958–970, 1999.

[95] J. A. Schetz and A. E. Fuhs. *Fundamentals of Fluid Mechanics.* John Wiley & Sons, 1999.

[96] I. H. Shames. *Mechanics of Fluids,* $3^{rd}$ *edition.* McGraw-Hill, 1992.

[97] D. Y. Shang and H. I. Anderson. Heat transfer in gravity driven film flow of power law fluids. *Int. J. Heat Mass Transfer*, 42(1):2085–2099, 1999.

[98] V. Shevtsova. Thermal convection in liquid bridges with curved free surfaces: Benchmark of numerical solutions. *J. Crystal Growth*, 280:632–651, 2005.

[99] A. M. Siddiqui, A. Zeb, Q. K. Ghori, and A. M. Benharbit. Homotopy perturbation method for heat transfer flow of a third grade fluid between parallel plates. *Chaos, Solitons Fractals*, 36:182–192, 2008.

[100] B. Šiška, H. Bedová, and I. Machač. Terminal velocity of non-spherical particles falling through a Carreau model liquid. *Chem. Eng. Processing*, 44(2):1312–1319, 2005.

[101] C. Wafo Soh and E. W. Mureithi. Exact and numerical solutions of a fully developed generalized second-grade incompressible fluid with power law temperature dependent viscosity. *Int. J. Non-linear Mech.*, 41:271–280, 2006.

[102] J. Stastna, L. Zanzotto, and O. J. Vacin. Viscosity function in polymer modified asphalts. *J. Colloid Interface Sci.*, 259:200–207, 2003.

[103] R. T. Steller. Generalised slit flow of an Ellis fluid. *Polymer Eng. Sci.*, 41(11):1859–1870, 2001.

[104] J. T. Stuart. On finite amplitude oscillations in laminar mixing layers. *J. Fluid Mech.*, 29:417–440, 1967.

[105] K. M. Sundaram and G. Nath. Heat transfer to an Ellis model fluid flowing between parallel plates. *Chem. Eng. Tech.*, 47(2):71–84, 1975.

[106] M. Tachibana, N. Kawabata, and H. Genno. Steady laminar flow of power law fluids in the inlet region of a rectangular ducts. *J. Rheology.*, 30(3):517–538, 1986.

[107] G. A. Tokaty. *A History and Philosophy of Fluid Mechanics.* Henley-on-Thomas, 1971.

[108] S. M. Troian, E. Herbolzheimer, S. A. Safran, and J. F. Joanny. Fingering instabilities of driven spreading films. *Europhys. Letters*, 10(1):25–30, 1989.

[109] S. Y. Tsai and T. H. Hsu. Thermal transport of a continuous moving plate in a non-Newtonian fluid. *Comp. Math. Applications*, 29(6):99–108, 1995.

[110] M. S. Tshehla and T. G. Myers. The flow of a variable viscosity fluid over an inclined plane with a free surface. *To appear in: Quaestiones Mathematicae*, pages 1–20, 2008.

[111] M. S. Tshehla, T. G. Myers, and J. P. F. Charpin. *Advances in Fluid Mechanics VI, M. Rahman and C. A. Brebbia, (editors).* WITpress, 2006.

[112] E. O. Tuck and L. W. Schwartz. A numerical and asymptotic study of some third-order Ordinary Differential Equations relevant to draining and coating flows. *SIAM Rev*, 32(3):453–469, 1990.

[113] D. E. Weidner and L. W. Schwartz. Contact line motion of shear thinning liquids. *Phys. Fluids*, 6(11):3535–3538, 1994.

[114] S. Whitaker. *Introduction to Fluid Mechanics.* Prentice-Hall, 1968.

[115] F. M. White. *Fluid Mechanics,* $3^{rd}$ *edition.* McGraw-Hill, 1994.

[116] F. M. White. *Viscous Fluid Flow,* $3^{rd}$ *edition.* McGraw-Hill, 2006.

[117] J. J. Wylie and H. Huang. Extensional flows with viscous heating. *J. Fluid. Mech.*, 571:359–370, 2007.

[118] X. Zhao, J. K. Johnson, and C. E. Rasmussen. Surface tension of quantum fluids from molecular simulations. *J. Chem. Phys.*, 120(18):8707–8715, 2004.

[119] X. Zhao, G. K. Stylios, and R. M. Christie. Rheological behaviour of polymer solutions during fabric coating. *J. Appl. Polymer. Sci.*, 107:2317–2321, 2008.

[120] L. C. Zheng and X. X. Zhang. Skin friction and heat transfer in power law fluid laminar boundary layer along a moving surface. *Int. J. Heat Mass Transfer*, 45(35):2667–2672, 2002.